Effect of grain size and Gd-Co substitutions on multiferroic $BiFeO_3$ thin films

A
Thesis
Submitted for the award of the degree of

DOCTOR OF PHILOSOPHY

By

Shiwani Sharma

(Registration No. 901012010)

Under the supervision of

Dr. Puneet Sharma
Associate Professor

Dr. O.P Pandey
Senior Professor &
Dean (R&SP)

School of Physics and Materials Science

Thapar University, Patiala-147004

(Punjab) INDIA

October 2016

Dedication

This thesis is dedicated to my loving and supportive family

My parents for their faith, support and passionate encouragement to achieve this dream

My beloved husband whose love, patience, acceptance and guidance have been my strength to keep me moving forward in a positive direction

&

Above all my dearest daughter Saanvi for her adorable smile and patience

Certificate

This is to certify that the thesis entitled **"Effect of grain size and Gd-Co substitutions on multiferroic $BiFeO_3$ thin films"** is a bonafide record of research work done by **Ms. Shiwani Sharma** (**Reg. No. 901012010**) being submitted to the School of Physics and Materials Science, Thapar University, Patiala for the award of the degree of **Doctor of Philosophy.**

In our opinion, the thesis has reached the standard of fulfilling the requirements of all the regulations related to the degree. The work presented in the thesis has not previously formed the basis for the award of any other degree, fellowship or any other title. The present thesis represents the independent and original work on the part of the candidate under my guidance.

Dr. Puneet Sharma
Associate Professor,
School of Physics and Materials Science,
Thapar University,
Patiala-147004 ,
Punjab (INDIA).

Dr. O.P Pandey
Senior Professor & Dean Research and
Sponsored Projects,
School of Physics and Materials Science,
Thapar University,
Patiala -147004,
Punjab (INDIA).

Dated: 13-10-2016

Place: Patiala

Acknowledgment

I pay my profound gratitude to the almighty GOD with whose grace I have been able to complete this work.

Though there are no words to express my gratitude, yet with a deep sense of regards I sincerely thank my esteemed and revered teacher, learned guide and Supervisor **Dr. Puneet Sharma**, Associate Professor, Thapar University Patiala without whose keen personal interest, constant encouragement, invaluable guidance and meticulous supervision this study would not have seen the light of the day. I am highly indebted to his immeasurable help and benevolent patronage.

It is my proud privilege to acknowledge with deep respect, the able and expert advice on the subject, unabated inspiration rendered by my honorable supervisor **Dr O.P Pandey**, Dean Research and sponsored projects, for providing the possible research facilities here at Thapar University campus. His keen interest, invaluable guidance and persuasive nature provided me enthusiasm and confidence for timely completion of my thesis. Diction is not enough to express my deep sense of gratitude and wishes to place my sincere and heartiest regards to **Dr. P. Saravanan**, Scientist 'E' Advanced Magnetics Group, Defence Metallurgical Research Laboratory, Hyderabad for his valuable guidance, encouragement, moral support and SQUID measurements.

I offer my special thanks to **Dr. Manoj Sharma**, Head, School of Physics and Materials Science, **Dr. Kulvir Singh**, Associate Dean, Thapar University Patiala, for providing all the necessary facilities in the department. I am thankful to my doctoral committee members; **Dr. B. N. Chudasama**, **Dr. S. D. Tiwari** and **Dr. Bonamoli Pal**, for their useful suggestions. I also wish to express my thanks to **Dr. D.P. Singh**, **Ms. Loveleen Brar**, **and Dr. Alka Upadhyay** for their valuable guidance**,** encouragement and moral support. I am also thankful to all the faculty and staff of School of Physics and Materials Science for their support. I gratefully acknowledge the University Grants Commission (UGC) for the fellowship (letter no. - SPMS/UGC/607).

I would like to thank SAI lab, Thapar University for XRD and SEM facilities. My special thanks to **Mani Mahajan,** my friend who has been with me all these years and who critically reviews my work and was always there to lend a friendly word of encouragement. I convey

my heartiest thanks to my labmates and all those who directly or indirectly have given me their full co-operation and devoted valuable time, for rendering their needy services, guidelines during the course of my thesis work.

Most of all, I would like to thank my family for their love, moral support and inconvenience experienced by them during the course of my thesis work. It would not have been possible for me to achieve this goal without their understanding and support. The amount of appreciation of their patience and generosity is enough for me. My greatest heartiest regards to a very special person whose moral support is precious to me; my husband, **Dr. Vishal Malhotra**, who nagged at just the right time and offered unwavering encouragement. Writing this thesis would not have been possible without him that gave me time and energy to work with the voluminous data. This thesis is dedicated to my mother- the woman who did everything for me and my loving daughter **Saanvi Malhotra** who taught me to happily do the same for her.

October, 2016 **Shiwani Sharma**

List of Publications

1. **Shiwani Sharma,** P. Saravanan, O.P. Pandey, V.T.P. Vinod, Miroslav Černík and Puneet Sharma **"Magnetic behaviour of sol-gel driven $BiFeO_3$ thin films with different grain size distribution"**, Journal of Magnetism and Magnetic Materials 401 (2016) 180–187.

2. **Shiwani Sharma,** P. Saravanan, O.P. Pandey, and Puneet Sharma **"Grain size distribution dependent magnetic and ferroelectric properties in sol-gel driven $BiFeO_3$ thin films"**, J Mater Sci: Mater Electron 27(6) (2016) 5909-5915.

3. **Shiwani Sharma,** Alok Mishra, P. Saravanan, O.P. Pandey, and Puneet Sharma **"Effect of Gd-substitution on the ferroelectric and magnetic properties of $BiFeO_3$ processed by high-energy ball milling"**, Journal of Magnetism and Magnetic Materials 418 (2016) 188-193. (Not included in thesis)

4. **Shiwani Sharma,** P. Saravanan, An-Cheng Sun, O.P. Pandey, and Puneet Sharma **"Observation of delayed magnetic transition in Gd-Co substituted $BiFeO_3$ thin films"**. (Communicated)

Conferences and Workshops Attended

1. **Shiwani Sharma**, P. Saravanan, O.P. Pandey, and Puneet Sharma "Micro-structural and morphological properties of sol gel driven $BiFeO_3$ thin film" 2nd Conference on "Microscopy In Materials Science" and 2nd Annual Meeting of Academy of Microscope Science & Technology (AMST-2016) 25-27 Feb., 2016, Thapar University, Patiala, India.

2. **Shiwani Sharma,** P. Saravanan, O.P. Pandey, and Puneet Sharma "Thickness induced grain size distribution dependent magnetic properties in sol-gel driven $BiFeO_3$ thin films" International Conference on Magnetic Materials and applications (ICMAGMA-2015), 2-4 Dec, 2015, VIT University, Vellore, India.

3. Alok Mishra, **Shiwani Sharma**, O.P. Pandey and Puneet Sharma "Effect of gadolinium substitution on the properties of high energy milled multiferroic $BiFeO_3$" National Seminar on Advanced Materials and Devices (NSAMD) held on (3-4 July, 2011) in GVM College Sonipat, Haryana, India.

4. Attended Summer School on Magnetism (SSM-2016), jointly organized by Thapar University, Patiala and Magnetic Society of India (MSI) 11-15 July, 2016, Thapar University, Patiala. India.

5. National Workshop on Advanced Techniques for surface characterization, 28-30 Oct, 2015, Thapar University, Patiala, India.

6. Attended 23rd Annual General Meeting of Materials Research Society of India (AGM: MRSI), (Functional Materials for sustainable Energy and Advanced Technologies), 13-15 Feb, 2012, Thapar University, Patiala, India.

Table of Contents

List of Figures

List of Tables

Symbols Used

T_N	Ne`el temperature
T_c	Curie temperature
Y^{obs}	Observed profile
Y^{cal}	Calculated profile
R_p	Profile residual factor
R_{wp}	Weight profile residual factor
R_{exp}	Expected profile residual factor
χ^2	Chi square
$C.S.$	Crystallite size
β	Full width half maxima
M	Magnetization
H	Magnetic field
M_s	Saturation magnetization
H_c	Coercivity
M_r	Remanent magnetization
$\tan \delta$	Dielectric loss
α	Magnetoelectric coupling coefficient
μ	relative permeability
P_r	Remanent polarization
P_s	Saturation polarization
E	Electric field
E_c	Coercive field (Electric)
ε_r'	Real part of dielectric constant
ε_o	Permittivity of free space
R_q	Root mean square roughness
f	Frequency
k_B	Boltzmann constant
λ	Wavelength
R	Resistance
C	Capacitance
C_g	Grain capacitance

Abbreviations Used

BFO	Bismuth ferrite
ITO	Indium tin oxide
FTO	Fluorine doped tin oxide
XRD	X-ray diffraction
FESEM	Field emission scanning electron microscopy
EDX	Energy dispersive X-ray spectroscopy
AFM	Atomic force microscopy
TEM	Transmission electron microscopy
SAED	Selected area diffraction
SQUID	Superconducting quantum interference device
EB	Exchange bias
FC	Field cooled
ZFC	Zero field cooled
VSM	Vibrating sample magnetometer
FWHM	Full width half maxima
RT	Room temperature
SG	Space group
Hz	Hertz
MHz	Megahertz
M-H	Magnetic hysteresis loop
P-E	Ferroelectric hysteresis loop

Abstract

Multiferroics has attracted attention of researchers worldwide due to its fundamental and technological applications. Amongst multiferroics $BiFeO_3$ (BFO) is the only known material to possess ferroelectric Curie temperature (T_C=1143K) and antiferromagnetic Ne`el temperature (T_N=643 K) well above room temperature. BFO crystallizes in a rhombohedrally distorted perovskite structure with *R3c* space group at room temperature. This is analogous to the hexagonal setting that contains six formula units of BFO in it with lattice constants a_h = 5.587 Å, c_h = 13.867 Å. The antiferromagnetic ordering of BFO is G-type having a spiral spin modulation with an incommensurate long-wavelength period of ~ 62 nm. Due to its antiferromagnetic nature; bulk BFO shows ineffectual magnetism that limits its device applications. On the other hand low resistivity of BFO leads to large leakage current limiting its ferroelectric applications. To overcome these limitations, attention has been diverted towards synthesis of thin films. Till date various techniques have been used to prepare and optimize conditions for preparation of BFO thin films. Considering the great potential of large magneto-electric effect in thin films, efforts have been made by researchers in the production of quality thin films of BFO. The magnetization and ferroelectric behaviour in BFO can be tailored by altering the grain size by adopting different methodology which includes varying annealing temperature and the film thickness. Besides, low level substitution of rare earth metal ions at Bi^{3+} site or transition metal ions at Fe^{3+} site also affects the magnetic and electrical properties. However, the recent approaches in the preparation of high quality polycrystalline thin films restrict the formation of grains with uniform size. It is therefore necessary to investigate the effect of grain size distribution to further reveal the intricate magnetic and electrical behaviour of BFO thin films. The present work focuses on the grain size distribution dependent magnetic and electrical properties of sol-gel driven BFO thin films. Further, the effect of substitution of Gd ion at Bi site and Co ion at Fe site has been studied. Also, the effect of simultaneous substitution of Gd and-Co has been investigated.

A layout of the thesis has been summarized below:

The thesis is organized into five chapters:

Chapter I (Introduction) The chapter gives a brief introduction about the magnetoelectric effect and multiferroics. Further, the classification of multiferroic materials based on its

ferroelectric origin and their future applications is briefly summarized. Finally, the chapter concludes with the motivation and objectives of the present work.

Chapter II (Literature review) In the present chapter crystal structure, magnetic structure and phase relationship of BFO are outlined. Further an extensive review of the research carried out on bulk BFO, nanopowders and thin films is summarized.

Chapter III (Experimental and characterization techniques) The chapter details the processing methodology adopted for synthesizing pure and Gd-Co substituted BFO thin films of different compositions. A brief description of the various characterization techniques employed for studying structural, micro structural, dielectric, ferroelectric, and magnetic properties are given.

Chapter IV (Results and discussion) This chapter details the experimental results of pure, Gd-Co substituted BFO thin films. This chapter is divided into two sections. In the first section the effect of annealing time, annealing temperature and film thickness on the properties of BFO thin films has been described. After selecting an optimized time the focus is laid on the selection of an optimized temperature where an optimal grain size distribution corresponds to high saturation magnetization (M_s), which is done by annealing the films between 525 and 600 °C. Afterwards the effect of varying thickness on BFO thin films has been discussed systematically by annealing the films at an optimized temperature of 575 °C. In the second section the effect of substitution and co-substitution of Gd ion at Bi site, Co ion at Fe site on the structural, magnetic and electrical properties has been investigated by annealing the films of constant thickness at 575 °C.

Brief summary of the results are given below:

Effect of grain size variation

To investigate the effect of grain size single-phase, polycrystalline BFO thin films were prepared. The grain size variations were imparted by adopting two methodologies. First, by annealing the films of constant thickness (200 nm) at different annealing temperature (525 °C to 600 °C) and second, by annealing the films of different thicknesses at constant temperature (575 °C).

Effect of annealing temperature

The study details the effect of grain size on multiferroic BFO thin films induced by varying the annealing temperature. BFO thin films were synthesized by the sol-gel spin-coating technique followed by annealing at different temperatures. The effect of annealing temperature on structural and magnetic properties of BFO thin film has been investigated. Single phase polycrystalline BFO films are confirmed by X-ray diffraction patterns. A strong dependence of grain size on annealing temperature was observed. All the films showed a well saturated *M-H* loops. However, the BFO film annealed at 575 ºC showed the maximum saturation magnetization (M_s). The grain-size distribution is found to broaden with increase in annealing temperature. The SQUID magnetic measurements demonstrated a weak ferromagnetic behaviour for the BFO films at 300 K as well as at 10 K, due to uncompensated spins generated by the breaking of spiral ordering. The observed magnetic properties in the BFO films depend entirely on the cumulative effect of uncompensated moments originating from the variation in grain-size distribution. An optimal grain-size distribution obtained at 575 °C is responsible for the high magnetization in the BFO film. The field cooled and zero field cooled (FC-ZFC) magnetization curves depict a rise in magnetization at lower temperature with an onset of spin glass state ~300 K.

Effect of film thickness

The study details the effect of grain size on multiferroic BFO thin films induced by varying the thickness. BFO thin films were synthesized by the sol-gel spin-coating technique followed by annealing at 575 °C. A particular optimized annealing temperature of 575 °C has been selected based on the above mentioned study and BFO thin films of varying thickness were prepared by annealing at 575 °C. The effect of grain size variation induced by thickness variation on structural, magnetic, dielectric and ferroelectric properties of BFO thin film has been investigated. Single phase polycrystalline BFO films are confirmed by X-ray diffraction patterns. A strong dependence of grain size on thickness variation has been observed. All the films showed a well saturated *M-H* loops with 156 nm thick BFO film showing the maximum M_s and 388 nm thick BFO film showing maximum remanent polarization (P_r). The ferroelectric properties improved due to better growth and densification with increasing film thickness. Appreciable increase in dielectric constant (ε') and corresponding decrease in dielectric loss ($\tan\delta$) with increase in BFO film thickness has been observed.

Effect of Gd and Co substitution in BFO thin films

It is concluded that the grain size variation has significant effect on magnetic behaviour of BFO thin films. Besides, the grain size variation; low level substitution of rare earth metal ions at Bi sites or transition metal ions at Fe sites is an alternative method for achieving enhanced magnetic and electrical properties, which is also reported to suppress the cycloidal spin structure. Following this, in this section the effect of substitution of Gd and Co ions at respective Bi and Fe sites on the structural, dielectric, ferroelectric and magnetic properties were investigated.

Effect of Gd substitution

Sol-gel driven $Bi_{1-x}Gd_xFeO_3$ (x=0, 0.05, 0.075, 0.100, 0.125) (BGFO) thin films have been studied for their structural, dielectric, ferroelectric and magnetic behaviour. The Rietveld refinement confirmed the formation of pure phase as well as the structural transformation from rhombohedral (*R3c*) to orthorhombic ($Pn2_1a$) with increasing Gd content in the film. FESEM and TEM images showed well-crystallized equiaxed grains with minimal porosity. The dielectric and ferroelectric properties improve with better densification of grains in the BGFO thin films with increasing Gd-content. The ε' at 100 Hz increases from 210 (x=0) to 3534 (x=0.10) whereas, tanδ decreases from 12.34 (x=0) to 1.02 (x=0.1). Ferroelectric loops with increase in P_r from 0.032 to 3.5 $\mu C/cm^2$ with increasing Gd content due to preferred (110) orientation and structural distortion has been observed. The saturation magnetization (M_s) is 7.18 and 27.93 emu/cm^3 for x=0 and x=0.10 BGFO thin films respectively. BGFO films with x=0.10 shows remarkable enhancement in M_s as compared to x=0 composition. Substitution with Gd has influential effect on M_s that may be due to greater lattice distortion and suppression of spiral spin cycloid due to decreased grain size. The measurement of T_N is made with high temperature FC-ZFC magnetization curves of BGFO thin films.

Effect of Co substitution

The multiferroic behaviour of sol-gel driven $BiFe_{1-y}Co_yO_3$ (y=0, 0.05, 0.075, 0.100 and 0.125) BFCO thin films with uniform thickness of ~200 nm has been investigated. FESEM micrographs showed well-crystallized equiaxed grains with minimal porosity. Lattice fringes with d-spacing of 0.28, and 0.27 nm has been observed for y=0 and 0.075 BFCO thin films. The dielectric and ferroelectric properties improve with better densification of grains with increasing Co content in the films. The ε' at 100 Hz increases from 210 (y=0) to 422 (y=0.075) whereas, tanδ decreases from 12.34 (y=0) to 5.38 (y=0.075). The effect of Co

substitution on ferroelectric behaviour is observed with P_r increasing from 0.023 (y=0) to 0.256 μC/cm^2 (y=0.125). The saturation magnetization (M_s) values for y=0 and y=0.075 BFCO thin films were 7.18, and 20.16 emu/cm^3 respectively indicating the ferromagnetic behavior of the system due to the presence of uncompensated spin at the grain boundaries and due to uncompensated moments at the surface. The high temperature FC-ZFC magnetization curves of BFCO thin films showed flat broad maxima near T_N.

Effect of Gd-Co substitution

Thin films of $Bi_{1-x}Gd_xFe_{1-y}Co_yO_3$ (x=0, 0.100; y= 0, 0.075) (BGFCO) of ~200 nm thickness were deposited via sol-gel assisted spin coating method. The XRD patterns were refined by the multiprofile Rietveld technique using FULLPROF program. The structure of polycrystalline BFO thin film changes from distorted rhombohedral to orthorhombic with Gd-Co substitution. FESEM micrographs showed dense microstructure with well-crystallized equiaxed smaller grains having a significant decrease in grain size from 96 to 28.96 nm with Gd-Co substitution. HRTEM images showed lattice fringes with d-spacing of 0.28 and 0.26 nm for x=0, y=0 and x= 0.100, y=0.075 BGFCO thin films. The dielectric and ferroelectric properties improve with better densification of grains in the Gd-Co codoped BFO thin films. S-shaped ferroelectric loops with P_r= 0.125 and 0.25 μC/cm^2 has been observed for Gd-Co substituted thin films. Well saturated M-H loops with enhanced M_s ~ 30.83 emu/cm^3 due to Gd-Co substitution is observed. Measurement of T_N has been done from the high temperature FC-ZFC magnetization plots for the BGFCO films.

Chapter V (Conclusions and future scope) gives the important conclusions and future scope in this field of research.

Chapter I

Introduction

Overview

The chapter gives a brief introduction about the magnetoelectric effect and multiferroics. Further, the classification of multiferroic materials based on its ferroelectric origin and their future applications is briefly summarized. Finally, the chapter concludes with the motivation and objectives of the present work.

1.1 Magnetoelectric effect and multiferroics

The observation of magnetic and electric field vectors and the coupling among them has prompted the researchers worldwide to exploit this effect in various technological applications. The dynamics of the intrinsic coupling between the electric and magnetic fields vectors are governed theoretically by the Maxwell's equation [1]. In 1888 Rontgen observed magnetization in a moving dielectric body under an applied electric field and the polarization in the same dielectric body when exposed to magnetic field [2]. The prediction of possible occurrence of magnetoelectric (*ME*) effect was first given by P. Curie in 1894 [3], but the term "*ME*" was coined in 1926 by P. Debye illustrating the coupling of magnetic and electric orders i.e inducing magnetization (electric) by an external electric (magnetic) field [4]. The real beginning of this started in 1959 by Landau and Lifshitz [5]. The *ME* effect in crystals can be understood on the basis of Landau theory by expanding free energy (F) of the crystal in terms of applied electric field ($\boldsymbol{E}$) and magnetic field ($\boldsymbol{H}$) [5] as,

$$F(\boldsymbol{E},\boldsymbol{H}) = F_o - \boldsymbol{P_i^s E_i} - \boldsymbol{M_i^s}.\boldsymbol{H_i} - \frac{1}{2}\boldsymbol{\varepsilon_o \varepsilon_{ij} E_i E_j} - \frac{1}{2}\boldsymbol{\mu_o \mu_{ij} H_i H_j} - \boldsymbol{\alpha_{ij} E_i H_j} - \frac{1}{2}\boldsymbol{\beta_{ijk} E_i H_j H_k} - \frac{1}{2}\boldsymbol{\gamma_{ijk} H_i E_j E_k} - \cdots \quad (\mathbf{1})$$

Differentiating the above equation *w.r.t* $\boldsymbol{H}$ and $\boldsymbol{E}$ gives the value of $\boldsymbol{M}$ and $\boldsymbol{P}$ as [5],

$$\boldsymbol{M_i}(\boldsymbol{E},\boldsymbol{H}) = -\frac{\partial F}{\partial \boldsymbol{H_i}} = \boldsymbol{M_i^s} + \boldsymbol{\mu_o \mu_{ij} H_j} + \alpha_{ij}.\boldsymbol{E_i} + \boldsymbol{\beta_{ijk} E_i H_j} + \frac{1}{2}\boldsymbol{\gamma_{ijk} E_j E_k} + \ldots \quad (\mathbf{2})$$

$$\boldsymbol{P_i}(\boldsymbol{E},\boldsymbol{H}) = -\frac{\partial F}{\partial \boldsymbol{E_i}} = \boldsymbol{P_i^s} + \boldsymbol{\varepsilon_o \varepsilon_{ij} E_j} + \alpha_{ij}.\boldsymbol{H_j} + \frac{1}{2}\boldsymbol{\beta_{ijk} H_j H_k} + \boldsymbol{\gamma_{ijk} H_i E_j} + \cdots \quad (\mathbf{3})$$

where, F_o is free energy independent of $\boldsymbol{E}$ and $\boldsymbol{H}$, $\boldsymbol{P}$ and $\boldsymbol{M}$ denotes spontaneous polarization and spontaneous magnetization, μ_{ij} and ε_{ij} represents the relative permeability and relative permittivity respectively. The forth term on right side of equation (1) gives contribution from electrical response to an $\boldsymbol{E}$. The fifth term is the magnetic equivalent of the first term. The sixth term describes the first order linear *ME* coupling through 'α' defined as the linear *ME* coupling coefficient and it will correspond to induction of $\boldsymbol{P}$ by $\boldsymbol{H}$ or induction of $\boldsymbol{M}$ by $\boldsymbol{E}$. The other terms in the equation depicts higher order *ME* coupling coefficients. The above equations (2) and (3) shows that coefficient of $\boldsymbol{P}$ against external $\boldsymbol{H}$ is basically the transposed tensor of coefficient of $\boldsymbol{M}$ against $\boldsymbol{E}$**.** Therefore, the prevalent cause of *ME* effect is the polarization, deformation of electron clouds and displacement of atoms induced by $\boldsymbol{E}$.

The phenomena of *ME* effect can thus be more suitably expressed in terms of ***M*** and ***P*** rather than ***H*** and ***E***. Furthermore, the *ME* response is limited by the relation

$$\alpha_{ij} = \sqrt{\boldsymbol{\mu_o \varepsilon_o \mu_{ij} \varepsilon_{ij}}} \qquad (4)$$

Considering the dependence of 'α' on μ and ε the ferromagnetic (ferroelectric) materials could be considered as prime candidates for enhanced *ME* effect as they possess large magnetic (dielectric) susceptibility [6-9]. Hence, such materials that simultaneously have two or more primary ferroic properties were termed as "Multiferroics" [10]. The *ME* effect and *ME* multiferroics has been a topic of interest to researchers since last four decades. A schematic representation showing the concept of multiferroic and the *ME* materials have been shown in Fig. 1.1. The blue region represent multiferroic and *ME* materials respectively. Multiferroics now includes those materials that present any sort of the long range magnetic ordering, ferroelasticity, or spontaneous electric polarization [6].

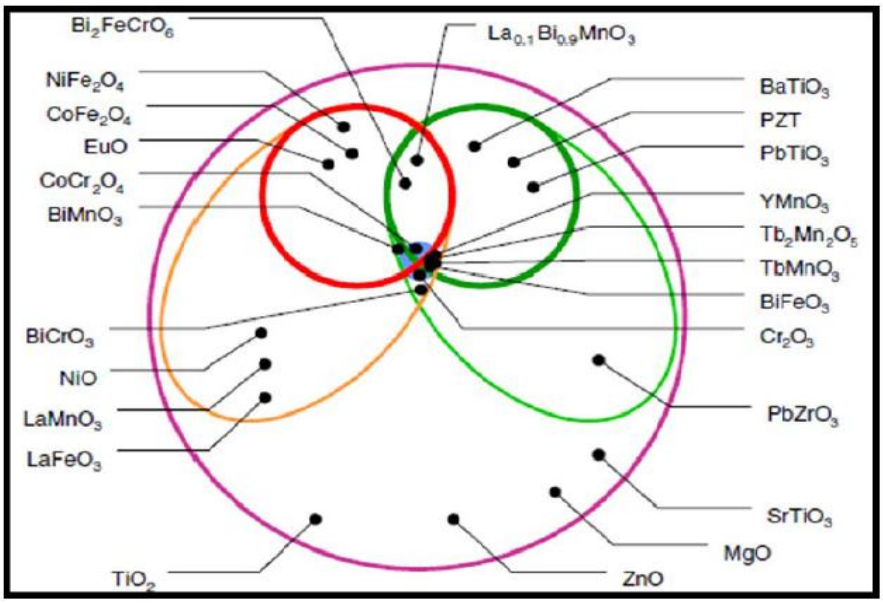

Fig.1.1 Relation between the multiferroic and *ME* materials. Ferromagnetic (red) and ferroelectric (dark green) form a subset division of the magnetically (orange) and electrically (light green) polarizable materials. The intersecting region of ferromagnetic and ferroelectric loop represents multiferroic materials. *ME* coupling (blue) is represented as an independent phenomenon which can, but necessarily need not arise in any material that will simultaneously show magnetically and electrically polarizable behavior. [6]

After the theoretical demonstrations, *ME* effect was first successfully witnessed in antiferromagnetic Cr_2O_3 [11, 12] and prompted researchers to synthesize and discover *ME* effect in many other materials [10-12]. The few important materials which show *ME* effect are $BiFeO_3$, $BiMnO_3$, $LuFe_2O_4$, $TbMnO_3$ etc [13-18]. Based on the origin of coupling in mentioned materials the multiferroics are further classified in Type I and Type II. Fig. 1.2

shows relationship between ferroelectricity (***P*** and ***E***), magnetism (***M*** and ***H***), and ferroelasticity [15] and the coupling between the ferroic orders.

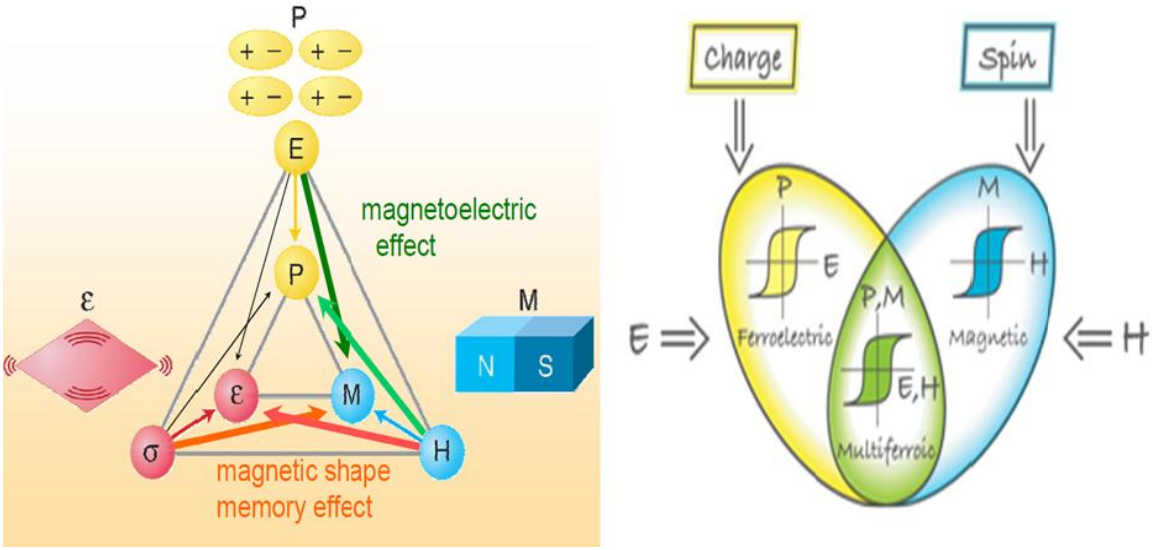

Fig.1.2 Interaction between the ferroelectricity (***P*** and ***E***), magnetization (***M*** and ***H***), and ferroelasticity (strain $\boldsymbol{\varepsilon}$ and stress $\boldsymbol{\sigma}$) along with coupling of these parameters. [15]

1.2 Types of multiferroics

The basis of magnetism is usually the same in magnetic materials i.e the presence of unpaired electrons mainly in partially filled *d* or *f* shells of the transition metal ion or rare-earth ions that have a resultant magnetic moment. The exchange interactions between the nearby localized moments lead to occurrence of magnetic order. But the scenario with ferroelectrics is somewhat different as there are numerous microscopic sources of its origin. Therefore, depending on the cause of origin of ferroelectricity the categorization of multiferroics is done accordingly.

- In Type-I multiferroics, magnetism and ferroelectricity have different origin and occur independently of each another, though they have some coupling between them. They are usually considered good ferroelectrics; the critical temperature of the ferroelectric and magnetic transitions is well beyond room temperature (*RT*) but the *ME* coupling between magnetic and ferroelectric orders is usually rather weak. As compared to magnetism the ferroelectricity in these multiferroics can exists even at very high temperatures, and the spontaneous polarization ***P*** often found to be very large (~10-100 μC/cm^2) [6-8]. Based on the cause of ferroelectricity in the system, there are different sub-classifications of type-I

multiferroics. (a) *Charge ordered multiferroics* oftenly seen in transition metal compounds with different valence states. These ions create a polar arrangement within the system leading to ferroelectricity. The existence of magnetic ion lead to coupling of magnetic and ferroelectric order. The phenomenon of such coupling is reported in $LuFe_2O_4$ that exhibit improper ferroelectricity at temperature below 330 K and ferrimagnetic behavior observed below 240 K [16]. The arrangements of electrons in this system occur due to charge frustration in a triangular lattice that have mixed valence states of Fe^{2+} and Fe^{3+} ions [16, 17]. (b) *Geometrically frustrated multiferroics*, in which structural phase transition at higher temperatures results in ferroelectricity. The ***P*** arises from the off-centre buckling or distortion of magnetic Mn-ions towards any one of the edged (apical) oxygen ions. For example the family of $RMnO_3$ (R-Ho, Lu or Y) i.e., hexagonal rare earth manganites shows a structural phase transition~1300 K leading to tilting or rotation of rigid polyhedra of MnO_5 trigonal bipyramids [19-21]. (c) L*one pair driven multiferroics* in which B-site ions causes ***M*** to occur and A-site ions through lone pair presence lead to ferroelectricity. Such phenomenon is observed in $BiMnO_3$, $BiFeO_3$ and $PbVO_3$, where Bi^{3+} and Pb^{2+} have key role in ferroelectricity origin. Particularly in these ions, the two outer 6s electrons called as "lone pairs" that do not participate in bonding. The ferroelectricity origin in such multiferroics was explained by shifting and ordering of these lone pairs along a particular direction giving rise to ferroelectricity. The A-site cation i.e Bi^{3+} and Pb^{2+} has a stereochemically active $6s^2$ lone-pair that causes the empty 6p orbital of Bi to come closer to energy level of 2p orbitals of O. This lowering of energy resulted in hybridization between the 6p orbitals of Bi and 2p orbitals of O that drives off-centering of cation towards neighbouring anion resulting in ferroelectricity [22].

- Type-II multiferroics are those where magnetism is responsible for ferroelectricity origin and hence cause a strong *ME* coupling between the magnetic and ferroelectric order [23, 24]. The polarization in comparison to type I multiferroics materials is usually much smaller (~ 10^{-2} $\mu C/cm^2$) [7]. Type-II multiferroics are further divided into two groups: (a) *"Spiral type-II multiferroics"* in which a particular type of magnetic spiral ordering causes ferroelectricity to occur. For example in $TbMnO_3$ where magnetic ordering occurs at Ne`el temperature (T_{N1}) =41 K, and at a lower temperature called as lock in transition temperature (T_{N2}) =28 K, magnetic structure changes. A non zero electric polarization appears only in the low-temperature phase. Somewhat similar behavior appears in $TbMn_2O_5$ [23, 24]. (b) *"Type-II multiferroics with collinear magnetic structures"* in which

ferroelectricity appears for the collinear magnetic structures i.e., all the magnetic moments are aligned along a definite axis without the required association of spin-orbit interaction. For example, at high temperature in Ca_3CoMnO_6 the distances between one-dimensional chains of alternating Co^{2+} and Mn^{4+} ions are the same, the chain possesses inversion symmetry with no polarization [25]. Magnetic ordering breaks the inversion symmetry i.e., the spins form ↑↑↓↓ type of magnetic structure. The ***P*** in these multiferroics appears as a consequence of exchange striction as magnetic coupling changes with atomic positions i.e., the distortion of the ferro and antiferro bonds (↑↑ & ↑↓) becomes different [26].

1.3 Importance of multiferroics in technological applications

The sensing /actuating industry depend extremely on ferroelectric materials, whereas the data storage industry relies heavily on ferromagnetic materials, therefore a material simultaneously possessing two or more of the ferroic properties are novel materials for designing such advance devices. For high density data storage, multiferroic bits can be used as a 4 stage memory i.e two magnetic M↑↓ and the two ferroelectric P↑↓ to store information in ***M*** and ***P*** [27-30]. Such type of memory doesn't require coupling between ferroelectricity and magnetism. Hence multiferroics provide a possible way in fabricating devices with data splitting over two mediums (magnetization ***M*** and the polarization ***P***) that can be stored and transmitted over compact devices in a faster and secure way than is currently possible. Therefore, it can be exploited for manufacturing memory elements where one can write using a voltage and read via magnetic field [31]. It can also be used in spintronics as tunnel junction barriers, as magnetically field-tuned capacitors where the frequency dependence of the electronic circuits can be tuned by magnetic fields, or as multiferroic sensors that measure magnetic fields through the zero field current measurements [32, 33].

1.4 Motivation and Objectives

Among the various Type I and Type II multiferroic materials it is clearly demonstrated from Table I that $BiFeO_3$ (BFO) is the only multiferroic whose Curie temperature (T_C) and Neel temperature (T_N) is far above *RT*. BFO has attracted much attention of researchers due to two main reasons. One, it is the only single phase multiferroic which shows room temperature *ME* coupling and other is its inherited peculiar magnetism that stimulated the interest of physicist as well as material scientists. BFO has a rhombohedrally distorted perovskite structure which belongs to the *R*3*c* space group.

Table 1.1 List of Multiferroics

Multiferroic		Neel temperature T_N (K)	Lock in transition temperature	Curie temperature T_C (K)
Type-I	$LuFe_2O_4$ [16]	230	-	340
	$BiMnO_3$ [34]	105	-	750
	$BiFeO_3$ [34]	653	-	1083
	$YMnO_3$ [35]	77	-	950
Type-II	$HoMnO_3$ [36]	76	33	875
	$TbMnO_3$ [23]	41	28	< 28
	$TbMn_2O_5$ [24]	33	27	38
	$GdMnO_3$ [37]	43	23	
	$DyMnO_3$ [38]	39	18	
	Ca_3CoMnO_6 [39]	13	-	48

The unit cell of BFO can be represented as pseudo cubic (a_c = 3.963 Å); and hexagonal (a_h = 5.587 Å, c_h = 13.867 Å) structure, where pseudo cubic direction $[111]_c$ is equivalent to $[1\ 0\ 0]_h$ [40, 41]. The spontaneous ***P*** in BFO is directed along one of the [111] directions of perovskite structure [27]. The exchange interaction between the neighbouring Fe magnetic moments within the $(0\ 0\ 1)_h$ planes is ferromagnetic and antiferromagnetic along $[110]_h$ [40, 41]. The magnetic structure of BFO has been studied by Kiselev *et al.* [42], who suggested G-type antiferromagnetic spin configuration, wherein each Fe^{3+} ion is surrounded by six antiparallel nearest neighbours. However, Sosnowska *et al.* [43], interpreted the origin of ***M*** in terms of magnetic cycloid structure with a long period of 62±2 nm along the $[1\ 1\ 0]_h$ direction. Several reports suggest that bulk BFO does not show ferromagnetic behavior, whereas BFO nanopowders reflect the evidence of ferromagnetism where ***M*** shows an inverse relationship with the particle size [44-50]. The high ***M*** in fine particles is explained on the basis of distortion of spin spiral structure giving uncompensated moments. Similar behavior is also observed in thin film structure. It was concluded that decreasing particle/grain size plays a key factor for obtaining high ***M***. Till date the available approaches to grow polycrystalline thin films have restricted the formation of uniform grain size. The magnetization in BFO arises due to cumulative effect of uncompensated surface moments from different grain-size distributions. Therefore, any induced variation in the grain size distribution may lead to the variation in uncompensated surface spin density and brings a noticeable difference in the properties. Study on annealing temperature or thickness induced

grain size distribution will provide a better understanding of structure property relationship in BFO thin films. Considering the fact that any variation in the annealing temperature or film thickness consequently imparts variation in grain size distribution; it is therefore necessary to investigate the effect of grain size distribution rather than the film thickness, to further reveal the complex structural, magnetic and electrical behaviour of BFO thin films.

The ***M*** can also be enhanced by doping at Bi^{3+} and Fe^{3+} sites which reportedly distorts the spiral structure. An extensive work on bulk BFO and nanopowders has been carried out. However, a systematic study of grain size variation, induced by different approaches lags behind in sol-gel driven BFO thin films. Also the effect of substitution of Gd and Co ions at Bi and Fe sites respectively are yet to be investigated. Therefore the main focus of the present work is to examine the grain size and Gd-Co substitution on the structural, electrical and magnetic properties of BFO thin films. Worth to mention that along with thorough studies on structural and electrical properties of BFO films, the main focus is to understand the intricate magnetism in such thin films.

Chapter II

Literature Review

Overview

In the present chapter crystal structure, magnetic structure and phase relationship of BFO are outlined. Further an extensive review of the research carried out on bulk BFO, nanopowders and thin films is summarized.

After a path breaking theoretical studies of *ME* effect [2, 3] and an experimental evidence of *ME* coupling in Cr_2O_3 [9, 11-12, 51] and in $TbMnO_3$ [23] various other *ME* multiferroics were studied afterwards [13-18, 52-57]**.** Among the various multiferroics BFO is one of the extensively studied materials due to its high T_N and T_C that is well above *RT*. The characteristic features and the important work carried out are described below.

2.1 Crystal and Magnetic structure of BFO

BFO is an oxide that belongs to the family of perovskite with the general formula ABO_3, (A can be mono, di, or trivalent and B a penta, tetra, or trivalent element, respectively). In BFO, both Bi and Fe are trivalent to balance the six negative charges of the three oxygen atoms [58]. BFO is well known to prevail in rhombohedrally distorted perovskite structure with *R*3*c* space group. The atomic structure of BFO was given as rhombohedral containing two formula units of BFO with space group *R3c* in its unit cell [40, 41]. However, due to off centring shift of the Fe^{3+} caused by the shifting of oxygen initiated by the stereo-chemically active lone pair of Bi^{3+} the magnitude of ion shift observed within the unit cell for Bi is 0.62 Å along the [111], 0.23 Å along [111] for Fe and 0.30 Å along [111] for O with ± 0.03 Å for all the mentioned values [40, 59]. The spontaneous *P* in BFO is directed along one of the [111] directions of perovskite structure [27] (Fig. 2.1).

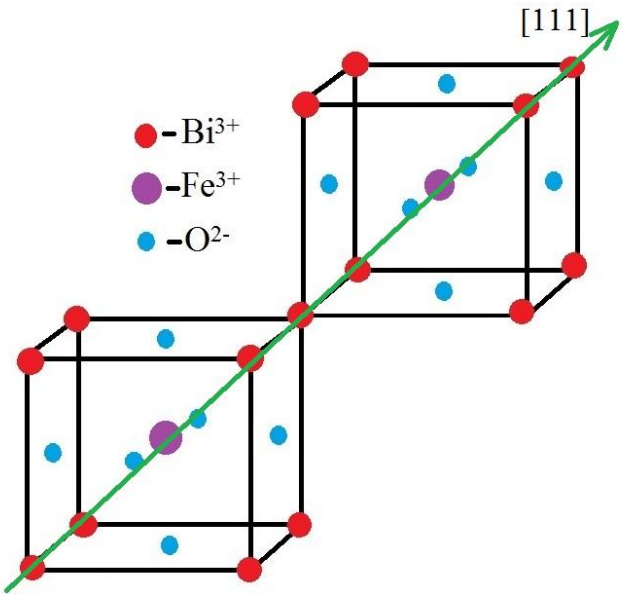

Fig. 2.1 Crystal structure of BFO

The rhombohedral structure of BFO is analogous to hexagonal setting embodying six formula units of BFO within it having lattice constants as a_h = 5.587 Å and c_h = 13.867 Å in which hexagonal c-axis is parallel to diagonals of perovskite cube i.e. $[001]_{hex}$// $[111]_{pseudo}$

[59-61]. Fig. 2.2 shows the unit cell of BFO in hexagonal and pseudo-cubic arrangement of *R*3*c* space group.

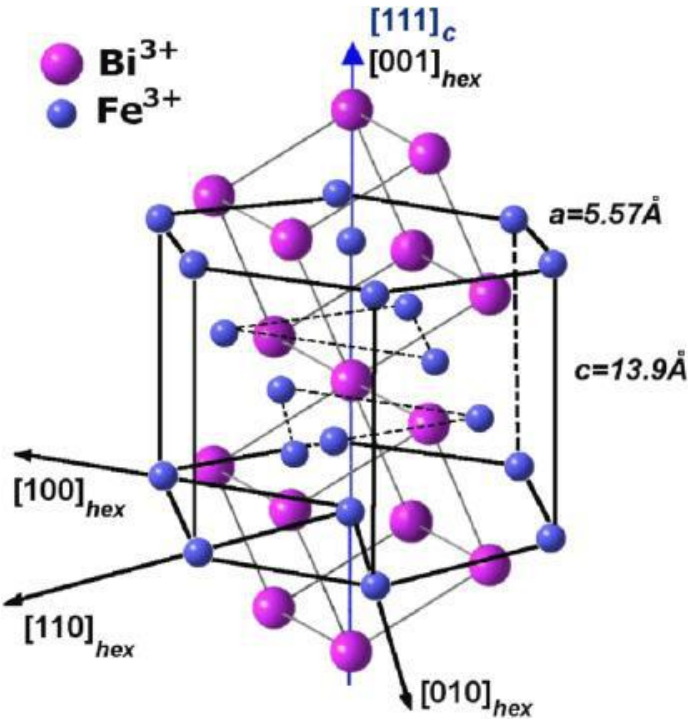

Fig. 2.2 Unit cell of BFO in hexagonal and pseudo-cubic arrangement of *R*3*c* space group [62].

The perovskite unit cell has a lattice parameter of a_{rh} =3.965 Å with a rhombohedral angle of α_{rh}= 89.3–89.4° at room temperature possessing ferroelectric polarization along $[111]_{pseudo}$ direction [43, 63-65]. The oxygen anions unit cell is slightly displaced from the centre of the unit cells for each of the two cations. This sort of separation of charges inside the unit cell generates a net electric dipole moment, imparting the system its ferroelectric properties [58]. The rotation or revolving angle of oxygen octahedra is one of the vital structural parameter. For a cubic perovskite having perfectly matched ionic sizes, this rotation angle would be zero. The ratio $(r_{Bi}+r_o)/\iota$ measures how perfectly the ions fit in a perovskite unit cell, with 'r' as the ionic radius of respective ions and ι, the length of the octahedral edge and is analogous to the most commonly used Goldschmid tolerance factor usually defined as $t=(r_{Bi}+r_o)/\sqrt{2}(r_{Bi}+r_o)$ [66]. From the ionic radii of Shannon t=0.88 [67] with Bi^{3+} in eight fold coordination and Fe^{3+} in six fold coordination with high spin. When the above ratio is smaller than one then, the oxygen octahedra should buckle so as to fit in a cell which is usually very small. For $BiFeO_3$, [40, 60, 68] ω is ca. 11–14° around the polar [111] axis with the directly related Fe–O–Fe angle, θ = 154–156°. The Fe–O–Fe angle serves dual purpose here in the sense that it controls equally the magnetic exchange and overlapping of orbital between Fe

and O, and is therefore, responsible for determining the magnetic ordering temperature and conductivity [60, 61].

The magnetic structure of BFO is G-type with cycloid spiral arrangement of Fe^{3+} ions where the antiferromagnetic axis rotates throughout the crystal with an incommensurate long wavelength period of ~62 nm with propagation vector along [110] direction [43, 69]. The magnetic dipoles arise from the unpaired spins on the Fe^{3+} cations. After a number of comprehensive studies through various techniques, Sosnowska *et al.* in 1982 [43] first suggested the spin cycloid model of BFO [63, 64, 70-72]. Fig. 2.3 represents spin cycloidal model of BFO showing two antiferromagnetic sublattices structured along a cycloidal spiral. Propagation vector q is directed along [110] with the plane of spin-rotation along (1 1 0) [73]. The plane in which the spins rotate called as magnetic easy plane is specified by a propagation vector and a polarization vector. The spins indeed altogether are not antiparallel due to weak canting moment caused by local magnetoelectric coupling to polarization [74]. However, superimposed on this canting is a long range splendid structure of an incommensurate spin cycloid of antiferromagnetically structured/organized sublattices.

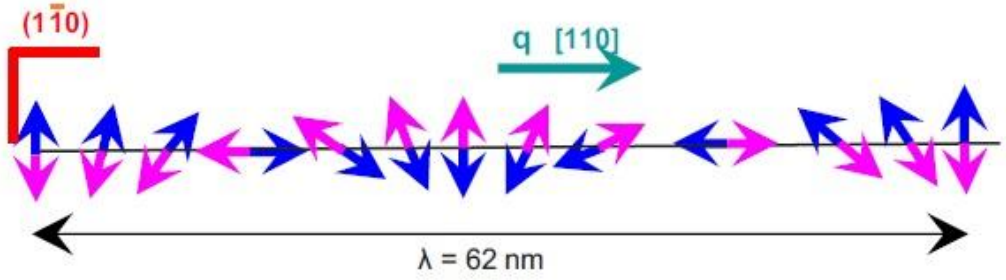

Fig. 2.3 Representation of spin cycloidal model of BFO showing two antiferromagnetic sub-lattices structured along a cycloidal spiral. The 'q' called as propagation vector is directed along [110] with the plane of spin-rotation along (1 $\bar{1}$ 0) [73].

2.2 Phase Diagram of BFO

BFO is a multiferroic where ferroelectricity is driven by hybridisation effects [27, 44, 54] and it has been synthesised in various forms like ceramics [27], crystals [69], nanopowders [27], and thin films [45, 75]. Tremendous efforts were made to enhance the *ME* properties of BFO perovskite by adopting different approaches. The most common is processing of pure BFO by chemical methods or solid state synthesis method without any impurity phase and another is by suitable chemical substitution for *A* and *B* site *i.e.* Bi and Fe sites. The various methods which are generally employed for the synthesis of BFO are (a) Solid state reaction

method in which the raw materials (Bi_2O_3 and Fe_2O_3) are allowed to react at 800–830 °C and secondary phases (Bi_2O_3/$Bi_2Fe_4O_9$) were removed by leaching in HNO_3 [76], (b) Autocombustion Method [77], which is based on propellant chemistry criteria with thermally induced redox reaction between an oxidant and fuel. An external supply of heat is required to instigate the ignition of reactants leading to self sustaining exothermic redox reaction, and (c) sol gel route [78-82] (or the chemical route), in which the compound/salts were diffused in a solvent in order to bring it back as solid in a very controlled manner or to form a viscous gel for thin film formation via spin coating method. The process needs careful monitoring of molar ratios of reactants and their dissolution in particular solvent to avoid any precipitation.

At the beginning BFO was usually prepared from equal parts of Bi_2O_3 and Fe_2O_3. In general, during BFO synthesis formation of parasitic phases occurs that nucleate near or at grain boundaries. Therefore, it is a challenge to produce single phase BFO. The phase diagram of Bi_2O_3 and Fe_2O_3 is shown in fig 2.4. The phase diagram shows that stoichiometry is an important parameter to produce single phase BFO. As, the melting point and calcination temperature of BFO is very close to each other therefore, it can decompose back to the starting materials according to the equation. [27]

$$2BiFeO_3 \rightarrow Fe_2O_3 + Bi_2O_3$$

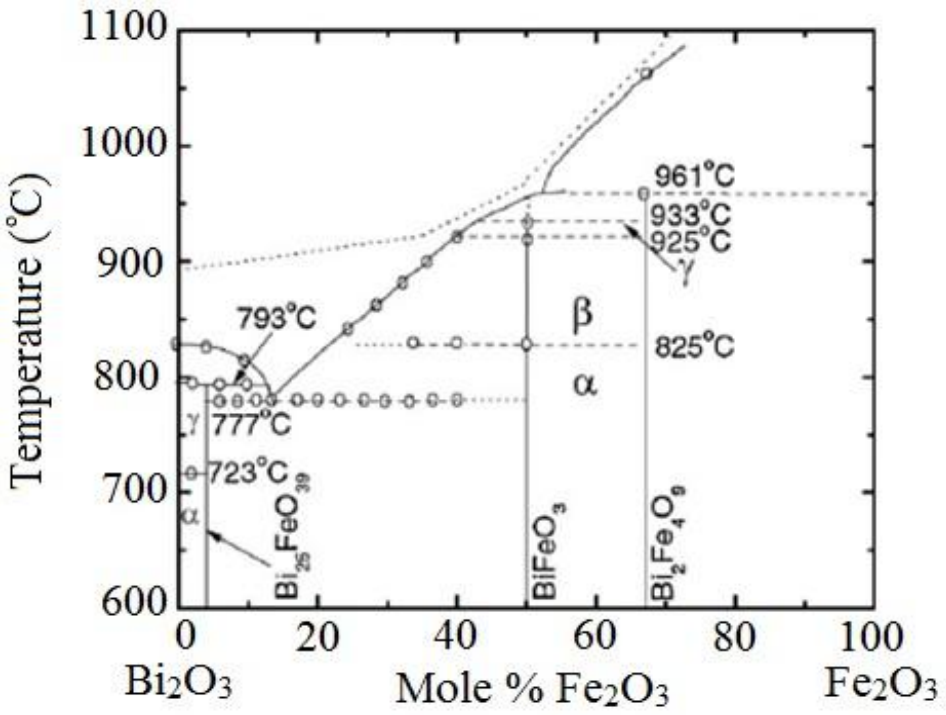

Fig. 2.4 Phase Diagram of Bi_2O_3 –Fe_2O_3 system [27, 83]

The phase diagram also confirms that BFO is unstable at high temperature leading to β–γ transition and its rapid decomposition into secondary phases such as $Bi_2Fe_4O_9$ or Fe_2O_3 [27]. The essentiality of leaching the undesired phases with acid and providing effectually a coarser powder is a major drawback of the solid state reaction method and also the reproducibility of the procedure is poor. Basically, the high temperature treatments (>800 °C) mostly leads to bismuth volatilization; therefore, low temperature synthesis methods are desired to overcome this problem [79]. The synthesis of BFO by ferrioxalate precursor technique with 0.5 metal ions to oxalic acid ratio has resulted in production of pure phase (90%) BFO when calcined at 600 $^{\circ}$C for 2 hour [80]. It results in the particle size in nanometer range and has got benefit over the initially used conventional solid state synthesis. It is well reported that a single phase BFO is achievable through chemical processing route [78, 81-82]. Being one of the inexpensive methods, it requires optimization of various parameters like temperature, stirring speed, and time etc. for achieving single phase BFO either in bulk or in the form of thin films.

BFO shows semiconducting behaviour at and above *RT*, making its electric poling very difficult due to which high dielectric losses were observed in the sample. This makes it difficult to measure the ferroelectric properties of bulk BFO at and above *RT*. Initially, small values of *P* and *M* were observed in bulk BFO samples that made researchers worldwide to overcome this issue by doping with rare earth or transition metal ion at the respective Bi^{3+} or Fe^{3+} sites [84-87]. Though some enhancement in *P* and *M* was observed but the technological implementation was an issue of concern [54]. For making better use in potential applications leakage density has to be reduced along with an enhancement in the dielectric, ferroelectric and magnetic properties; paves way towards the production of high quality thin films of BFO [44, 88-89]. Herein we gave a brief review on the work done in past few decades pertaining to various properties like structural, electrical and magnetic of pristine and doped bulk BFO, nanopowders and thin films.

2.3 Studies on bulk BFO

Multiferroics have recently gained a considerable attention due to their multifunctional device applications and underlying new physics. BFO is one of the widely investigated materials due to its ferroelectric and magnetic transition temperature well above *RT* [6, 27]. BFO perovskite was first produced in late 1950s by Royen *et al.* [90] and most of studies done during that time were focused on concepts that were important even today i.e., potential

for *ME* coupling [60]. Later Smolensky [91] in the year 1959 synthesized BFO but that was not suitable for practical application due to the presence of undesired secondary phases. However, Achenbach in the year 1967 [76] successfully produced single phase BFO by leaching the undesired phases using nitric acid. Kubel and Schmid in 1990 examined the mono domain single-phase using XRD [60]. Over the past several years, extensive efforts were made to achieve both strong ferroelectric and ferromagnetic polarizations. It has already been reported in literature that other than long Bi-Fe bond distance, lattice parameter (*a* and *c*), volume 'V' of the unit cell, short bond distances between Bi and Fe along with the bond angles gradually increases on increasing temperature. Apparent to these variations, *M* and *P* gradually falls, inducing a very clear structural transformation from rhombohedral (*R3c*) to orthorhombic (*Pnma*) at 1098 K and to a cubic above 1204 K [92].

Researchers have done a considerable work on processing techniques and microstructural aspect to improve BFO properties [93-95]. Enhancing magnetization by reducing the particle size of BFO was the greatest obstacle to overcome. Henceforth, the effect of rare earth and transition metal ion substitution has been investigated on structural, electric and magnetic properties [96-98]. The partial substitution of rare-earth elements (*RE*) (La, Pr, Nd, Gd, Dy, Ho) at Bi-site reportedly eliminated the secondary phases along with the structural phase transition, improved ferroelectric and magnetic properties in BFO ceramic [96-103]. However, the relationship between structural evolution and magnetic properties in doped BFO ceramics still need to be further investigated. Mathe *et al.* [104] observed a structural phase transition to orthorhombic ($x = 0.6$) and triclinic ($x = 0.8$) with La^{3+} substitution at Bi^{3+} site. The variation of dielectric constant (ε') with temperature shows a broad peak that broadens with varying composition and shifts corresponding to frequency change reflecting relaxor-type behaviour [104]. Palkar *et al.* [105] studied the coexistence of ferroelectricity and ferromagnetism in $Bi_{0.9-x}Tb_xLa_{0.1}FeO_3$ powder samples ($0 < x < 0.3$) and the samples were found to exhibit high dielectric constant and *ME* coupling at *RT*. The temperature-dependent magnetic measurement in single phase BFO indicated *RT* antiferromagnetic behaviour. Though ferroelectric hysteresis loops were saturated in BFO ceramics synthesized at 880 °C, the *P* was less due to high loss and low permittivity caused by high leakage current [93]. A clear structural transformation from rhombohedral to orthorhombic has been observed for $x = 0.3$ in $Bi_{1-x}La_xFeO_3$ that enhanced *ME* interaction in the system [96].

In case of Nd doped BFO a number of structural transitions were observed depending on the value of dopant concentration '*x*'. Transformation of structure starting from rhombohedral at $x = 0$, triclinic between $x = 0.05–0.15$, and a pseudo tetragonal between $x= 0.175–0.2$ has been reported [97]. On the other hand $Bi_{1-x}Nd_xFeO_3$ ceramics synthesized via rapid liquid phase sintering method reportedly lead to structural phase transition from rhombohedral to monoclinic for $x = 0.0 - 0.15$ [100]. Ferroelectromagnetic measurements revealed existence of ferroelectricity with P_r of ~9 μC/cm^2 for x=0–0.175, paraelectricity for x=0.2, and a weak ferromagnetism with M_r of 0.07–0.227 emu/g in x=0.15–0.2 compositions. *ME* coupling was observed for x=0.15–0.175 near T_N~380 °C. The same group further polarized the samples and studied piezo and pyro-electric effects in substituted samples [100].

The success in polarization of ceramics originated from the controlled low electrical conductivities basically by Poole-Frenkel conduction process. Limited internal traps from reduced oxygen vacancies resulted in lowering leakage current densities <30 mA/m^2 even at a high strength of the applied electric field. Before and after annealing the samples at 550 °C for nearly 4 hour, the piezoelectric coefficients (d_{33}) of ~28 and ~24 pC/N were obtained respectively. The d_{33} values were higher than generally most of lead-free high-temperature piezo-electric ceramics. In the same year, Yuan and his group investigated the effect of Sm substitution in BFO [106]. The triclinic structure with space group *P1* showed large d_{33} of 29 pC/N, and higher remnant polarization ~15.09 μC/cm^2 at *RT*, leading to long-range ferroelectric order on a macroscopic scale. The small M_r of 0.071 emu/g at *RT* due to collapse of spin cycloid indicated the existence of canted antiferromagnetic order over a long range [106]. The *ME* coupling was exposed by the increase in dielectric constant with increasing *H*. For $Bi_{0.75}Ba_{0.25}FeO_3$ with H = 8 kOe, the values of $[\varepsilon_r(H) - \varepsilon_r(0)/\varepsilon_r(0)]$ were 1.7% and 1% at 80 and 300 K, respectively [107]. Su *et al.* [95] prepared single phase BFO ceramics (named as BFO-1) one by sol-gel method and another by high-pressure synthesis (named as BFO-2). The lattice parameters of BFO-2 were altered due to high pressure process. The enhanced *M* should be ascribed to suppression of magnetic spin cycloid and by change of canting angle in BFO-2. The values of P_r and E_c were 46 μC/cm^2 and 73 kV/cm, respectively under an applied electric field of 120 kV/cm. The better crystallization, high density, structural distortion and high resistivity accounted for better ferroelectric and enhanced magnetic properties in BFO-2 [95].

Substitution by rare earth Gd ion at Bi site was found to induce structural phase transition from *R3c* to *Pn2₁a* at *x*=0.1. Further increase in '*x*' suppressed the spontaneous polarization (P_s) in $Bi_{1-x}Gd_xFeO_3$ and resulted in a phase transition from ferroelectric to paraelectric (*Pn2₁a*→ *Pnma*) around 0.2 < *x* < 0.3 [101-102, 108]. Fanggao *et al.* [109] showed that substituting Gd^{3+} at Bi^{3+} site eliminates the impurity phases in BFO ceramics; also the lattice constants *a* and *c* become smaller as the Gd^{3+} content is increased. A remarkable change in the dielectric constant and loss with Gd-substitution has been observed. The intervention of Zn in chains of Fe atom weakened the antiferromagnetic Fe ions spin chains and enhanced the paramagnetic properties. Slope of the *M–H* curve of $BiFe_{0.95}Zn_{0.05}O_3$ was reported to be 1.1×10^{-5} $emug^{-1}$ Oe^{-1}, which was larger than linear part of the *M–H* curve of BFO (6.2×10^{-6} $emug^{-1}$ Oe^{-1}), giving stronger paramagnetism in $Bi(Fe_{0.95}Zn_{0.05})O_3$. Ferromagnetism in BFO was attributed to lattice distortion inducing enhanced spin canting of Fe^{3+} ions [110]. The temperature dependent properties of $Bi_{0.91}La_{0.05}Tb_{0.04}FeO_3$ ceramics revealed phase transition ~ 700 °C. The temperature dependent dielectric behaviour demonstrated a dielectric abnormal peak ~ 697 °C, along with the two well known dielectric abnormal peaks ~337 °C (T_N) and 831 °C (T_C). All the observations with thermal depoled behaviour, suggested a phase transition from *R3c* to *Pbnm* at around 700 °C [111]. Xu *et al.* [112] reported enhanced, M_s of 1.6 emu/g and M_r of 0.7 emu/g at in $BiFe_{0.95}Co_{0.05}O_3$ ceramics at 300 K with an observed clear metamagnetism. Raman study indicated compressive lattice distortion induced by Co substitution at Fe sites [112]. Ramachandran *et al.* [113] reported anomalies close to low temperature phase transitions in the magnetic entropy change of BFO ceramics. The relative errors in magnetic entropy change were found to vary from 4% to 15% with increasing temperature. At 1100 and 1190 K BFO showed α-β and β-γ phase transitions respectively. The decomposition occurred at 1226 and 1256 K, compared to BFO single crystal. FC-ZFC plots demonstrated spin glass behaviour below 150 K, and weak ferromagnetic nature below 10 K were observed in *M-H* measurements [113].

Catalan *et al.* [114] synthesized the Ca-BFO ceramic samples by sol-gel route and observed an increase in T_N with Ca substitution at a rate of 0.66 K per 1% of Ca (molar), consistent with charge compensation by generation of O vacancies making iron to stay in oxidation state of +3. Hence the change in T_N was entirely via structural effects and not by changes in magnitude of Fe spin. They argued that hydrostatic pressure should increase T_N of BFO at a rate of around $\partial T_N/\partial P$~2.2 K/GPa. They suggested that any pressure whether its chemical or is hydrostatic, could be used to bring T_C and T_N closer together, thereby,

enhancing *ME* coupling provided very low electrical conductivity should be maintained [114]. La doped $BiFeO_3$, $Bi(Fe_{0.95}Co_{0.05})O_3$ and $Bi(Fe_{0.95}Mn_{0.05})O_3$ ceramics were prepared by sol–gel rapid sintering technique. Impurity phases get suppressed effectively on La doping. 10% doping of La at Bi sites slightly influences the *M* of BFO and $Bi(Fe_{0.95}Co_{0.05})O_3$, but improves the *M* in $Bi(Fe_{0.95}Mn_{0.05})O_3$ [115]. A P_r of 4 μC/cm^2 and *M* of 0.153 emu/g has been observed in $Bi_{0.7}Ca_{0.3}FeO_3$ composition along with an observation of converse *ME* effect. Ferroelectric loops were observed at *RT* owing to high resistivity and the suppression of charge defects, whereas, enhanced magnetic properties were due to suppression of space spin-modulated magnetic structure in these BCFO ceramics [116]. When the samples were field cooled from 350 to 10 K, exchange bias field (HEB), vertical magnetization shifts (M Shift) and enhanced M_s were observed in $Bi_{1/3}Sr_{2/3}FeO_3$, which shows strong dependence on the cooling field's strength. Furthermore, HEB shows a linear dependence on M-Shift. The observed EB effect is explained in terms of exchange coupling between ferromagnetic clusters and spin-glass like phases at the interface [117]. La-modified BFO (with x = 0.2 and 0.4) ceramic powders were synthesized by ferrioxalate precursor method at a relatively low temperature. La-substitution in BFO promoted the perovskite phase with maximum elimination of unwanted phases leading to pure phase formation at x=0.4 composition. Improved leakage current and dielectric characteristics were obtained for x=0.4 composition. An enhanced magnetic moment attributed to pure phase formation and broken spin structure was observed for x = 0.4 composition [118].

Enhanced ferromagnetic and dielectric properties in $Bi_{1-x}La_xFeO_3$ (x = 0.0, 0.1, 0.2, and 0.3) micro-particles were attributed to structure distortions caused by La-substitution. The morphologies of particles changes from spheroidal to octahedral as per doping levels. The ε′ increased on La doping, attaining maximum value for x = 0.2. M_s enhanced from 0.264 emu/g for x=0 to 0.658 emu/g for x=0.1 in 3 T field at 77 K. The observed enhancements in magnetic moments and dielectric properties were attributed to the changes in lattice parameters and bond lengths of Fe–O on La substitution [119]. At x = 0.10, phase transition from rhombohedral to orthorhombic in single-phase $Bi_{1-x}Y_xFeO_3$ oxides has been observed. Enhanced *M* and low band-gap of $Bi_{1-x}Y_xFeO_3$ ceramics make them fit for potential *ME* plus photo catalytic applications [120]. Sen *et al.* [121] in the year 2010 synthesized $BiCo_xFe_{1-x}O_3$ (with x varying from 0.0-0.25) ceramics by combustion technique with an average particle size of 16–20 nm for the 800 °C calcined sample. The dielectric properties improved with Co-substitution. No saturation observed in the ferroelectric loops of Co substituted BFO ceramics

[121]. The P_r along with switching characteristic enhanced at low fields by reduced leakage current apart from enhanced magnetic moment on Ho substitution in bulk BFO [103]. Role of co-doping of 20% La at Bi-site and 10% Mn at Fe-site showed structural transition to orthorhombic (*Pnma*) on La doping whereas, no structural change occurred on Mn doping. DTA showed a fast decrease in ferroelectric transition temperature ($\boldsymbol{T_C}$) on La-doping and slowly on Mn-doping. Enhanced magnetization in $Bi_{0.8}La_{0.2}Fe_{0.9}Mn_{0.1}O_3$ was due to introduction of mixed valance state, suppression or partial destruction of spiral spin cycloid [122]. As the most important difficulty in implementing BFO for practical applications was its compositional instability associated with inconstancy of functional behaviour. Therefore sorting out this issue was essential if BFO has to be succeeded to be used as technologically relevant material. This led to a fast growing area of research devoted in manufacturing and characterizing complex nanoscopic structures other than ceramics. Such three dimensional BFO nanostructures have their own confined distinctive size effects that may be due to large fraction of uncompensated moments at the surface of nanocrystals [123, 124].

2.4 Studies on BFO nanopowders

The early work deals with the production of bulk BFO ceramics. In order to enhance its magnetic and electrical properties, some of Bi^{3+} or Fe^{3+} sites have been replaced with rare earth and transition metal ions. However, its implementation for technological applications was a big challenge due to high leakage current issues and low values of magnetic moments. This diverted the attention of researchers towards synthesis of nanoparticles via sol gel route. The major interest was on improving the *M* by the suppression of the spin cycloidal structure by synthesizing BFO nanoparticles below ~62 nm. It was in the year 2004 when Wong reported BFO nanotubes with 240–300 nm diameter and length 50 mm synthesized via sol gel route using long porous alumina template (AAO) technique [125]. The alumina templates were removed by using NaOH leaving piles of nanotubes that made their electrical characterization very difficult. This led Kim *et al.* [94] in 2005 to synthesize BFO powders of particle size ~200 nm mainly with rhombohedral phase having dielectric constant of 15 in 10^4~10^6 Hz frequency range at *RT*. The minor Bi_2O_3 secondary phase was leached out using diluted HNO_3 from the BFO samples annealed at 600 °C in N_2 ambience. DTA analysis showed reversible phase transformation at 836 and 821 °C while heating and cooling respectively. Nanopowders synthesized via sol-gel route significantly lower the formation

temperature of pure phase BFO. A low-temperature (200°C) hydrothermal synthesis route using KOH resulted in submicron sized BFO powders with a T_C of 825 °C [126].

Size induced magnetism was reported for BFO nanopowders [127] and nanowires [124] due to presence of large fraction of uncompensated spins at the surface of the BFO nanocrystals. Later in the year 2007 Park *et al.*, [123] showed a strong correlation between the particle size and magnetic properties of BFO nanoparticles with M_s ~1.55 emu/g for 14 nm particle. He correlated the magnetic properties with increased suppression of the cycloidal spin spiral with decreasing particle size, to the uncompensated spins and the strain anisotropies at their surface. They attributed the observed spin glass behaviour to very intricate relationship between the finite size effects and the inter-particle interactions, and to random distribution of the anisotropy axes in synthesized nanoparticles assemblies. The formation of BFO nanoparticles by the addition of a suitable polymer helps in decreasing the growing speed of BFO nuclei was successfully studied by Wang *et al.* [128]. BFO nanoparticles of about 10 nm size and sphere shaped were synthesized at 160 °C by polymer assisted hydrothermal technique. Annealing temperature and heat treatment time are critical parameters for synthesizing pure BFO phase. Using urea as fuel BFO was prepared via sol-gel combustion method and the obtained powders were heated thermally at temperature between 300–840 °C and for 1–64 hour time interval. 99 molar % of BFO phase with a mean particle size of 120 nm were obtained after annealing the samples at 600°C for 1 hour. Thermal treatment of samples above or below this temperature or in air or argon up to 64 hour gives higher number of secondary phases according to the reaction,

$$49\ BiFeO_3 \rightarrow 12\ Bi_2Fe_4O_9 + Bi_{25}FeO_{39}$$

indicating the fact that BFO was not thermodynamically stable at 600 °C [129]. In one such process by using NH_3 as a precipitant and NaOH as a mineralizer single-phase BFO powders were produced at 180°C with measured T_N, T_C and decomposition temperature of 301, 828 and 964 °C respectively [130]. The micro-morphology of BFO powders seem to be affected with varying reaction temperatures and varying concentrations of NaOH. Morphology seems to vary from lamellar to nano-lines as temperature varied from 160 to 180 °C and from lamellar structure to double-layered plates as concentration of NaOH varied from 0.2 mol/L to 0.15 mol/L [130]. Nanocrystalline BFO ultrafine fibers were synthesized with 100–300 nm diameters and 20 nm average grain size by Xie *et. al.* [131] in 2008. Impurity phases were eliminated or minimized after firing the obtained BFO fibers in Ar atmosphere. Excellent ferroelectricity and enhanced M_s ~4 emu/g and H_c ~200 Oe from the nanocrystalline structure

of BFO ultrafine fibre was attributed to their nanometer grain size. Large amplitude piezo-response force microscopy (PFM) signals were recorded in many regions of the BFO fibres separated by the boundaries where amplitude nearly reaches zero and thus flips the phase of PFM signal. The domains of opposite *P* show same PFM amplitude and hence, indistinguishable in an amplitude image. The domain walls exhibited themselves in PFM amplitude image as within the domain walls *P* was reduced, resulting in somewhat smaller PFM amplitude [131]. BFO nanocubes with size between 50-200 nm showed photo-induced water oxidation activity in both photo-catalytic and photo-electrochemical modes making it useful for photo-electrode and photo-catalytic applications [132]. Single phase $La_{0.5}Bi_{0.5}Mn_{0.5}Fe_{0.5}O_{3.09}$ powders with orthorhombic structure prepared by sol-gel method were grounded, pressed in the form of parallelepiped bars, sintered at 1223 K for 24 hour in O_2 atmosphere exhibited ferromagnetic transition near 240 K and a significant reversible P_r below 67 K. The magnetic interaction was due to the ferromagnetic Fe^{3+}–O–Mn^{3+} and antiferromagnetic Fe^{3+}(Mn^{3+})–O–Fe^{3+}(Mn^{3+}) interactions competeting with each other [133].

Multiferroic material that have good value of ε' and show ferroelectricity and ferromagnetism in same phase were of great importance in technological applications [77]. $Bi_{0.9}Pb_{0.1}Fe_{0.9}Ti_{0.1}O_3$ (BPFTO), with 15–25 nm particle size showed significant enhancement in magnetic moment with M_r of 285 memu/g and P_r, P_m of 1.056 and 1.866 μC/cm^2 respectively at 20 kV/cm. Dielectric studies confirm its multiferroic nature with T_N of ~310°C and T_C ~600°C [77]. Single phase nanocrystalline BFO with average crystallite size ~25 nm with very high *M* at *RT* showed deviation between FC and ZFC magnetization above *RT* and a T_N below 645 K. Observation of broad magnetic transition above T_N of BFO that extended up to 800K suggested presence of Fe_3O_4 as magnetic impurity phase that was confirmed by the detailed XRD of the sample. Therefore, the observed high ferromagnetic component was due to contribution of Fe_3O_4 (magnetite) and hence was not an intrinsic property of the system [134]. The same year they reported [135] the changes in magnetic properties of nanocrystalline BFO with average crystallite sizes of ~50 and ~100 nm attributed to the observed phase transitions at sufficiently low temperatures and the changes in domain structure as evident from the FC-ZFC magnetization plots. Remarkable enhancement of ferromagnetic property was achieved on synthesizing nanoparticles of 30-100 nm diameter range by doping BFO with Mn and Sr at low temperature. The synthesized nanoparticles diameter was controlled by tuning tartaric acid concentration. Mn, Sr doped BFO

nanoparticles with perfectly improved ferroelectric and ferromagnetic properties were considered important for ferro-electromagnetic applications [136].

Single phase BFO powders calcined between 450 to 650 °C [137] showed weak ferromagnetism at *RT* with strong size-dependent magnetic properties in contrast to the linear *M–H* in BFO ceramics. Reversible ferroelectric phase transition was confirmed by DTA at 827 °C and a dielectric anomaly observed near 330 °C corresponded to antiferromagnetic to paramagnetic phase transitions. Gonjal *et al.* in 2009 [138] adopted three different routes to synthesize BFO (a) conventional hydrothermal synthesis, (b) microwave-assisted solid state synthesis and (c) the combination of both. The third method was the optimal one as it was possible to synthesize well crystallized BFO in 30 minutes at low temperature of 200°C without requiring high purity of reactants. Moreover the yield of reaction was ~100% with excellent crystallinity and purity and the microwave radiation has double absorption effect i.e., providing heat through reaction media (water) and decomposing the reactants. Profile analysis by Rietveld refinement provided the lattice parameters as a=b=5.5799 Å and c=13.8692 Å. Dy doped (x=0 - 0.20) BFO nanoparticles with average grain size between 24-65 nm have shown increased M_s as grain size decreases on increasing Dy content. Phase transition from "rhombohedral (x=0) to orthorhombic (x=0.10 and 0.20)" has been observed with sufficiently large magneto-dielectric coefficient of 4.7% and -6.3% in as-prepared BFO and $Bi_{0.8}Dy_{0.2}FeO_3$ nanoparticles respectively at H=100 Oe and f =75 MHz. It was observed that doping with Dy was effective in improving dielectric ordering and reducing the losses [139]. Later in 2010, [140] they studied the effect of Co substitution with varying concentration (x=0, 0.005, 0.01, 0.02) on the magnetic and dielectric behaviour of $Bi_{0.8}La_{0.2}FeO_3$. Co^{3+} substitution at Fe^{3+} site improved the dielectric properties in the frequency range below 25 MHz at RT. The *M-H* hysteresis loop of all BLFCO nanoparticles gave wasp-waisted shape making them suitable in applications requiring low hysteresis loss under low magnetic fields [140].

Effect of the rare earth Gd on structural, photo-catalytic and ferromagnetic properties of BFO nanoparticles (x = 0, 0.05, 0.1, and 0.15) have been studied in detail by Guo *et al.* [141] in 2010. The crystal structure was stable till x < 0.1, and at x = 0.1, structural phase transition from rhombohedral to orthorhombic was observed. The doping of magnetically active rare earth Gd^{3+} ion (effective magnetic moment ~8.0 μB) lead to large structural distortion as its ionic radius is smaller (0.938 Å with CN 8) than Bi^{3+} ion (1.17 Å with CN 8). Photo-catalytic

activity to decompose Rhodamine-B via visible light illumination enhanced as x was increased from 0 to 0.1 and decreased afterwards for x = 0.15. Enhancement of photo-catalytic activity at x = 0.1 was associated with the change of polar behavior of BGFO nanoparticles. The ferromagnetic coupling between Gd^{3+} and Fe^{3+} ions and the distortion of the spiral spin cycloid on Gd doping caused significant rise in M_r of Gd-doped BFO than the undoped BFO. This enhancement in M allowed the photo-catalyst to separate efficiently from the aqueous media [141]. The average particle size showed an exponential decline with increasing Sr concentration and at 5% concentration of Sr a transformation from multifaceted polygon shape to a spherical one was seen. The second derivative FTIR spectra showed an intensity of vibration peak near to 593 cm^{-1} a characteristic of rhombohedral BFO was decreased after Sr doping. $Bi_{1-x}Sr_xFeO_3$ with x=0.03 displayed high M_s~1.37 emu/g and M_r~0.32 emu/g among other Sr doped samples studied before. Exchange coupling attributable to interaction amid antiferromagnetic core and the ferromagnetic shell observed in $Bi_{1-x}Sr_xFeO_3$ (x = 0, 0.01, 0.03, 0.05 and 0.07) nanoparticles. Band gap of 1.8 to 2.3 eV in BFO and BSFO nanoparticles respectively make them suitable for photo-catalytic decomposition of the organic contaminants under the visible light irradiation [142].

Following high-pressure synthesis technique Wen *et al.* [143] prepared BFO nanoparticles and ceramics successfully with good crystallization, density and crystal structure deformation. The enhanced M was attributed to crystal structure deformation and the enhanced dielectric properties resulted from good crystallization. Improved microwave absorption properties were obtained by high-pressure synthesis where the minimum reflection losses elevated to -17 dB at 11.2 GHz from -13 dB at 12.4 GHz as compared to samples synthesized via sol-gel route. Li *et al.* [144] successfully synthesized BFO uniform micro-crystals with various sort of morphologies by controlled hydrothermal technique. The optical properties of micro sized BFO crystals were strongly linked to their shape and size. The degradation of Congo red under the visible-light irradiation revealed photo-catalytic activity of the regular-shaped structures. Magnetic responses too were influenced by morphology of the as-synthesized BFO product and BFO micro-crystals of uniform morphologies exhibited a suitable narrow band gap of 2.2 eV making them useful for designing of the devices with the aim of combining optical, magnetic and electronic functionalities [144].

The type of solvent used during synthesis also influences the shape of particles and the properties of multiferroic BFO as reported by Chaudhuri *et al.* [81] who synthesized well-

crystallized BFO nanoparticles without adding any mineraliser using solvothermal method. The shape of particles varying from spindle, cylindrical, plate, hexagonal was controlled by varying synthesis temperature and change of solvent. The particles showed antiferromagnetism in the measured temperature range of 80 to 300 K. Only the hexagonal shaped particles exhibited a marked difference in the coercivity values at *RT* as compared to other particles with different shapes. Wang *et al.* [78] credited the formation of pure BFO phase to hetero-metallic polynuclear complexes formed in tartaric acid system during synthesis. The ferroelectric nature of as-prepared BFO nanoparticles was revealed by the determination of T_C ~851 °C whereas; the presence of weak ferromagnetic order was ascribed to size confinement effect. The observation of strong absorption in UV region enabled them to consider as potential substance for photo catalytic decomposition material. Magnetic properties of BFO and trivalent rare earth doped nanocrystalline BFO ($Bi_{0.875}R_{0.125}FeO_3$ (R=La, Eu, Pr, Sm, Nd, , Tb, Gd, Ho, Er, Tm, Dy and Yb)) gave enhanced *M* at *RT*. At 6T, sufficiently high *M* almost three times to that of undoped composition was observed for Ho, whereas, highest M_r was obtained for Nd and Sm. The magnetic transition temperature was increased by 20 K after La substitution. Hence the magnetic properties can be tuned by the suitable selection of the rare earth ions [145]. BFO nanoparticles with narrow size distributions showed better magnetic properties with reducing particle size [146].

Optimization of the various synthesizing parameters like Bi content, pH level, calcination temperature were necessary in the production of single phase BFO nanoparticles. A slight excess of Bi content was important in the synthesis of single phase BFO production as Bi being volatile in nature leads to its loss at high synthesizing temperature. Hence compensating this loss by addition of excess Bi resulted in formation of pure phase with *R3c* crystal structure under the optimized conditions [147]. Single phase nanoceramics of $BiFe_{1-x}Cr_xO_3$ (with *x* varying from 0-0.08) formed around 450 °C with particle size ~80 nm showed enhanced *M* with increasing Cr content and magneto-capacitance was increased with applied magnetic field. The change in ε′ induced by applied magnetic field was approximated by $\Delta\varepsilon/\varepsilon = \gamma M^2$, where a linear fit gave 'γ' the *ME* interaction value ~18.4×10^{-2}, 12.3×10^{-2} and 3.3×10^{-2} for *x*=0.04, 0.06 and 0.08 i.e., small and positive value of γ [148]. Highly ordered $Bi_{0.85}Nd_{0.15}FeO_3$ (BNF) nanotube arrays having diameter of 200 nm, length of 60 µm, and wall thickness of 20 nm obtained by sol gel template method showed ferroelectricity with $2P_r$ ~68.7 µC/cm^2 and $2E_c$ ~141.9 kV/cm at an applied 1 KHz frequency. The leakage current behaviour was dominated by an ohmic conduction mechanism with *E* <30 kV/cm and space-

charge-limited current mechanism with E = 30 to 200 kV/cm [149]. Du *et al.* in 2011 [150] synthesized first time preferably using electro spray route hollow spherical polycrystalline BFO nanoparticles with shell thickness of 35 nm (Ostwald ripening formation mechanism). Improved ferromagnetism was exhibited by hollow and core-shell BFO nanoparticles from 5 to 600 K due to breaking of the spiral spin cycloidal structure. The ferroelectricity of the hollow BFO nanoparticles exhibited smaller switching electric field as confirmed by the Kelvin probe force microscopy [150]. Pure and well-crystallized BFO nanocrystallites synthesized at temperature of 400 °C showed strong band-gap (2.1eV) absorption ~590 nm and weak ferromagnetism at *RT* due to the size confinement effects [151]. $BiFe_{1-x}Co_xO_3$ showed cell volume shrinkage along with appearance of different types of magnetic ground states like superparamagnetic (x=0), glassy antiferromagnetic (x=0.01) and glassy ferrimagnetic (x=0.02). An existing spinoidal cyclic model based arrangement of spins was proposed for explaining the first order magnetic transition and thermally induced magnetic transition in Arrott plot and magnetization data of Co doped BFO respectively [152]. Single phase $Bi_{1-x}Nd_xFeO_3$ (x = 0.0, 0.175, 0.20) multiferroics showed a gradual structural transition from rhombohedral to triclinic accompanied by weakening of the long-range ferroelectric order as content of Nd was increased from 0 to 0.2 [153]. On the other hand Sm doping in nanocrystalline BFO lead to development of lattice strain and decrease of oxygen vacancies demonstrating giant enhancement in magneto-dielectric, electrical and magnetic properties [154]. With the advent of 21st century numerous studies were done on the quality production of BFO thin films via PLD, RF sputtering, sol-gel method and more with magnitude of P_r much larger than that reported in bulk and nanopowders [44, 73].

2.5 Studies on BFO thin films

A major drawback that restricts the multifunctional applications of BFO is its weak magnetic response [40, 74] and the low resistivity of bulk samples that makes their electrical characterization very difficult. The dissension whether BFO is ferroelectric or is antiferroelectric was resolved by the hysteresis loop observed by Teague *et al.* [54]. It was in year 2003, when the work on production of thin films of BFO finds huge attention after Ramesh and his group produced BFO thin films with P_r ~ 60 μC/cm^2 which were 15 times larger than that of bulk BFO [44, 155]. Motivated by this, the same year Yun and his co-workers reported saturated P-E loops with $2P_r$ = 71.3 μC/cm^2 and $2E_c$ = 125 kV/cm in BFO thin films [156] and later in 2004 reported the deposition pressure effect on the crystal structure and ferroelectric properties [157]. BFO thin films were known to exhibit larger P_r

due to the strain enhancement and existence of the impurity phase of γ-Fe_2O_3 in comparison to their bulk counterparts [158]. *Wang et al.* [44] reported enhancement of *P* and other properties in "heteroepitaxially constrained" BFO thin films. The structural analysis indicated difference between films having monoclinic structure and single crystals of bulk BFO with rhombohedral structure with a marked enhancement in *P* ~90 μCcm^{-2} at *RT* that represents the intrinsic polarization of BFO [44]. A weak ferromagnetism i.e., net macroscopic magnetization has been observed that might have resulted due to small canting of antiferromagnetic sublattices of BFO [159].

There have been tremendous efforts for enhancing *ME* properties of BFO by adopting different approaches. Researchers worldwide have taken immense interest and challenge due to their numerous technological applications and the prevalent usage of such materials in devices [160]. Therefore, efforts have been made by researchers in last few years where the *M* and *P* in BFO thin films can be tailored either by annealing them over a wide temperature range or by varying their thickness. The leakage current density of 10^{-7} A/cm^2 with P_r ~40 μC/cm^2 at 600 kV/cm of applied field was obtained after optimization of process parameters for BFO sol [161]. Wang *et al.* [162] grown single-phase BFO films on (111) oriented Pt/Ti/SiO_2 /Si substrates by controlling the thickness via number of spin coated layers. The films with *R3m* space group presented continuous granular and dense morphology. BFO films have shown coexistence of ferromagnetic and ferroelectric ordering at *RT* with P_s ~1.8 μC/cm^2 and M_s ~95 emu/cm^2 with XPS suggesting presence of Fe^{3+} and Fe^{2+} the reason for observed ferromagnetism in the films [162]. The rhombohedral structure with *R3c* space group of the BFO film annealed at 500 °C reported lattice constants a_o=b_o= 5:5728 Å and c_o = 13:8412 Å [163]. Also, fully saturated weak ferromagnetic *M-H* loop with M_s of 6.1 emu/cm^3 has been observed with applied magnetic field of 10 kOe in BFO thin films at *RT* [163]. Grain size variation in BFO films by annealing them at different temperatures has remarkably affected *M* by suppression of cycloidal spin structure [45, 164-165]. Siwach *et al.* [45] too have noticed rhombohedrally distorted perovskite structure having *R3m* space group after annealing the as deposited films in air and oxygen at ~550 °C for 1hour. Oxygenation leads to a sudden enhancement in *RT* ferromagnetism which is evident by the presence of large M_s ~250 emu/cm^3 owned to nanoclusters of iron oxide formed during annealing in oxygen. On the other hand M_s falls sharply with temperature for the films annealed in air [45].

Effect of thickness on magnetic characteristics of BFO thin films has been meticulously studied and evidently, inverse relation has been validated between *M* and film thickness by various research groups [46-48]. A remarkable leap was observed on variation of thickness as is observed in a 40 nm thick BFO film that show rather small P_s ~3 μC/cm^2 in comparison to a 115 nm thick BFO film with P_s ~ 14.3 μC/cm^2 [46]. Thickness induced enhanced *M* in BFO films resulted due to strain-induced canting antiferromagnetic structure and magneto-elastic effect with a remarkable anisotropy observation in 40 nm thick BFO film. Significantly large M_s was also observed in epitaxially strained thin films which further decreases from 19.3 to 5.3 emu/cm^3 on increasing film thickness from 40 to 115 nm [46]. Rana *et al.* [47] reported the epitaxial strain effect on *M* and structure with thickness. Similarly, thickness effect on the *ME* properties were studied and the results were explained entirely on the basis of grain size and shape [49-50, 166]. Huang *et al* [49] reported a significant fall in M_s from 33 to 4 emu/cm^3 as the film thickness increases from 35 to 230 nm. Tang *et al.* [50] reported improved crystallization, enhanced dielectric constant, reduced leakage current, and a decrease in M_s with increase in thickness from 210 to 830 nm. Enhanced M_s from 2.32 to 26 emu/cm^3 with decrease in thickness (480 to 40 nm) due to suppression of spiral spin cycloid was observed [166]. The above studies indicate that the tailoring of film thickness modulates the spin cycloid of BFO and thereby, promotes the *M* and the better grain growth improves its electrical properties *w.r.t* their bulk counterpart.

The basic challenges or hurdles required to overcome included high leakage currents, ferroelectric reliability, high coercive fields, small remnant polarizations, and inhomogeneous magnetic spin structures. In an endeavour for improving the listed areas of concern, attention was diverted to study doped BFO thin films specifically processing of pure BFO by chemical methods without any impurity phase and chemical substitution for *A* and *B* site *i.e.* Bi and Fe. One of such earliest studies concerned with the doping of B-site of BFO with transition metal ions like Ti^{4+} and Ni^{2+} having size similar to the Fe^{3+} ion [167] stated that addition of 4+ ions at Fe^{3+} site of BFO required charge compensation that can be achieved by a number of ways like by compensating oxygen vacancies, creation of cation vacancies, or decreasing Fe-ions valence. Accordingly addition of divalent ions would likely to create anion vacancies within the system or may change the valence of Fe-ion. A general perception was that doping with Ti^{4+} will eliminate oxygen vacancies and doping of Ni^{2+} will introduce more of oxygen vacancies; instead it was observed that Ti^{4+} doping lead to an increase in film resistivity (nearly three orders of magnitude) whereas, Ni^{2+} doping caused decrease of resistivity over

two orders of magnitude. Hence the above mechanism of doping suggested that the current–voltage response of the film was affected by doping and increased densities of oxygen vacancies presents higher levels of free carriers with more conductivity. Few other studies that focused on B-site doping, like with Nd, helped to boost the piezoelectricity and electric properties of thin films [100, 168], doping with Cr markedly reduce leakage currents in BFO films [169] and others.

There are a number of studies on Fe-site doping of BFO, though greater attention has been given to Bi-site doped phases. Another exciting discovery occur when the researchers have doped rare-earth elements into BFO; drastically influencing the electrical and magnetic properties of BFO thin films. Doping at Bi site tend to suppress bismuth loss while annealing that lead to reduced leakage current in the films [170-173]. Initially the most commonly preferred dopants for Bi-site were La^{3+} and Ce^{3+}; their ionic radii being very near to that of Bi^{3+} seems to reduce leakage current by overcoming Bi loss during annealing [170-173]. The dielectric constant of pristine BFO film was nearly 50 at 1MHz which on doping with 5% Cr increased to 66 along with an enhanced P_s [170]. The ferroelectric measurements on BFO films doped with varying La content give dominance to leakage current over intrinsic ferroelectricity of the films. Though a gradual change in structure of the films from rhombohedral to pseudocubic, increases the *M*, and dielectric constant with marginal fall in leakage current density up to x=0.20; followed by reverse trend as doping content increases [174-176]. Mukherjee *et al.* [177] showed lattice distortion for x<0.15 in $BiFe_{1-x}Zr_xO_3$ (x=0.0–0.15) thin films. Reduction in P_r and increase in coercive field has been witnessed on Zr doping which is primarily attributed to lattice distortion; doped compositions were deprived of low frequency relaxation in dielectric measurements normally linked/cognate to defects and grain boundaries [177]. BFO thin films deposited on glass substrates were found to be amorphous which crystallizes to pure rhombohedral phase after annealing at 450 °C for 2 hour in air. Average grain size of the film was found to be 16 nm with a very high transmittance observed for the as-annealed film at 250 °C that decreased after crystallization [178]. Fabrication of $Bi_{1-x}Ce_xFeO_3$ (BCFO) film capacitors (x varying from 0 to 0.2) on indium tin oxide coated glass substrate showed phase transition from rhombohedral to tetragonal structure [179]. The leakage current density found to be reduced by many orders of magnitude in BFO thin films doped with Ce on ITO coated glass substrates due to small grain size and smoothness in surface. Fowler Nordheim tunnelling and the space charge limited

current are recognized as the major cause for leakage behaviour in BCFO thin films at the high and the moderate field regions respectively [179].

It was observed that Co addition has induced high M_s at *RT* with a large magnetic coercivity (H_c) of 16 kOe at 10 K [180]. Substituting Fe-site by Co, Ni, and Cu resulted in enhanced M_s [181]. Naganuma *et al.* [180] investigated the influence of Cr, Mn, Co, Ni, and Cu doping on properties of BFO films. Except Ni, all other dopants caused reduction in the leakage current density under a high applied electric field. P-E loops of films doped with Co and Cu measured at low temperature indicated decrease in coercive field without affecting the P_r. While the addition of Co, Cu, and Mn to the BFO film suppressed the leakage current density in high electric field region. The conduction mechanism of Mn doped BFO film was dominated by the Ohmic conduction. Annealing temperature tend to influence the P_r thin films with 63 μC/cm^2 for the sample annealed at 773 K and 46 μC/cm^2 for the sample annealed at 923 K [181]. La substitution found to prominently induce M_s in antiferromagnetic BFO showing better piezoelectric properties along with an observation of maximum *ME* coefficient close to 12 V/cmOe in the longitudinal direction [182].

La provides better ferroelectric properties with improved leakage current density. The unipolar strain was minimized by the quantity of lanthanum doped in the film; due to mere stress in plane of the film very less dispersion in dielectric constant and loss with frequency has been observed [182]. Though doping with Mn does not affect the intrinsic magnetism of BFO thin films, in spite of that it exhibit weak ferromagnetism at 300 K. An analysis of weak magnetic behaviour by Mn doping was done by careful observation of the complex oxidation states of Fe and Mn ions along with its interaction at Fe-site that is responsible for the slight change in M_s [183]. Substitution of Fe-sites by 5% of Mn ions facilitated the stabilization of Fe^{3+} in the films, whereas increasing Mn doping content to 10% or 15% lead to increase in Fe^{2+} concentration with well saturated loops having P_r of 32 μC/cm^2 and 53 μC/cm^2 for 5% and 10% Mn-doped BFO films, respectively [183]. La–Co co-doped thin films of BFO give saturated ferroelectric hysteresis loops and under the influence of low applied field dominantly ohmic conduction mechanism was seen [184]. Annealing in O_2 at 500 °C gives comparatively larger P_r of 35.3 μC/cm^2 with E_c (coercive field) of 310 kV/cm along with a lower leakage conduction at lower applied fields, whereas for the film annealed at 550 °C, lower P_r=4.8 μC/cm^2 observed due to low breakdown electric field [185]. Redistribution of oxygen vacancies at grain boundaries had a major role on resistance switching in the

polycrystalline BFO films as proved by c-AFM and retention results; causing a freshly prepared sample to be converted into low-resistive state by application of high positive voltage that later on switched to high resistive state by a negative voltage pulse [186]. BFO films doped with 5% Co at Fe site grown on conductive ITO coated glass substrates preferably show high (012) orientation with well saturated *PE* loops of P_r ~22 μC/cm^2 at *RT* and the full P_s ~ 38 μC/cm^2 along [001] direction [187].

The studies carried out on nanocrystalline BFO gave a better idea for implementing the composition of rare earth in thin films with improved magnetic behaviour [145]. GdMBFO thin films owing to its high *M,* make direct measurement of its Neel temperature possible for the first time. This enhancement in *M* was due to change of tilting angle between Fe^{3+}, caused by the change in nature of octahedral distortion [188]. Magnetic field annealing improved the microstructural properties attributed to improved link and diffusion of the ions in the film. The *M* increases on increasing strength of annealing magnetic field with the observed magneto-capacitance value of magnetic field annealed BFO film higher than that of non-field-annealing one [189]. Enhanced *M* and finely saturated piezoelectric loops with enhanced d_{33} were acquired by 5% doping of Co in BFO. PFM was utilized for characterizing the nanoscale electro-mechanical properties of BFCO films that showed larger piezoresponse signal and negative self polarization with calculated self polarization factor of −0.94 in BFCO than BFO film. In-plane lateral signal was changed in sign upon 180° rotation of sample that ruled out any spurious electrostatic contribution confirming the piezoelectric effect [190]. Pure BFO, $BiFe_{0.97}Co_{0.03}O_3$ (named BFCO) and $Bi_{0.90}Gd_{0.10}Fe_{0.97}Co_{0.03}O_3$ (named BGFCO) thin films deposited on the FTO (fluorine doped tin oxide) substrate revealed more compact and uniform surface morphology for BGFCO thin film. BFCO showed slight lattice distortion while tetragonal phase transition and preferentially (1 1 0) orientation has been observed with 10% Gd doping in BFCO thin film. XPS clarified increased oxygen vacancies in BFCO film, while Gd doping to BFCO lattice resulted in decreased oxygen vacancies and less of Fe^{2+} ions in the doped films than its BFO counterpart. The BFCO film showed P_r ~11.2 μC/cm^2 compared 1.4 μC/cm^2 for BFO film. Improved dielectric properties, large breakdown strength and low leakage current density under high strength electric field in BGFCO thin film all together contribute to enormously large P_r ~139.6 μC/cm^2 at *RT* [191]. Pure phase polycrystalline $BaTiO_3/BiFeO_3/BaTiO_3$ trilayer thin films with different thicknesses of BFO layer prepared by RF-magnetron sputtering showed maximum $2P_r$ of 13.5 μC/cm^2 and M_s of 61 emu/cm^3 at *RT*. Magnetic field induced changes

in capacitance and resistance of grain and grain boundary was explained by a model of combined impedance and the modulus spectroscopy. Enhanced intrinsic *ME* coupling was attained by 20% increase in the grain capacitance (Cg) with an applied field of 2 kG on the trilayer with 20 nm thick BFO layer. Thinner films showed significantly higher *ME* coupling due to bonding between the Fe and Ti atoms at the interface via oxygen atoms [192].

In conclusion we have summarized the important research carried out on multiferroic BFO ceramics, nanoparticles and thin films. However, in our review the focus is mainly laid on the research related with structural, electrical and magnetic properties of multiferroic BFO in recent years. Many other studies done were not included in this present literature as those do not fall in the present domain of our discussion. On the basis of the above discussion on BFO thin films synthesized via sol gel spin coating technique we concluded that the grain size effect on the multiferroic properties of BFO has not been investigated thoroughly. Also the effect of Gd, Co and Gd-Co codoping and the effect of dispersion in BFO films have not been investigated intensively. Table 2.1 below summarizes some important work carried out on pure and doped BFO thin films during past few years.

Table 2.1 Brief summary of some important work on BFO thin films.

Year	Deposition method	Summarized results
2005	$BiFeO_3$ by sol-gel [161]	P_r= 40 μC/cm^2 at 600 kV/cm, leakage current density ~ 10^7A/cm^2.
2006	$BiFeO_3$ by high-rate off-axis sputtering [75]	P_r= 71, 86, 98 μC/cm^2 at 300, 300 and 350 kV/cm for films grown on (100), (101) and (111) $SrTiO_3$ substrate respectively.
2006	$BiFeO_3$ by sol-gel [162]	P_r= 0.36 and 0.69 μC/cm^2; P_s= 0.88 and 1.87 μC/cm^2 for the films of thickness 100 and 130 nm at an applied electric field of 450 and 300 kV/cm respectively. M_s=95 emu/cm^3 for 130 nm films by VSM, whereas M_s=12 and 70 emu/cm^3 for 100 and 130 nm films by SQUID, coexistence of Fe^{3+} and Fe^{2+}.
2006	$BiFeO_3$ by sol-gel [163]	M_s ~6.1 emu/cm^3 at applied field of 10 KOe. DSC confirmed an antiferromagnetic to paramagnetic phase change at 354 °C.
2007	$BiFeO_3$ by nebulized spray pyrolysis technique [45]	Oxygen annealed films exhibit $2M_s$=250 emu/cm^3, $2M_r$=60 emu/cm^3, and $2H_c$=380 Oe.

2008	$BiFeO_3$ by sol-gel [46]	P_s increases from 3-14.3 μC/cm^2 as thickness increases from 40 to 115 nm at an applied electric field between 75-90 kV/cm. Enhancement in M ~5.3, 10.8, 12.3 and 19.3 emu/cm^3 as thickness decreases from 115 to 40nm due to large compressive strain in thinner films.
2008	$Bi_{1-x}La_xFeO_3$ (x= 0-0.30) by sol-gel [175]	La doping causes decrease in unit cell vol., Improved electrical properties at structural transition at x=0.15-0.20. Improved magnetic properties at structural transition at x=0.15-0.20.
2008	$BiFe_{1-x}A_xO_3$ (A=Cr, Mn, Co, Ni & Cu) by chemical solution deposition [180]	Mn, Cu and Co suppress the leakage current density, Co addition enhances M_s, reduces the coercive field without degrading P_r.
2009	$BiFeO_3$ & $Bi(Fe_{0.95}Cr_{0.05})O_3$ by chemical solution deposition [170]	P_r ~ 4.5 and 6.5 μC/cm^2 for $BiFeO_3$ at 300 and 250 K respectively. at an applied voltage of 7.5 and 10 V; P_r ~9 and 12.5 μC/cm^2 for $Bi(Fe_{0.95}Cr_{0.05})O_3$ at 300 and 250 K respectively at an applied voltage of 15 and 20 V. M_s~33 and 80 emu/cm^3 for $BiFeO_3$ & $Bi(Fe_{0.95}Cr_{0.05})O_3$ respectively
2009	$Bi_{1-x}La_xFeO_3$ by chemical solution deposition [176]	P_r=15.5 μC/cm^2 at 40 kV/cm, dielectric constant increases from 450 to 900 at 1 kHz with increase in x. M_s~ 5.5 emu/cm^3 for x=0.2.
2009	$BiFe_{1-x}Mn_xO_3$ by chemical solution deposition [181]	P_r=63 and 46 μC/cm^2 for films annealed at 773 and 923 K respectively at 1.4 mV/cm. M_s/ M_r ~0.4 with H_c~1 kOe at annealing temp. of 923 and 973 K.
2009	$Bi_{1-x}La_xFeO_3$ by the soft chemical method [182]	ε' and tanδ at 100 kHz were found to be 122 and 0.05. M_s ~ 2.5 emu/g, *ME* coefficient ~12 V/cmOe.
2009	$BiFe_{1-x}Mn_xO_3$ by chemical solution deposition [183]	P_r=32 and 53 μC/cm^2 for x= 0.05 and 0.10 at an applied electric field between 750-1000 kV/cm. M_s~ 1, 2 and 1.5 emu/cm^3 for x=0.05, 0.10 and 0.15 respectively.
2010	$BiFe_{1-x}Zr_xO_3$ by chemical solution deposition [177]	P_r=66, 55, 47 and 36 μC/cm^2 for x=0, 0.05, 0.10 and 0.15 respectively at field between 500-1500 kV/cm, Improved dielectric behaviour with absence of low frequency relaxation.
2010	$Bi_{1-x}La_xFe_{1-y}Co_yO_3$ by chemical solution	At 950 kV/cm, P_r=66, 44, 27 & 30 μC/cm^2, P_s=76, 55, 33 & 46 μC/cm^2 for BLFO-Co10%, BLFO-

	deposition [184]	Co5%, BFO and BLFO thin film. M_s=2.4, 2.9, 3.8 and 5.9 emu/g for BLFO, Co doped BFO thin film, BLFO-Co5% and BLFO-Co10% respectively.
2010	$BiFeO_3$ by sol-gel [185]	P_r ~34.3 and 4.8 μC/cm^2 for films annealed at 500 and 550 °C at an applied electric field ~480 and 280 kV/cm.
2010	$BiFeO_3$ & $Bi_{0.9}Gd_{0.1}Fe_{0.9}Mn_{0.1}O_3$ by sol-gel [188]	P_r=12 μC/cm^2 for $Bi_{0.9}Gd_{0.1}Fe_{0.9}Mn_{0.1}O_3$ at an applied electric field of 650 kV/cm. $2M_r$= 6 and 10 emu/cm^3 at *RT* and -100 °C respectively.
2010	$BiFeO_3$ by chemical solution deposition [189]	Grain growth and P_r ~ 2.5, 9, 11 μC/cm^2 for films synthesized under the application of 0, 3 and 6.5 kOe magnetic field resp. at an applied electric field ~250 kV/cm. M_s~3, 2, 0.5 emu/cm^3 for films synthesized under the application of 0, 3 and 6.5 kOe magnetic field respectively.
2011	$BiFeO_3$ by pulsed laser deposition [48]	M_s ~ 28, 18, and 6 emu/cm^3 for 38, 86 and 114 nm thick BFO film respectively.
2012	$BiFeO_3$ & $BiFe_{0.95}Co_{0.05}O_3$ by chemical solution deposition [190]	Piezoelectric Coefficients values (d_{33}) were 17.4 and 25.1 pm/V for BFO and BFCO films respectively. M_s ~0.6×10^3 J/T-m^3 for $BiFeO_3$, M_s ~8.5×10^3 J/T-m^3 for $BiFe_{0.95}Co_{0.05}O_3$.
2013	$Bi_{1-x}RE_xFeO_3$ (RE=La, Nd, Gd; x = 0, 0.05, 0.15) by pulsed laser deposition [62(b)]	P= 40 μC/cm^2 at an applied electric field of 200 kV/cm. M_s ~12, 20, 25 emu/cm^3 for 15% doped La, Nd and Gd respectively.
2013	BFO, $BiFe_{0.9}Mn_{0.1}O_3$ and $Bi_{0.88}Ce_{0.12}FeO_3$ by chemical solution deposition [179(a)]	P_r ~2.4, 15 and 20.6 μC/cm^2 at an applied electric field ~500 kV/cm. M_s ~10,19.65 emu/g and wasp waist shape *M-H* loop for BFO, $BiFe_{0.9}Mn_{0.1}O_3$ and $Bi_{0.88}Ce_{0.12}FeO_3$ respectively.
2013	$BiFeO_3$, $BiFe_{0.97}Co_{0.03}O_3$ and $Bi_{0.90}Gd_{0.10}Fe_{0.97}Co_{0.03}O_3$ [191]	P_r ~1.4, 11.2, 139.6 μC/cm^2 for BFO, BFCO and BGFCO films respectively at *RT*.
2014	$Bi_{1-x}Ce_xFeO_3$ (x = 0, 0.04 and 0.08) by chemical solution deposition [179(b)]	Leakage current density of BFO, $Bi_{0.96}Ce_{0.04}FeO_3$ and of $Bi_{0.92}Ce_{0.08}FeO_3$ were 1.3×10^{-3}, 5.9×10^{-5} and 1.9×10^{-6} A/cm^2 respectively at an electric field of 100 kV/cm. M_s ~12.8 emu/cm^3 for x=0.08.

2015	$BiFeO_3$ by radio frequency sputtering method [166]	P_{max} and E_c at maximum applied fields are 64 μC/cm^2, 382 kV/cm & 71 μC/cm^2, 486 kV/cm at an applied electric field of 1200 and 2000 kV/cm for 240 and 335 nm thin films respectively. M_s ~26 and 2.32 emu/cm^3 for 40 and 480 nm thick BFO film respectively.
2015	$BaTiO_3/BiFeO_3/BaTiO_3$ heterostructure by RF-magnetron sputtering [192]	$2P_r$ ~13.5 μC/cm^2 at an applied electric field of 50 kV/cm. *RT* existence of *ME* coupling (α_{ME}) ~515 mV/cm Oe. M_s ~61, 36, 23 and 19 emu/cm^3 found to be reduced with increasing thickness 20, 40, 60 and 80 nm of BFO layer.

Chapter III

Experimental Procedure and Characterization Techniques

Overview

The chapter details the processing methodology adopted for synthesizing pure and doped BFO thin films of different compositions. A brief description of the various characterization techniques employed for studying structural, micro structural, dielectric, ferroelectric, and magnetic properties are given.

3. 1 Sample preparation

The sample preparation section is divided in two subsections. In the first subsection the samples preparation by varying the annealing time, annealing temperature and varying thickness of BFO thin films is given. In the second subsection the procedure adopted to prepare the Gd-Co doped BFO thin films by sol-gel method has been given in order to study the influence of grain size on structural, electrical and magnetic properties.

3.1.1 Synthesis of pure BFO thin films

BFO thin films of uniform and varying thickness were prepared by controlling the number of layers deposited via sol-gel assisted spin coating method. In a typical synthesis process, bismuth nitrate pentahydrate $Bi(NO_3)_3.5H_2O$ and iron nitrate nonahydrate $Fe(NO_3)_3.9H_2O$ were weighed on an electronic weighing balance in stoichiometric proportion and dissolved initially in 2-methoxyethanol. The mixture was allowed to stir continuously for 2 hours at *RT* till a clear light brown transparent sol was obtained. A 10 % excess of bismuth nitrate was added to compensate the bismuth loss. After that a known calculated amount of acetic acid was added in solution and was kept for stirring at *RT* for 30 minutes. The purpose of adding glacial acetic acid was to maintain the pH of the sol between 1 and 2. Later on temperature was increased to 60 °C and the sols were stirred with a constant stirring rate at 60 °C until dark transparent reddish brown sols of desired concentration were obtained. The as prepared sols were coated on glass substrate using spin coater (spin NXG –p1) at rpm of 4000 for nearly 40 seconds. The precursor films thus obtained were baked at 300 °C for 5 minutes. Later on three different methodologies were adopted for annealing the film: **(a)** the spin coating and baking processes repeated 4 times in order to produce films of desired thickness on a plane glass substrate. Later the films with uniform thickness were annealed for 15, 30 60, 75 and 90 minutes in muffle furnace at 575 °C, **(b)** BFO films were coated 4 times on ITO substrates in order to produce films of required thickness. Afterwards the films with uniform thickness were annealed for 1 hour in muffle furnace between 525 and 600 °C with a temperature difference of 25 °C and were kept in open air to cool, and **(c)** spin coating and the required pyrolysis cycle were repeated 2, 4, 6 and 8 times for obtaining films of varying thickness on the ITO substrates. Later the films of varying thickness were finally annealed in ambient atmosphere for 1 hour using muffle furnace at 575 °C and finally were kept for cooling in open atmosphere. A general methodology adopted for the synthesis of BFO thin

films using sol-gel technique is shown with the help of flow diagram in fig. 3.1 and pictorially in fig 3.2.

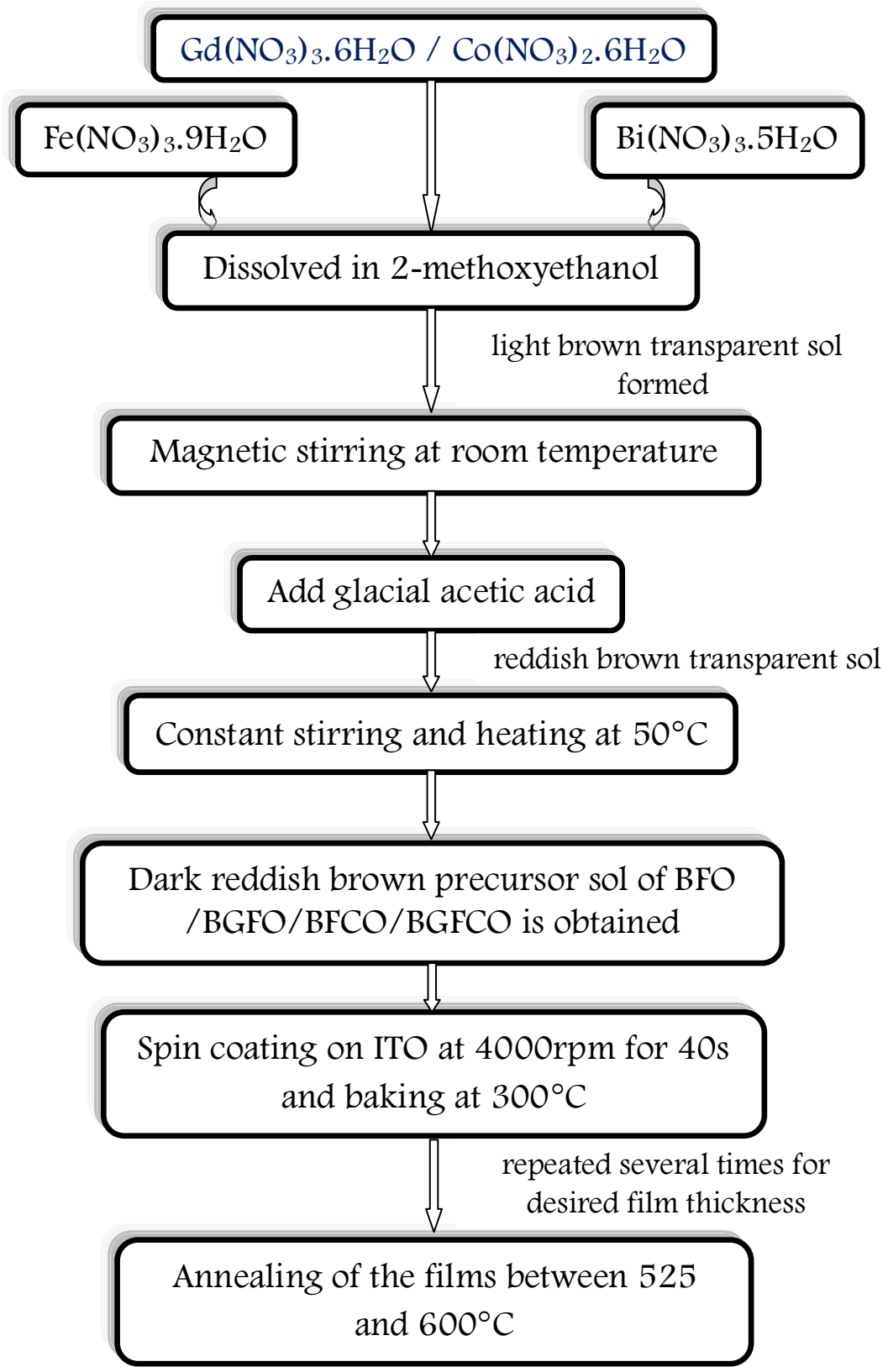

Fig. 3.1 Flow chart representing the synthesis of BFO thin films

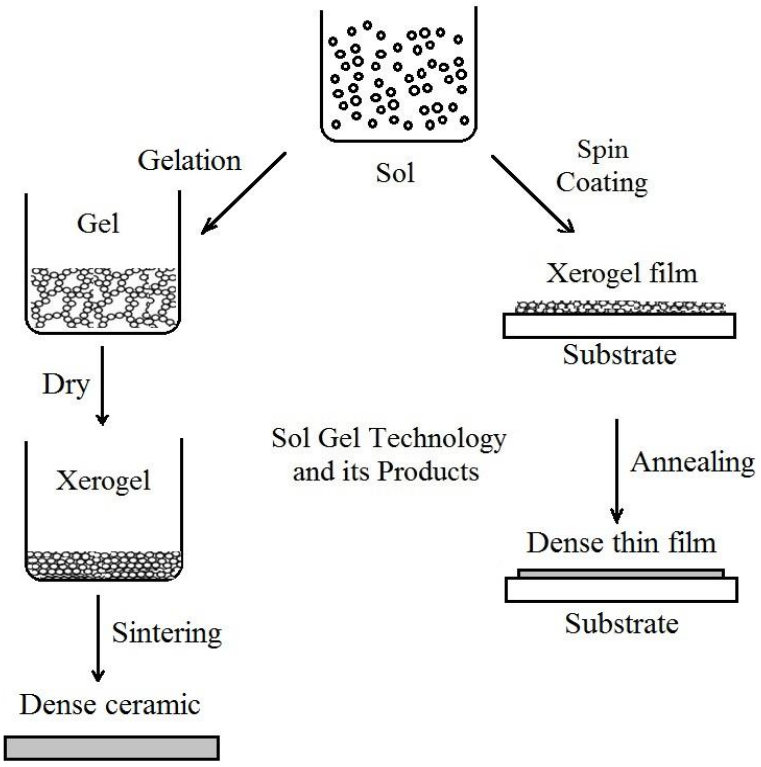

Fig. 3.2 Sol-gel technology

3.1.2 Synthesis of Gd and Co substituted BFO thin films

Gd and Co substituted BFO films with uniform thickness were prepared by deposition on ITO coated glass substrate via sol-gel spin coating technique. Bismuth nitrate pentahydrate $Bi(NO_3)_3.5H_2O$, iron nitrate nonahydrate $Fe(NO_3)_3.9H_2O$, gadolinium nitrate hexahydrate $Gd(NO_3)_3.6H_2O$ and cobalt nitrate hexahydrate $Co(NO_3)_2.6H_2O$ were weighed in stoichiometric proportion with the molar ratio of 1.10:1 (10% Bi excess to compensate the Bi loss) for the synthesis of

(a) $Bi_{1-x}Gd_xFeO_3$ (x=0, 0.05, 0.075, 0.100, 0.125),

(b) $BiFe_{1-y}Co_yO_3$ (y=0, 0.05, 0.075, 0.100, 0.125), and

(c) $Bi_{1-x}Gd_xFe_{1-y}Co_yO_3$ (x=0, 0.100; y= 0, 0.05, 0.075) thin films.

The salts were dissolved initially at *RT* in 2-methoxyethanol and were left for continuous stirring for 2 hours. When a clear light brown transparent sol was formed, a measured quantity of glacial acetic acid was added for maintaining the pH of the solution between 1 and 2. The solution was again stirred at *RT* for 30 min. Afterwards the sol was heated at constant temperature of 60 °C till a clear transparent sol of reddish brown colour of 0.4M concentration was obtained. The sol thus prepared was spin coated (spin NXG –p1) on ITO at rpm of 4000 for nearly 40 seconds. The films so obtained by deposition were then pre-

annealed for 5 minutes at 300 °C. The cycles of spin coating and of pyrolysis were repeated 4 times for obtaining desired thickness of the film. The films were finally annealed in ambient atmosphere for 1 hour using muffle furnace at 575 °C and were kept in open air to cool. The entire methodology for synthesis of BGFCO thin films is represented with flow diagram in fig. 3.1 and .pictorially in fig 3.2.

3.2 Characterization Techniques

The characterization techniques used for analyzing the various properties of thin films are discussed below:

3.2.1 X-ray Diffraction (XRD)

The structural and phase characterization of BFO films were done by XRD (Philips X-pert PRO) using the standard CuKα radiation (λ = 1.54178 Å). The glancing incidence angle taken was 0.5° to remove the ITO peaks from the XRD patterns. The diffraction peaks in the XRD pattern were recorded as a function of diffraction angle 2θ and the planes were indexed after matching with the JCPDS data cards. The diffraction of X-ray happens only at certain angles in the crystal structure that were controlled by the inter-planar spacing and wavelength of the X-rays. It follows the Bragg's equation

$$2d \sin\theta = n\lambda$$

where, *n* is the order of the reflection (generally first order), λ is the wavelength of X-ray source, *d* is spacing between the crystal planes or lattice planes and θ is the incident angle or glancing angle relative atomic planes. The XRD patterns were refined by the multiprofile Rietveld technique using FULLPROF program [193, 194]. The peak profile refinement function used in the refinement was pseudo-Voigt function. The Rietveld technique was used for refining the diffraction data to determine the crystal structure, fraction of other phases present in the sample, lattice parameters and crystallite size. This technique makes use of least square approach for refining theoretical line profile till it matches with the measured profile. The crystallite size was calculated from Scherrer formula defined by the equation [195]

$$Crystallite\ size\ (C.S) = \frac{k\chi}{\beta cos\theta}$$

where, k is a constant depending upon the shape of crystallite, β is FWHM (full width at half maximum) of intensity *vs.* 2θ profile, λ is wavelength of radiation used in XRD and θ is the

well known Bragg's diffraction angle. The value of FWHM were obtained from the Rietveld refinement of the respective XRD patterns of the films using Caglioti formula [196] given by

$$H = \sqrt{Utan^2\theta + Vtan\theta + W}$$

where, U, V and W are defined as usual peak shape parameters obtained from Rietveld refinement and θ is Bragg's diffraction angle.

3.2.2 Field Emission Scanning Electron Microscopy (FESEM)

The morphological and cross sectional study of the thin films was carried out using 'field emission scanning electron microscope' (FESEM) ("Carl Zeiss Model No.: Ultra Plus-55"). The principle of operation of FESEM is that it makes use of a focussed beam of electrons for generating an image or for analysing a sample. The focussed electron beam scans the surface of the specimen under study. When a primary electron strikes a sample, some interaction is supposed to occur between the electron beam and the sample generating a series of secondary and backscattered electrons. FESEM is fitted with specific type of detectors that are able to detect these secondary and backscattered electrons. The signal from the detector can then be used to create images and to obtain information about properties of sample under study [197]. A thin film of gold or platinum was deposited over the sample to avoid charging of electrons inside the film before analysis. The FESEM can reveal topographic details of thin film surface with great clarity and detail. Its high magnification, depth of focus, resolution and easiness of sample observation made FESEM one of the most frequently used instruments in materials research today. FESEM was used to measure thickness of the film, to analyze surface morphology, and porosity of the thin films. Also the measurement of the grain size was done from FESEM micrographs using linear intercept method (ASTM E112) by considering a minimum number of 100 grains. Correspondingly, estimated grain size distributions were plotted as a function of annealing temperature and later as a function of film thickness.

3.2.3 Atomic Force Microscopy (AFM)

AFM (NT-MDT Solver next) was used for analyzing the surface morphology and to measure roughness of sample surface at much higher resolution. AFM was invented in 1986 by Gerd Binnig, Calvin F. Quate and Christopher Herber [198, 199]. In general AFM is a high resolution scanning probe microscopy (SPM) that is having resolution of fractions of nanometer; 1000 times better than optical diffraction limit. AFM basically uses a very fine

cantilever tip for generating topographic image of the film. It works on the principle of determination of interactive force in between the sample surface and tip by use of special probes designed using an elastic cantilever having a very sharp tip at its end. The force that is applied to the tip by surface results in deflection of the cantilever. By careful monitoring of the cantilever deflection, the interactive force between the tip and the surface can be evaluated [199, 200].

In case of BFO thin films the AFM images are taken in the semi-contact topo mode. A very high sensitivity and the stability of feedback system is required for detecting any changes in amplitude and phase of the cantilever oscillations in semi-contact topo mode also called as tapping or intermittent-contact mode. The forced cantilever oscillations were excited near to resonance frequency with an amplitude of about 10–100 nm. A constant force is desired to be maintained between the tip and sample surface as the probe is raster scanned (parallel lines) through the surface for generating a two or three dimensional image [199].

3.2.4 Transmission Electron Microscopy (TEM)

The microstructure and the phase determination of the films were done by TEM using an accelerated voltage of 200 keV and selected area diffraction (SAED) pattern. TEM is one of the most versatile techniques suitable of collecting information over a wide magnification range. TEM is capable of imaging and analyzing the samples at significantly much higher resolution attributed to small wavelength (de-Broglie) of electrons. Thin films of BFO can also be analyzed by transmission electron microscopy (TEM) for obtaining SAED patterns. The samples used for TEM analysis must have suitable thickness so that electrons can easily pass through the sample. Therefore, sample for TEM analysis i.e. a very thin layer of BFO was removed using ion beam milling technique. There are two modes of operation for TEM: (a) forming electron diffractions and (b) imaging. Elastically scattered electrons in general don’t lose energy during its interaction with the system. Therefore, all those incident electrons that were scattered by the same atomic plane will get deflected by the same angle. The deflected electrons can then be collected using magnetic lenses forming pattern of spots i.e the desired electron diffraction pattern. It is also possible to generate images using TEM by a slight readjustment of the lens system. There are in general two main imaging modes: (a) Bright field imaging in which the image is formed completely by the unscattered electrons and the contrast in such images is wholly because of variation in thickness and density in the sample under study. (b) Dark field imaging implies a single diffracted beam for image

generation. Due to this all other regions other than the diffracted area having different orientation or crystal structure appear dark [201].

In case of thin films TEM and the HRTEM (high resolution transmission electron microscopy) were used for determining the d-spacing. By indexing the corresponding SAED patterns for the pure and Gd-Co substituted BFO thin films the lattice parameters and unit cell volume respectively is calculated using the plane spacing formula for the hexagonal structure given by the equation [202],

$$\frac{1}{d^2} = \frac{4}{3}\left\{\frac{h^2 + hk + k^2}{a^2}\right\} + \frac{l^2}{c^2}$$

3.2.5 Electrical measurements

The electrical measurements of thin films were done by deposition of Au or Pt electrodes by sputtering technique using the masks with 0.5mm diameter. Dielectric and ferroelectric measurements (*PE* loops) for the thin films were performed at *RT*. The frequency variation of dielectric constant (ε') and dielectric loss (tanδ) of thin films were analyzed using an impedance analyzer. The ε' of thin films can be calculated from the observed capacitance value using the relation.

$$\varepsilon' = Cd/\varepsilon_o A$$

where, d: thickness of the films, A: area of the electrode deposited on film and ε_o: permittivity (8.85×10^{-12} F/m) of free space. Ferroelectric measurements for the thin films were performed using the RT 66A ferroelectric tester (Radiant technologies, USA). There is a facility in a measurement set up to measure the *PE* loops at different frequencies. The various parameters like P_r, P_{max} and E_c can be measured from the observed *PE* loops.

3.2.6 Magnetic measurements

The magnetic measurements of BFO thin films were made by SQUID (superconducting quantum interference device) magnetometer which is a very sensitive tool for detecting magnetic flux. The high temperature FC-ZFC (field cooled and zero field cooled) measurements were done using the Physical Property Measurement System (PPMS). SQUID works on the combined phenomena of flux quantization and Josephson tunnelling [203, 204]. The most widely commercialized SQUID system in use is Quantum Design's MPMS (Magnetic Property Measurement System). It makes use of gradiometer having *RT* access,

where the sample used for analyzing the magnetic properties is inserted through a vertical tube in its pickup loop. The temperature of sample and magnetic field can be varied from about 10-300K and from 0-4T. MPMS has found various applications in physics, electronics, materials science, geology and biology. Its few applications include antiferromagnets, ceramics, spin glasses, magnetic–optic materials, high & heavy fermions superconductors, nanocomposites, metalloproteins, fullerenes, sea-bed lava and amorphous alloys [205].

Chapter IV

Results and Discussion

Overview

This chapter details the experimental results of pure and Gd-Co substituted BFO thin films. This chapter is divided into two sections. In the first section the effect of annealing time, annealing temperature and film thickness on the properties of BFO thin films has been studied. In the second section the effect of Gd and Co ion substitution at Bi and Fe site respectively on the structural, magnetic and electrical properties has been investigated.

4.1 Effect of grain size variation

To obtain the suitable annealing time and temperature for the preparation of well crystalline pure BFO films, annealing were carried out for different time and temperatures. Fig. 4.1 (a & b) shows the XRD pattern of the films annealed at 525 and 575 °C respectively for 15, 30 60, 75 and 90 minutes. All the XRD patterns are indexed to perovskite BFO with space group: *R3c* (JCPDS card No.86-1518). Reflection peaks from (104), (110) and (012) planes are well evident from XRD pattern. The films annealed at 525 °C shows that with increasing annealing time the intensity of the peaks is increasing. The similar behaviour is observed for the films annealed at 575 °C. Minor impurity peaks of $Bi_{25}FeO_{40}$, Fe_2O_3 and $Bi_2Fe_4O_9$ phase are also evident in the films annealed for 15 minute. With increasing annealing time to 60 minutes, the fraction of the impurity phase decreases and nearly pure BFO phase is obtained. Further increasing the annealing time to 75 and 90 minutes lead to the formation of secondary phases. It is evident that annealing time plays a key role to obtain well crystallized single phase BFO film irrespective to the annealing temperature. Therefore, an annealing time of 60 minutes has been chosen for further preparation of BFO thin films at different annealing temperature.

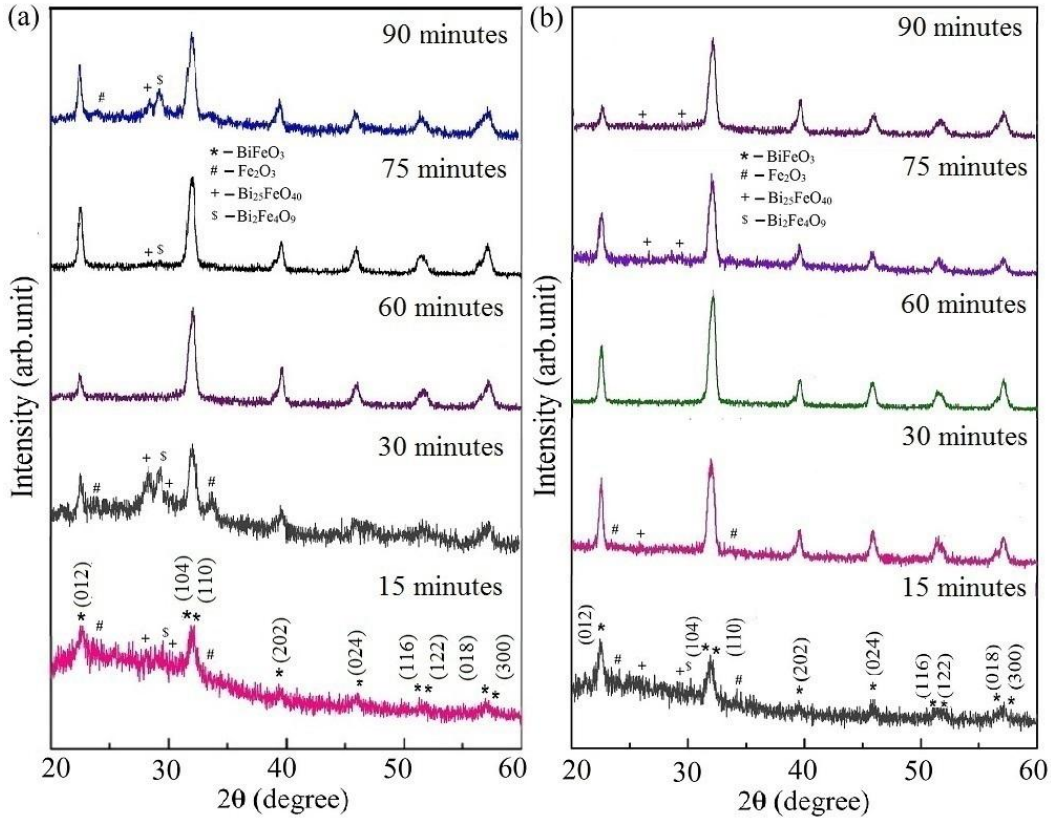

Fig. 4.1 XRD patterns of BFO thin films annealed at (a) 525 and (b) 575 °C for 15, 30 60, 75 and 90 minutes.

After obtaining the suitable processing conditions, the grain size variations were imparted in the films by adopting two methodologies. First, by annealing the films with constant thickness (200 nm) at different annealing temperature (525 to 600 °C) and second, by annealing the films with different thicknesses at constant temperature (575 °C). The effects on structural, magnetic and electrical properties are discussed below.

4.1.1 Effect of annealing temperature

4.1.1.1 XRD analysis

Fig. 4.2 shows the XRD patterns of BFO thin films annealed at 525, 550, 575 and 600 °C. All the XRD patterns were refined by the multiprofile Rietveld technique using FULLPROF program [193-194]. The peak profile refinement function used in the refinement was pseudo-Voigt function. All the major reflection peaks in the XRD pattern are indexed to perovskite BFO with space group: *R3c*. A minor impurity peak of γ-Fe_2O_3 is also evident in the XRD patterns, which corresponds to the characteristic (3 1 1) peak of bulk maghemite with space group of $P4_332$. Table 4.1 summarizes the refined parameters obtained for the BFO films. The diffraction profile fits very well, as indicated by the refined parameter values. The low value of χ^2 (goodness of fit) suggest the goodness of refinement.

Table 4.1 Refined parameters for the BFO films annealed at (a) 525, (b) 550, (c) 575 and (d) 600 °C.

Annealing temperature			Lattice parameters (Å)		Atom coordinates			R_B	R_F	χ^2
			a	c	x	y	z			
525°C	Bi	6a			0	0	0.28177			
	Fe	6a	5.578	13.872	0	0	0	5.86	4.04	2.54
	O	18b			0.67091	0.83479	0.54093			
550°C	Bi	6a			0	0	0.28399			
	Fe	6a	5.58	13.876	0	0	0	8.06	5.34	2.95
	O	18b			0.67111	0.83479	0.52888			
575°C	Bi	6a			0	0	0.28717			
	Fe	6a	5.591	13.898	0	0	0	7.69	5.06	2.44
	O	18b			0.63864	0.82491	0.53198			
600°C	Bi	6a			0	0	0.28617			
	Fe	6a	5.586	13.89	0	0	0	7.99	5.96	2.84
	O	18b			0.62839	0.83479	0.5258			

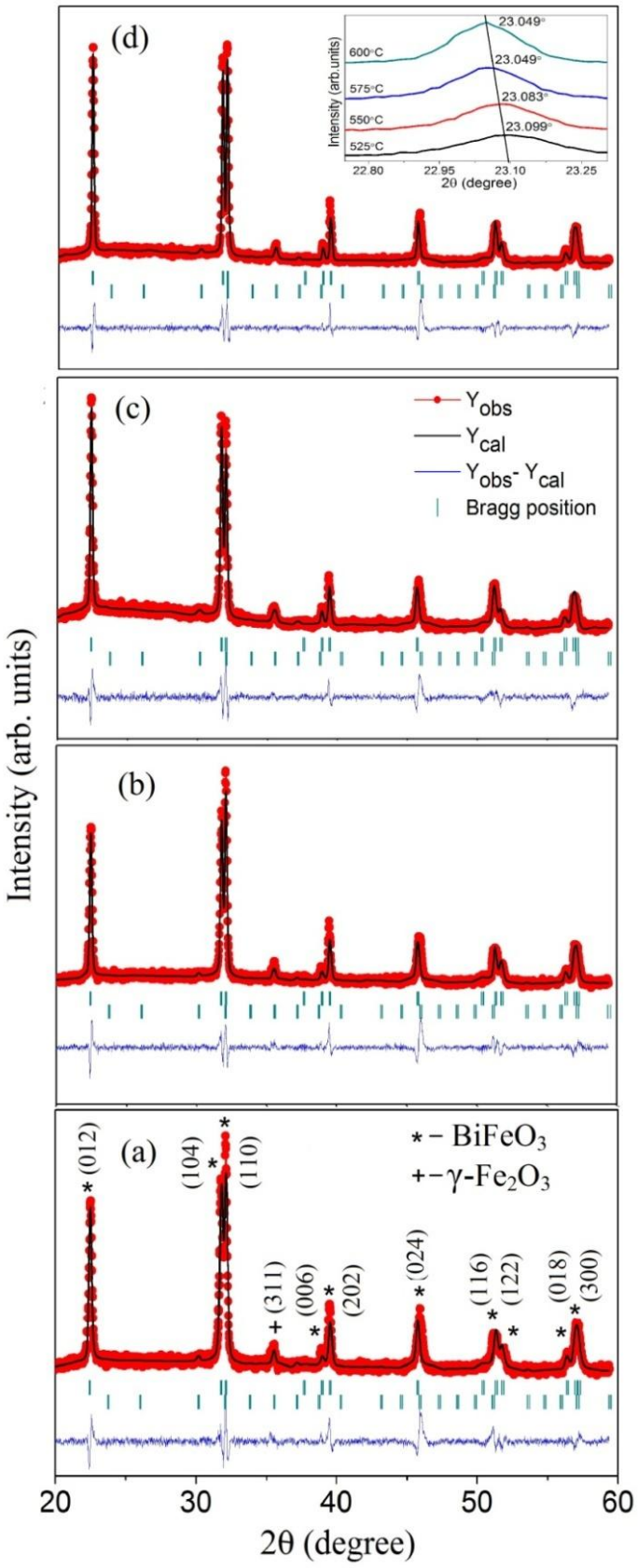

Fig. 4.2 Refined X-ray diffraction patterns of sol-gel driven BFO films annealed at (a) 525, (b) 550, (c) 575 and (d) 600 °C. The inset in Fig 1(d) shows the shift in (0 1 2) peak with annealing temperature.

As the annealing temperature increases, the full width at half maximum (FWHM) of (0 1 2) peak decreases, indicating better crystallization of BFO-phase in the films. The volume fraction of γ-Fe_2O_3 phase as obtained from the refinement is nearly constant (~ 0.08) in all the annealed samples. The magnified view of (0 1 2) peak (inset of Fig. 4.2 (d)) depicts a shift towards lower angle with increase in annealing temperature. This shift is due to the difference in thermal expansion coefficients of ITO and BFO, which is more pronounced at higher annealing temperatures.

4.1.1.2 FESEM analysis

Fig. 4.3 (a) depicts a representative cross-sectional FESEM image of BFO films deposited on ITO coated glass substrate. It can be seen that the interfaces between the ITO and BFO film is well defined without any inter diffusion. The measured thickness of BFO film is ~200 nm. No variation in the film thickness was observed with annealing temperature. Fig.4.3 (b, c and d) shows the FESEM surface morphology of the films annealed at 550, 575 and 600 °C, respectively. The microstructures of films reveal a well crystallized equiaxed BFO grains, separated by sharp grain boundaries. A little porosity is also observed in the films and the porosity fraction is below 0.01 in all the films, as calculated by areal analysis.

Fig. 4.4 shows the EDX line scan analysis of BFO thin films showing their elemental composition. This qualitative analysis leads to determine the elements present in the sample by identification of the lines in X-ray spectrum using the standard tables of energies or the wavelengths [206, 207].

Fig. 4.5 shows EDX dot mapping images of BFO thin films showing the elemental distribution in BFO film annealed at 525 °C. Fig. 4.5 (a) shows the mixed elemental composition i.e compositions of all the elements constituting the film, whereas fig. 4.5 (b-f) represents the EDX dot mapping for O, Fe, In, Bi and Sn respectively. Here, a particular X-ray line is identified with a capital letter like K, L or M that indicates the shell embodying the vacancy created inside. The Greek letter like α or β specifies the group to which a particular line belongs and a number in descending order like 1, 2, etc. denotes the intensity of those lines within the group [206, 207]. The representative FESEM micrographs showing the grain size measurement of BFO thin films was shown in Fig. 4.6. The average grain size was measured by considering a minimum number of 100 grains.

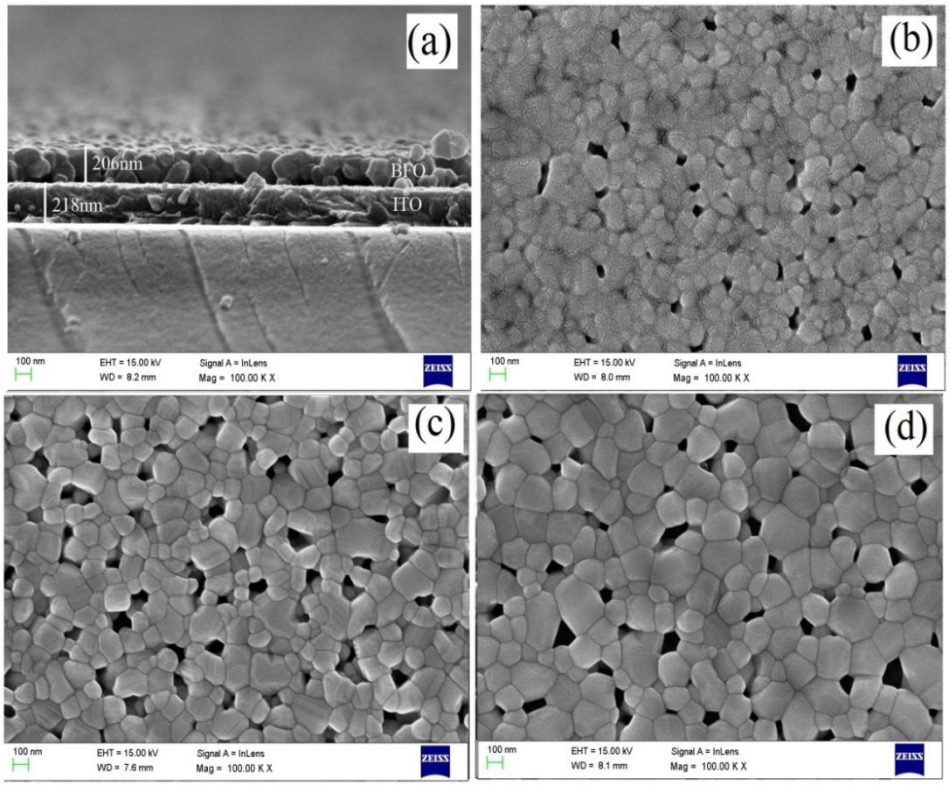

Fig. 4.3 FESEM micrographs of BFO thin films (a) cross-sectional view and (b-d) surface morphology of films annealed at 550, 575 and 600 °C, respectively.

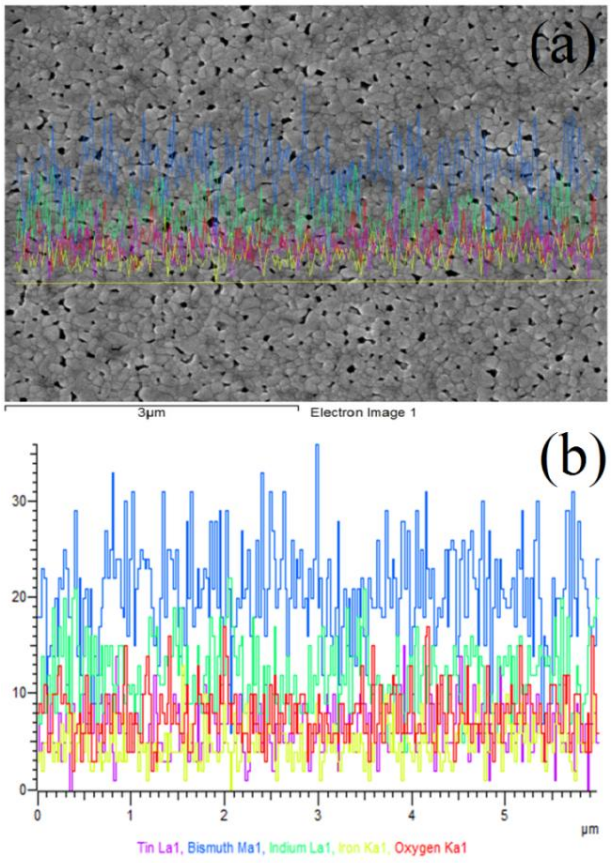

Fig. 4.4 EDX line scan analysis of BFO thin film annealed at 550 °C.

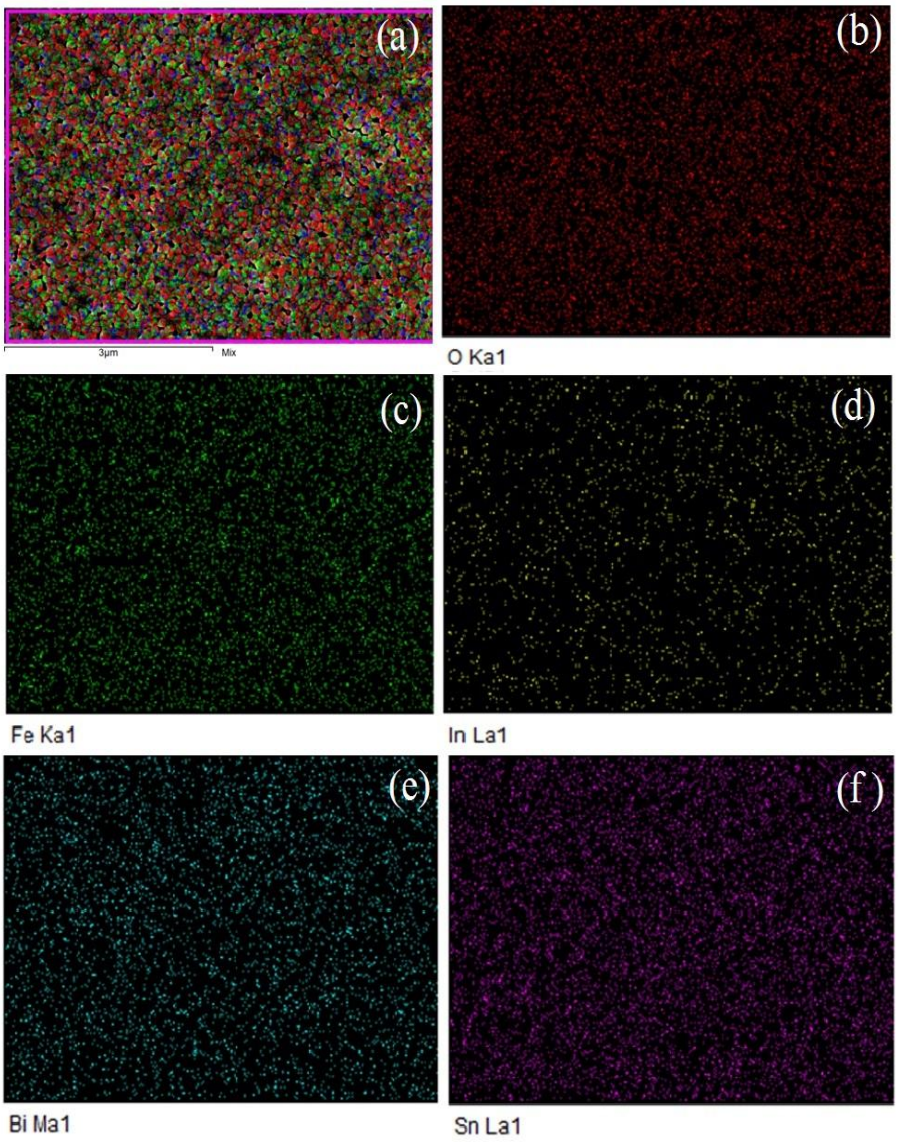

Fig. 4.5 EDX dot mapping images of BFO thin film annealed at 525 °C showing their elemental composition.

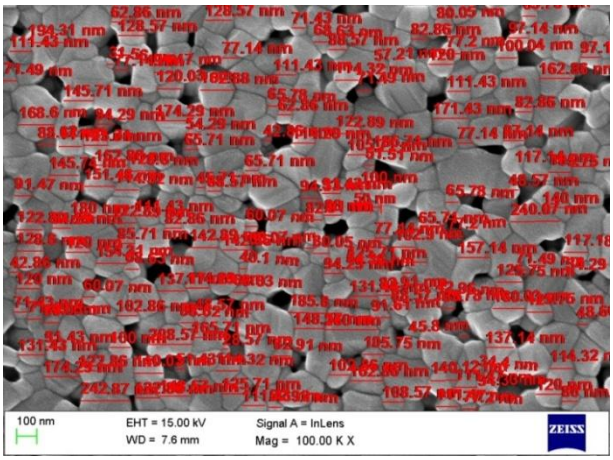

Fig. 4.6 Representative FESEM micrograph of BFO thin films showing the grain size measurement.

4.1.1.3 Grain size distribution analysis

The estimated grain-size distribution values from the FESEM images are plotted as a function of annealing temperature and are shown in Fig. 4.7. The grain size values were measured using linear intercept method (ASTM E112) by considering a minimum number of 100 grains. The *x-y* axis scale were kept constant for visual comparsion of grain size distribution.

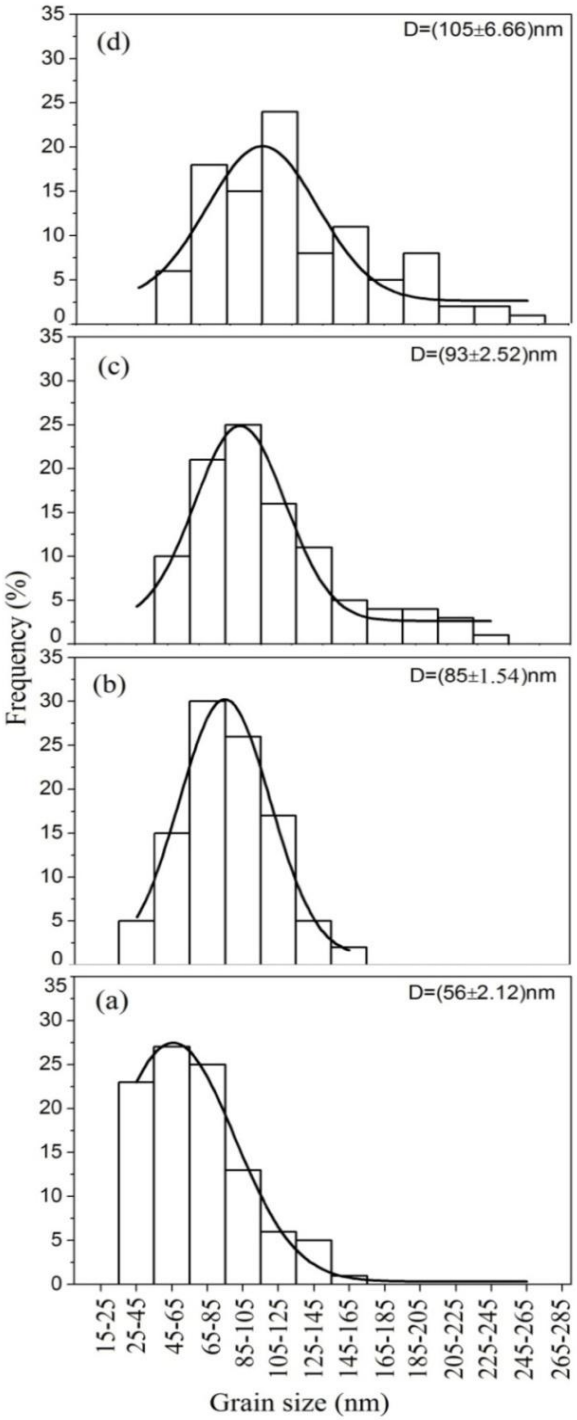

Fig. 4.7 Grain-size distributions in the BFO thin films annealed at (a) 525, (b) 550, (c) 575 and (d) 600°C.

For the film annealed at 525 °C, majority of the grain lies in the size-distribution range of 25-105 nm and half of the grain fraction is below 65 nm. This size range remains the same on increasing annealing temperature to 550 °C; however, majority of the grain fraction is between 65-105 nm. With the further increase in annealing temperature (575 °C), the size range broadens and no grains with sizes below 45 nm are visible; whereas a significant fraction of grains below 45 nm is observed for the film annealed at 525 °C. Besides, coarser grains with sizes of >150 nm are also observed and their percentage increases from ~10 to 20% with increase in annealing temperature from 575 to 600 °C. The average grain size analysis shows a normal Gaussian fit with mean grain sizes of 56, 85, 93 and 105 nm for the films annealed at 525, 550, 575 and 600 °C, respectively (Fig.4.7).

4.1.1.4 AFM analysis

Fig. 4.8 shows the AFM micrographs of BFO films annealed at 525, 550, 575 and 600 °C with their respective height profiles.

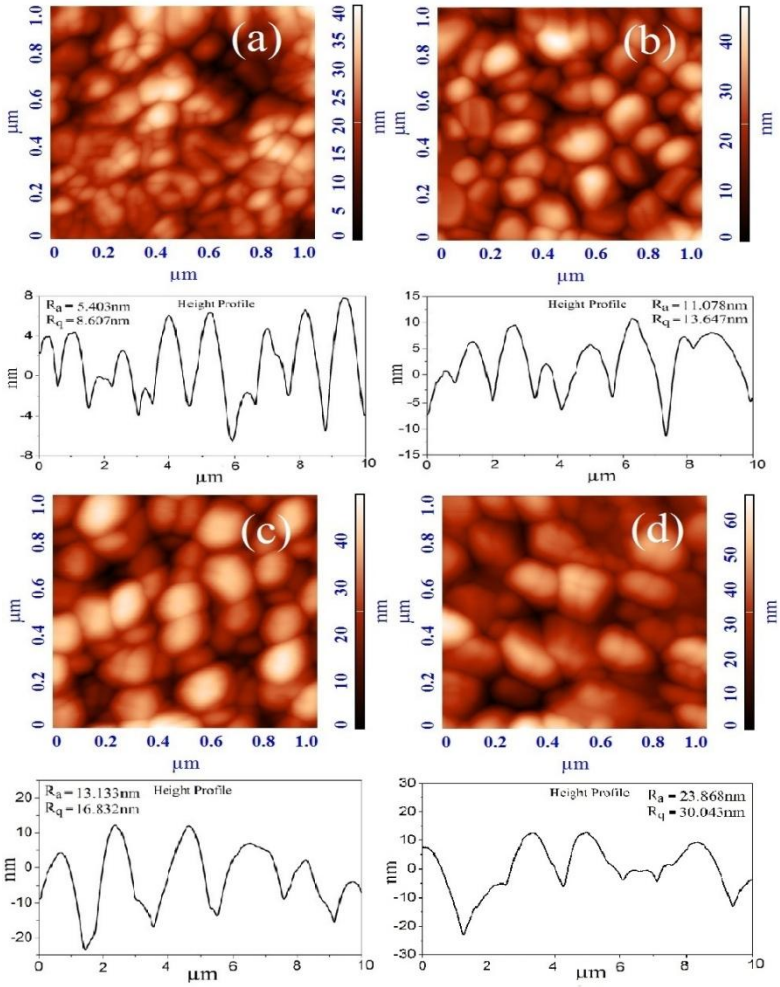

Fig. 4.8 AFM images of the BFO thin films annealed at (a) 525, (b) 550, (c) 575 and (d) 600 °C with their respective height profiles.

The root mean square roughness (R_q) of the films was measured over an area of 50×50 μm^2 and the estimated R_q values tend to increase with annealing temperature. A maximum R_q value of < 30 nm was obtained for the film annealed at 600 °C, suggesting that the smooth surface of the films is retained, even at higher annealing temperature. It is evident from the micrographs that the grain-size is increasing with increase in annealing temperature and these observations are in agreement with the FESEM analysis.

4.1.1.5 Magnetic measurements

Fig. 4.9 (a&b) shows the in-plane *M-H* behaviour of BFO thin films obtained at 300 and 10 K, respectively. The *M-H* behaviour of the films at 300 K shows a well-saturated hysteresis loop suggesting the ferromagnetic nature of BFO thin films [208-210]. Inset 1 of Fig. 4.9 (a) represents the *M-H* behaviour of film without subtracting the diamagnetic contribution of glass substrate. The diamagnetic contribution was eliminated by subtraction of the slope of linear portion of *M-H* loop at higher magnetic field (M/H= -χ). It is evident that the saturation magnetization (M_s) increases with annealing temperature up to 575 °C and then decreases for the film annealed at 600 °C (inset 2 of Fig 4.9 (a)). At 10 K, non-saturated *M-H* loops are observed (Fig. 4.9 (b)), suggesting the spin glass behaviour of the films. The variation in magnetization at 4 T (inset of Fig. 4.9 (b)) is similar to the films at 300 K. However, larger magnetization values are observed at 10 K.

Fig. 4.9 (c) shows the enlarged view of magnetization behaviour at 10 K. The variation of coercivity (H_c) and remanence (M_r) is shown in the inset. It is clear that the H_c and M_r is maximum for the BFO film annealed at 575 °C. H_c and M_r show similar trend as M_s at 10 K. It is clear that H_c and M_r is increasing with temperature and found maximum for films annealed at 575 °C and then decreases. This shows the grain size distribution of sample annealed at 575 °C, provide maximum pinning to demagnetization of uncompensated moments. Hence the ferromagnetic component is only due to the uncompensated spin of the helical antiferromagnetic structure of BFO. The inherent magnetization in the film is mainly contributed by the uncompensated spins at grain boundaries and the presence of small fraction of magnetic γ-Fe_2O_3 phase. However, constant volume fraction of γ-Fe_2O_3 phase, as obtained from XRD refinement, excludes its contribution in magnetization variation of the films.

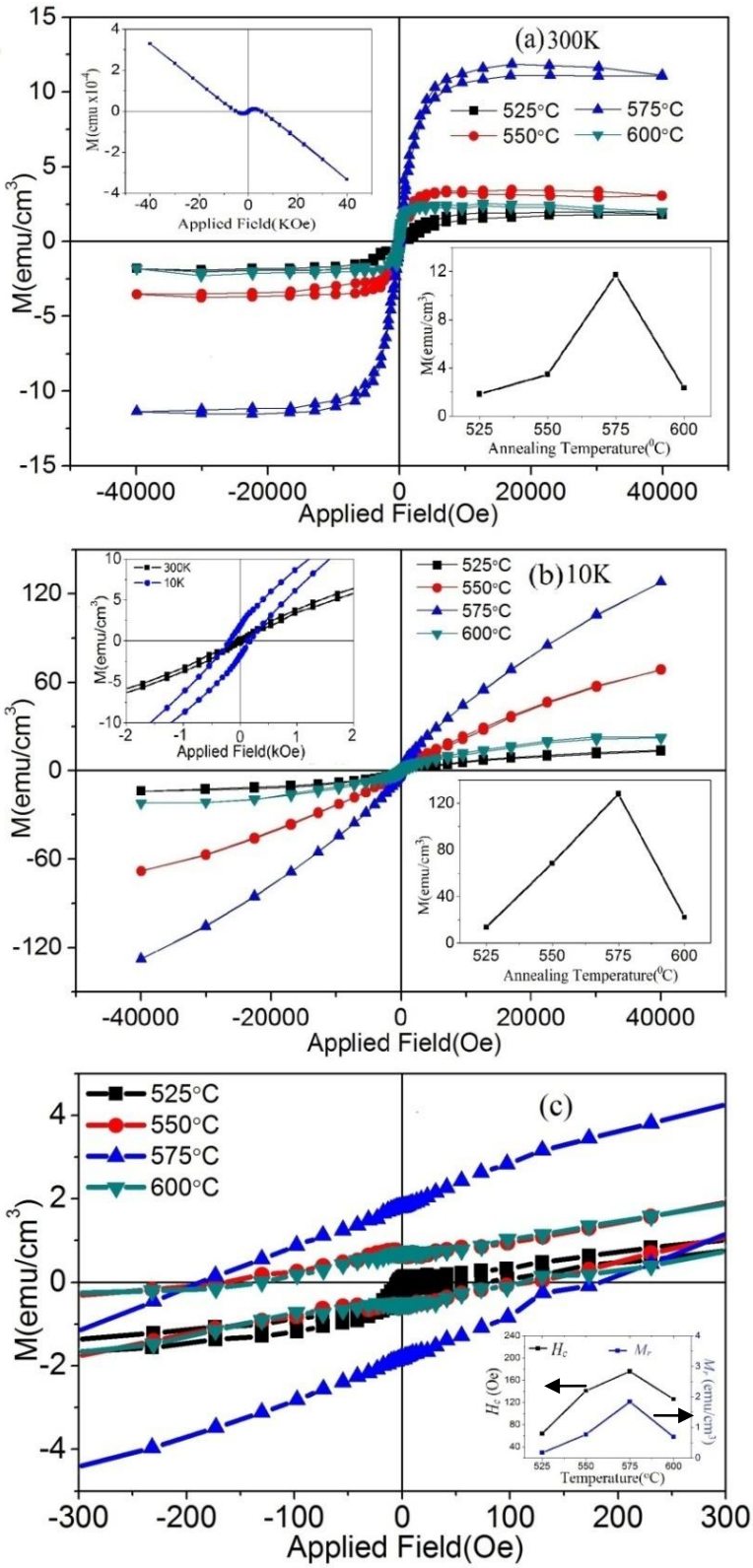

Fig. 4.9 Magnetic hysteresis loops of BFO thin films (a) room temperature (b) 10 K annealed at 525, 550, 575 and 600 °C. The inset in fig. (a) shows the representative as obtained plot of a film annealed at 575 °C and the variation in M_s with annealing temperature at 300 K. The inset in fig. (b) shows the enlarged view of the magnetic hysteresis loop of BFO films at 300 and 10 K for the 575°C annealed films and the variation in M_s with annealing temperature at 10 K. Fig. (c) shows the enlarged view of magnetization behaviour at 10 K. The variation of coercivity and remanence is shown in the inset.

The ferromagnetic component in films may arise due to the uncompensated spins at the grain boundaries or due to uncompensated moments at the surface. The surface contribution is primarily governed by the roughness of the films. The large surface roughness provides more uncompensated moments. In the present case highest roughness in the films annealed at 600 °C does not account for large value of magnetization. Therefore, the uncompensated spins at the grain boundaries is the origin of high magnetization, ignoring any surface contribution. Therefore, it is expected that the uncompensated moment present at the grain boundary is apparently different for different grain size distribution and this variation is responsible for the changes in magnetization values. Considering the fact that the integral multiple of the spin spiral length will constitute a compensated magnetic structure; grain sizes below or above the spiral length may provide uncompensated moments. Practically it is not feasible to obtain films with constant grain size; hence the presence of magnetization will be a cumulative effect of uncompensated moment present at the grain boundaries with different grain-size distribution. The obtained results thus suggest that the grain-size distribution plays an important role which lead to different surface spins to volume ratio [211]. The above results are contradictory with the previously reported studies on nanopowders, wherein the *M* increases with decreasing particle size [123, 212-213]. In addition, the results of present study cannot be compared with the thickness dependent magnetic behaviour of BFO thin films, wherein the magnetization is also found to decrease with thickness [47-49]. In the present study, the highest *M* (~12 emu/cm^3) at 300 K is observed for the films annealed at 575 °C. The average grain size of the BFO films annealed at 525 °C (~56 nm) is smaller than the film annealed at 575 °C (~93 nm), hence, the inverse relationship between size and magnetization may be ruled out in the present system [123]. Moreover, the BFO films annealed at 575 °C shows better crytallization, therefore an optimal grain size distribution and crystallization may be responsible for the enhanced *M* in sol-gel driven thin films.

Fig. 4.10 shows FC and ZFC magnetization curves of annealed BFO thin films, measured at an external field of 200 Oe in the temperature range of 10-300 K. The contribution of substrate was subtracted from the magnetization data. It can be noticed that the FC and ZFC curves are well bifurcated within the measured temperature range. The divergence between FC and ZFC increases progressively with decrease in temperature, which reveals the spin glass like behaviour [48]. As evident from the fig.4.10, the trends of FC-ZFC curves are almost similar for all the films, suggesting that the grain-size variation in the 200 nm thick BFO film has no effect on the temperature-dependent magnetization behaviour. A broad

maxima and sharp minima around 25 K is visible in all the FC and ZFC curves of the BFO films. Magnetization (*M*) value for all the ZFC curves is increasing with decreasing temperature up to 60 K; whereas for all the FC curves, *M* increases up to 25 K. The initial gradual increase in *M* with decreasing temperature may be attributed to the local clustering of spins [210]. Moreover, H_c at room temperature is nearly zero, which is found to increase at 10K (shown in the inset of fig. 4.9 (b)). This appearance of coercivity at low temperature (10K) is also an indication of the spin glass behaviour.

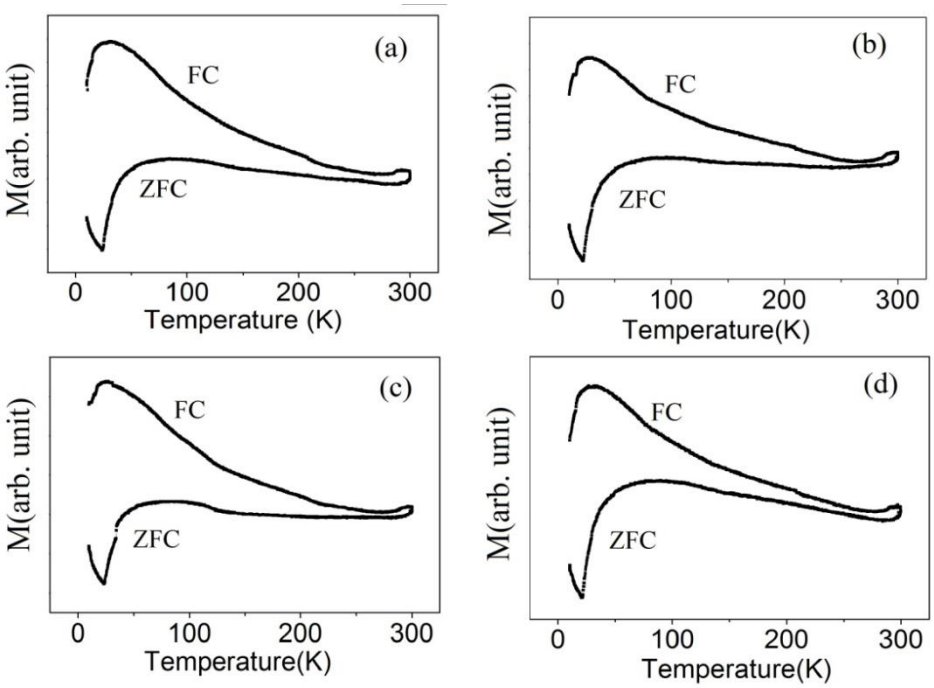

Fig. 4.10 FC-ZFC magnetization plots for the BFO thin films obtained at an applied magnetic field of 200 Oe for the samples annealed at (a) 525, (b) 550, (c) 575, and (d) 600 °C.

In summary, the effect of grain-size distribution induced by varying annealing temperature was investigated. The grain-size distribution is found to broaden with increase in annealing temperature. The SQUID magnetic measurements demonstrated a weak ferromagnetic behaviour for the BFO films at 300 and 10 K, due to uncompensated moments created at the grain boundaries by breaking of spiral spin cycloid ordering. The observed magnetic properties in the BFO films depend entirely on the cumulative effect of uncompensated moments originating from the variation in grain-size distribution. An optimal grain-size distribution obtained at 575 °C is responsible for the high *M* in the BFO film. The FC-ZFC magnetization curves depict a rise in *M* at lower temperature with an onset of spin glass state ~300 K.

4.1.2 Effect of film thickness

A detailed study of literature indicate that the tailoring of film thickness modulates the spin cycloid of BFO; thereby, promotes the magnetic properties (*w.r.t* its bulk counterpart) and improves the electrical properties due to better grain growth. Nevertheless, films with uniform thickness does not account for uniform grain sizes. A study on the thickness induced grain size distribution will therefore provide a better understanding on the structure-magnetic-ferroelectric property correlations in the BFO thin films. Accordingly, in the present work, a special emphasis is laid on the effect of thickness induced grain size distribution on the magnetic and electrical behaviour of polycrystalline BFO thin films. Thin films with variable thickness (156 - 388 nm) were prepared by sol-gel spin coating method followed by annealing at a constant temperature of 575 °C. The effect of thickness induced grain size distribution on the structural, magnetic and electric properties were systematically investigated.

4.1.2.1 XRD analysis

The X-ray diffraction (XRD) of BFO thin films is shown in Fig. 4.11. BFO films of varying thickness were refined by the multiprofile Rietveld system using FULLPROF software [193-194]. Minor characteristic (311) peak of maghemite (γ-Fe_2O_3) with space group $P4_332$ is present as a secondary phase. The refinements were done with space group *R3c* as phase I and $P4_332$ as phase II. As evident from Rietveld refinement, the volume fraction of γ-Fe_2O_3 was found to be same (0.08) in all the BFO films.

4.1.2.2 FESEM analysis

Fig.4.12 shows the FE SEM micrographs for BFO films of varying thickness. The cross sectional view of the BFO/ITO/glass is shown in fig. 4.12 (a-d). It is evident from the micrographs that the interfaces are well defined and distinguishable with thickness ~156, 206, 270, 388 nm of BFO and 218 nm of ITO layer. Fig. 4.12 (e & f) shows the microstructure of the 156 and 388 nm BFO films with well crystallized equiaxed grains separated by sharp grain boundaries having minimal porosity. The micrographs show an increase in grain size with varying thickness. Fig. 4.13 shows EDX spectra of the BFO films along with the expected elemental composition in the insets of respective system.

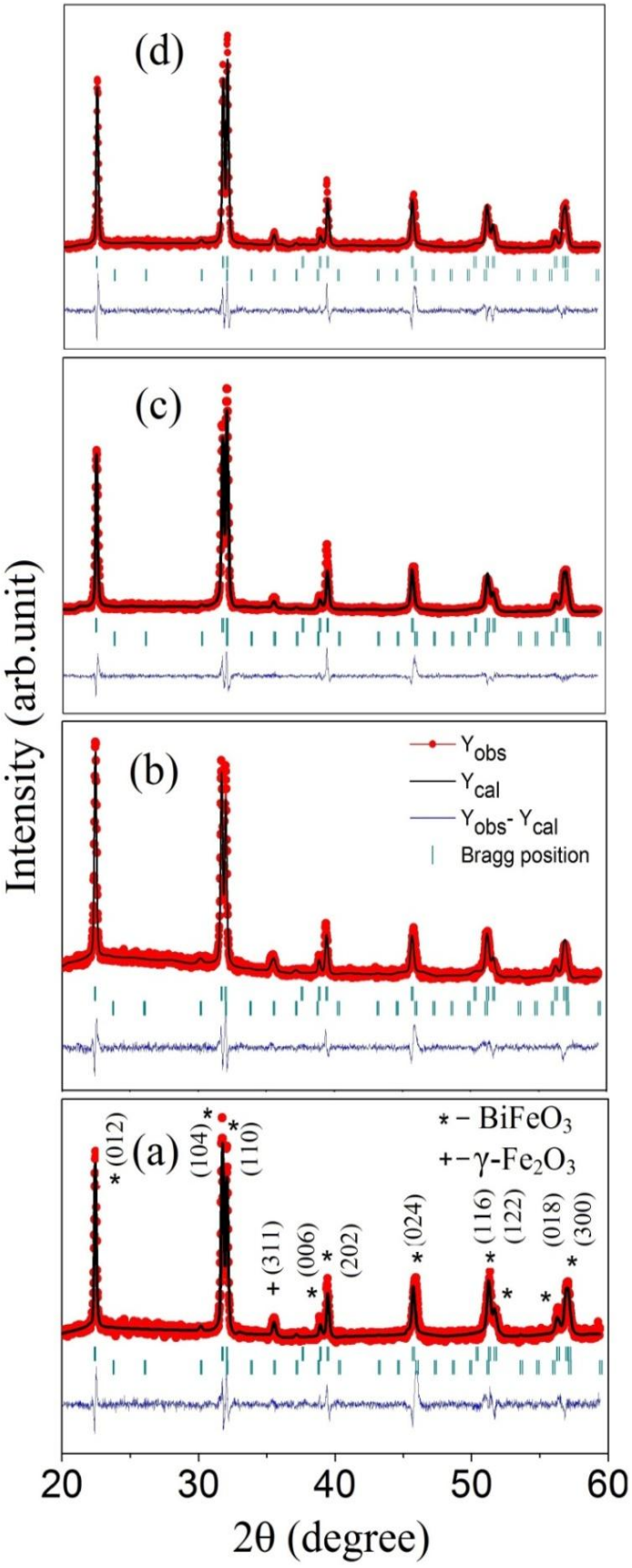

Fig. 4.11 Refined X-ray diffraction patterns of (a) 156, (b) 206, (c) 270 and (d) 388 nm thick BFO films annealed at 575 °C films.

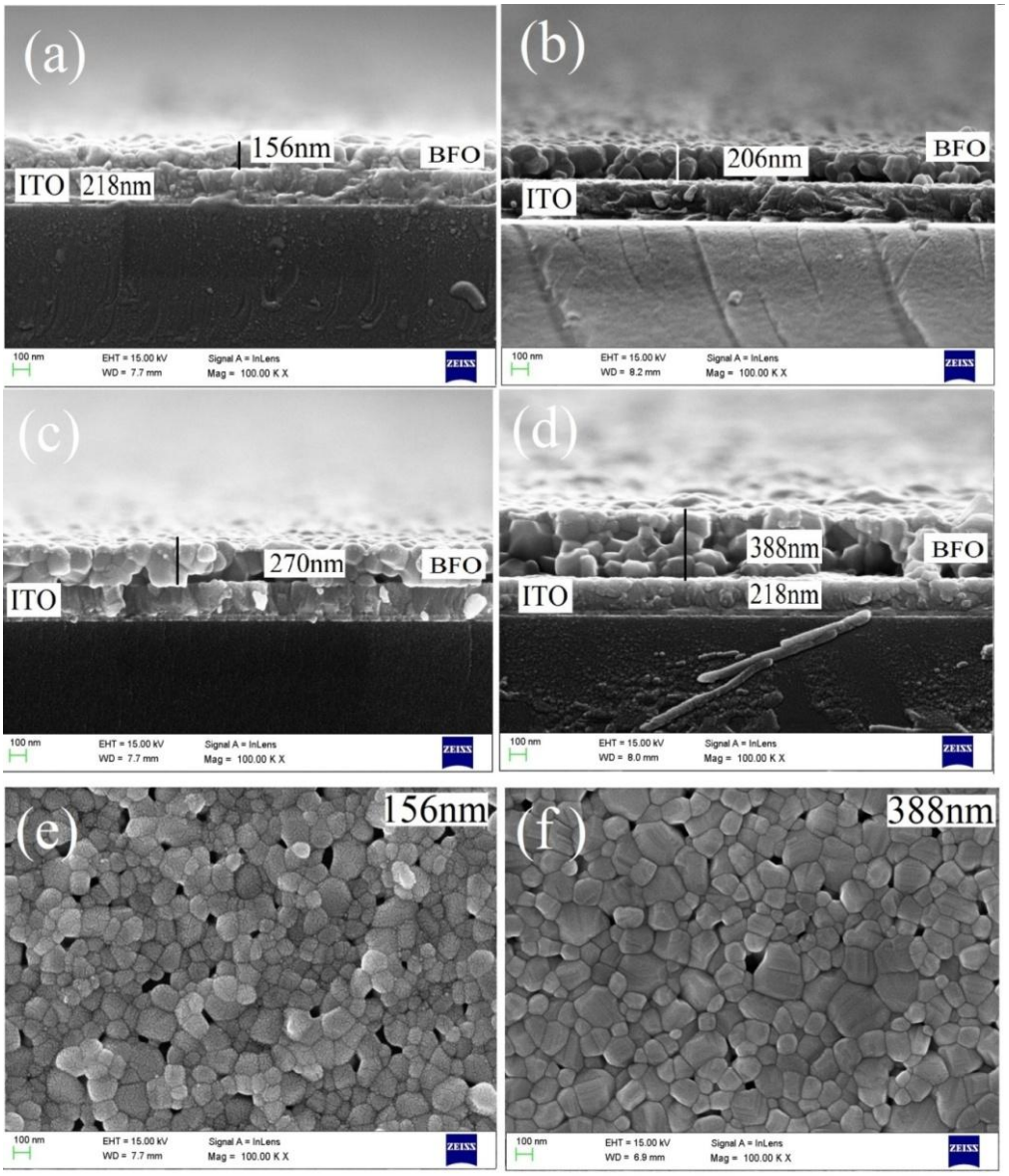

Fig. 4.12 FESEM micrographs of BFO thin films (a-d) cross- sectional view showing different thickness, and (e & f) surface morphology of 156 and 388 nm thick films.

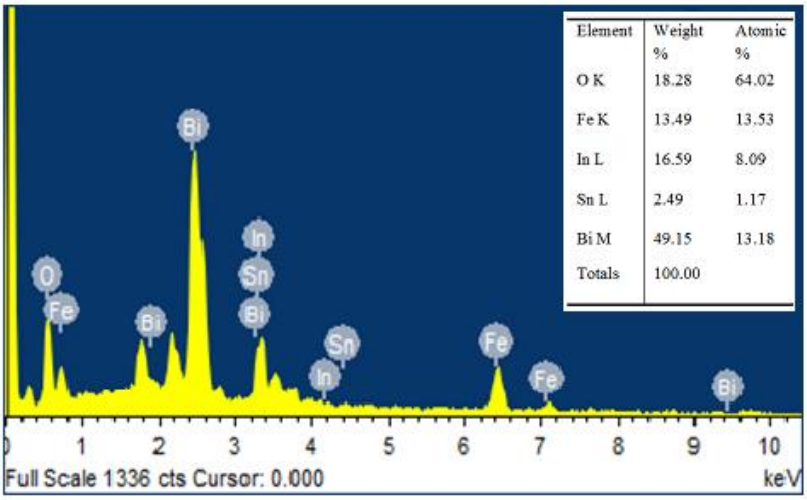

Fig. 4.13 EDX spectra of BFO thin film.

4.1.2.3 Grain size distribution analysis

Fig. 4.14 shows the grain size distribution plotted using ASTM E112 (linear intercept method) from FESEM micrograph by considering a minimum of 100 grains. The *x-y* axis scale of grain size distribution was kept constant for better visual comparsion. A Gaussian fit analysis of the distribution give mean grain size 82, 93, 135 and 219 nm for 156, 206, 277 and 388 nm BFO thick films respectively. Fig.4.14 (a) shows that 20% population of grains have size less than 65 nm for 156 nm film. With increasing film thickness, the distribution broadens; giving grains in 65-365 nm range for 388 nm thick film. Although, with thickness, the grain size increases but the possibility of percent fraction of grains having size less than the integral multiple of spiral spin cycloid period cannot be ruled out.

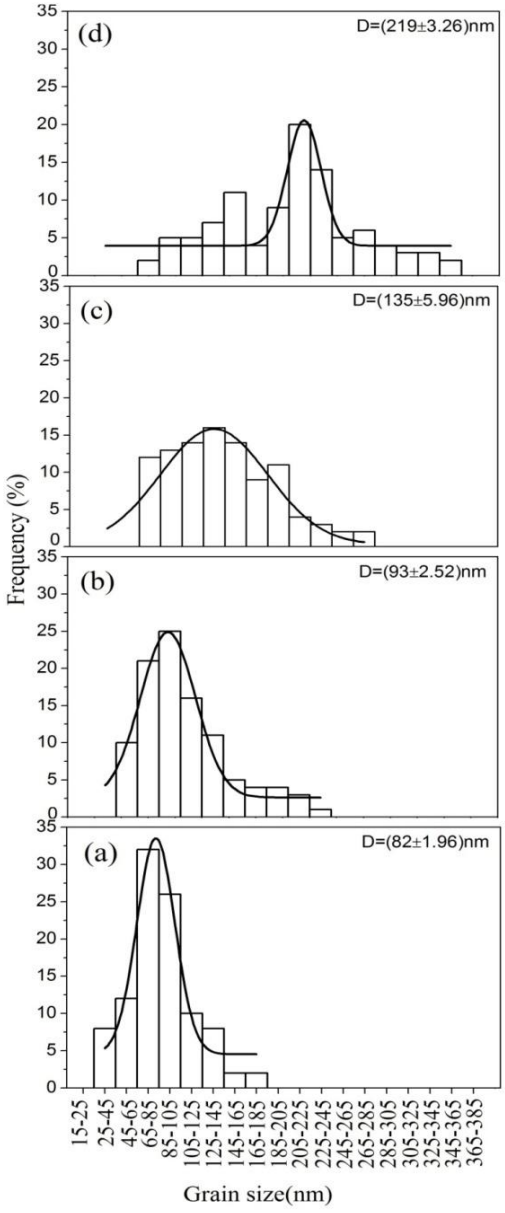

Fig. 4.14 Grain size distributions of the BFO thin films for (a) 156, (b) 206, (c) 270 and (d) 388 nm.

4.1.2.4 AFM analysis

The two dimensional AFM micrographs of (1×1) μm^2 area of BFO films of varying thickness annealed at 575 °C were shown in Fig.4.15. The micrographs presents uniform, smooth, continuous and dense morphology with minimal porosity. Increase in the grain size with thickness is evident from the AFM micrographs. Although average grain size increases with increasing thickness, a wide distribution in grain size is also evident in the AFM micrographs which are in agreement with FESEM (fig.4.12).

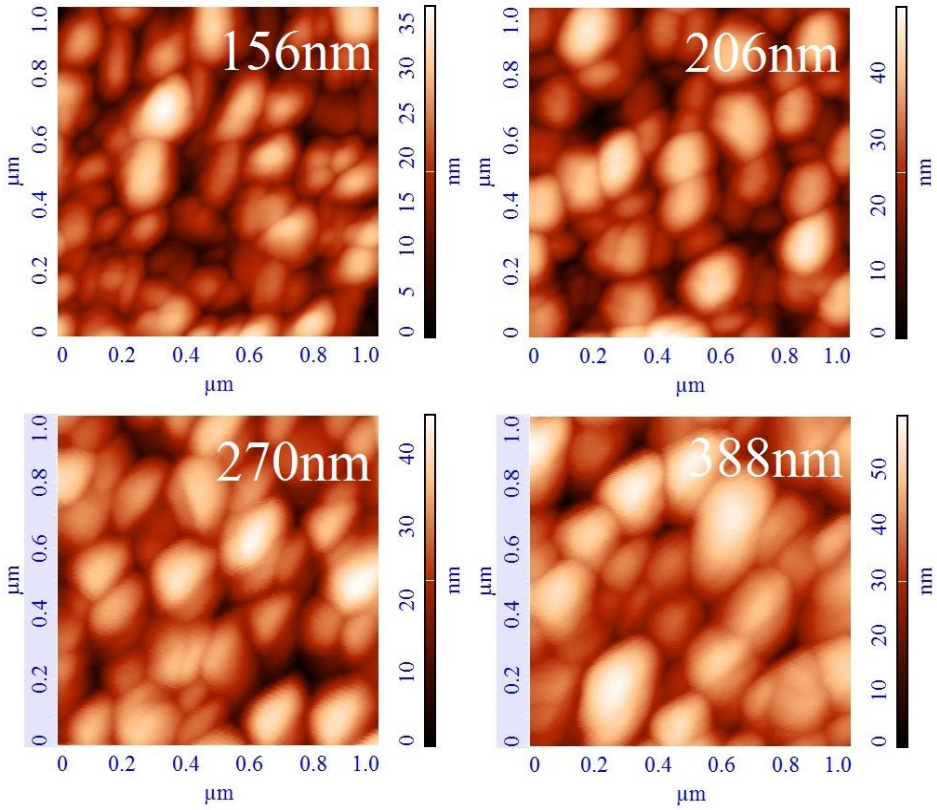

Fig. 4.15 AFM images of the BFO thin films of varying thickness.

4.1.2.5 Magnetic measurements

Fig. 4.16 shows the *M-H* loops of BFO thin films of varying thickness measured at 300 and 10 K respectively. The formula $M_{dia}/H = -\chi$ is used to subtract the diamagnetic contribution from the raw data. At 300 K, well saturated *M-H* curve is observed for all the BFO films and the estimated M_s values are found to decrease with the films thickness. A maximum M_s of ~18.99 emu/cm^3 while a minimum of 0.93 emu/cm^3 were obtained for the 156 nm and 388 nm thick BFO films, respectively. For a particular film thickness, the grain size is not uniform rather it varies over a wide distribution range (Fig.4.12 and Fig. 4.14).

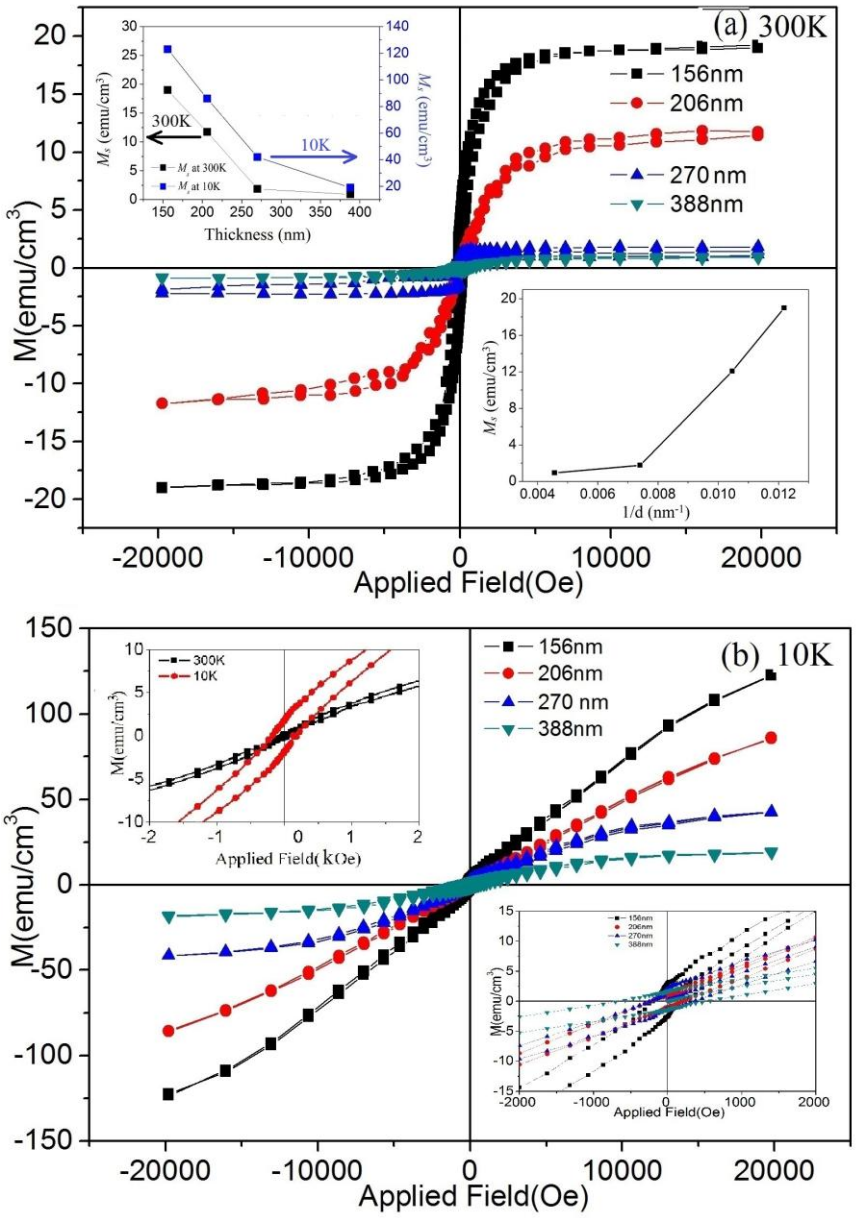

Fig. 4.16 Magnetic hysteresis loop of BFO thin films at room temperature (above) and at 10 K (below). The inset 1 and 2 of figure (a) shows $\boldsymbol{M_s}$ variation with thickness at 300 and 10K; and the variation in $\boldsymbol{M_s}$ (at 300K) with 1/d (d-grain size). The inset 1 and inset 2 of figure (b) shows the enlarged view of the magnetic hysteresis loop of BFO thin films at 300 and10K for the 206nm thick film and the hysteresis loop at 10K respectively.

The observed *M* trend arises from the grain size distribution, where the relative proportion of the uncompensated spins at the grain boundaries becomes larger with decreasing film thickness. The grain size distribution for 156 and 206 nm thick films gives higher magnetization values. The fact that the integral multiple of the spin spiral will constitute a compensated magnetic structure; the grain sizes below or above the spiral length may provide uncompensated moments at grain boundaries. Therefore, every individual grain has two magnetic component i.e. antiferromagnetic within the grain as core and ferromagnetic component at the grain surface. The relative contribution of each component will strongly be

size dependent. The uncompensated spin density at the grain surface will be higher for smaller grains as is evident from the inset 2 of fig. 4.16 (a) that the magnetization increases with decrease in average grain size. Hence, the BFO grains can be modelled by a superposition of an antiferromagnetic core with a ferromagnetic surface, and their magnetization is mainly contributed by the uncompensated spins at the grain surface [123-124, 213]. The contribution to *M* due to presence of minor magnetic γ-Fe_2O_3 phase can be ignored as its fraction (0.08) as obtained from the rietveld refinement of the XRD patterns is almost same in all the films. At lower temperature (10 K), the *M-H* loops are non-saturated due to spin freezing [27, 74]. The inset 1 in Fig. 4.16 (b) shows an enlarged view of the *M-H* loops for the 206 nm thick BFO film at 300 and 10 K indicating an increase in H_c at 10 K. Also shown in the inset 2 of fig. 4.16 (b) is an enlarged view of the hysteresis at 10 K for BFO films of varying thickness.

4.1.2.6 Dielectric measurements

Fig.4.17 shows the *RT* dielectric measurements in the frequency range of 100 Hz to 1 MHz. At low frequencies, the dielectric constant (ε′) increases and dielectric loss (tanδ) decreases with increasing thickness. The ε′ at 100 Hz increases from 71 (156 nm) to 435 (388 nm). The porosity decreases while the density of the film increases with increase in film thickness (Figs.4.12 and 4.15). Therefore, increase in ε′ and decrease in tanδ observed with increasing thickness is because of reduction in voids between the grains or the local defects, improved crystallization, densification and growth of grains [166]. There are different types of polarizations that contribute in enhancing the ε′ at lower frequencies but lag to follow the field reversal at higher frequencies. Upon increasing the thickness, all the films present a similar trend, i.e. increasing ε′ and decreasing tanδ against frequency governing the cumulative effect of grains comprising the film. A sharp decrease in ε′ with increasing frequency and decreasing film thickness is evident by the shifting of falling slope of ε′ towards left in fig. 4.19 (a). However, in the high frequency region, ε′ gradually decreases and becomes nearly constant for the films of variable thickness.

The dielectric loss (tanδ) variation with frequency is shown in Fig. 4.17 (b). A sudden decrease in tanδ upto 10 kHz is observed for all the films, which tends to become fairly constant in the higher frequency region. Increasing film thickness decreases tanδ from 11.2 (156 nm) to 5.8 (388 nm) at 100 Hz and 0.305 (156 nm) to 0.097 (388 nm) for BFO thick film

at 1 MHz. As is evident from fig.4.14, the grain size distribution broadens with increasing thickness giving more fraction of bigger size grains due to which the pinning of domain walls gets restricted, causing a significant decrease in tanδ [166]. Though, the contribution from smaller size grains cannot be ignored resulting in somewhat higher value of tanδ in contradiction with the previously reported values [166, 185].

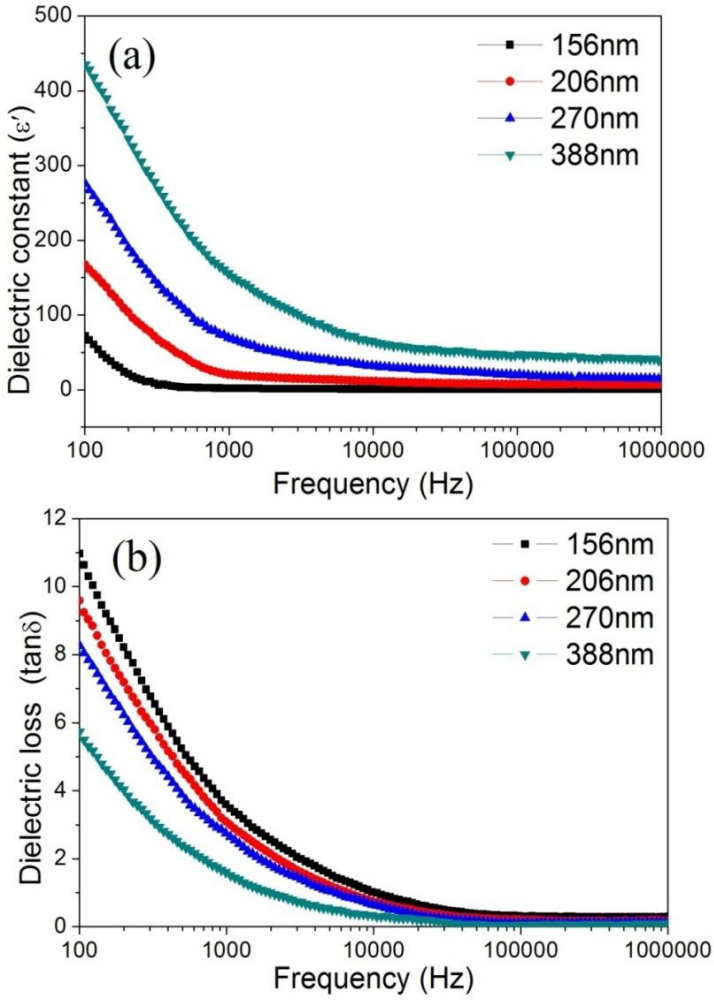

Fig. 4.17 Frequency dependent (a) dielectric constant (ε′) and (b) dielectric loss (tanδ) behaviour at room temperature of BFO thin films.

4.1.2.7 Ferroelectric measurements

Fig. 4.18 shows the room temperature *PE* loops for BFO films of varying thickness at 10 kHz frequency. The BFO films seem to be highly resistive, as they withstand an applied electric field of 600 kV/cm without undergoing any breakdown. The hysteresis loop for 156 nm thick BFO film is non-saturated. The thickness effect on polarization is clearly visible with increase in polarization and loops gaining saturation on increasing thickness from 156 to 388 nm [166]. An increase in coercive field (E_c) has been observed with increasing film thickness which is probably due to the presence of smaller size grains as is visible in the grain

size distribution curves of fig. 4.14 that makes polarization switching more difficult. The remnant polarization (P_r) increases from 0.0178 to 1.63 μC/cm^2 with increase in thickness of BFO films. The observed increase in the ferroelectric properties is due to better growth and densification of the films with increasing thickness.

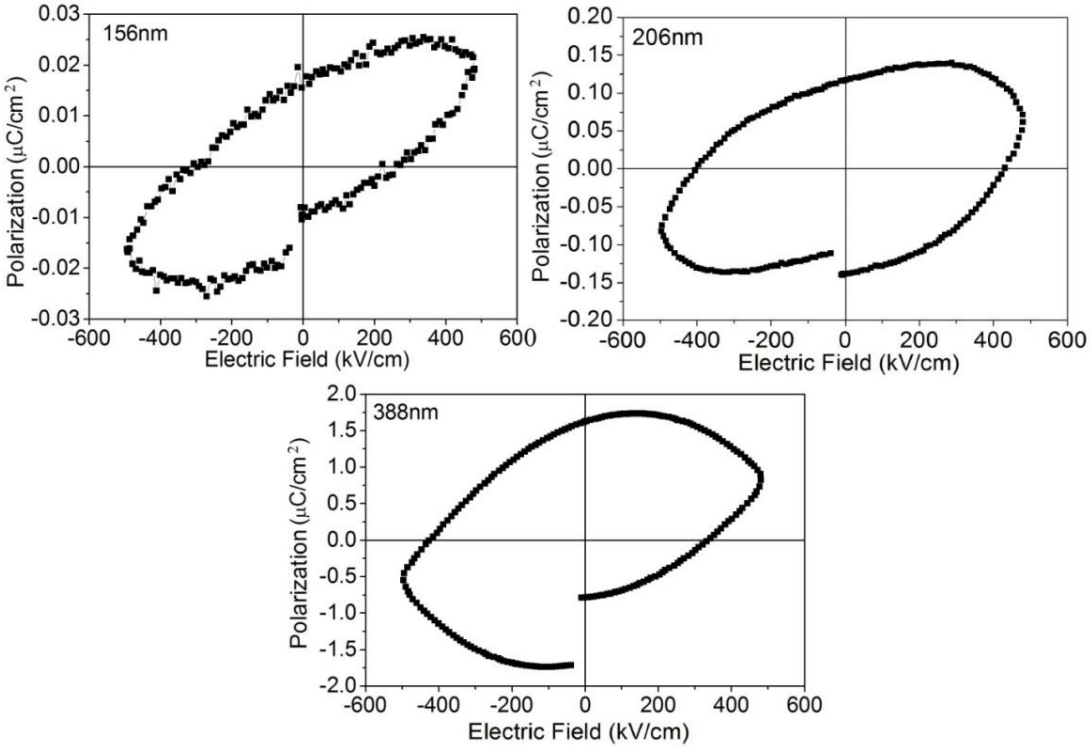

Fig. 4.18 Room temperature *PE* loops for 156, 206 and 388 nm thick BFO films taken at a frequency of 10 kHz.

In summary, the effect of thickness induced grain size distribution on the magnetic and electrical properties of the BFO thin films was investigated. The FESEM and AFM micrographs clearly indicated well crystallized grains with wide distribution. The observed trends in *M-H* curves indicated the strong dependence of magnetization on the grain size distribution. The occurrence of ferromagnetic behaviour at 300 and 10 K is due to the uncompensated spins at grain boundaries. At 10 K, the *M-H* loops are non saturated due to spin freezing. The ferroelectric properties found to be improved due to better growth and densification with increasing film thickness. The dielectric constant (ε′) increases and dielectric loss (tanδ) decreases with increase in BFO film thickness.

4.2 Effect of Gd and Co substitution in BFO thin films

It is concluded that the grain size variation has significant effect on magnetic behaviour of BFO thin films. Besides, the grain size variation; low level substitution of rare earth metal ions at Bi^{3+} sites or transition metal ions at Fe^{3+} sites is an alternative method for achieving enhanced magnetic and electrical properties, which also reportedly suppresses the cycloidal spin structure [170-171, 179-184, 190]. In this section the effect of Gd and Co ion substitution at respective Bi and Fe sites on the structural, dielectric, ferroelectric and magnetic properties are investigated.

4.2.1 Effect of Gd substitution

4.2.1.1 XRD analysis

Fig. 4.19 shows the refined XRD pattern of $Bi_{1-x}Gd_xFeO_3$ (BGFO) thin films, where; x=0, 0.05, 0.075, 0.100, and 0.125. The annealing temperature was kept constant (575 °C) in this study. The refinements were done using space group *R3c* and $Pn2_1a$. The effects of Gd-substitution on the crystal structure were analyzed and the obtained results are summarized in Table 4.2. Both *R3c* and $Pn2_1a$ structural models fits adequately but the better fit was obtained with the *R3c* space group upto x=0.100. At x=0.125, the better fitting was obtained for $Pn2_1a$ as compared to *R3c* (Table 4.2). The small R-factors and χ^2 suggest the goodness of fit. A corresponding decrease in lattice parameters and shrinkage in unit cell volume observed with increasing Gd content. The smaller ionic radii of Gd^{3+} (1.053 Å) *w.r.t* Bi^{3+} (1.17Å) [64] is responsible for the observed shrinkage (Table 4.2). Merging of (104) and (110) peaks (Fig. 4.19 (c)) with Gd-substitution indicates the transformation from rhombohedral to orthorhombic phase ($Pn2_1a$) [103]. Also shifting of peaks towards higher angle with Gd content suggests the tensile stress in the system. It is worth to mention that substitution with smaller ionic radii ion creates tensile stresses while larger ion provides compressive stress. The crystallite size as calculated from Scherrer formula [195] for different Gd compositions is shown in fig. 4.20. It is evident that crystallite size decreases on increasing the Gd content revealing the compressive lattice distortion.

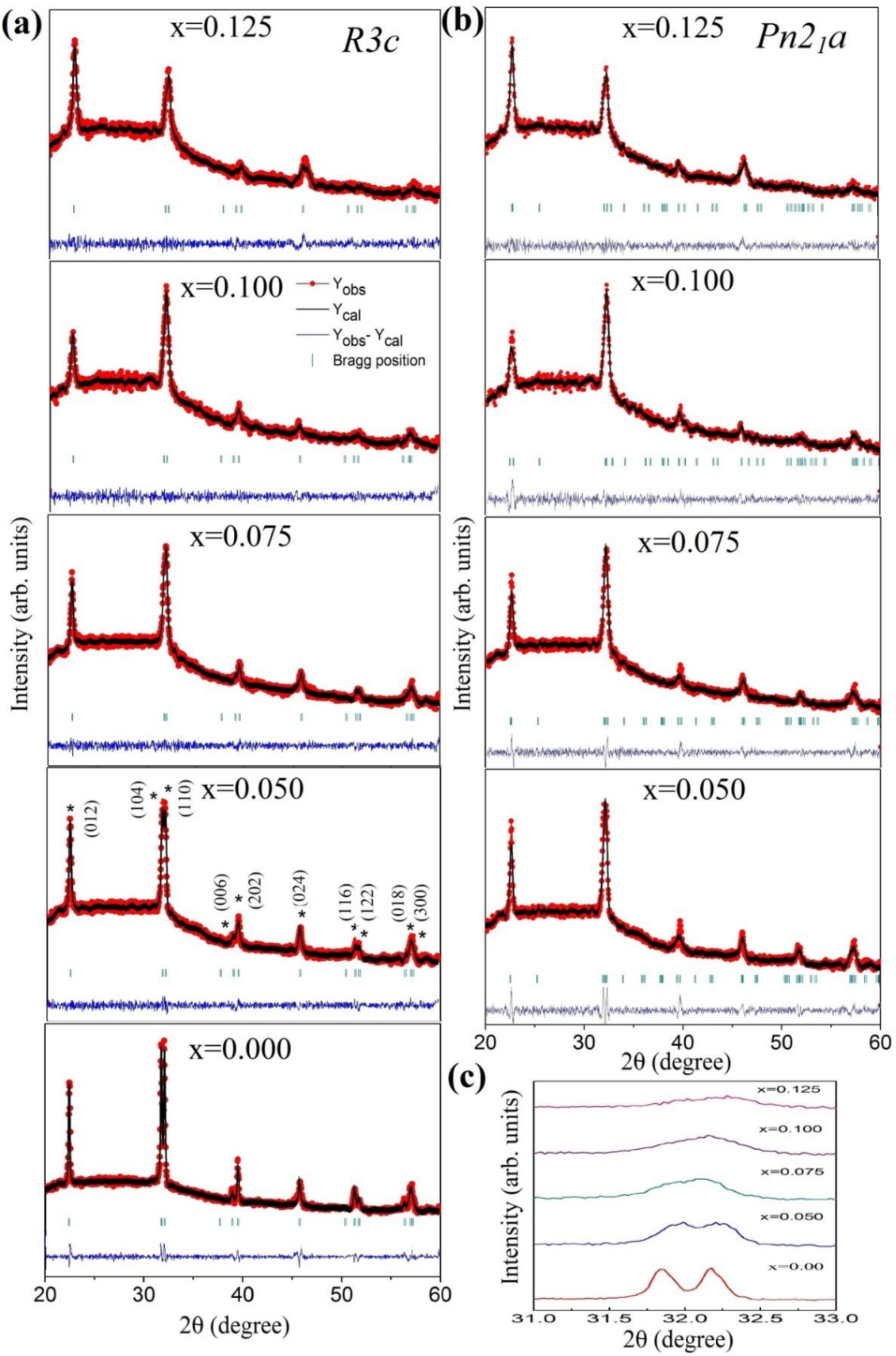

Fig. 4.19 Refined X-ray diffraction patterns of sol-gel driven BGFO thin (a) *R3c* (b) *$Pn2_1a$* space groups. Fig (c) shows the merging and shifting of (104) and (110) peak with Gd-substitution.

Table 4.2 Refined parameters for the $Bi_{1-x}Gd_xFeO_3$ (x=0, 0.05, 0.075, 0.100, and 0.125) thin films with space group *R3c* and $Pn2_1a$.

Composition & Structural model	**Cell parameters [*a* & *c* (Å), *V*(Å^3)]**	**Atoms**	**Position**	**Atom Coordinates**			**R-factors & χ^2**
				x	***y***	***z***	
x=0.000	*a*=5.5797	Bi	6a	0	0	0.21172	R_B=3.69
R3c	*c*=13.8768	Fe	6a	0	0	0	R_F=2.59
	V=374.146	O	18b	0.81767	0.63566	0.80874	χ^2=1.82
x=0.050	*a*=5.5814	Bi/Gd	6a	0	0	0.23797	R_B=2.14
R3c	*c*=13.8592	Fe	6a	0	0	0	R_F=1.49
	V=373.907	O	18b	0.74320	0.65804	0.86842	χ^2=1.21
$Pn2_1a$	*a*=5. 6098	Bi/Gd	4a	0.04177	0.27216	0.99024	R_B=2.82
	b=7.8974	Fe	4a	0.05126	0.00000	0.50887	R_F=2.32
	c=5.5465	O1	4a	0.46261	0.42514	0.33815	χ^2=1.95
	V=245.817	O2	4a	0.11664	0.50481	0.23242	
		O3	4a	0.38646	0.29946	0.78607	
x=0.075	*a*=5.5858	Bi/Gd	6a	0	0	0.21681	R_B=2.41
R3c	*c*=13.8158	Fe	6a	0	0	0	R_F=1.68
	V=371.985	O	18b	0.78684	0.56360	0.87271	χ^2=1.09
$Pn2_1a$	*a*=5. 5914	Bi/Gd	4a	0.04103	0.27670	0.96683	R_B=1.96
	b=7.8946	Fe	4a	0.04133	0.00000	0.50887	R_F=1.98
	c=5.5317	O1	4a	0.42893	0.38347	0.10376	χ^2=1.32
	V=244.180	O2	4a	0.10822	0.50372	0.26056	
		O3	4a	0.32956	0.29851	0.79790	
x=0.100	*a*=5.5753	Bi/Gd	6a	0	0	0.21230	R_B=2.13
R3c	*c*=13. 8541	Fe	6a	0	0	0	R_F=1.51
	V=371.248	O	18b	0.78240	0.64722	0.84443	χ^2=1.19
$Pn2_1a$	*a*=5. 5602	Bi/Gd	4a	0.04987	0.25802	0.97779	R_B=1.96
	b=7.8925	Fe	4a	0.02599	0.00000	0.50469	R_F=1.46
	c=5.4433	O1	4a	0.50278	0.28400	0.10628	χ^2=1.36
	V=241.873	O2	4a	0.16700	0.57779	0.20610	
		O3	4a	0.23270	0.58639	0.78422	
x=0.125	*a*=5.5640	Bi/Gd	6a	0	0	0.21541	R_B=1.98
R3c	*c*=13.8333	Fe	6a	0	0	0	R_F=1.45
	V=370.875	O	18b	0.49837	0.68114	0.81592	χ^2=1.33
$Pn2_1a$	*a*=5. 5786	Bi/Gd	4a	0.04368	0.31659	0.93640	R_B=1.53
	b=7.8283	Fe	4a	0.00724	0.00000	0.42756	R_F=1.05
	c=5.4753	O1	4a	0.26671	0.28204	0.54795	χ^2=1.27
	V=238.323	O2	4a	0.11879	0.55492	0.19023	
		O3	4a	0.30627	0.51887	0.69766	

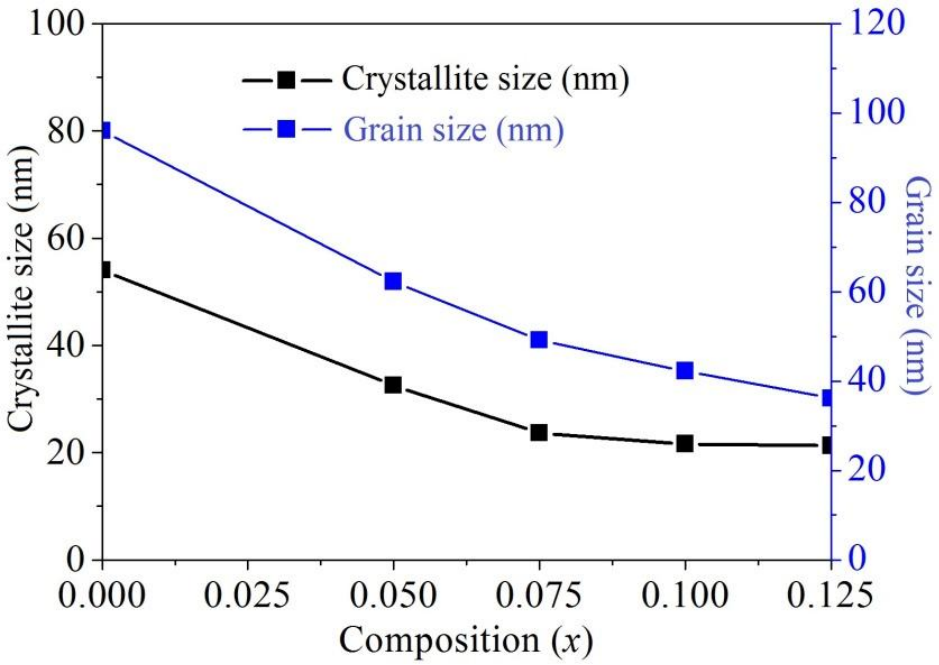

Fig. 4.20 Crystallite and grain size as calculated from XRD (black) and FESEM micrographs (blue).

4.2.1.2 FESEM analysis

Fig. 4.21 shows the FESEM micrographs of BGFO films deposited on ITO coated glass substrate. Inset of fig.4.21 (a) shows well defined interface between the ITO and BGFO film. The measured thickness of BFO and BGFO film is ~200 nm. Figs. 4.21 (b-f) show the FESEM surface morphology of BGFO thin films for different Gd substitution amount. The microstructures of films reveal a well crystallized equiaxed BGFO grains separated by sharp grain boundaries. A little porosity is also observed for x=0; the porosity fraction is found to decrease with Gd-substitution. It is evident from the FESEM micrographs that the grain size is decreasing with increasing Gd content. The average grain size values were measured by considering a minimum of 150 grains. The grain size for pure and Gd-substituted BFO were found to be 96, 62.27, 49.23, 42.25 and 36.18 nm for x=0, 0.05, 0.075, 0.100 and 0.125 respectively (Fig. 4.20). The difference in the crystallite size as calculated from the obtained XRD pattern and the grain size calculated from the FESEM micrographs showed that the grains are not single crystalline but are rather made up of a large number of crystallites.

Fig. 4.22 shows EDX spectra of BGFO thin films with their elemental compositions in the insets of respective compositions. It is evident from the EDX that Gd content in the BFO film is increasing with substitution.

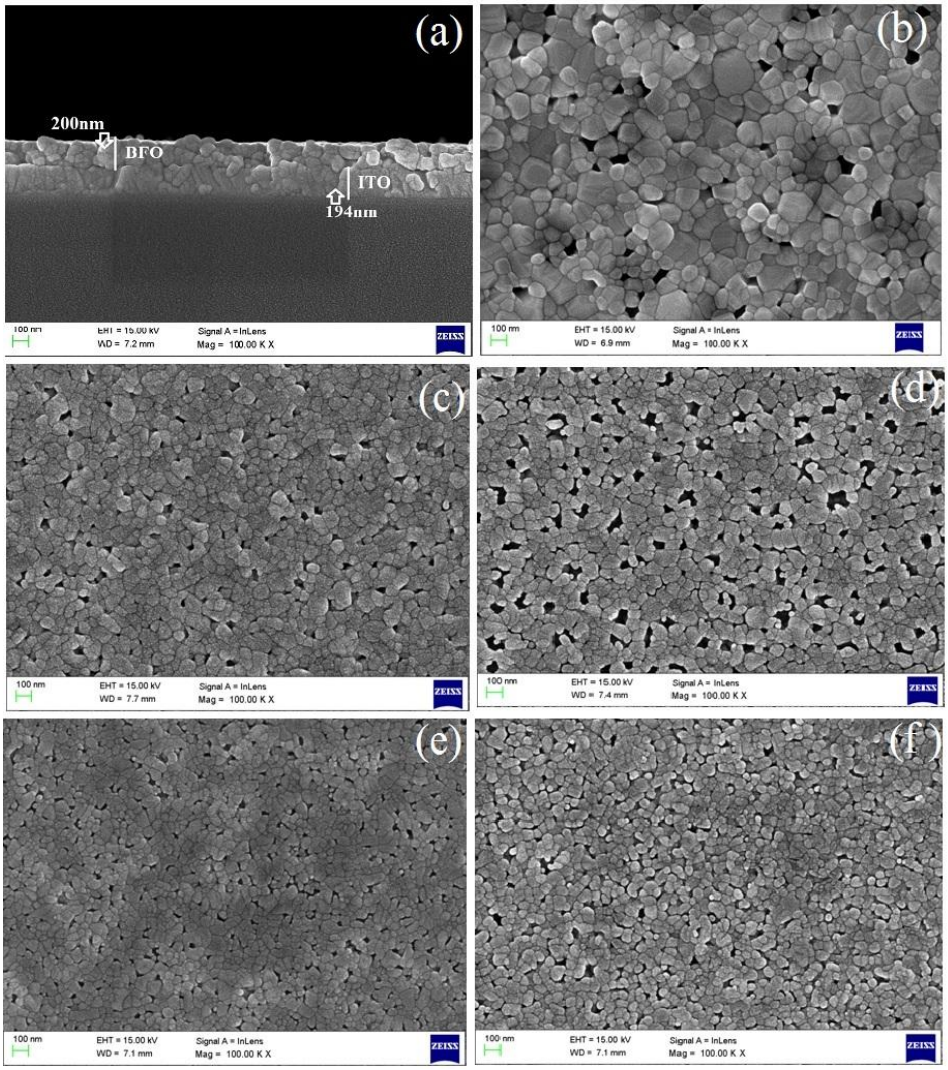

Fig. 4.21 FESEM micrographs of BGFO thin films showing (a) cross-sectional image and surface morphology for (b) x=0, (c) x=0.05, (d) x=0.075, (e) x=0.10 and (f) x=0.125 compositions.

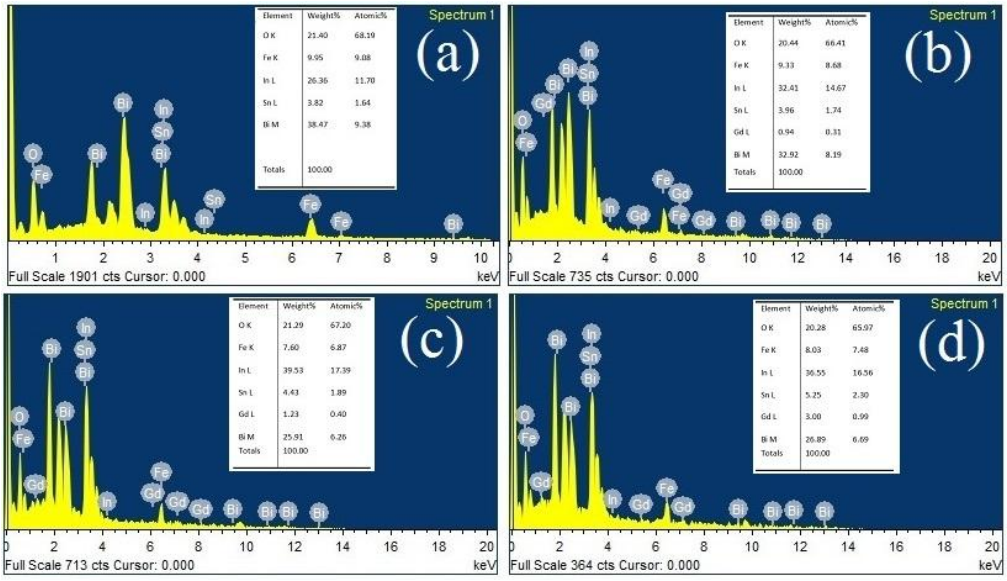

Fig. 4.22 EDX spectra of BGFO thin films showing their elemental composition for (a) x=0.0, (b) x=0.075, (c) x=0.10 and (d) x=0.125.

4.1.2.3 AFM analysis

Fig. 4.23 shows the AFM micrographs of (2×2) μm^2 area of BGFO films. The AFM surface shows smooth, uniform, continuous and dense morphology with minimal porosity. The AFM micrographs indicate an obvious decrease in the grain size with Gd-substitution. The AFM observations are in agreement with the FESEM analysis. The root mean square roughness (R_q) of the BGFCO films were obtained over an area of (10×10) μm^2 and the observed R_q values tend to increase from 10.059 nm (*x*=0) to 14.890 nm (*x*=0.1).

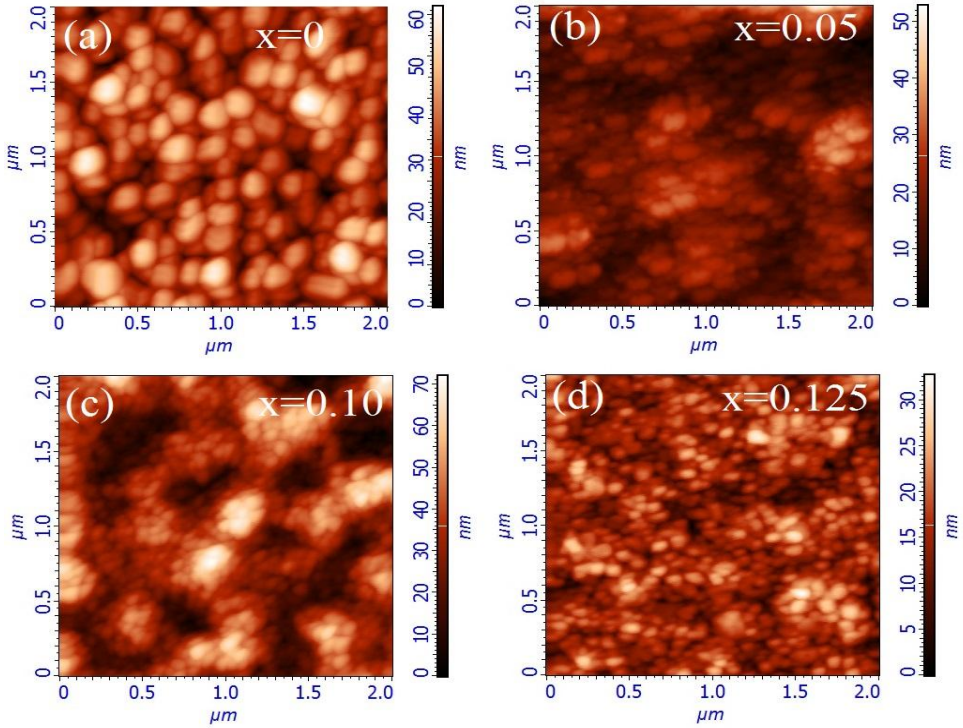

Fig. 4.23 AFM images of the BGFO thin films with (a) *x*=0, (b) *x*=0.05, (c) *x*=0.10 and (d) *x*=0.125.

4.2.1.4 TEM analysis

Fig. 4.24 (a & e) shows the TEM images of pure and Gd-substituted (*x*=0.1) BFO thin films on a 50 nm scale. It is clear from the TEM images that the grains are well distinguised and nearly spherical in shape. Although with Gd substitution the decrease in grain size is clearly visisble. The decrease in grain size could be ascribed to two reason, one may be due to smaller ionic radii (1.053 Å) of Gd^{3+} in comparison to Bi^{3+} (1.17Å) [67], which provide lattice shrinkage as confirmed by XRD analysis. However, the dramatic decrease in grain size can not be soleley ascribed to the lattice shrinkage. The other one may be the presence of dispersed Gd, which remained unsubstituted at Bi site. There is strong possibilty that the dispersed Gd impedes the grain growth and resulted in very small grain size.

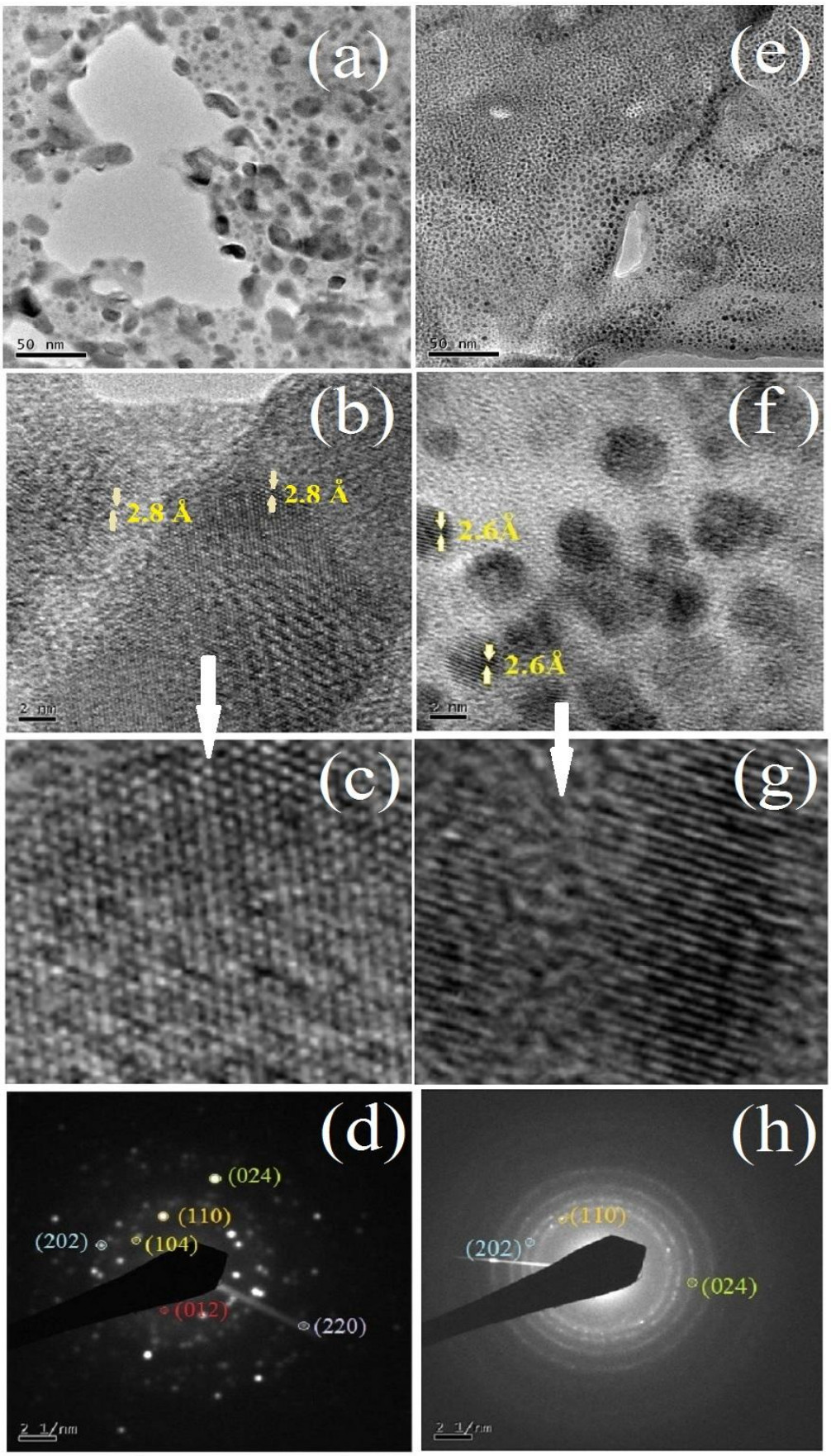

Fig. 4.24 TEM, HRTEM image, magnified HRTEM and corresponding SAED pattern for (a-d) x=0 and (e-h) x=0.10 BGFO thin films respectively.

HRTEM images (Fig. 4.24 (b & f)) gives lattice fringes with d-spacing of 2.8 Å and 2.6 Å for pure and Gd-substituted (x=0.1) BFO thin film respectively. Also the magnified HRTEM images (Fig. 4.24 (c & g)) confirms the structural transformation on Gd substitution. (Fig. 4.24 (d&h)) shows the indexed SAED patterns with sharp discrete spots though not continuous for pure BFO thin film, whereas Gd-substituted (x=0.1) BFO showed continuous ring pattern indicating the nanocrystallinite nature of films. Table 4.3 shows the structural parameters for x=0 and x=0.1 calculated from XRD and SAED pattern. This difference in cell parameters might be due to errors associated with XRD refinement.

Table 4.3: Structural parameters for pure and Gd- substituted BFO

Composition	Cell parameters obtained from XRD		Cell parameters obtained from Rietveld refinement		Cell parameters calculated from SAED pattern	
	Lattice parameters (Å)	V (Å^3)	Lattice parameters (Å)	V (Å^3)	Lattice parameters (Å)	V (Å^3)
x=0	a=5.5798 c=13.8720	374.031	a=5.5797 c=13.8768	374.146	a=5.6153 c=14.122	385.641
x=0.10	a=5.5634 c=13.8348	370.839	a=5.5753 c=13.8541	371.248	a=5.4354 c=14.5674	372.716

4.2.1.5 Dielectric measurements

Fig. 4.25 (a) shows the *RT* dielectric measurements in 100 to1 MHz frequency range. At low frequencies (<1000Hz), the dielectric constant (ε′) increases and dielectric loss (tanδ) decreases with Gd substitution. At 100 Hz, ε′ is increased from 210 (x=0) to 3534 (x=0.1). It is clearly evident from the FESEM and AFM images (Fig. 4.21 & 4.23) that the grain size decreases with Gd-substitution leading to more grain boundaries which are primarily responsible for enhanced surface polarization and hence the ε′. However, ε′ decreases gradually with frequency upto 1000 Hz and becomes almost constant beyond 10 kHz. Fig 4.25 (b) shows the variation in tan δ with frequency. The tanδ initially increases with frequency, gradually starts falling and becomes nearly constant beyond 100 KHz for pure and Gd-substituted BFO films. The presence of a relaxation regime ~500 Hz is observed; however, few studies have reported the presence of two relaxation regimes; one at low frequency ~1 KHz and other ~10 MHz [177, 179, 214]. As our measurements are limited only upto 1MHz, therefore, only one relaxation regime is observed. This low frequency relaxation behaviour observed for x=0 can be attributed to the grain boundary conduction [177, 214]. Gd substitution suppresses this relaxation regime due to enhanced grain boundary insulation

caused by decrease in grain size. The tanδ decreases from 12.34 for x=0 to 1.02 for x=0.1 at 100 Hz. The grain boundary enhancement and densification is assumed to be the main cause for the observed decrease in tanδ with Gd- substitution.

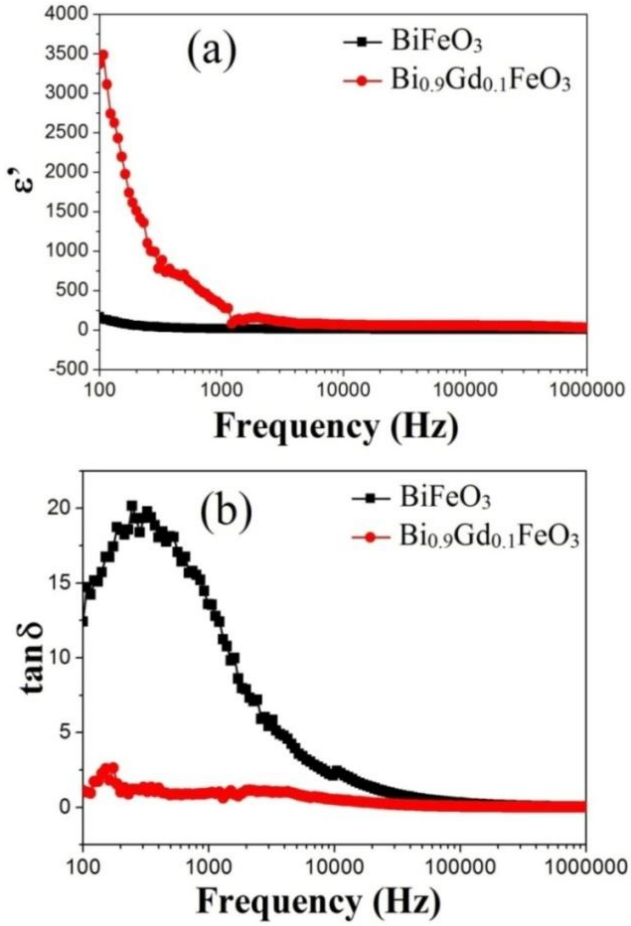

Fig. 4.25 Room temperature frequency dependent (a) dielectric constant and (b) dielectric loss curves for the BGFO thin films for (a) x=0, and (b) x=0.10 compositions.

4.2.1.6 Ferroelectric measurements

Fig. 4.26 shows the room temperature *PE* loops at 10 kHz for the BGFO films with different Gd content. The measurements for Gd- substituted films were taken at different applied fields. The hysteresis loop for x=0 is non-saturated with remnant polarization (P_r) = 0.032 μC/cm^2 and E_c =48 kV/cm at an applied electric field of 250 kV/cm (Fig. 4.26 (a)). However, the effect of Gd-substitution on polarization is clearly visible with observed saturation in loops and increase in P_r. The P_r of the film is increasing from 0.12 to 3.5 μC/cm^2 as Gd content increases from x=0.075 to 0.125 for same applied field of 250 kV/cm. The saturated loops suggest decrease in leakage current [179]. On the other hand P_r also increases with the applied field for same composition (Fig. 4.26 (c & d)) [191]. A significant increase in coercivity and P_r has been observed. For x =0.10 (Fig. 4.26 (c)) at an applied

electric field of 200, 750 and 1000 kV/cm, P_r ~ 0.62, 3.12 and 6.23 μC/cm^2 and E_c ~ 143, 544 and 753 kV/cm has been observed. Alternatively for x =0.125 (Fig. 4.26 (d)) at an applied electric field of 250 and 425 kV/cm, P_r= 3.5 and 6.36 μC/cm^2 and E_c = 150, and 306 kV/cm has been observed. The observed increase in the ferroelectric properties with increasing Gd content may be attributed to lattice distortion, densification and decrease in grain size leading to surface area enhancement due to large grain boundaries that tends to increase the surface boundary resistance [179].

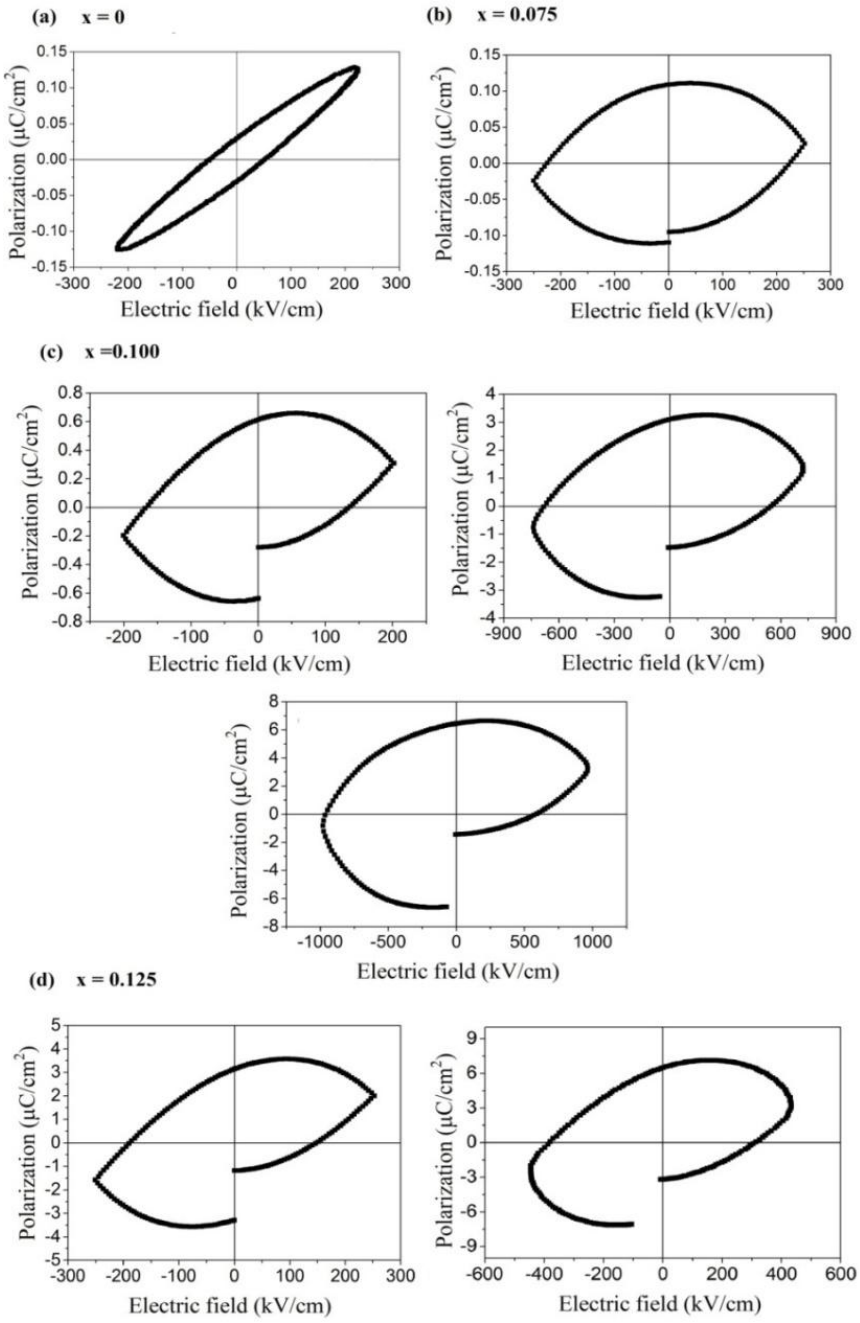

Fig. 4.26 Room temperature *PE* loops for the BGFO thin films obtained at a frequency of 10 kHz for (a) x=0, and (b) x=0.075, (c) x=0.10 and (d) x=0.125 compositions.

4.2.1.7 Magnetic measurements

Fig. 4.27 shows the in-plane *M-H* behaviour of BGFO thin films with x=0 and x=0.1 compositions obtained at 300 K. The *M-H* behaviour of the films at 300 K presents well-saturated hysteresis loop depicting the ferromagnetic nature of BGFO thin films [184, 191]. Inset of Fig. 4.27 (a) shows the as measured *M-H* behaviour of the x=0 and x= 0.1 BGFO films without subtraction of the diamagnetic contribution from substrate. The diamagnetic contribution was subtracted as mentioned in section 4.1.1.5.1. BGFO films shows remarkable enhancement in M_s from 7.18 emu/cm^3 (x=0) and 27.93 emu/cm^3 (x=0.1). The increase in M_s with Gd substitution may be due to greater lattice distortion and suppression of spiral spin cycloid. The origin of ferromagnetic component in BGFO films may be attributed to uncompensated spins at the grain boundaries due to finer grain size. Similar results were observed in rare earth doped BFO [62, 103].

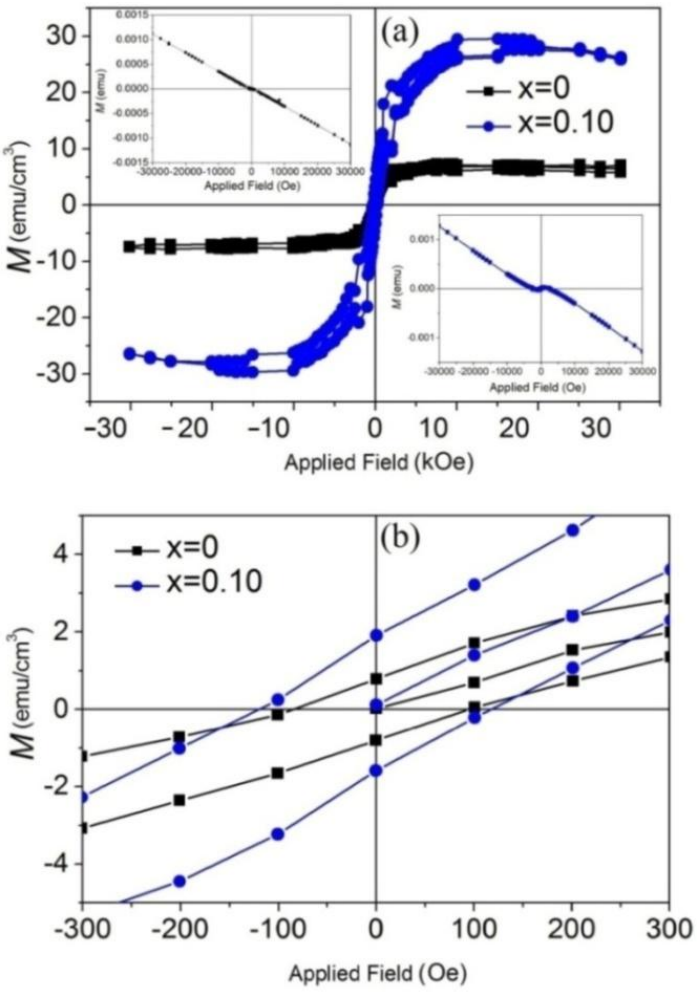

Fig. 4.27 Magnetic hysteresis loops of BGFO thin films obtained at *RT*. The inset in (a) shows representative as obtained plot for x=0 and x= 0.10 BGFO thin films. Fig. (b) shows the enlarged view of magnetization behaviour at 300 K showing the variation of coercivity and remanence in the films.

Fig. 4.27 (b) shows the magnified view of the *M-H* plot which shows coercivity and remanence increase with Gd content. The fraction of grain boundaries is more in Gd substituted films, which provides hindrance to demagnetization of the moments leading to higher coercivity. The observed increase in M_r (fig. 4.27 (b)) from 0.786 emu/cm^3 for x=0 to 1.807 emu/cm^{3}for x= 0.1 composition also favours the enhanced M_s for BGFO thin films. In previous studies, an interaction between rare earth ion (R^{3+}) and Fe^{3+} has been suggested for enhanced *M* [141, 215], however, at composition x = 0.10, only one Gd ion will replace for ten Bi^{3+} ion, therefore an interaction among the Fe and Gd ion can be ignored. Moreover Gd is paramagnetic at room temperature, which further suggests its counter contribution to the magnetization.

Fig.4.28 shows the high temperature FC-ZFC magnetization curves of BGFO thin films (x=0 and 0.10), measured at an external field of 1000Oe in the temperature range of 30-600 °C. The divergence between FC-ZFC magnetization curves increases progressively with decrease in temperature. As evident, the *M* is relatively higher in FC curve, which is due to the applied field that helps magnetic moments to align in the field direction. With the increase in temperature, the magnetic moments randomize and *M* falls sharply. On other hand, in ZFC curve, the fall in *M* with temperature is not as sharp as in FC curve that may be due to non alignment of magnetic moments in the absence of field. A peak is observed at 395 °C and 432 °C in the ZFC magnetization curves for x=0 and x=0.10 respectively, that corresponds to T_N of the respective systems.

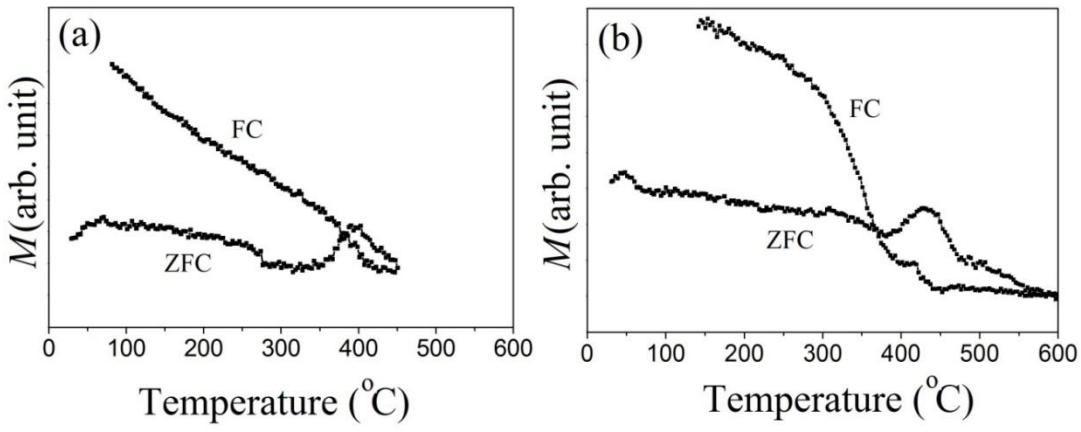

Fig. 4.28 High temperature FC and ZFC magnetization curves for the BGFO thin films obtained at an applied magnetic field of 1000 Oe for (a) x=0, and (b) x=0.10 compositions.

It is clearly evident from Fig. 4.28 (b) that T_N is increased with Gd–substitution. Small ionic radii of Gd caused slight shrinkage in the distance between the antiferromagnetically

coupled Fe^{3+} ions in [110] direction. This may enhance the antiferromagnetic exchange interaction among Fe^{3+} ions which leads to the higher T_N in Gd substituted thin films. Also, the structural phase transformation from rhombohedral to orthorhombic and the grain boundary restriction may also be the reason for higher T_N.

4.2.2 Effect of Co substitution

4.2.2.1 XRD analysis

Fig. 4.29 shows the refined X-ray diffraction patterns of $BiFe_{1-y}Co_yO_3$ (y=0, 0.05, 0.075, 0.100, 0.125) (BFCO) thin films annealed at 575 °C. The refinements were done using the space group *R3c*. The structures fitted well to rhombohedral (space group *R3c*) for all the thin films as predicted by fitting parameters (Table 4.4). Phase transformation from *R3c* to *Pn2₁a* is not observed as occurred in Gd substituted thin films. It is evident from Table 4.4 that the lattice parameters '*c*' shrinks slightly with the substitution, also marginal decrease in unit cell volume is also observed. The ionic radii of Co (0.545 Å in LS and 0.61 Å in HS) is smaller than Fe (0.645 Å in HS) [152]. As evident from the inset that peaks (104) and (110) is shifting toward higher angles, the tensile stresses generated in the system due to smaller ionic radii of Co is responsible for the peak shift. The crystallite size was also found to decrease gradually with Co substitution from 54.02 nm (y=0), to 41.29 nm (y=0.125).

Table 4.4 Refined parameters for the $BiFe_{1-y}Co_yO_3$ (y=0, 0.05, 0.075, 0.100, 0.125) thin films with space group *R3c*.

Composition	Cell parameters [*a* & *c* (Å), *V*(Å^3)]	Atoms	Position	Atom coordinates			R-factors & χ^2
				x	y	z	
y=0 *R3c*	*a*=5.5797 *c*=13.8768 *V*=374.146	Bi	6a	0	0	0.21172	R_B=3.69
		Fe	6a	0	0	0	R_F=2.59
		O	18b	0.81767	0.63566	0.80874	χ^2=1.82
y=0.05 *R3c*	*a*=5.5784 *c*=13.8751 *V*=373.927	Bi	6a	0	0	0.19442	R_B=4.86
		Fe/Co	6a	0	0	0	R_F=3.88
		O	18b	0.87761	0.58655	0.81958	χ^2=1.62
y=0.075 *R3c*	*a*=5.5790 *c*=13.8663 *V*=373.747	Bi	6a	0	0	0.21479	R_B=3.09
		Fe/Co	6a	0	0	0	R_F=2.20
		O	18b	0.77722	0.66325	0.82848	χ^2=1.56
y=0.10 *R3c*	*a*=5.5782 *c*=13.8675 *V*=373.436	Bi	6a	0	0	0.20396	R_B=5.19
		Fe/Co	6a	0	0	0	R_F=3.86
		O	18b	0.75692	0.69137	0.79538	χ^2=1.56
y=0.125 *R3c*	*a*=5.5729 *c*=13.8560 *V*=372.558	Bi	6a	0	0	0.20051	R_B=4.48
		Fe/Co	6a	0	0	0	R_F=3.20
		O	18b	0.75557	0.65920	0.82232	χ^2=1.52

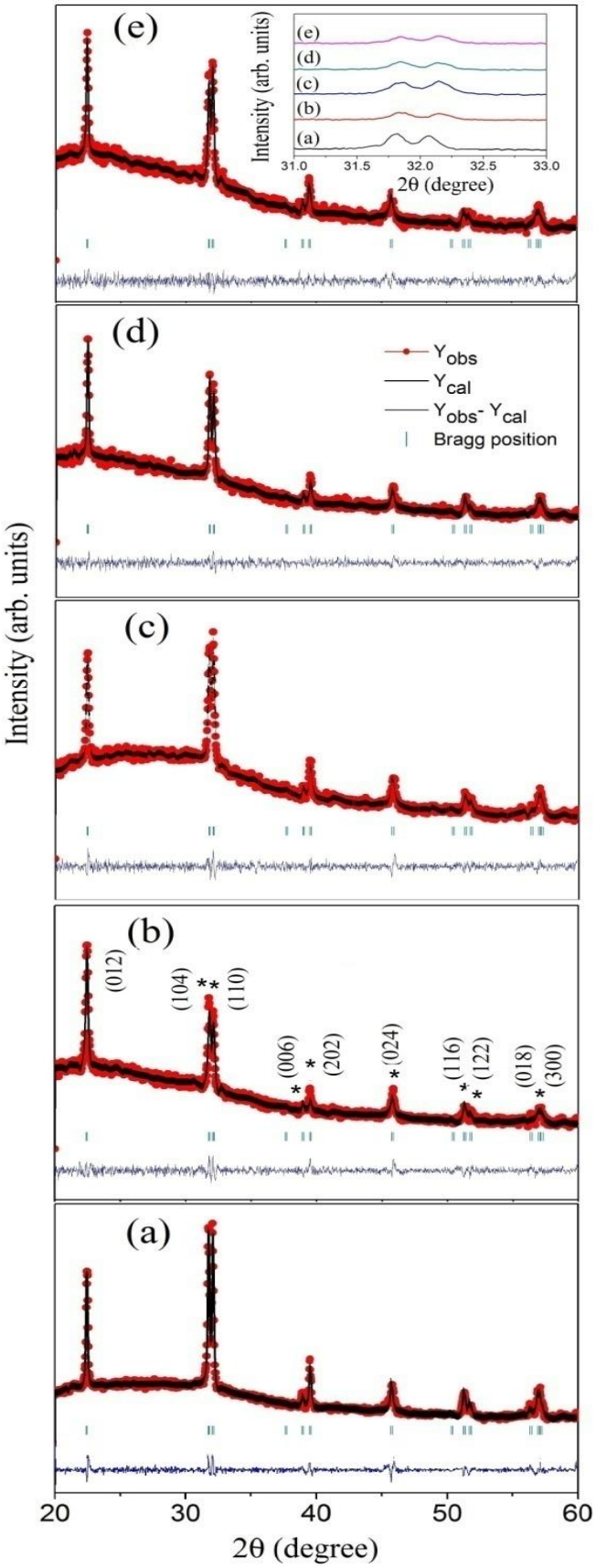

Fig. 4.29 Refined X-ray diffraction patterns for (a) *y*=0, (b) *y*=0.05, (c) *y*=0.075, (d) *y*=0.10 and (e) *y*=0.125 BFCO thin films compositions. The inset of fig (c) shows the shifting of (104) and (110) peak with Co-substitution.

4.2.2.2 FESEM analysis

Fig. 4.30 shows the FESEM micrographs of BFCO films deposited on ITO coated glass substrate. Fig. 4.30 (a) shows well defined interfaces between the ITO and BFCO film without any inter diffusion. The measured thickness of BFO and BFCO film is ~200 nm. Fig. 4.30 (b-f) shows the FESEM surface morphology for *y*=0, 0.05, 0.075, 0.100 and 0.125 BFCO thin films.

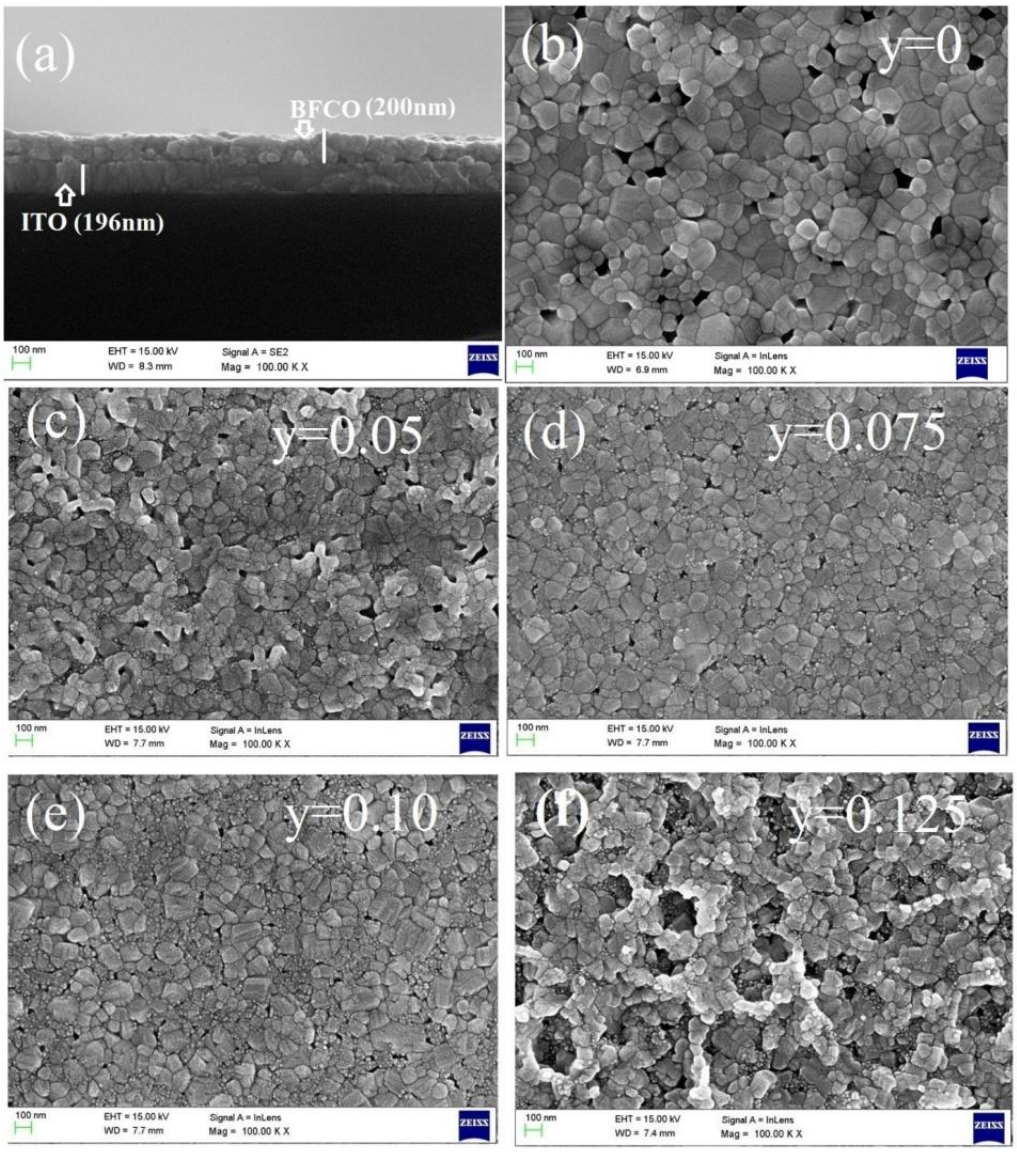

Fig. 4.30 FESEM micrographs of BFCO thin films showing (a) cross section and (b-f) surface morphology for various Co content.

The microstructures of films reveal a well crystallized equiaxed BFCO grains separated by sharp grain boundaries. It can be seen that the shape has not affected by the type of substitution. Initially, a visible decrease in grain size is observed with the substitution (*y* =

0.05), further increase in substitution amount, no visible grain size reduction is observed. In substituted films, tiny grains (dots) are visible and their fraction is increasing with the substitution amount. These tiny dots could be the dispersed Co particles or the tiny grains whose grain growth is restricted due to Co substitution. However, the shrinkage observed in lattice parameter suggests the substitution. Further the lattice spacing is measured in HRTEM, which is discussed in the coming section. A little porosity is also observed for composition y=0, however, the porosity fraction is found to decrease with substitution. For y=0.125, non uniform film surface with poor surface density is observed. Fig. 4.31 shows EDX spectra of the BFCO films along with the elemental composition in the insets of respective system. It displays the presence of Bi, Fe, Co, In, Sn and O elements (Fig. 4.31 (b-d)).

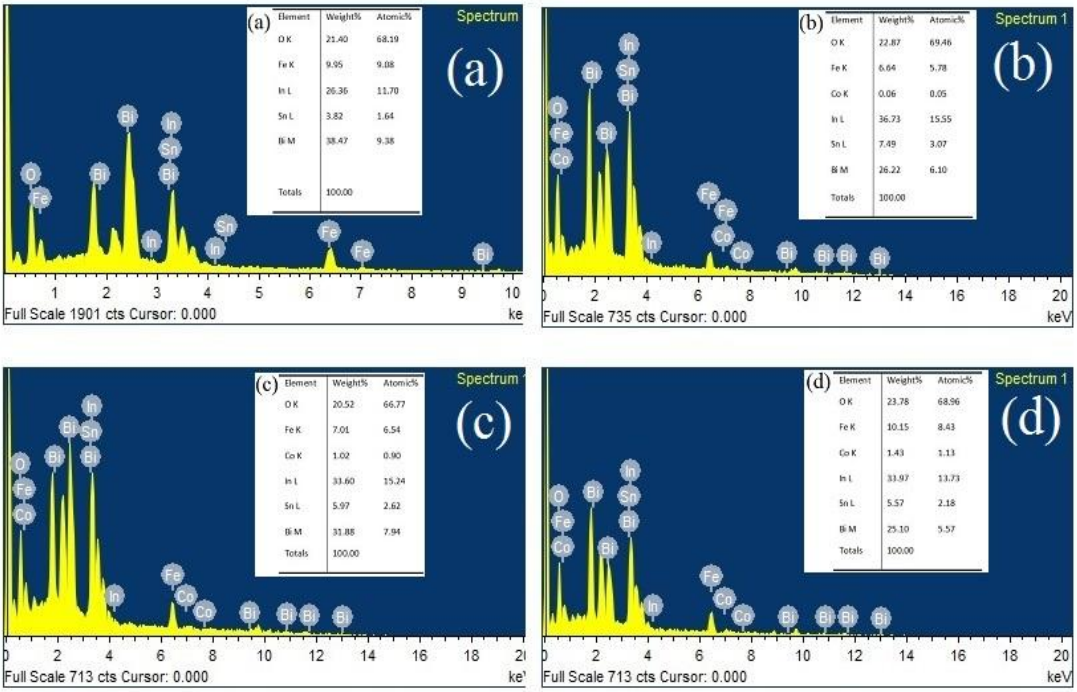

Fig. 4.31 EDX spectra of BFCO thin films showing their elemental composition for (a) y=0, (b) y=0.075, (c) y=0.10 and (d) y=0.125.

4.2.2.3 AFM analysis

Fig. 4.32 shows the AFM micrographs of (5×5) μm^2 area of BFCO thin films along with their respective (1×1) μm^2 micrographs in the inset of each figure. The AFM surface topography shows continuous and dense morphology, which is in agreement with the FESEM micrographs (fig. 4.30). The root mean square roughness (R_q) of the BFCO films were obtained over an area of (10×10) μm^2 and the observed R_q values tend to increase from 10.059 nm (y=0) to 21.175 nm (y=0.1).

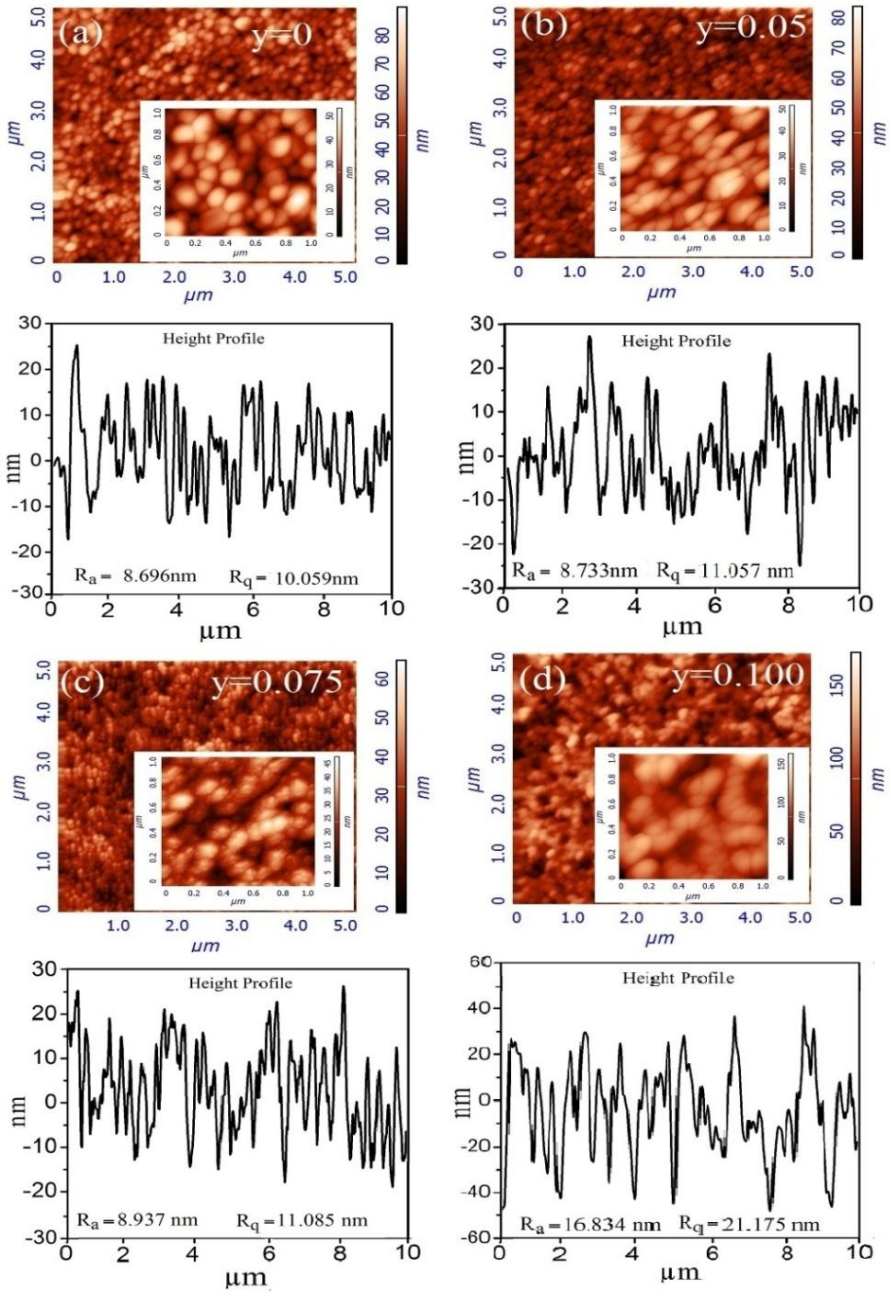

Fig. 4.32 AFM images of the BFCO thin films with (a) *y*=0, (b) *y*=0.05, (c) *y*=0.075 and (d) *y*=0.100 along with their respective height profiles below.

4.2.2.4 TEM analysis

Fig. 4.33 (a & b) shows the TEM images for *y*=0, and *y*=0.075 BFCO thin films. It is very clear from the TEM images that grains are well dispersed, homogeneous and nearly spherical in shape. Smaller grain size is evident in Co substituted film. Fig.4.33 (c & d) shows the lattice fringes of pure and substituted sample. The measured d-spacing are 2.8 Å and 2.7 Å for *y*=0 and *y*=0.075 respectively. As evident, the d spacing is decreasing with substitution amount which confirms the Co substitution at Fe site. SAED pattern shows the experimental

results in reciprocal space where each ring has been assigned an *hkl* value after calculating the d-values for the corresponding rings. Fig.4.33 (e & f) shows the SAED patterns with sharp discrete spots though not continuous for pure BFO thin film, whereas Co-substituted (y=0.075) BFO shows continuous diccrete spot pattern indicating the polycrystalline nature of films. Table 4.5 shows the structural parameters as obtained from XRD and SAED pattern for y=0 and y=0.075 compositions of BFCO thin films. No measureable difference is observed from both the methods.

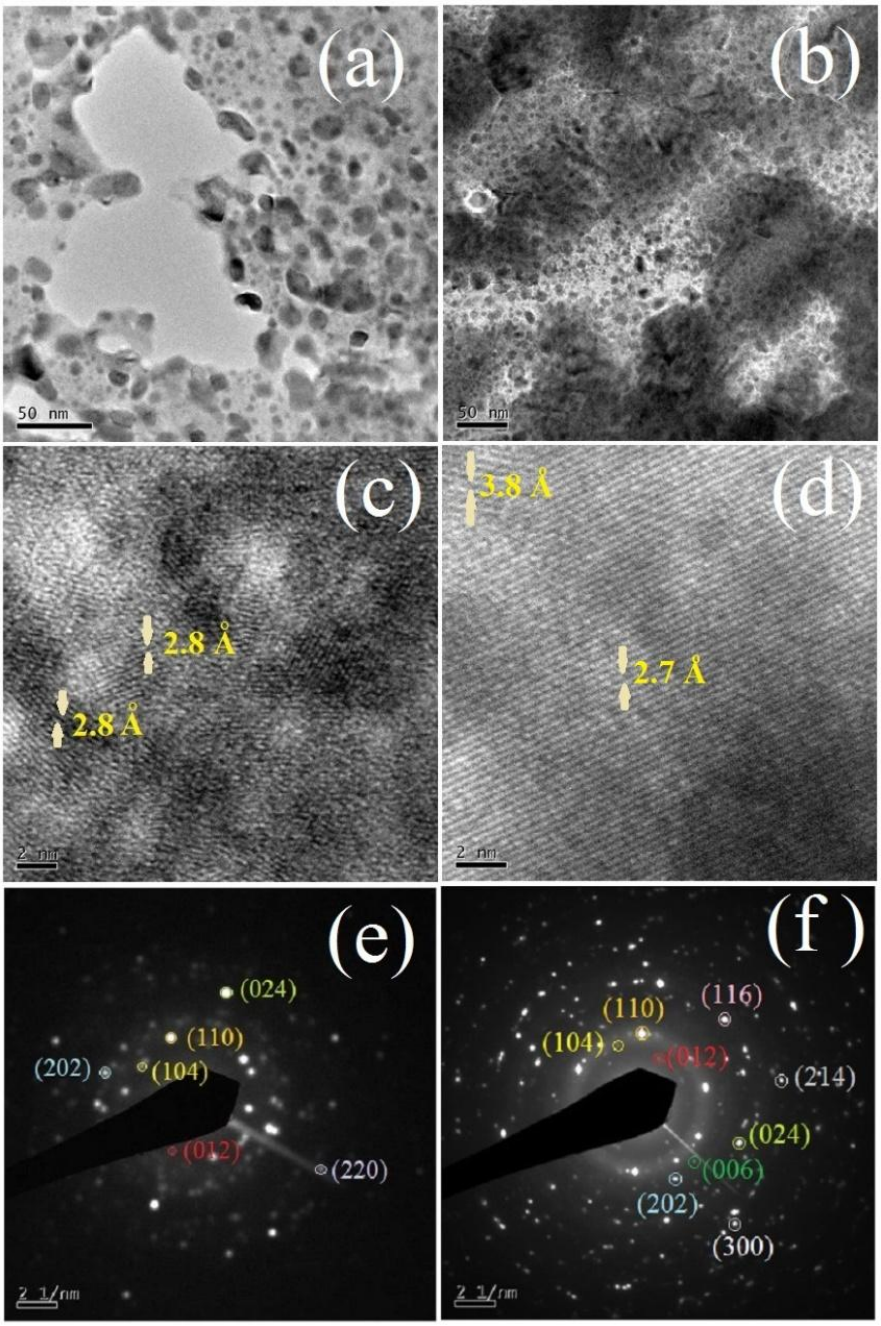

Fig. 4.33 (a & b) TEM image, (c & d) HRTEM images and (e & f) corresponding SAED pattern for y=0 and y=0.075 BFCO thin films respectively.

Table 4.5 Structural parameters for pure and Co- substituted BFO film.

Composition	Cell parameters obtained from XRD		Cell parameters obtained from Rietveld refinement		Cell parameters calculated from SAED pattern	
	Lattice parameters (Å)	V (Å^3)	Lattice parameters (Å)	V (Å^3)	Lattice parameters (Å)	V (Å^3)
y=0	a=5.5798 c=13.8720	374.031	a=5.5797 c=13.8768	374.146	a=5.6153 c=14.122	385.641
y=0.075	a=5.5718 c=13.8352	371.970	a=5.5790 c=13.8663	373.747	a=5.5540 c=13.9717	373.249

4.2.2.5 Dielectric measurements

Fig. 4.34 (a) shows the *RT* dielectric measurements in the frequency range of 100 Hz to 1 MHz. At low frequencies, the dielectric constant (ε′) increases and dielectric loss (tanδ) decreases with Co substitution. At 100 Hz, the ε′ increases from 210 (y=0) to 422 (y=0.075). It is clearly evident from the FESEM and AFM micrographs that the grain size decreases on Co-substitution leading to more grain boundaries thus enhancing the ε′. However, in the high frequency region, ε′ gradually decreases and becomes almost constant for BFCO films. At 100 Hz, the ε′ is quite large in Gd (~3534) substituted film as compared to Co, which may be a consequence of structural transformation and relatively finer grain size.

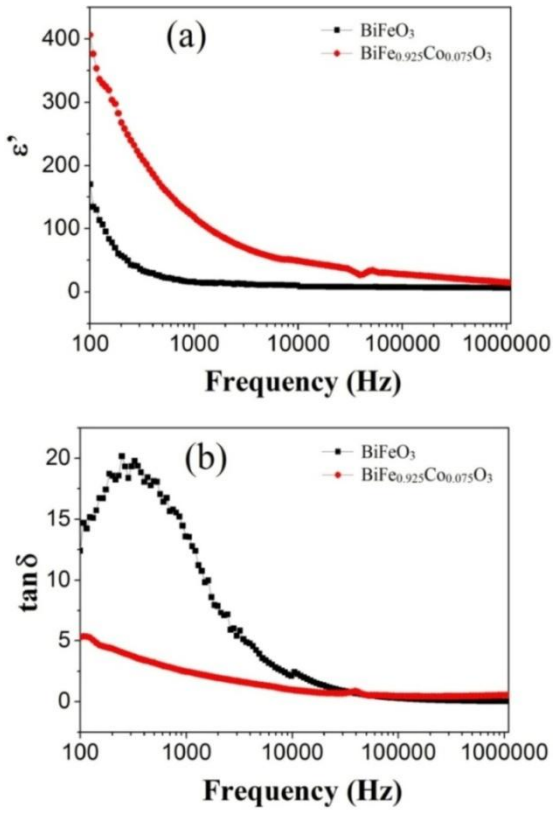

Fig. 4.34 Frequency dependent (a) dielectric constant and (b) dielectric loss at room temperature curves for the BFCO thin films for (a) y=0, and (b) y=0.075 compositions.

Fig. 4.34 (b) shows the dielectric loss (tanδ) variation with frequency. The tanδ initially increases with frequency, gradually starts decreasing and becomes fairly constant beyond 100 KHz for pure and Co-substituted BFO films. The densification and reduction in voids between the grains is assumed to be the main cause for observed decrease in tanδ with Co-substitution. This low frequency relaxation behaviour observed can be attributed to the grain boundary conduction [177, 214]. Due to decrease in the grain size with Co-substitution, the grain boundary resistance increased which probably is the reason for the reduced relaxation regime and loss in Co-substituted BFO film. At 100 Hz, the tanδ decreases from 12.34 (y=0) to 5.38 (y=0.075). The increase in grain boundary fraction and densification is assumed to be the main cause for the observed decrease in tanδ with Co- substitution.

4.2.2.6 Ferroelectric measurements

Fig. 4.35 shows the *RT* ferroelectric hysteresis (*PE*) loops at 10 kHz for the BFCO films. It is evident that BFO films shows lossy ferroelectric loops with P_r=0.023 μC/cm^2 and E_c= 36 kV/cm at an applied electric field of 150 kV/cm preferably due to large leakage current (Fig. 4.35 (a)). P_r is increasing with the substitution amount and found to be 0.012, 0.124 and 0.256 μC/cm^2 for y= 0.050, 0.075 and 0.125 at an applied electric field of 400, 1000 and 150 kV/cm respectively.

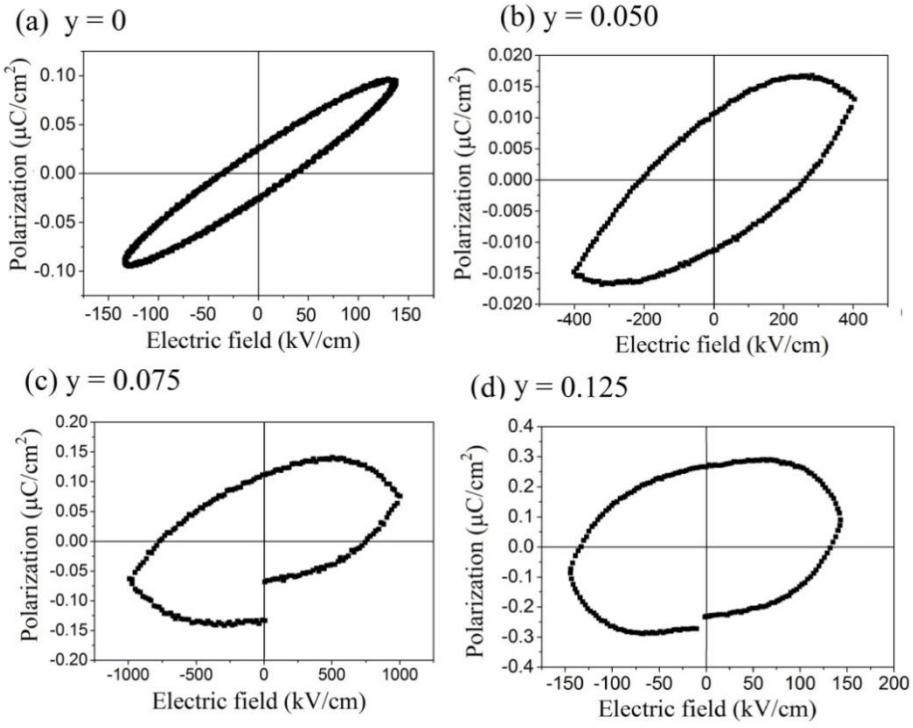

Fig. 4.35 Room temperature *PE* loops for the BFCO thin films obtained at a frequency of 10 kHz for (a) y=0, and (b) y=0.050, (c) y=0.075 and (d) y=0.125 compositions.

To obtain an optimized *PE* loop the electric field is applied accordingly. However, nearly saturated improved loop shape is observed in substituted films. At y = 0.125, non saturated *PE* loop is observed. The film with y=0.075 seems highly resistive, as it withstands an applied electric field of 1000 kV/cm without undergoing any breakdown. As evident from fig. 4.30 grain size decreases and density of the system increases with Co substitution resulting in reduced leakage current and hence improving the ferroelectric behavior *w.r.t* non substituted BFO film.

4.2.2.7 Magnetic measurements

Fig. 4.36 shows the *M-H* behaviour of BFCO thin films with y=0 and y=0.075 compositions obtained at 300 K. The *M-H* behaviour shows well-saturated hysteresis loop depicting the ferromagnetic nature of BFCO thin films [180, 190]. The M_s is increased from 7.18 emu/cm^3 (y=0) and 20.16 emu/cm^3 (y=0.075).

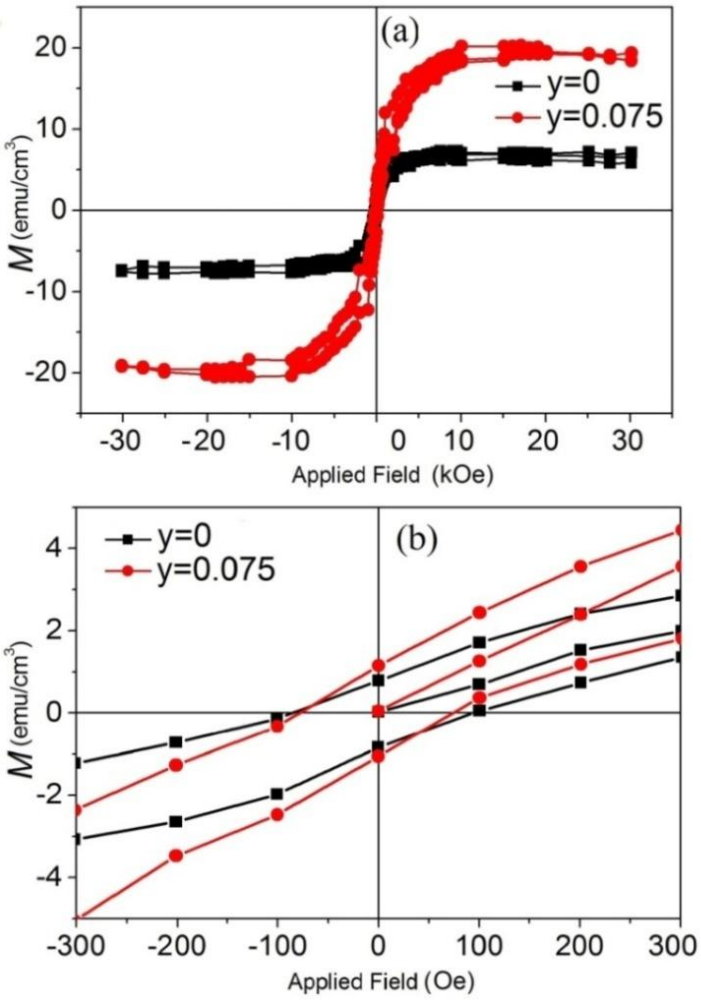

Fig. 4.36 (a) Magnetic hysteresis loops of BFCO thin films obtained at *RT*. (b) enlarged view of magnetization behaviour.

The origin of higher magnetization in BFCO films may be attributed to uncompensated spins originated at the grain boundaries. Also ferrimagnetic interaction through d^6 and d^5orbitals of Co ($4\mu_B$) and Fe ($5\mu_B$) ions respectively is also reported for enhanced magnetization [190]. The magnified view of the *M-H* plot (Fig. 4.36 (b)) shows slightly high remanence in Co substituted film. However, coercivity is relatively low as compared to pure film. The presence of magnetically active Co ions favours the demagnetization due to which a decrease in coercivity *w.r.t y*=0 has been observed.

Fig. 4.37 shows the high temperature FC-ZFC magnetization curves of BFCO thin films (*y*=0 and 0.075), measured at an external field of 1000 Oe in the temperature range of 30-600 °C. As evident, the *M* is relatively higher in FC curve, which is due to the applied field and helps uncompensated moments to align in the field direction. The divergence between FC-ZFC magnetization curves increases progressively with decrease in temperature. With the increase in temperature, the magnetic moments randomize and *M* decreases. The decrease in *M* with temperature in FC curve is relatively sharp as compared to ZFC curve. This may be due to non alignment of magnetic moments in the absence of field. A peak is observed at 395 °C in the ZFC magnetization curves for *y*=0, whereas a broad flat maximum from 368 -450 °C for *y*=0.075 has been observed. The transition corresponds to T_N of the respective systems. Substitution at Fe-site by Co ions (*y*=0.075) results in replacement of few Fe ions by Co ions resulting in the change in the ions composition in the spin cycloid structure. The presence of Co ion hinders the antiferro to paramagnetic transition over a broad temperature range of 100 °C.

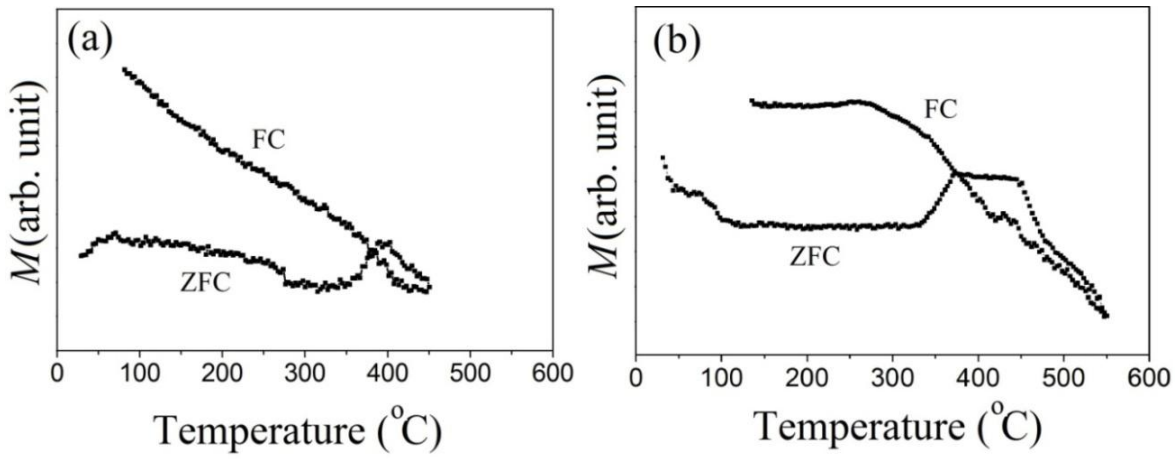

Fig. 4.37 High temperature FC and ZFC magnetization curves for the BFCO thin films obtained at an applied magnetic field of 1000 Oe for (a) *y*=0, and (b) *y*=0.075 compositions.

4.2.3 Effect of Gd-Co substitution

It was observed from the above discussion that low level substitution of rare earth metal Gd ion at Bi site and substitution of transition metal Co ion at Fe site tends to influence the behaviour of BFO thin films. It is reported that the simultaneous substitution significantly modifies the electrical and magnetic properties of BFO and these improvements were attributed to reduced oxygen vacancies, decreased leakage current, and the suppression of the spin spiral cycloid structure [171-174]. However, studies based on simultaneous substitution of Gd and Co on Bi and Fe site respectively is not reported for thin films. Therefore, in this section we have selected a simultaneously substituted composition for BGFCO i.e. $Bi_{0.90}Gd_{0.10}Fe_{0.925}Co_{0.075}O_3$ and their structural, electrical and magnetic properties is studied and compared with the pure BFO films.

4.2.3.1 XRD analysis

Fig. 4.38 shows the refined XRD pattern of Gd-Co substituted BFO thin films annealed at 575 °C. No impurity peaks from other phases were detected. The effects of Gd-Co substitution on the crystal structure of the BGFCO films were analyzed and the obtained results are summarized in Table 4.6.

Table 4.6 Refined parameters for the $Bi_{1-x}Gd_xFe_{1-y}Co_yO_3$ (x=0, y=0 and x= 0.100, y=0.075) thin films with space group *R3c* and *Pn2₁a*.

Composition & Structural model	**Cell parameters [*a* & *c* (Å), *V*(Å^3)]**	**Atoms**	**Position**	**Atom Coordinates**			**R-factors & χ^2**
				x	***y***	***z***	
x=0, *y*=0 *R3c*	*a*=5.5797 *c*=13.8768 *V*=374.146	Bi	6a	0	0	0.21172	R_B=3.69 R_F=2.59 χ^2=1.82
		Fe	6a	0	0	0	
		O	18b	0.81767	0.63566	0.80874	
x=0.10, *y*=0.075 *R3c*	*a*=5.5545 *c*=13.7006 *V*=366.071	Bi/Gd	6a	0	0	0.21355	R_B=1.31 R_F=0.92 χ^2=1.46
		Fe/Co	6a	0	0	0	
		O	18b	0.88156	0.52174	0.91530	
Pn2₁a	*a*=5.5828 *b*=7.8753 *c*=5.4887 *V*=241.432	Bi/Gd	4a	0.03975	0.24416	0.96421	R_B=1.55 R_F=1.16 χ^2=1.45
		Fe/Co	4a	0.02494	0.00000	0.55337	
		O1	4a	0.31578	0.26312	0.32037	
		O2	4a	0.17989	0.58200	0.18554	
		O3	4a	0.17467	0.55892	0.56253	

The structures fit very well to *R3c* as well as to $Pn2_1a$ space group, however, the merging of (104)/(110), (006)/(202), (116)/(122), and (214)/(300) peaks suggests the structural transformation from rhombohedral to orthorhombic [101-102, 108]. A decrease in lattice parameters and shrinkage in unit cell volume with Gd-Co substitution has been evidenced due to smaller ionic radii of Gd and Co as compared to Bi and Fe respectively. Shifting of (104) and (110) peaks at 2θ=31.92° towards higher angles 32.39° with Co and Gd substitution is due to tensile field within the system. The crystallite size as calculated from Scherrer formula for BFO and BGCFO were 54.02 and 21.61 nm respectively evidenced a significant decrease in grain size with Gd-Co substitution.

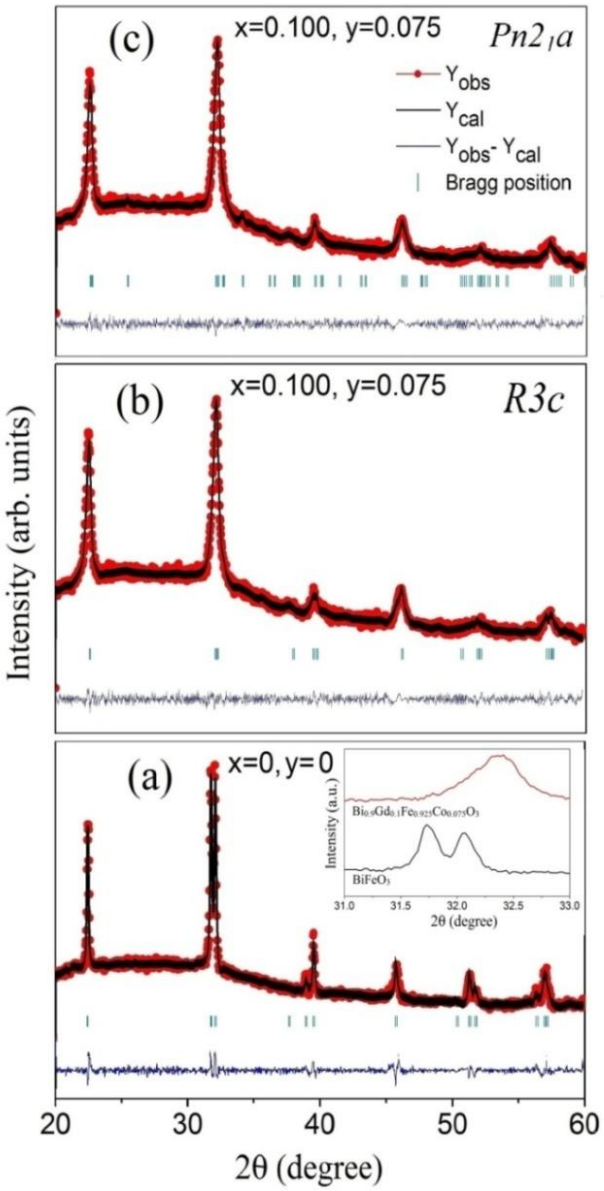

Fig. 4.38 Refined X-ray diffraction patterns of (a) Pure BFO refined with *R3c* space group (b & c) substituted BGFCO refined with *R3c* and $Pn2_1a$ space group respectively. The inset in fig (a) shows the shift in (104) and (110) peak of BGFCO.

4.2.3.2 FESEM analysis

Fig. 4.39 shows the FESEM micrographs of BGFCO films deposited on ITO coated glass substrate. The microstructure of films reveals a well crystallized equiaxed BGFCO grains separated by sharp grain boundaries. The FESEM micrographs shows decrease in grain-size on substitution with Co and Gd. The average grain size is decreased from ~96 nm to ~29 nm with the substitution. The wide difference in the crystallite size obtained from the XRD analysis and the grain size calculated from the FESEM micrographs suggest that the smaller grains are agglomerated and appeared like a one big grain, distinction between the smaller grains are beyond the resolution of FESEM used. Fig. 4.40 shows EDX spectra of the BGFCO films along with the elemental composition in the insets of respective system. It displays the presence of Bi, Fe, Gd, Co, In, Sn and O elements in the film.

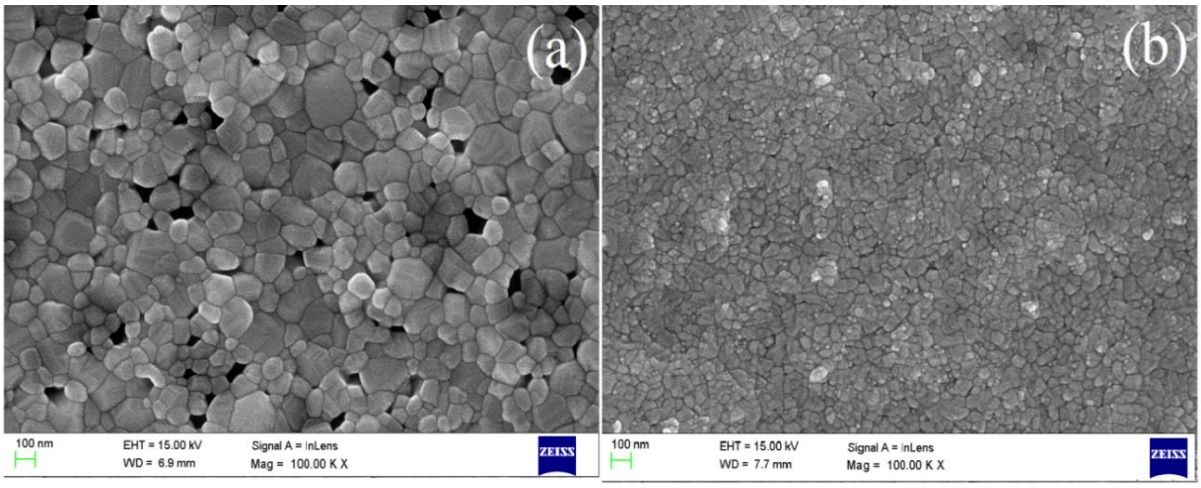

Fig. 4.39 FESEM micrographs of BGFCO thin films showing surface morphology (b) x=0, y=0 and (d) x=0.10, y=0.075.

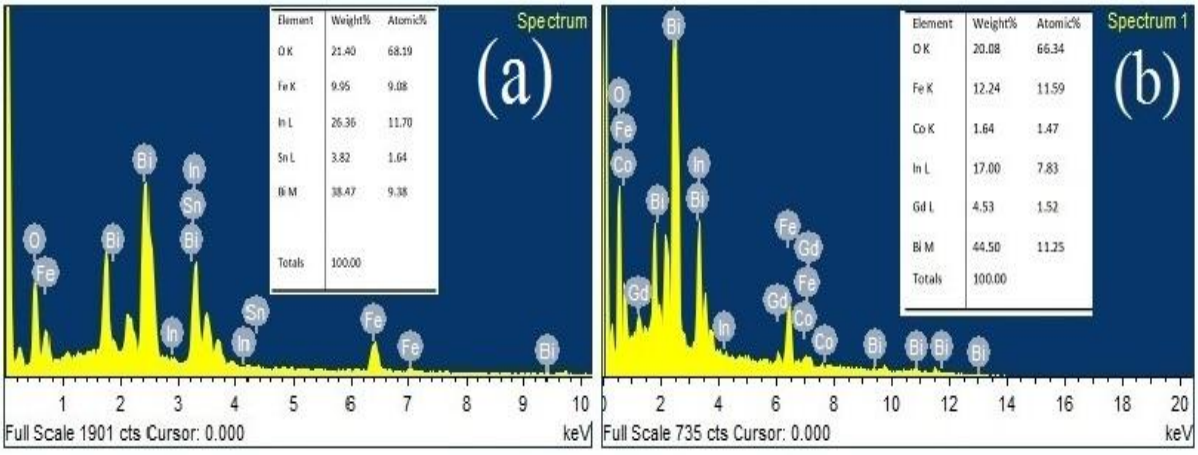

Fig. 4.40 EDX spectra of BGFCO thin films showing their elemental composition for (a) x=0, y=0, and (b) x=0.10, y=0.075.

4.2.3.3 AFM analysis

Fig. 4.41 shows the AFM micrographs of BGFCO thin films along with their respective height profiles. The AFM surface topography shows smooth, uniform, continuous and dense morphology with minimal porosity, which is in agreement with the FESEM micrographs.The root mean square roughness (R_q) found over an area of (10 × 10) μm^2 tend to increase from 10.059 to 37.933 nm with substitution.

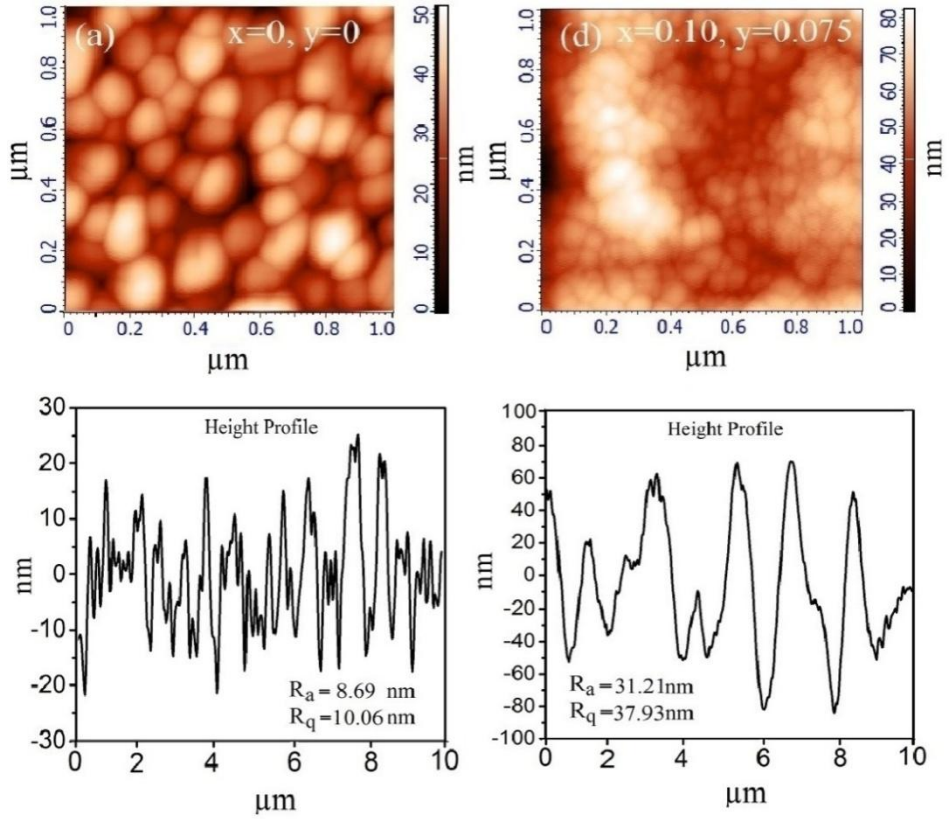

Fig. 4.41 AFM images of the BGFCO thin films with (a) *x*=0, *y*=0, and (d) *x*= 0.100, *y*=0.075 along with their respective height profiles.

4.2.3.4 TEM analysis

Fig. 4.42 (a&e) shows the TEM images of BFO and BGFCO thin film along with the SAED patterns. With Gd and Co substitution the decrease in average grain size is observed. Lattice fringes with d-spacing of 2.8 and 2.6 Å, corresponds to (110) plane, has been observed for BFO and BGFCO thin films respectively (Fig. 4.42 (b & f)). In the BGFO film, lattice fringes of (012) plane with lattice spacing of 3.3 Å is also visible. The magnified HRTEM images (Fig. 4.42 (c&g)) of fig. 4.42 (b & f)) clearly depicts structural transformation from rhombohedral to orthorhombic on Gd-Co substitution. Highly intense diffraction spots of SAED patterns indicate well crystalline nature of the film (Fig. 4.42

(d&h)). SAED patterns of BGFCO showed continuous ring pattern indicating the nanocrystalline nature of films.

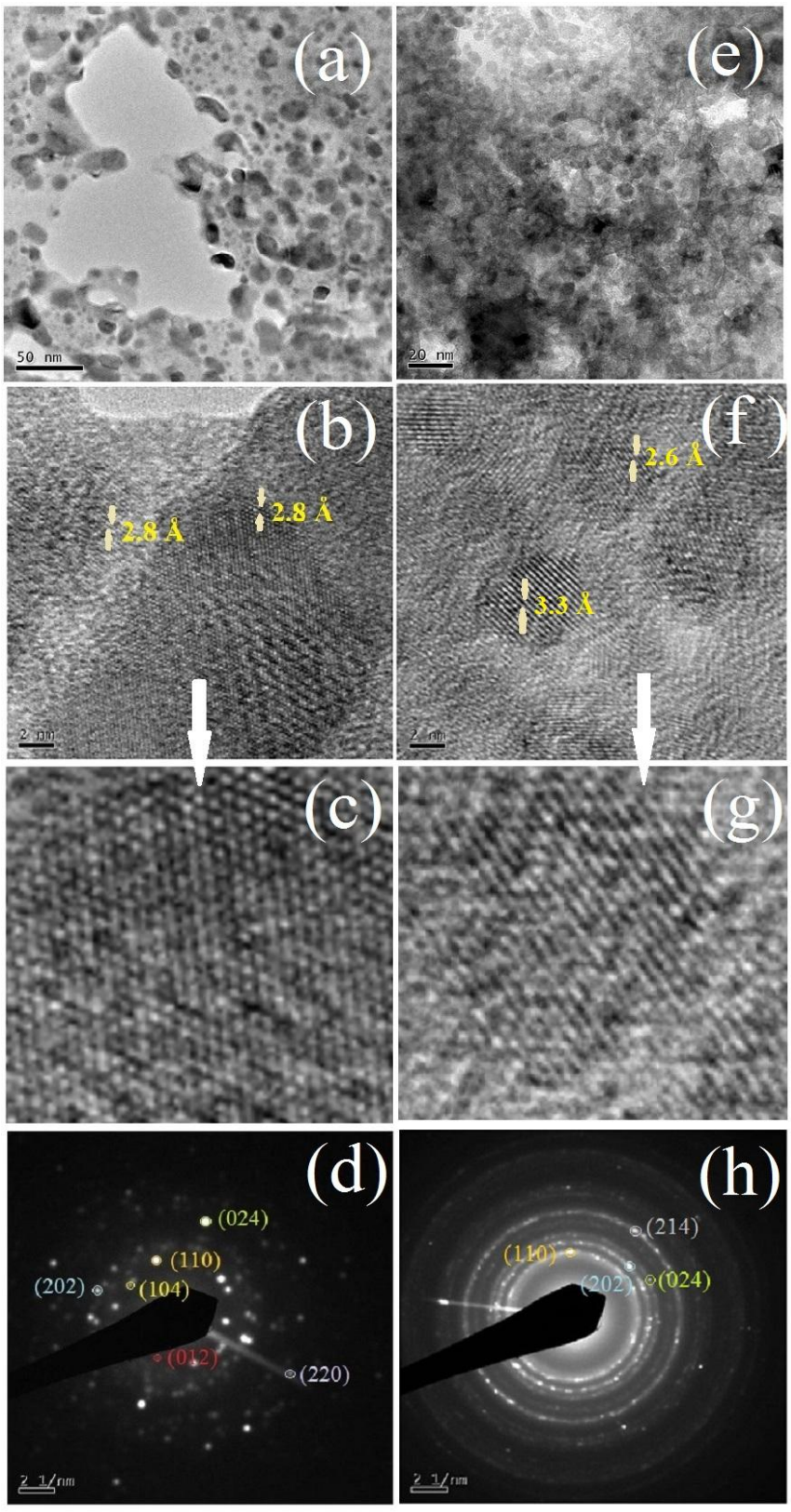

Fig. 4.42 TEM, HRTEM image, magnified HRTEM and corresponding SAED pattern for (a-d) x=0, y=0 and (e-h) x= 0.100, y=0.075 BGFCO thin films respectively.

Table 4.7 shows the structural parameters for x=0, y=0 and x= 0.100, y=0.075 compositions of BGFCO thin films showing the variation in lattice parameters and the unit cell volume when calculated from XRD and SAED. XRD is a quantaitive analysis therfore the observed difference might arise from errors associated with XRD refinement.

Table 4.7 Structural parameters for x=0, y=0 and x= 0.100, y=0. BGFCO thin films

Composition	**Cell parameters obtained from XRD**		**Cell parameters obtained from Rietveld refinement**		**Cell parameters calculated from SAED pattern**	
	Lattice parameters (Å)	***V*** **(Å^3)**	**Lattice parameters (Å)**	***V*** **(Å^3)**	**Lattice parameters (Å)**	***V*** **(Å^3)**
x=0, y=0	a=5.5798 c=13.8720	374.031	a=5.5797 c=13.8768	374.146	a=5.6153 c=14.122	385.641
x=0.10, y=0.075	a=5.5422 c=13.7181	364.914	a=5.5545 c=13.7006	366.071	a=5.4337 c=14.4026	368.269

4.2.3.5 Dielectric measurements

Fig. 4.43 shows the *RT* dielectric measurements in the frequency range of 100 Hz to 1 MHz. At low frequencies, the dielectric constant (ε′) increases and dielectric loss (tanδ) decreases with substitution. The ε′ at 100 Hz increased from 210 to 574 with substitution. Highly dense film with immense decrease in grain size on Gd-Co substitution resulted in reducing oxygen coupled defects that further lead to reduced leakage current; enhancing the ε′.

Fig. 4.43 (b) shows the dielectric loss (tanδ) variation with frequency. The tanδ initially increases with frequency, gradually starts falling afterwards and becomes fairly constant beyond 100 KHz. At100 Hz, tanδ is decreased from 12.34 to 3.46 with substitution. Relaxation regime ~500 Hz observed in pure BFO is found absent in Gd-Co substituted film whereas this relaxation regime is suppressed in Gd-substituted and Co-substituted film. Gd-Co substitution has entirely suppressed this relaxation regime due to enhanced grain boundary insulation caused by a substantial decrease in grain size and highly dense microstructure.

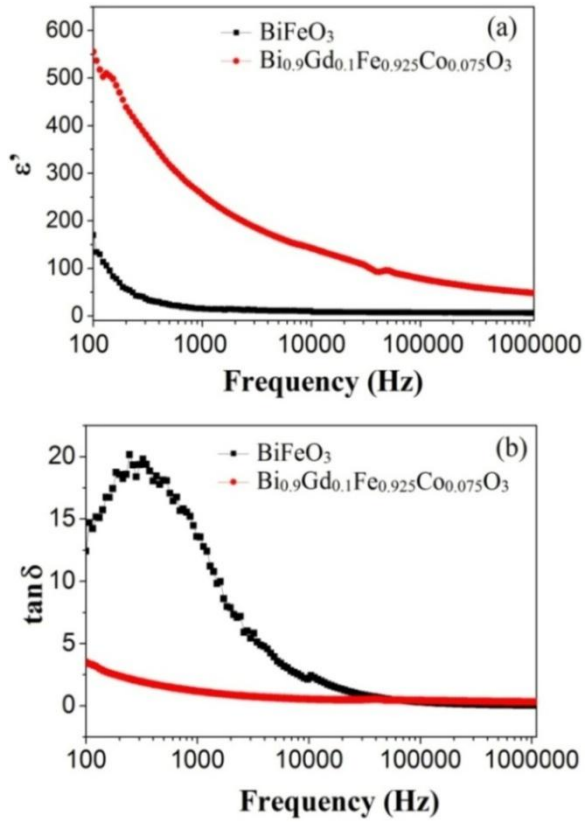

Fig. 4.43 Frequency dependent (a) dielectric constant and (b) dielectric loss curves at room temperature for the BGFCO thin films.

4.2.3.6 Ferroelectric measurements

Fig. 4.44 shows the room temperature *PE* loops for the BFO and BGFCO films at 10 kHz. The hysteresis loop for the BFO film is non-saturated with P_r = 0.027 μC/cm^2 and E_c = 53 kV/cm at an applied electric field of 225 kV/cm. *PE* loop for the BGFCO film is well saturated with P_r= 0.25 μC/cm^2 and E_c=2260 kV/cm at an applied electric field of 3000 kV/cm. The enhanced P_r due to reduced leakage current density may be attributed to decrease in grain size (Fig. 4.39 and 4.41) which simultaneously increases grain boundary resistance.

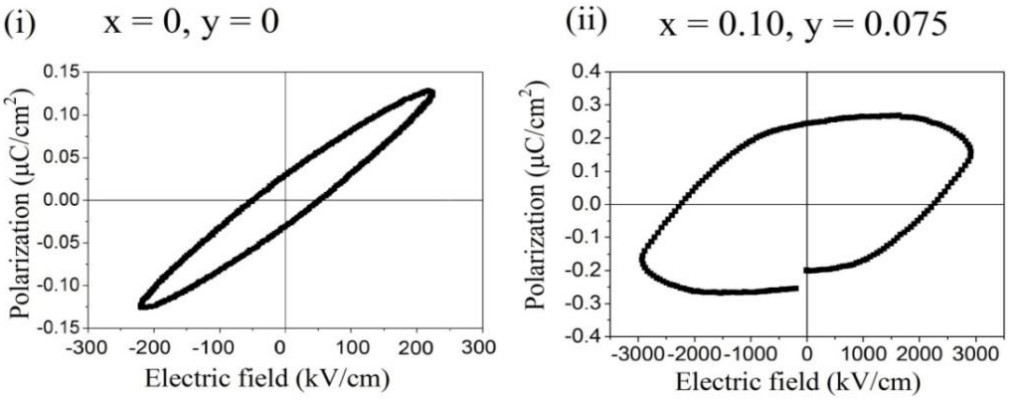

Fig. 4.44 Room temperature *PE* loops for the BGFCO thin films obtained at a frequency of 10 kHz for (i) x=0, y=0 and (ii) x= 0.100, y=0.075.

4.2.3.7 Magnetic measurements

Fig. 4.45 shows the in-plane *M-H* behaviour of BGFCO thin films obtained at 300 K. The *M-H* behaviour of the films presents well-saturated hysteresis loop depicting the ferromagnetic nature of BGFCO thin films [180, 190]. The M_s is 7.18 and 30.83 emu/cm^3 for BFO and BGFCO thin films respectively. The enhancement in M_s is attributed to uncompensated moments at grain boundaries as discussed in preceding section. We also expect the larger fraction of uncompensated moments at the film surface due the larger surface roughness (~39 nm) in the substituted thin films. Fig. 4.45 (b) shows the magnified view of the *M-H* plot where the trend in coercivity and remanence variation can be clearly seen.

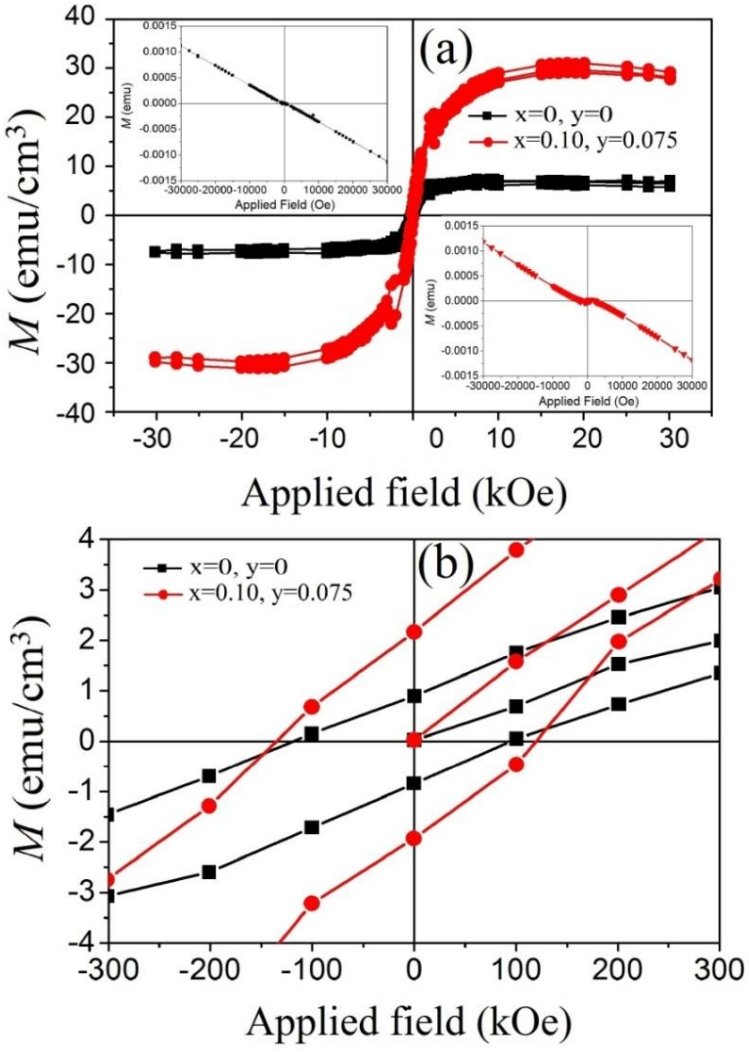

Fig. 4.45 Magnetic hysteresis loops of BGFCO thin films obtained at *RT*. The inset in (a) shows representative as obtained plot for *x*=0, *y*=0 and *x*= 0.100, *y*=0.075 BGFCO thin films. Fig. (b) show the enlarged view of magnetization behaviour showing the variation of coercivity and remanence in the films.

Fig.4.46 shows the high temperature FC-ZFC magnetization curves of BGFCO thin films measured at an external applied field of 1000 Oe in the temperature range of 30-600 °C. The behaviour of the BGFCO film is similar to the Co substituted films, where the transition is taking place over a range of temperature. Therefore it can be concluded that Gd substituted film shows higher T_N whereas Co ion impedes the transitions, and also increases the T_N.

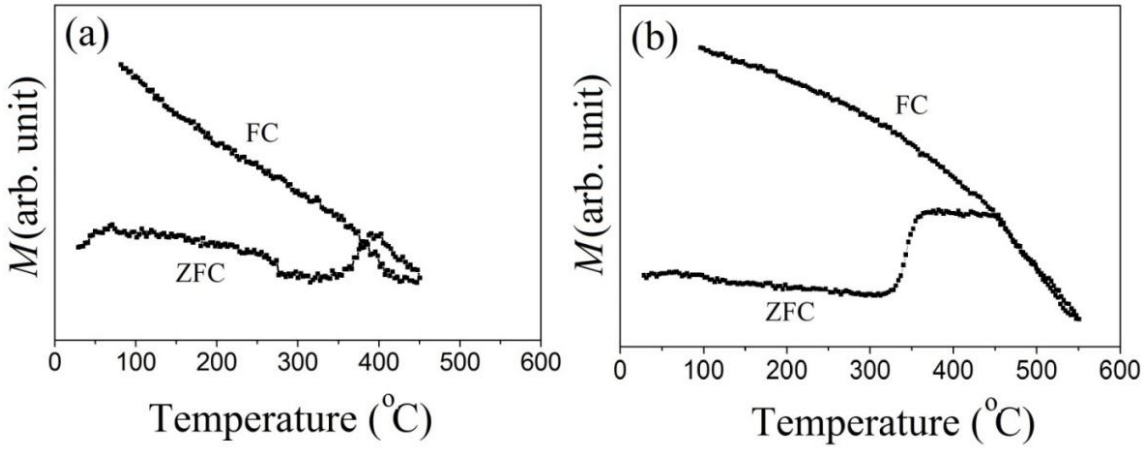

Fig. 4.46 High temperature FC-ZFC magnetization curves for the BGFCO thin films obtained at an applied magnetic field of 1000 Oe for (a) x=0, y=0 and (d) x= 0.100, y=0.075.

Chapter V

Conclusions and Future Work

Overview

The present chapter summarizes the results of the various experiments described in the previous chapter. The effect of grain size distribution induced by varying the annealing temperature and the film thickness on the structural, electrical and magnetic properties of $BiFeO_3$ is summarized. Further, the results obtained due to the effect of Gd and Co substitution at Bi and Fe site respectively, on the structural, magnetic and electrical properties are mentioned. In the end, the suggestions for further research work in this area are outlined.

.

To start with, the phase formations of BFO films at different annealing time were studied. From XRD results an annealing time of 60 minutes is found to be optimum irrespective to the studied temperature for single phase well crystallized films.

Further, the effect of grain size distribution is investigated. First, grain-size variation is induced by varying annealing temperature. Refined XRD patterns showed a minor peak of γ-Fe_2O_3 phase. The volume fraction of γ-Fe_2O_3 remained constant (~0.08) for all the studied temperature range. FESEM and AFM micrographs showed well crystallized equiaxed BFO grains, separated by sharp grain boundaries. The root mean square roughness (R_q) of the films measured over an area of 50×50 μm^2 increases with annealing temperature. The grain-size distribution as plotted from the FESEM micrographs broadens with increase in annealing temperature. Magnetization was found to vary with varying annealing temperature. The magnetization in the BFO films is attributed to uncompensated moments originated at grain boundaries. The grain-size distribution obtained at 575 °C is responsible for the high magnetization (~11.02 emu/cm^3) in the BFO film. The FC-ZFC magnetization curves depict a rise in magnetization at lower temperature with an onset of spin glass state ~300 K.

Second, the grain size variation is induced by varying thickness of the film. Rietveld refined patterns shows a minor impurity peak of γ-Fe_2O_3 with nearly constant (~0.08) volume fraction in all the films of varying thickness. The FESEM and AFM micrographs gives well crystallized equiaxed grains with wide distribution. The observed trends in *M-H* curves indicated the strong dependence of magnetization on the grain size distribution. The saturation magnetization (M_s) decreases with increase in thickness. At 300 K, M_s decreases from 18.9 emu/cm^3 (156 nm) to 0.93 emu/cm^3 (388 nm). At 10 K, the *M-H* loops are unsaturated due to spin freezing. The ferroelectric properties improve due to better growth and densification with increasing film thickness. The remnant polarization (P_r) of BFO films increases from 0.0178 μC/cm^2 (156 nm) to 1.63 μC/cm^2 (388 nm). Dielectric constant (ε′) showed an appreciable increase whereas a corresponding decrease in dielectric loss (tanδ) with increase in BFO film thickness is observed. The ε′ at 100 Hz increases from 71 to 435 whereas tanδ decreases from 11.2 to 5.8 for 156 and 388 nm thick BFO films respectively.

The BFO films with Gd, Co and Gd-Co substitutions were prepared. The refinements of the Gd-substituted BFO films ($Bi_{1-x}Gd_xFeO_3$ (x=0, 0.05, 0.075, 0.100, 0.125) (BGFO)) using space group *R3c* and *Pn2₁a* shows transformation from rhombohedral to orthorhombic phase (*Pn2₁a*). FESEM images showed well-crystallized equiaxed grains, continuous dense

morphology with minimal porosity. The FESEM and AFM micrographs showed decrease in the grain size with Gd-substitution. Lattice fringes with d-spacing of 2.8 and 2.6 Å is observed for x=0 and x=0.1 BGFO thin film. SAED patterns for x=0.1 BGFO film showed continuous ring pattern indicating the nanocrystalline nature of the films. The dielectric and ferroelectric properties found to improve with increasing Gd-content. The increase is attributed to better densification of grains in the BGFO thin films. The ε′ at 100 Hz increases from 210 (x=0) to 3534 (x=0.1) whereas, tanδ decreases from 12.34 (x=0) to 1.02 (x=0.1). P_r is increased from 0.032 to 3.5 μC/cm^2 with increasing Gd content. A remarkable enhancement in M_s from 7.18 and 27.93 emu/cm^3 is observed in BGFO (x=0.10) thin films. Neel temperature (T_N) is increased from 395 to 432 °C with Gd substitution.

In Co-substituted BFO thin films ($BiFe_{1-y}Co_yO_3$ (y=0, 0.05, 0.075, 0.100 and 0.125) (BFCO)) no structural transformation is observed. All the BFCO films showed *R3c* space geometry. However, a decrease in lattice parameters and the cell volume is observed with increasing Co content. FESEM and AFM micrographs showed well-crystallized equiaxed grains with minimal porosity. Co-substitution resulted in decrease of grain size from 96 (y=0) to 46 nm (y=0.125). The root mean square roughness (R_q) of the BFCO films obtained over an area of (10×10) μm^2 increased from 10.059 (y=0) to 21.175 (y=0.1). The TEM shows a shrinkage in the lattice spacing with Co substitution. The dielectric and ferroelectric properties improved due to better densification of grains with increasing Co content in the films. The ε′ at 100 Hz increases from 210 (y=0) to 422 (y=0.075) whereas, tanδ decreases from 12.34 (y=0) to 5.38 (y=0.075). The P_r is increased from 0.023 (y=0) to 0.256 μC/cm^2 (y=0.125). The M_s values for y=0 and y=0.075 BFCO thin films were 7.18 and 20.16 emu/cm^3 respectively. The high temperature FC-ZFC magnetization curves for y=0 composition showed a sharp transition from antiferromagnetism to paramagnetism at 395 °C. However, the transition in Co- substituted film (y=0.075) is not sharp rather it takes place over a broad temperature range from 368-450 °C. The ferromagnetic Co ion provides hindrance to randomization of antiferromagnetically coupled Fe ions that resulted in transformation over a wide temperature range.

Finally the effect of simultaneous substitution Gd and Co in BFO thin film is studied. The structure of polycrystalline BFO film changes from distorted rhombohedral (*R3c*) to orthorhombic ($Pn2_1a$) with Gd-Co substitution as confirmed by Rietveld refinement. FESEM micrographs indicated a significant decrease in grain size from 96 to 28.96 nm for pure and

Gd-Co substituted BFO thin films respectively. The root mean square roughness (R_q) of the BGFCO films obtained over an area of (10×10) μm^2 increases from 10.059 nm (x=0, y=0) to 37.933 nm (x=0.1, y=0.075). Well saturated ferroelectric loops with P_r=0.25 $\mu C/cm^2$ are observed. Enhanced M_s ~30.83 emu/cm^3 is due to the presence of uncompensated moments at the surface and grains boundaries. The high temperature FC-ZFC magnetization plots showed sharp transition temperature (T_N) at 395 °C for x=0, y=0 and a broad flat transition from 368 - 455 °C for x=0.100, y=0.075 in the ZFC plot.

The summarized results of the work are mentioned in table below.

Table 5.1 Summarized properties of BFO thin films

System	**Parameters**	**~ ε'**	**tanδ**	**~ P_r ($\mu C/cm^2$)**	**~ M (emu/cm^3)**		**~H_c (Oe)**	
					300K M_s	**10K M**	**300K**	**10K**
Effect of the annealing temperature	525 °C	-	-	-	1.58	14.07	-	63
	550 °C	-	-	-	3.18	68.86	-	135
	575 °C	-	-	-	11.02	128.50	-	173
	600 °C	-	-	-	2.20	23.76	-	264
Effect of the film thickness	156 nm	71	11.2	0.018	19.31	122.72	-	157
	206 nm	164	9.8	0.122	11.02	85.56	-	173
	270 nm	378	8.3	-	1.88	42.71	-	315
	388 nm	435	5.8	1.630	0.68	19.33	-	618
Effect of Gd substitution	x=0	210	12.34	0.032	7.18	-	95	-
	x=0.050	-		-	-	-	-	-
	x=0.075	-		0.12	-	-	-	-
	x=0.100	3534	1.02	0.62	27.93	-	120	-
	x=0.125	-		3.50	-	-		-
Effect of Co substitution	y=0	210	12.34	0.023	7.18	-	95	-
	y=0.050	-		0.012	-	-		-
	y=0.075	422	5.38	0.124	20.16	-	76	-
	y=0.100	-		-	-	-		-
	y=0.125	-		0.256	-	-		-
Effect of Gd and Co substitution	x=0, y=0	210	12.34	0.027	7.18	-	95	-
	x= 0.100, y=0.075	574	3.46	0.25	30.83	-	112	-

Suggestion for Future Work

The work in the present thesis provides direction for future work in the area of multiferroic BFO as mentioned below:

- The results indicated an important role of transition metal ion Co and rare earth Gd ion substitution in tailoring the properties of BFO thin films. Hence the effect of other rare earth and transition metal ions and their combinations could be an alternative study for future work.
- The influence of swift heavy ion irradiation on the structural, morphological and magnetic properties of the thin films could be an interesting topic for future analysis.

References

[1] Maxwell, James Clerk, "A dynamical theory of the electromagnetic field", *Philosophical Transactions of the Royal Society of London* 155 (1865) 459-512.

[2] W.C. Rontgen, "Uber die durch Bewegung eines im homogenen electrischen Fel de befindlichen Dielectricums hervorgerufene electrodynamische Kraft," *Ann. Phys.,* 35 (1888) 264-270.

[3] P. Curie, "Sur la symétrie dans les phénomènes physiques. Symétrie d'un champ électrique d'un champ magnétique", *J. Physique,* 3 (1894) 393-416.

[4] *P. Debye*, "Bemerkung zu einigen neuen Versuchen über einen magneto-elektrischen Richteffekt," *Z. Phys.,* 36 (1926) 300-301.

[5] L. D. Landue and E. Lifshitz, "Electrodynamics of Continuous Media", Addison- Wesley, Reading, Mass, USA (1960).

[6] W. Erenstein, N. D. Mathur and J. F. Scott, "Multiferroic and magnetoelectric materials", *Nature,* 442 (2006) 759-765.

[7] R. Ramesh and N.A. Spaldin, "Multiferroics: progress and prospects in thin films", *Nature Mater.,* 6 (2007) 21-29.

[8] S. W. Cheong, M. Mostovoy, "Multiferroics: a magnetic twist for ferroelectricity" *Nature Mater.,* 6 (2007) 13-20.

[9] K. F. Wang, J. M. Liu and Z. F. Ren, "Multiferroicity: the coupling between magnetic and polarization orders", *Adv. Phys.,* 58 (2009) 321-448.

[10] H. Schmid, "Multi-Ferroic Magnetoelectrics", *Ferroelectrics,* 162 (1994) 665-685.

[11] I. E. Dzyaloshinskii, "On the magnetoelectrical effects in antiferromagnetics", *Sov Phys. JETP,* 37 (1960) 628–629.

[12] D. N. Astrov, "The magnetoelectric effect in antiferromagnetics", *Sov. Phys. JETP,* 11 (1960) 708–709.

[13] G. A. Smolenskii and I. E. Chupis, "Ferroelectromagnets", *Sov. Phys. Usp.* 25 (1982) 475-493.

[14] G. A. Smolenskii, A. I. Agranovskaya, S. N. Popov, and V. A. Isupov, *Zh. Tekh. Fiz.,* 28 (1958) 2152-2153. [*Sov. Phys. Tech. Phys*. 3 (1958) 1981].

[15] N. A. Spaldin and M.Fiebig, "The renaissance of magnetoelectric multiferroics" *Science,* 309 (2005) 391-392.

[16] N. Ikeda, H. Ohsumi, K. Ohwada, K. Ishii, T. Inami, K. Kakurai, Y. Murakami, K. Yoshii, S. Mori, Y. Horibe and H. Kitô, "Ferroelectricity from iron valence ordering in the charge-frustrated system $LuFe_2O_4$", *Nature*, 436 (2005) 1136-1138.

[17] M. A. Subramanian, T. He, J. Chen, N. S. Rogado, T. G. Calvarese, A. W. Sleight, "Giant Room–Temperature Magnetodielectric Response in the Electronic Ferroelectric $LuFe_2O_4$", *Adv. Mater.*, 18 (2006) 1737-1739.

[18] Y. J. Choi, H. T. Yi, S. Lee, Q. Huang, V. Kiryukhin and S. W. Cheong, "Ferroelectricity in an Ising chain magnet", *Phys. Rev. Lett.*, 100 (2008) 047601/1-047601/4.

[19] D. V. Efremov, J. van den Brink, and D. I. Khomskii, "Bond-versus site-centred ordering and possible ferroelectricity in manganites", *Nature Mater.*, 3 (2004) 853-856.

[20] F. Yen, C. De la Cruz, B. Lorenz, E. Galstyan, Y. Y Sun, M. Gospodinov, and C. W. Chu, "Magnetic phase diagrams of multiferroic hexagonal $RMnO_3$ (R = Er, Yb, Tm, and Ho)", *J. Mater. Res.*, 22 (2007) 2163-2173.

[21] F. Yen, C. De la Cruz, B. Lorenz, Y. Y Sun, Y. Q. Wang, M. M Gospodinov, and C. W. Chu, "Low-temperature dielectric anomalies in $HoMnO_3$: The complex phase diagram", *Phys. Rev. B.*, 71 (2005) 180407/1-180407/4(R).

[22] R. Seshadri and N. A. Hill, "Visualizing the role of Bi 6s "lone pairs" in the off-center distortion in ferromagnetic $BiMnO_3$", *Chem. Mater.*, 13 (2001) 2892-2899.

[23] T. Kimura, T. Goto, H. Shintani, K. Ishizaka, T. Arima and Y. Tokura, "Magnetic control of ferroelectric polarization", *Nature*, 426 (2003) 55-58.

[24] N. Hur, S. Park, P. A. Sharma, J. S. Ahn, S. Guha and S-W. Cheong, "Electric polarization reversal and memory in a multiferroic material induced by magnetic fields", *Nature*, 429 (2004) 392-395.

[25] Y. J. Choi, H. T. Yi, S. Lee, Q. Huang, V. Kiryukhin and S.-W. Cheong, "Ferroelectricity in an Ising chain magnet", *Phys. Rev. Lett.*, 100 (2008) 047601/1-047601/4.

[26] H. Wu, T. Burnus, Z. Hu, C. Martin, A. Maignan, J. C. Cezar, A. Tanaka, N. B. Brookes, D. I. Khomskii, and L. H. Tjeng, "Ising Magnetism and Ferroelectricity in Ca_3CoMnO_6", *Phys. Rev. Lett.*, 102 (2009) 026404/1-026404/4.

[27] G. Catalan and J. F. Scott, "Physics and application of bismuth ferrite", *Adv. Mater.*, 21 (2009) 2463-2485.

[28] Y. H. Chu, L. W. Martin, M. B. Holcomb, and R. Ramesh, "Controlling magnetism with multiferroics", *Mater. Today*, 10 (2007) 16-23.

[29] J. Seidel, L. W. Martin, Q. He, Q. Zhan, Y. H. Chu, A. Rother, M. E. Hawkridge, P. Maksymovych, P. Yu, M. Gajek, N. Balke, S. V. Kalinin, S. Gemming, F. Wang, G. Catalan, J. F. Scott, N. A. Spaldin, J. Orenstein, and R. Ramesh, "Conduction at domain walls in oxide multiferroics", *Nature Mater.*, 8 (2009) 229-234.

[30] Y.H. Chu, L.W. Martin, M.B. Holcomb, M. Gajek, S.J. Han, Q. He, N. Balke, C.H. Yang, D. Lee, W. Hu, Q. Zhan, P.L. Yang, A. Fraile-Rodriguez, A. Scholl, S.X. Wang, and R. Ramesh, "Electric-field control of local ferromagnetism using a magnetoelectric multiferroic", *Nature Mater.*, 7 (2008) 478-482.

[31] M. Bibes and A. Barthelemy, "Multiferroics: Towards a magnetoelectric memory," *Nature Mater.* 7 (2008) 425-426.

[32] H. Bea, M. Gajek, M. Bibes, and A. Barthelemy, "Spintronics with multiferroics," *J. Phys.: Cond. Mat.* 20 (2008) 434221/1-434221/11.

[33] I. Boerasu, L. Pintilie, M. Pereira, M. I. Vasilevskiy and M. J. M. Gomes, "Competition between ferroelectric and semiconductor properties in $Pb(Zr_{0.65}Ti_{0.35})O_3$ thin films deposited by sol-gel", *J. Appl. Phys.*, 93 (2003) 4776-4783.

[34] W. Prellier, M. P Singh and P. Murugavel "The single-phase multiferroic oxides: from bulk to thin film", *J. Phys.: Condens. Matter.*, 17 (2005) R803.

[35] B. B. Van Aken, T. T. M. Palstra, A. Filippetti and N. A. Spaldin, "The origin of ferroelectricity in magnetoelectric $YMnO_3$", *Nature Mater.*, 3 (2004) 164-170.

[36] M. Fiebig, C. Degenhardt and R. V. Pisarev, "Magnetic phase diagram of $HoMnO_3$", *J. Appl. Phys.*, 91 (2002) 8867-8869.

[37] J. Hemberger, S. Lobina, H. A. Krug von Nidda, N. Tristan, V. Yu. Ivanov, A. A. Mukhin, A.M. Balbashov, and A. Loidl, "Complex interplay of 3d and 4f magnetism in $La_{1-x}Gd_xMnO_3$", *Phys. Rev. B,* 70 (2004) 024414/1-024414/8.

[38] T. Kimura, S. Ishihara, H. Shintani, T. Arima, K. T. Takahashi, K. Ishizaka, and Y. Tokura, "Distorted perovskite with e^1_g configuration as a frustrated spin system", *Phys. Rev. B,* 68 (2003) 060403/1-060403/4(R).

[39] Y. J Guo, S. Dong, K. F. Wang, and J. M. Liu, "Mean-field theory for ferroelectricity in Ca_3CoMnO_6", *Phys. Rev.* B , 79 (2009) 245107/1-245107/9.

[40] J. M. Moreau, C. Michel, R. Gerson, and W. J. James, "Ferroelectric $BiFeO_3$ X-ray and neutron diffraction study", *J. Phys. Chem. Solids*, 32 (1971) 1315-1320.

[41] C. Michel, J-M Moreau, G. D. Achenbach, R. Gerson, and W. J. James, "The atomic structure of $BiFeO_3$", *Solid State Commun.,* 7 (1969) 701-704.

[42] S. V. Kiselev, R. P. Ozerov, and G. S. Zhdanov, "Detection of Magnetic Order in Ferroelectric $BiFeO_3$ by Neutron Diffraction", *Sov. Phys. Dokl.,* 7 (1963) 742-744.

[43] I. Sosnovska, T. Peterlin-Neumaier, E. Steichele, "Spiral magnetic-ordering in bismuth ferrite", *J. Phys. C-Solid State Phys.*, 15 (1982) 4835-4846.

[44] J. Wang, J. B. Neaton, H. Zheng, V. Nagarajan, S. B. Ogale, B. Liu, D. Viehland, V. Vaithyanathan, V. Schlom, D. G. Waghmare, U. V. Spaldin, N. A. Rabe, K. M. Wuttig, M. Ramesh, R., "Epitaxial $BiFeO_3$ multiferroic thin film heterostructures", *Science*, 299 (2003) 1719-1722.

[45] P. K. Siwach, H. K. Singh, Jai Singh and O. N. Srivastava, "Anomalous ferromagnetism in spray pyrolysis deposited multiferroic $BiFeO_3$ films", *Appl. Phys. Lett.*, 91 (2007) 122503/1-122503/3.

[46] Y. Wang, Y. Lin, and C.W. Nan, "Thickness dependent size effect of $BiFeO_3$ films grown on $LaNiO_3$-buffered Si substrates", *J. Appl. Phys.,* 104 (2008) 123912/1-123912/4.

[47] D. S. Rana, K. Takahashi, K. R. Mavani, I. Kawayama, H. Murakami, and M. Tonouchi, "Thickness dependence of the structure and magnetization of $BiFeO_3$ thin films on $(LaAlO_3)_{0.3}(Sr_2AlTaO_6)_{0.7}$ (001) substrate", *Phys. Rev. B*, 75 (2007) 060405(R)/1-060405/4.

[48] C. J. Cheng, C. Lu, Z. Chen, L. You, L. Chen, J. Wang, and T. Wu, "Thickness-dependent magnetism and spin-glass behaviors in compressively strained $BiFeO_3$ thin films", *Appl. Phys. Lett.*, 98 (2011) 242502/1-242502/3.

[49] F. Huang, X. Lu, W.I Lin, Y. Kan, J. Zhang, Q. Chen, Z. Wang, L. Li, and J. Zhu, "Thickness-dependent structural and magnetic properties of $BiFeO_3$ films prepared by metal organic decomposition method", *Appl. Phys. Lett.*, 97 (2010) 222901/1-222901/3.

[50] X. Tang, J. Dai, X. Zhu, J. Lin, Q. Chang, D. Wu, W. Song, and Y. Sun, "Thickness-Dependent Dielectric, Ferroelectric, and Magnetodielectric Properties of $BiFeO_3$ Thin Films Derived by Chemical Solution Deposition", *J Am Ceram Soc,* 95 (2012) 538–544.

[51] G. T. Rado and V. J. Folen, "Observation of the magnetically induced magnetoelectric effect and evidence for antiferromagnetic domains", *Phys. Rev. Lett.,* 7 (1961) 310-311.

[52] D. L. Fox and J. F. Scott, "Ferroelectrically induced ferromagnetism", *J. Phys. C: Sol. State Phys.*, 10 (1977) L329-331.

[53] R. E. Newnham, J. J. Kramer, W. A. Schulze and L. E. Cross, "Magneto-ferroelectricity in Cr_2BeO_4," *J. Appl. Phys.*, 49 (1978) 6088-6091.

[54] J. R. Teague, R. Gerson and W. J. James, "Dielectric hysteresis in single crystal $BiFeO_3$", *Solid State Commun.*, 8 (1970) 1073-1074.

[55] E. F. Bertaut and M. Mercier, "Magnetoelectricity in theory and experiment", *Mater. Res. Bull.*, 6 (1971) 907-21.

[56] M. Fiebig, Th. Lottermoser, D. Fröhlich, A. V. Goltsev & R. V. Pisarev, "Observation of coupled magnetic and electric domains", *Nature*, 419 (2002) 818-820.

[57] G. A. Smolenskii, and I. E. Chupis, "Thermodynamic Theory of Crystals Possessing Ferroelectric and Ferromagnetic Properties", *Sov. Phys. Solid State*, 4 (1962) 807-809.

[58] F. Jona, and G. Shirane, "Ferroelectric Crystals", *Dover: New York*, (1993) 216-261.

[59] V. S Filip'ev, I. P Smol'yaninov, E. G Fesenko, and I. I Belyaev, "Synthesis of $BiFeO_3$ and determination of the unit cell", *Kristallografiya* 5 (1960) 958.

[60] F. Kubel, and H. Schmid, "Structure of a ferroelectric and ferroelastic monodomain crystal of the perovskite $BiFeO_3$", *Acta Crystallogr., Sect. B: Struct. Sci.*, 46 (1990) 698-702.

[61] J. D. Bucci, B. K. Robertson, W. J. James, "The precision determination of the lattice parameters and the coefficients of thermal expansion of $BiFeO_3$", *J. Appl. Cryst.*, 5 (1972) 187-191.

[62] (a) V. V. Lazenka, G. Zhang, J. Vanacken, I. I. Makoed, A. F. Ravinski, V. V. Moshchalko, "Structural transformation and magnetoelectric behavior in $Bi_{1-x}Gd_xFeO_3$ multiferroics", *J. of Phys. D: Appl. Phys.*, 45 (2012) 125002/1-125002/7. (b) V V Lazenka, M Lorenz, H Modarresi, K Brachwitz, P Schwinkendorf, T Bontgen, J Vanacken, M Ziese, M Grundmann and V V Moshchalkov, "Effect of rare-earth ion doping on the multiferroic properties of $BiFeO_3$ thin films grown epitaxially on $SrTiO_3$ (1 0 0)", J. *Phys. D: Appl. Phys.*, 46 (2013) 175006/1-175006/9.

[63] J. P. Rivera, H. Schmid, "On the birefringence of magnetoelectric $BiFeO_3$", *Ferroelectrics*, 204 (1997) 23-33.

[64] R. Przeniosło, M. Regulski, I. Sosnowska, "Modulation in Multiferroic $BiFeO_3$: Cycloidal, Elliptical or SDW?", *J. Phys. Soc. Jpn.*, 75 (2006) 084718/1-084718/3.

[65] A. Palewicz, R. Przeniosło, I. Sosnowska, A. W. Hewat, "Atomic displacements in $BiFeO_3$ as a function of temperature: neutron diffraction study", *Acta Cryst.*, B63 (2007) 537-544.

[66] V. M. Goldschmidt, "Die gesetze der krystallochemie", *Naturwissenschaften*, 14 (1926) 477-485.

[67] R. D. Shannon, "Revised effective ionic radii and systematic studies of interatomic distances in halides and chalcogenides", *Acta Cryst. A,* 32 (1976) 751-767.

[68] H. D. Megaw, C. N. W. Darlington, "Geometrical and structural relations in the rhombohedral perovskites", *Acta Cryst. A,* 31 (1975) 161-173.

[69] D. Lebeugle, D. Colson, A. Forget, M. Viret, A. M. Battaille, and A. Gukasov, "Electric-Field-Induced Spin Flop in $BiFeO_3$ Single Crystals at Room Temperature", *Phys. Rev. Lett.*, 100 (2008) 227602-227608.

[70] (a) J. F. Scott, M. K. Singh, R. S. Katiyar, "Critical phenomena at the 140 and 200 K magnetic phase transitions in $BiFeO_3$", *J. Phys.: Condens. Matter,* 20 (2008) 322203/1-322203/4. (b) J. F. Scott, M. K. Singh, R. S. Katiyar, "Critical slowing down of spin fluctuations in $BiFeO_3$", *J. Phys.: Condens. Matter,* 20 (2008) 425223/1-425223/5**.**

[71] A. Palewicz, T. Szumiata, R. Przeniosło, I. Sosnowska, I. Margiolaki, "Search for new modulations in the $BiFeO_3$ structure: SR diffraction and Mössbauer studies", *Solid State Commun.*, 140 (2006) 359-363.

[72] R. Przeniosło, A. Palewicz, M. Regulski, I. Sosnowska, R. M. Ibberson, K. S. Knight, "Does the modulated magnetic structure of $BiFeO_3$ change at low temperatures?", *J. Phys.: Condens. Matter*, 18 (2006) 2069-2075.

[73] D. Lebeugle, D. Colson, A. Forget, M. Viret, P. Bonville, J. F. Marucco, and S. Fusil, "Room-temperature coexistence of large electric polarization and magnetic order in $BiFeO_3$ single crystals", *Phys. Rev. B,* 76 (2007) 024116/1-024116/8.

[74] C. Ederer and N. A. Spaldin, "Weak ferromagnetism and magnetoelectric coupling in bismuth ferrite", *Phys. Rev., B* 71 (2005) 060401(R)/1-060401/4.

[75] R. R. Das, D. M. Kim, S. H. Baek, C. B. Eoma, F. Zavaliche, S. Y. Yang, R. Ramesh, Y. B. Chen, X. Q. Pan, X. Ke, M. S. Rzchowski, and S. K. Streiffer, "Synthesis and ferroelectric properties of epitaxial $BiFeO_3$ thin films grown by sputtering", *Appl. Phys. Lett.*, 88 (2006) 242904/1-242904/3.

[76] G. Achenbach, W. J. James, and R. Gerson, "Preparation of Single-Phase Polycrystalline $BiFeO_3$", *J. Am. Ceram. Soc*., 8 (1967) 437/1-437/1.

[77] K. Singh, R. K. Kotnala, and M. Singh "Study of electric and magnetic properties of $Bi_{0.9}Pb_{0.1}Fe_{0.9}Ti_{0.1}O_3$ nanomultiferroic system" *Appl. Phys. Lett.*, 93 (2008) 212902/1-212902/3.

[78] X. Wang, Y. Zhang, and Z. Wu, "Magnetic and optical properties of multiferroic bismuth ferrite nanoparticles by tartaric acid-assisted sol–gel strategy", *Mater. Lett.*, 64 (2010) 486-488.

[79] C. Paraschiv, B. Jurca, A. Ianculescu, and O. Carp, "Synthesis of nanosized bismuth ferrite ($BiFeO_3$) by a combustion method starting from $Fe(NO_3)_3{\cdot}9H_2O$-$Bi(NO_3)_3{\cdot}9H_2O$-glycine or urea systems", *J. Therm. Anal. Calorim.*, 94 (2008) 411-416.

[80] S. Ghosh., S. Dasgupta., A. Sen., and H. S. Maiti, " Low temperature synthesis of bismuth ferrite nanoparticles by a ferrioxalate precursor method", *Mater. Res. Bull.*, 40 (2005) 2073-2079.

[81] A. Chaudhuri, S. Mitra, M. Mandal, K. Mandal, "Nanostructured bismuth ferrites synthesized by solvothermal process", *J. Alloys Compd*. 491 (2010) 703-706.

[82] S. H. Han, K. S. Kim, H. G. Kim, H-G Lee, and H-W Kang, "Synthesis and characterization of multiferroic $BiFeO_3$ powders fabricated by hydrothermal method", *Ceram. Int.* 36 (2010) 1365-1372.

[83] R. Palai, R. S. Katiyar, H. Schmid, P. Tissot, S. J. Clark, J. Robertson, S. A. T. Redfern, G. Catalan, J. F. Scott, "β Phase and γ–β metal-insulator transition in multiferroic $BiFeO_3$", *Phys. Rev., B,* 77 (2008) 014110/1-014110/11.

[84] J. R. Chen, W. L. Wang, J. B. Li, and G. H. Rao, "X-ray diffraction analysis and specific heat capacity of $Bi_{1-x}La_xFeO_3$ perovskites", *J. Alloys Compd*., 459 (2008) 66-70.

[85] Z. V. Gabbasova, M. D. Kuzmin, A. K. Zvezdin, I. S. Dubenko, V. A. Murashov, D .N. Rakov and I. B. Krynetsky, "$Bi_{1-x}R_xFeO_3$ (R = rare earth): a family of novel magnetoelectrics". *Phys. Lett. A*, 158 (1991) 491-498.

[86] A V. Zalesskii, A. A. Frolov, T. A. Khimich, A. A. Bush, "Composition-induced transition of spin-modulated structure into a uniform antiferromagnetic state in a $Bi_{1-x}La_xFeO_3$ system studied using ^{57}Fe NMR", *Phys. Solid. State*, 45 (2003) 141-145.

[87] G. L. Yuan, S. W. Or, H. L. W. Chan, "Structural transformation and ferroelectric–paraelectric phase transition in $Bi_{1-x}La_xFeO_3$ (x = 0–0.25) multiferroic ceramics", *J. Phys. D: Appl. Phys.*, 40 (2007) 1196-1200.

[88] R.Y. Zheng, X. S. Gao, Z. H. Zhou, and J. Wang, "Multiferroic $BiFeO_3$ thin films deposited on $SrRuO_3$ buffer layer by rf sputtering", *J. Appl. Phys.*, 101 (2007) 054104/1-054104/5.

[89] S. Y. Yang, F. Zavaliche, L. Mohaddes-Ardabili, V. Vaithyanathan, D. G.Schlom, Y. J. Lee, Y. H. Chu, M. P. Cruz, Q. Zhan, T. Zhao, and R. Ramesh, "Metalorganic chemical vapour deposition of lead-free ferroelectric $BiFeO_3$ films for memory applications", *Appl. Phys. Lett.*, 87 (2005) 102903/1-102903/3.

[90] P. Royen and K. Swars, "Das System Wismutoxyd-Eisenoxyd im Bereich von 0 bis 55 Mol% Eisenoxyd", *Angew. Chem.*, 69 (1957) 779/1-779/24.

[91] G. A. Smolensky, V. A. Isupov, and A. I. Agronovskaya., "A new group of ferroelectrics-(with layered structure)", *Sov Phys Solid State*, 1 (1959) 149-150.

[92] J.F Scott, "Magnetic phases of bismuth ferrite", *J Magn Magn. Mater.*, 321 (2009) 1689-1691.

[93] A. K. Pradhan, K. Zhang, D. Hunter, J. B. Dadson, and G. B. Loutts, "Magnetic and electrical properties of single phase multiferroic", *J. Appl. Phys.*, 97 (2005) 093903/1-093903/4.

[94] J. K. Kim, S.S. Kim, and W-J Kim, "Sol–gel synthesis and properties of multiferroic $BiFeO_3$", *Mater Lett.*, 59 (2005) 4006-4009.

[95] W. N. Su, D. H. Wang, Q. Q. Cao, Z. D. Han, J. Yin, J. R. Zhang, and Y. W. Du, "Large polarization and enhanced magnetic properties in $BiFeO_3$ ceramic prepared by high-pressure synthesis", *Appl. Phys. Lett.*,91 (2007) 092905/1-092905/3.

[96] S-T Zhang, Y. Zhang, M-H Lu, C-L Du, Y-F Chen, Z-G Liu, Y-Y Zhu, and N-B Ming, "Substitution-induced phase transition and enhanced multiferroic properties of $Bi_{1-x}La_xFeO_3$ ceramics", *Appl. Phys. Lett.*, 88 (2006) 162901/1-162901/3.

[97] G. L. Yuan and S. W. Or, "Structural transformation and ferroelectromagnetic behavior in single-phase $Bi_{1-x}Nd_xFeO_3$ multiferroic ceramics", *Appl. Phys. Lett.*, 89 (2006) 052905/1-052905/3.

[98] D. Kothari, V. R. Reddy, A. Gupta, V. Sathe, and A. Banerjee, "Multiferroic properties of polycrystalline $Bi_{1-x}Ca_xFeO_3$", *Appl. Phys. Lett.*, 91 (2007) 202505/1-202505/3.

[99] D. Varshney, P. Sharma, S. Satapathy, and P. K. Gupta, "Structural, magnetic and dielectric properties of Pr-modified $BiFeO_3$ multiferroic", *J. Alloys Compd.*, 584 (2014) 232-239.

[100] G. L. Yuan and S. W. Or, "Enhanced piezoelectric and pyroelectric effects in single-phase multiferroic $Bi_{1-x}Nd_xFeO_3$ (x=0–0.15)", *Appl. Phys. Lett.*, 88 (2006) 062905/1-062905/3.

[101] V. A. Khomchenko, D. A. Kiselev, I. K. Bdikin, V. V. Shvartsman, P. Borisov, W. Kleemann, J. M. Vieira, and A. L. Kholkin, "Crystal structure and multiferroic properties of Gd-substituted $BiFeO_3$", *Appl. Phys. Lett.*, 93 (2008) 262905/1-262905/3.

[102] V.A. Khomchenko, D.V. Karpinsky, A.L. Kholkin, N.A. Sobolev, G.N. Kakazei, J.P. Araujo, I.O. Troyanchuk, B.F.O. Costa, and J.A. Paixão, "Rhombohedral-to-orthorhombic transition and multiferroic properties of Dy-substituted $BiFeO_3$", *J. Appl. Phys.*, 108 (2010) 074109/1-074109/5.

[103] N. Jeon, D. Rout, W. Kim, and S. L. Kang, "Enhanced multiferroic properties of single-phase $BiFeO_3$ bulk ceramics by Ho doping," *Appl. Phys. Lett.*, 98 (2011) 072901/1-072901/3.

[104] V. L. Mathe, K. K. Patankar, M. B. Kothalei, S. B. Kulkarni, P. B. Joshi and S. A. Patil, "Preparation, structural analysis and dielectric properties of $Bi_xLa_{1-x}FeO_3$ perovskite", *Pramana- J Phys.*, 58 (2002) 1105-1113.

[105] V. R. Palkar, Darshan C. Kundaliya, S. K. Malik, and S. Bhattacharya, "Magnetoelectricity at room temperature in the $Bi_{0.9-x}Tb_xLa_{0.1}FeO_3$ system", *Phys. Rev., B* 69 (2004) 212102/1-212102/3.

[106] G. L. Yuan and Siu Wing Ora, "Multiferroicity in polarized single-phase $Bi_{0.875}Sm_{0.125}FeO_3$ ceramics", *J. Appl. Phys.*, 100 (2006) 024109/1-024109/5.

[107] D. H. Wang, W. C. Goh, M. Ning, and C. K. Ong, "Effect of Ba doping on magnetic, ferroelectric, and magnetoelectric properties in multiferroic $BiFeO_3$ at room temperature", *Appl. Phys. Lett.*, 88 (2006) 212907/1-212907/3.

[108] V.A. Khomchenko, V.V. Shvartsman, P. Borisov, W. Kleemann, D.A. Kiselev, I.K. Bdikin, J.M. Vieira, A.L. Kholkin, "Effect of Gd substitution on the crystal structure and multiferroic properties of $BiFeO_3$", *Acta Mater.*, 57 (2009) 5137–5145.

[109] C. Fanggao, S. Guili, F. Kun, Q. Ping, Z. Qijun, "Effect of Gadolinium substitution on dielectric properties of Bismuth Ferrite", *J. Rare Earth*, Spec. Issue 24 (2006) 273-276.

[110] Q. Xu, H. Zai, D. Wu, Y.K. Tang, and M.X. Xu "The magnetic properties of $BiFeO_3$ and $Bi(Fe_{0.95}Zn_{0.05})O_3$", *J. Alloys Compd.*, 485 (2009) 13-16.

[111] Q. H. Jiang, F. T. Liu, C-W Nan, Y-H Lin, M. J. Reece, H. X. Yan, H. P. Ning and Z. J. Shen,"High-temperature ferroelectric phase transition observed in multiferroic $Bi_{0.9}1La_{0.05}Tb_{0.04}FeO_3$", *Appl. Phys. Lett.*, 95 (2009) 012909/1-012909/3.

[112] Q. Xu, H. Zai, D. Wu, T. Qiu, and M. X. Xu, "The magnetic properties of $BiFe_{0.95}Co_{0.05}O_3$ ceramics" *Appl. Phys. Lett.*, 95 (2009) 112510/1-112510/3.

[113] B. Ramachandran and M. S. Ramachandra Rao, "Low temperature magnetocaloric effect in polycrystalline $BiFeO_3$ ceramics" *Appl. Phys. Lett.*, 95 (2009) 142505/1-142505/3.

[114] G. Catalan, K. Sardar, N. S. Church, J. F. Scott, R. J. Harrison, and S. A. T. Redfern, "Effect of chemical substitution on the Néel temperature of multiferroic $Bi_{1-x}Ca_xFeO_3$", *Phys. Rev. B,* 79 (2009) 212415/1-212415/4.

[115] X. Zheng, Q. Xu, Z. Wen, X. Lang, D. Wu, T. Qiu, and M.X. Xu, "The magnetic properties of La doped and codoped $BiFeO_3$", *J. Alloys Compd.*, 499 (2010) 108-112.

[116] S. Chen, L. Wang, H. Xuan, Y. Zheng, D. Wang, J. Wu, Y. Du, and Z. Huang, Multiferroic properties and converse magnetoelectric effect in $Bi_{1-x}Ca_xFeO_3$ ceramics' *J. Alloys Compd.*, 506 (2010) 537-540.

[117] Z. M. Tian, S. L. Yuan, X. F. Zheng, L. C. Jia, S. X. Huo, H. N. Duan, and L. Liu, "Spin-glasslike behavior and exchange bias in multiferroic $Bi_{1/3}Sr_{2/3}FeO_3$ ceramics" *Appl. Phys. Lett.*, 96 (2010) 142516/1-142516/3.

[118] S. Kazhugasalamoorthy, P. Jegatheesan, R. Mohandoss, N.V. Giridharan, B. Karthikeyan, R. J. Joseyphus, and S. Dhanuskodi, "Investigations on the properties of pure and rare earth modified bismuth ferrite ceramics", *J. Alloys Compd.*, 493 (2010) 569-572.

[119] Y. Du, Z. X. Cheng, M. Shahbazi, E. W. Collings,.S. X. Dou, and X. L. Wang, "Enhancement of ferromagnetic and dielectric properties in lanthanum doped $BiFeO_3$ by hydrothermal synthesis", *J. Alloys Compd.*, 490 (2010) 637-641.

[120] B. Bellakki, V. Manivannan, "Citrate-gel synthesis and characterization of yttrium-doped multiferroic $BiFeO_3$", *J Sol-Gel Sci Technol*, 53 (2010) 184–192.

[121] K. Sen, K. Singh, A. Gautam, and M. Singh, "Study of Dielectric and Ferroelectric Properties of Multiferroic $BiCo_xFe_{1-x}O_3$ Ceramic", *Integr. Ferroelectr.*, 120 (2010) 122- 130.

[122] A. K. Ghosh, G.D. Dwivedi, B. Chatterjee, B. Rana, A. Barman, S. Chatterjee, and H. D. Yang, "Role of codoping on multiferroic properties at room temperature in $BiFeO_3$ ceramic", *Solid State Commun.*, 166 (2013) 22-26.

[123] T. Park, G.C. Papaefthymiou, A. J. Viescas, A. R. Moodenbaugh, and S. S. Wong, "Size dependent magnetic properties of single crystalline multiferroic $BiFeO_3$ nanoparticles", *Nano Lett.* 7 (2007) 766-772.

[124] F. Gao, Y. Yuan, K. F. Wang, X. Y. Chen, F. Chen, J.-M. Liu, Z. F. Ren, "Preparation and photoabsorption characterization of $BiFeO_3$ nanowires", *Appl. Phys. Lett.*, 89 (2006) 102506/1-102506/3.

[125] T. J. Park, Y. B. Mao, S. S. Wong, "Synthesis and characterization of multiferroic $BiFeO_3$ nanotubes", *Chem. Commun.*, 23 (2004) 2708-2709.

[126] C. Chen, J. Cheng, S. Yu, L. Che, and Z. Meng "Hydrothermal synthesis of perovskite bismuth ferrite crystallites", *J. Cryst. Growth.*, 291 (2006) 135-139.

[127] R. Mazumder, S. Ghosh, P. Mondal, D. Bhattacharya, S. Dasgupta, N. Das, A. Sen, A. K. Tyagi, M. Sivakumar, T. Takami, H. Ikuta, "Particle size dependence of magnetization and phase transition near T_N in multiferroic $BiFeO_3$", *J. Appl. Phys.*, 100 (2006) 033908/1-033908/9.

[128] Y. Wang, G. Xu, Z. Ren, X. Wei, W. Weng, P. Du, G. Shen, and G. Han, "Low temperature polymer assisted hydrothermal synthesis of bismuth ferrite nanoparticles", *Ceram. Int.*, 34 (2008) 1569-1571.

[129] T. T. Carvalho, and P. B. Tavares, "Synthesis and thermodynamic stability of multiferroic $BiFeO_3$", *Mater. Lett.*, 62 (2008) 3984-3986.

[130] M. Hongyan, Z. Qiong, T. Guoqiang and Z. Gangqiang, "Co-precipitation/ Hydrothermal Synthesis of $BiFeO_3$ powder", *J. Wuhan Univ. Technol-Mat. Sci. Edit.*, 23 (2008) 507-509.

[131] S. H. Xie, J. Y. Li, R. Proksch, Y. M. Liu,Y. C. Zhou, Y. Y. Liu, Y. Ou, L. N. Lan, and Y. Qiao, "Nanocrystalline multiferroic $BiFeO_3$ ultrafine fibers by sol-gel based electrospinning" *Appl. Phys. Lett.*, 93 (2008) 222904/1-222904/3.

[132] U. A. Joshi, J. S. Jang, P. H. Borse, and J. S. Lee, "Microwave synthesis of single-crystalline perovskite $BiFeO_3$ nanocubes for photoelectrode and photocatalytic applications" *Appl. Phys. Lett.*, 92 (2008) 242106/1-242106/3.

[133] A. K. Kundu, R. Ranjith, B. Kundys, N. Nguyen, V Caignaert, V Pralong, W. Prellier, and B. Raveau, "A multiferroic ceramic with perovskite structure: "$La_{0.5}Bi_{0.5}Mn_{0.5}Fe_{0.5}O_{3.09}$" , *Appl. Phys. Lett.*, 93 (2008) 052906/1-052906/3.

[134] S. Vijayanand, H. S. Potdar, and P. A. Joy "Origin of high room temperature ferromagnetic moment of nanocrystalline multiferroic $BiFeO_3$", *Appl. Phys. Lett.,* 94 (2009) 182507/1-182507/3.

[135] S. Vijayanand, M. B. Mahajan, H. S. Potdar, and P. A. Joy, "Magnetic characteristics of nanocrystalline multiferroic $BiFeO_3$ at low temperatures", *Phys. Rev. B,* 80 (2009) 064423/1-064423/5.

[136] Xuelian Yu, X. An, "Enhanced magnetic and optical properties of pure and (Mn, Sr) doped $BiFeO_3$ nanocrystals", *Solid State Commun.,* 149 (2009) 711-714.

[137] D-C Jia , J-H Xu, H. Ke, W. Wang, Y. Zhou, "Structure and multiferroic properties of $BiFeO_3$ powders", *J. Eur. Ceram. Soc.,* 29 (2009) 3099-3103.

[138] J. Prado-Gonjal, M. E. Villafuerte-Castrejo´n, L. Fuentes, E. Mora´n, "Microwave–hydrothermal synthesis of the multiferroic $BiFeO_3$", *Mater. Res. Bull.,* 44 (2009) 1734-1737.

[139] F. Z. Qian, J. S. Jiang, S. Z. Guo, D. M. Jiang, and W. G. Zhang, "Multiferroic properties of $Bi_{1-x}Dy_xFeO_3$ nanoparticles" *J. Appl. Phys.,* 106 (2009) 084312/1-084312/6.

[140] F. Z. Qian, J.S .Jiang, D. M. Jiang, C. M. Wang, and W. G. Zhang, "Improved multiferroic properties and a novel magnetic behaviour of $Bi_{0.8}La_{0.2}Fe_{1-x}Co_xO_3$ nanoparticles" *J. Magn. Magn. Mater.,* 322 (2010) 3127-3130.

[141] R. Guo, L. Fang, W. Dong, F. Zheng, and M. Shen, "Enhanced Photocatalytic Activity and Ferromagnetism in Gd Doped $BiFeO_3$ nanoparticles", *J. Phys. Chem.* C, 114 (2010) 21390-21396.

[142] B. Bhushan, A. Basumallick, N.Y. Vasanthacharya, S. Kumar, and D. Das, "Sr induced modification of structural, optical and magnetic properties in $Bi_{1-x}Sr_xFeO_3$ (x = 0, 0.01, 0.03, 0.05 and 0.07) multiferroic nanoparticles" *Solid State Sci.,* 12 (2010) 1063-1069.

[143] F. Wen, N. Wang, and F. Zhang, "Enhanced microwave absorption properties in $BiFeO_3$ ceramics prepared by high-pressure synthesis" *Solid State Commun.,* 150 (2010) 1888-1891.

[144] S. Li, Y-H Lin, B-P Zhang, Y. Wang, and C-W Nan, "Controlled fabrication of $BiFeO_3$ uniform microcrystals and their magnetic and photocatalytic behaviors", *J. Phys. Chem. C,* 114 (2010) 2903-2908.

[145] P. Thakuria and P. A. Joy, "High room temperature ferromagnetic moment of Ho substituted nanocrystalline $BiFeO_3$", *Appl. Phys. Lett.*, 97 (2010) 162504/1-162504/3.

[146] Y. Hu, L. Fei, Y. Zhang, J. Yuan, Y. Wang, and H. Gu, "Synthesis of Bismuth Ferrite Nanoparticles via a wet Chemical Route at Low Temperature", *J. Nanomater.*, 2011 (2011) Article ID 797639, 6pp.

[147] H. Ke, W. Wang, Y. Wang, J. Xu, D. Jia , Z. Lu, and Y. Zhou, "Factors controlling pure-phase multiferroic $BiFeO_3$ powders synthesized by chemical co-precipitation", *J. Alloys and Compd*., 509 (2011) 2192-2197.

[148] A. Kumar, and K. L. Yadav, "Magnetic, magnetocapacitance and dielectric properties of Cr doped bismuth ferrite nanoceramics" *Mater. Sci. Eng. B*, 176 (2011) 227-230.

[149] D. Guo, Y. Gong, C. Liu, C. Wang, Q. Shen, and L. Zhang, "Preparation of $Bi_{0.85}Nd_{0.15}FeO_3$ Nanotube Arrays by a Sol–Gel Template Method", *J. Electron. Mater.*, 40 (2011) 340-343.

[150] Y. Du, Z. X. Cheng, S. X. Dou, D. J. Attard, and X. L. Wang, "Fabrication, magnetic, and ferroelectric properties of multiferroic $BiFeO_3$ hollow nanoparticles", *J. Appl. Phys.* 109 (2011) 073903/1-073903/5.

[151] S. K. Srivastav and N. S. Gajbhiye, "Low temperature synthesis, structural, optical and magnetic properties of bismuth ferrite nanoparticles", *J Am Ceram Soc*, 95 (2012) 3678-3682.

[152] J. Ray, A. K. Biswal, S. Acharya, V. Ganesan, D. K. Pradhan, P. N. Vishwakarma, "Effect of Co substitution on the magnetic properties of $BiFeO_3$", *J. Magn. Magn. Mater.* 324 (2012) 4084-4089.

[153] A. Kumar, D. Varshney, "Crystal structure refinement of $Bi_{1-x}Nd_xFeO_3$ multiferroic by the Rietveld method," *Ceram. Int.*, 38 (2012) 3935-3942.

[154] A. Mukherjee, S. Basu, P. K. Manna, S. M. Yusuf and M. Pal, "Giant magnetodielectric and enhanced multiferroic properties of Sm doped bismuth ferrite nanoparticles", *J. Mater. Chem.*, 2 (2014) 5885-5891.

[155] J. Wang, H. Zheng, Z. Ma, S. Prasertchoung, M. Wuttig, R. Droopad, J. Yu, K. Eisenbeiser, and R. Ramesh, "Epitaxial $BiFeO_3$ thin films on Si", *Appl. Phys. Lett.*, 85 (2004) 2574-2576.

[156] K.Y. Yun, M. Noda and M. Okuyama, "Prominent ferroelectricity of $BiFeO_3$ thin films prepared by pulsed-laser deposition", *Appl. Phys. Lett.*, 83 (2003) 3981-3983.

[157] K.Y. Yun, M. Noda, M. Okuyama, H. Saeki, H. Tabata, and K. Saito, "Structural and multiferroic properties of $BiFeO_3$ thin films at room temperature", *J. Appl. Phys.*, 96 (2004) 3399-3403.

[158] J. D. Lebeugle, D. Colson, A. Forget, and M. Viret, "Very large spontaneous electric polarization in $BiFeO_3$ single crystals at room temperature and its evolution under cycling fields", *Appl Phys. Lett.*, 91 (2007) 022907/1-022907/3.

[159] C. Ederer, N. A. Spaldin, "Influence of strain and oxygen vacancies on the magnetoelectric properties of multiferroic bismuth ferrite", *Phys. Rev. B.*, 71 (2005) 224103/1-224103/9.

[160] Y. H. Lee, J. M. Wu and C. H. Lai, "Influence of La doping in multiferroic properties of $BiFeO_3$ thin films", *Appl. Phys. Lett.*, 88 (2006) 042903/1-042903/3.

[161] S. K. Singh, H. Funakuba, H. Uchida and H. Ishiwara, "Structural and electrical properties of $BiFeO_3$ thin films", *Integrated Ferroelectrics*, 76 (2005) 139-146.

[162] Y. Wang, Q. H Jiang, H. C He, and C. W. Nan, "Multiferroic $BiFeO_3$ thin films prepared via a simple sol-gel method", *Appl. Phys. Lett.*, 88 (2006) 142503/1-142503/3.

[163] S. W. Lee, and C. S. Kim, "Growth of multiferroics $BiFeO_3$ thin films by sol–gel method", *J. Magn. Magn. Mater.*, 304 (2006) e772-e774.

[164] H. Naganuma, Y. Inoue, and S. Okamura, "Dependence of ferroelectric and magnetic properties on measuring temperatures for polycrystalline $BiFeO_3$ films", *IEEE Trans. Ultrason. Ferroelect. Freq.Contr.*, 55 (2008) 1046-1050.

[165] L.W. Martin, S. P. Crane, Y-H Chu, M. B. Holcomb, M. Gajek, M Huijben, C-H Yang, N Balke and R Ramesh, "Multiferroics and magnetoelectrics: thin films and nanostructures", *J. Phys.: Condens. Matter*, 20 (2008) 434220/1-434220/13.

[166] S. Hussain, S.K. Hasanain, G. H. Jaffari, S. I. Shah, "Thickness dependent magnetic and ferroelectric properties of $LaNiO_3$ buffered $BiFeO_3$ thin films", *Curr. Appl. Phys.*, 15 (2015) 194-200.

[167] X. Qi, J. Dho,R. Tomov, M.G. Blamire and J. L. MacManus-Driscoll, "Greatly reduced leakage current and conduction mechanism in aliovalent-ion-doped $BiFeO_3$", *Appl. Phys. Lett.*, 86 (2005) 062903/1-062903/3.

[168] C. F. Chung, J. P. Lin and J. M. Wu, "Influence of Mn and Nb dopants on electric properties of chemical-solution-deposited $BiFeO_3$ films", *Appl. Phys. Lett.*, 88 (2006) 242909/1-242909/3.

[169] J. K. Kim, S. S. Kim, W.-J. Kim, A. S. Bhalla and R. Guo, "Enhanced ferroelectric properties of Cr-doped $BiFeO_3$ thin films grown by chemical solution deposition", *Appl. Phys. Lett.*, 88 (2006) 132901/1-132901/3.

[170] N. M. Murari, R. Thomas, A. Winterman, R. E. Melgarejo, S. P. Pavunny, and R. S. Katiyar, "Structural, electrical, and magnetic properties of chemical solution deposited $Bi(Fe_{0.95}Cr_{0.05})O_3$ thin films on platinized silicon substrates", *J. Appl. Phys.*, 105 (2009) 084110/1-084110/6.

[171] J. M. Park, S. Nakashima, F. Gotoda, T. Kanashima, and M. Okuyama, "Pulsed Laser Deposition and Characterization of Sr and Zn co-Substituted $BiFeO_3$ Thin films", *Jpn. J. Appl. Phys.*, 48 (2009) 09KB03.

[172] (a) J. Wu and J. Wang, "Ferroelectric and Impedance Behavior of La- and Ti-Codoped $BiFeO_3$ Thin Films", *J. Am. Ceram. Soc.*, 93 (2010) 2795-2803. (b) J. Wu and J. Wang, "Effects of buffer layer thickness on multiferroic thin films", *J. Appl. Phys.*, 106 (2009) 054115/1-054115/5.

[173] S. K. Singh, H. Ishiwara, K. Sato, and K. Maruyama, "Microstructure and frequency dependent electrical properties of Mn-substituted $BiFeO_3$ thin films", *J. Appl. Phys.*, 102 (2007) 094109/1-094109/5.

[174] A.Z. Simões, E. C. Aguiar, A. H. M. Gonzalez, J. Andrés, E. Longo, and J. A. Varela, "Strain behavior of lanthanum modified $BiFeO_3$ thin films prepared via soft chemical method", *J. Appl. Phys.*, 104 (2008) 104115/1-104115/6.

[175] V. R. Singh, A. Garg, and D. C. Agrawal, "Structural changes in chemical solution deposited lanthanum doped bismuth ferrite thin films", *Appl. Phys. Lett.*, 92 (2008) 152905/1-152905/3.

[176] V. R. Singh, A. Garg and D. C. Agrawal, "Structure and properties of lanthanum-doped bismuth ferrite thin films", *Solid State Commun.*, 149 (2009) 734-737.

[177] S Mukherjee, R Gupta, A Garg, V Bansal, and S. Bhargava, "Influence of Zr doping on the structure and ferroelectric properties of $BiFeO_3$ thin films", *J. Appl. Phys.*, 107 (2010) 123535/1-123535/5.

[178] H.B. Sharma, S. Bobby Singh, Ng Boinis Singh, "Structural and optical properties of low temperature synthesized Nanostructured $BiFeO_3$ thin films", *Physica B: Condensed Matter* 406 (2011) 351-353.

[179] (a) S. Gupta , M. Tomar , A. R. James & V. Gupta, "Study of A-site and B-site Doping on Multiferroic Properties of BFO Thin Films", *Ferroelectrics*, 454(1) (2013) 41-46. (b) S. Gupta, M. Tomar & V. Gupta, "Enhanced Magnetic and

Electric Properties of Nanocrystalline Ce Modified BFO Thin Films", *Ferroelectrics*, 470 (2014) 272-279. (c) S. Gupta, M. Tomar, A.R. James, V. Gupta, "Ce-doped bismuth ferrite thin films with improved electrical and functional properties", *J Mater Sci*, 49 (2014) 5355-5364.

[180] H. Naganuma, J. Miura, and S. Okamura, "Ferroelectric, electrical and magnetic properties of Cr, Mn, Co, Ni, Cu added polycrystalline $BiFeO_3$ films", *Appl. Phys. Lett.*, 93 (2008) 052901/1-052901/3.

[181] H. Naganuma, J. Miura & S. Okamura, "Annealing temperature effect on ferroelectric and magnetic properties in Mn-added polycrystalline $BiFeO_3$ films", *J. Electroceram.*, 22 (2009) 203-208.

[182] Alexandre Zirpoli Simões, Filiberto Gonzalez Garcia, and Francisco Moura, "Magnetoelectric Coefficient in Strontium Ruthenate Buffered Lanthanum Modified Bismuth Ferrite Thin Films Grown by Chemical Method", *Journal of Scanning Probe Microscopy*, 4 (2009) 94-99.

[183] J. Z. Huang, Y. Wang, Y. Lin, M. Li, and C. W. Nan, "Effect of Mn doping on electric and magnetic properties of $BiFeO_3$ thin films by chemical solution deposition", *J. Appl. Phys.* 106 (2009) 063911/1-063911/5.

[184] K. G. Yang, Y. L. Zhang, S. H. Yang, and B. Wang, "Structural, electrical, and magnetic properties of multiferroic Bi $La_xFeCo_yO_3$ thin films", *J. Appl. Phys.*, 107 (2010) 124109/1-124109/6.

[185] X. Wang, B. Yan, Z. Dai, M. Liu , S. Xu, W. Li, H. Liu, "Effect of annealing temperature on the ferroelectric properties of $BiFeO_3$ thin films prepared by sol-gel process", *J. Wuhan. Univ. Technol. Mat. Sci. Edit.*, 25 (2010) 384-387.

[186] K. Yin, M. Li, Y. Liu, C. He, F. Zhuge, B. Chen, W. Lu, X. Pan, and R-W. Li, "Resistance switching in polycrystalline $BiFeO_3$ thin films", *Appl. Phys. Lett.*, 97 (2010) 042101/1-042101/3.

[187] Q. Xu, Z. Wen, J. Gao, D. Wu, S. Tang, M. Xu, "The multiferroic properties of $Bi(Fe_{0.95}Co_{0.05})O_3$ films", *Physica B*, 406 (2011) 2025-2027.

[188] A. Lahmar, S. Habouti, C-H. Solterbeck, M. Dietze, and M. Es-Souni, "Multiferroic properties of $Bi_{0.9}Gd_{0.1}Fe_{0.9}Mn_{0.1}O_3$ thin film", *J. Appl. Phys.* 107 (2010) 024104/1-024104/8.

[189] X. Tang, J. Dai, X. Zhu, H. Lei, L. Yin, W. Song, Y. Cheng, D. Wu, and Y. Sun, "Magnetic field annealing effects on self-oriented $BiFeO_3$ thin films prepared by chemical solution deposition", *J. Magn. Magn. Mater.*, 322 (2010) 2647-2652.

[190] I. Coondoo, N. Panwar, A. Tomar, I. Bdikinc, and A. L. Kholkin, "Improved magnetic and piezoresponse behavior of cobalt substituted $BiFeO_3$ thin film", *Thin Solid Films* 520 (2012) 6493-6498.

[191] X. Xue, G. Tan, H. Hao, and H. Ren, "Comparative study on substitution effects in $BiFeO_3$ thin films fabricated on FTO substrates by chemical solution deposition", *Appl. Surf. Sci.*, 282 (2013) 432- 438.

[192] R. K. Kotnala, R. Gupta, and S. Chaudhary, "Giant magnetoelectric coupling interaction in $BaTiO_3/BiFeO_3/BaTiO_3$ trilayer multiferroic heterostructures", *Appl. Phys. Lett.*, 107 (2015) 082908/1-082908/5.

[193] H. M. Rietveld, "Line profiles of neutron powder-diffraction peaks for structure refinement", *Acta Cryst.*, 22 (1967) 151-152.

[194] H. M. Rietveld, "A profile refinement method for nuclear and magnetic structures", *J. Appl. Cryst.*, 2 (1969) 65-71.

[195] B.D. Cullity (1978) "Elements of X-ray diffraction" 2nd ed. Addison-Wesley series.

[196] R.Y. Young (1996) "The Rietveld Method 3rd ed." Oxford University Press.

[197] Operator's User Guide en01, ΣIGMA^{TM} Field Emission Scanning Electron Microscope, Instruction manual, May 2011@ by Carl Zeiss NTS Limited.

[198] G. Binnig, C. F. Quate, Ch. Gerber, "Atomic force microscope", *Phys. Rev. Lett.* 56(9) (1986) 930-933.

[199] V. L. Mironov, "Fundamentals of the scanning probe microscopy" The Russian Academy Of Sciences Institute of Physics of Microstructures, Nizhniy Novgorod, 2004.

[200] Scanning Probe Microscope Solver Next, Instruction Manual, 4th May 2010, Copyright @ NT-MDT, Zelenograd, Moscow, Russia.

[201] D. B. Williams and C. B Carter. "Transmission Electron microscopy (A Textbook for Materials Science)", Plenum Press, NewYork, (1996).

[202] A. Sahai and N. Goswami, "Structural and vibrational properties of ZnO nanoparticles synthesized by the chemical precipitation method", *Physica E.*, 58 (2014) 130-137.

[203] F. London, "Superfluids", New York: Wiley, 1950.

[204] B. D. Josephson, "Possible new effects in superconductive tunneling," *Phys. Lett.*, 1 (1962) 251-253.

[205] R. Kleiner, D. Koelle, F. Ludwig, and J. Clarke, "Superconducting Quantum Interference Devices: State of the Art and Applications", *Proceedings of the IEEE*, 92 (2004) 1534-1548.

[206] J. C. Russ, "Fundamentals of Energy Dispersive X-ray Analysis", Butterworths. London (1984).

[207] V. D. Scott, and G. Love, "Quantitative Electron Probe Microanalysis", 2nd edn. Ellis Horwood, Chichester (1994).

[208] M. K. Singh, W. Prellier, M. P. Singh, R. S. Katiyar, and J. F. Scott, "Spin glass transition in single crystal $BiFeO_3$", *Phys. Rev. B*, 77 (2008) 144403/1-144403/5.

[209] F. Bai, J. Wang, M. Wuttig, J. F. Li, N. Wang, A. P. Pyatakov, A. K. Zvezdin, L. E. Cross, and D. Viehland, "Destruction of spin cycloid in (111) c -oriented $BiFeO_3$ thin films by epitiaxial constraint: Enhanced polarization and release of latent magnetization", *Appl. Phys. Lett.*, 86 (2005) 032511/1-032511/3.

[210] M. K. Singh, R. S. Katiyar, W. Prellier and J. F. Scott, "The Almeida–Thouless line in $BiFeO_3$: is bismuth ferrite a mean field spin glass?", *J. of Phys.: Condens. Matter* 21 (2009) 042202/1-042202/5.

[211] a) J. T. Richardson, W. O. Milligan, *Phys. Rev.*, 102 (1956) 1289. b) J. T. Richardson, D. I. Yiagas, B. Turk, K. Forster and M. V. Twigg, "Origin of superparamagnetism in nickel oxide", *J. Appl. Phys.*, 70 (1991) 6977-6982.

[212] F. Huang, Z. Wang, X. Lu, J. Zhang, K. Min, W. Lin, R. Ti, T.T. Xu, J. He, C. Yue1 & J. Zhu, "Peculiar magnetism of $BiFeO_3$ nanoparticles with size approaching the period of the spiral spin structure", *Sci. Rep.*, 3 (2013) 2907/1-2907/7.

[213] A. Jaiswal, R. Das, K. Vivekanand, P. Abraham, S. Adyanthaya and P. Poddar, "Effect of reduced particle size on the magnetic properties of chemically synthesized $BiFeO_3$ nanocrystals", *J. of Phys. Chem. C*, 114 (2010) 2108-2115.

[214] A. Srivastava, A. Garg, and F.D. Morrison, "Impedance spectroscopy studies on polycrystalline $BiFeO_3$ thin films on Pt/Si substrates", *J. Appl. Phys.*, 105 (2009) 054103/1-054103/6.

[215] P. Suresh and S. Srinath, "Effect of Gd substitution on structure and magnetic properties of $BiFeO_3$", *IOP Conf. Series: Materials Science and Engineering* 73 (2015) 012082 doi:10.1088/1757-899X/73/1/012082.

Journal of Magnetism and Magnetic Materials 401 (2016) 180–187

Contents lists available at ScienceDirect

Journal of Magnetism and Magnetic Materials

journal homepage: www.elsevier.com/locate/jmmm

Magnetic behaviour of sol–gel driven $BiFeO_3$ thin films with different grain size distribution

Shiwani Sharma [a], P. Saravanan [b], O.P. Pandey [a], V.T.P. Vinod [c], Miroslav Černík [c], Puneet Sharma [a,*]

[a] School of Physics and Materials Science, Thapar University, Patiala 147004, Punjab, India
[b] Defence Metallurgical Research Laboratory, Hyderabad 500058, India
[c] Institute for Nanomaterials, Advanced Technologies and Innovation, Department of Natural Sciences, Technical University of Liberec, Studentská 1402/2, Liberec 1, 461 17, Czech Republic

ARTICLE INFO

Article history:
Received 4 June 2015
Received in revised form
3 September 2015
Accepted 9 October 2015

Keywords:
$BiFeO_3$
Sol–gel
Spin coating
Magnetic thin films
Spin glass behaviour

ABSTRACT

$BiFeO_3$ (BFO) thin films with uniform thickness of ~200 nm were prepared by the sol–gel assisted spin coating method. Different grain size distributions in the as-grown BFO films were then induced by varying the annealing temperature between 525 and 600 °C. It is found that the grain size distribution become wider as the annealing temperature increases. All the films showed a well-saturated magnetization (M) versus magnetic field (H) hysteresis loops at 300 K. A strong dependence of M on the grain size distribution is observed. An optimal grain size distribution with average grain size ~90 nm is responsible for high M in the BFO films. The non-saturated M–H loops obtained at 10 K suggest the spin glass behaviour of BFO films. The zero field cooled (ZFC) and field cooled (FC) magnetization curves shows split at 300 K and a cusp at ~50 K in the ZFC curve, which further confirms the spin glass state of polycrystalline BFO thin films.

1. Introduction

$BiFeO_3$ (BFO) is one of the most extensively studied multiferroic material due to the presence of magneto-electric coupling at room temperature (*RT*) [1,2]. BFO is known to have rhombohedrally distorted perovskite structure which belongs to the space group *R*3*c*. The unit cell of BFO can be represented as pseudo cubic (a_c = 3.963 Å); and hexagonal (a_h = 5.587 Å, c_h = 13.867 Å) structure, where pseudo cubic direction $[1\,1\,1]_c$ is equivalent to $[1\,0\,0]_h$ [3]. The magnetic structure of BFO has been studied by Kiselev et al., who suggested G-type antiferromagnetic spin configuration, wherein each Fe^{3+} ion is surrounded by six antiparallel nearest neighbours [4]. However, Sosnowska et al., interpreted the origin of magnetization in terms of magnetic cycloid structure with a long period of 62 ± 2 Å along the $[1\,1\,0]_h$ direction [5]. The net magnetic moment averaged to zero over the spin cycloid period length and cancels out the net magnetization. The latent magnetization in BFO films can be released through the suppression of spin cycloid structure. Wang et al., has epitaxially deposited the (1 0 0) BFO thin film and reported significantly high-strain induced magnetization (150 emu/cc) [6]. However, their results are contradictory with the other research groups; they suggested that the high magnetization is due to the presence of substantial Fe^{2+} fraction in the film. Other reported methodology to suppress the cycloid structure is low level substitution at Bi^{3+} site by rare earth metal ions [7–10]. The magnetization behaviour of BFO in the form of both nanocrystalline powders and thin films has been studied well. Park et al., showed a strong correlation between the particle size and magnetic properties of BFO nanoparticles [11]. Huang et al., also investigated the magnetization behaviour of BFO nanoparticles and reported higher magnetization values for the BFO nanoparticles having sizes close to the spin cycloid range [12]. In addition, the polycrystalline BFO thin films also exhibit magnetization due to uncompensated spins at the grain boundaries [13]. All the previous studies suggest that the grain size play an important role in the occurrence of magnetization in BFO. However, the currently available approaches to grow polycrystalline thin films or nanoparticles restricts the formation of uniform size, therefore the magnetization in BFO is cumulative sum of uncompensated surface moments originated from different grain-size distributions. Any induced variation in the particle or grain size distribution may lead to variation in the uncompensated surface spin density and magnetization. Up to now, effect of

* Corresponding author.
E-mail address: puneet.sharma@thapar.edu (P. Sharma).

http://dx.doi.org/10.1016/j.jmmm.2015.10.035
0304-8853/

thickness on the magnetic behaviour of BFO thin films has been intensively studied and apparently, inverse relationship between magnetization and film thickness was demonstrated by several researchers [14–16]. Considering the fact that any variation in the film thickness consequently imparts variation in grain size distribution; it is therefore necessary to investigate the effect of grain size distribution rather than the film thickness, to further reveal the complex magnetic behaviour of BFO thin films.

Accordingly, we herein report the effect of grain-size distribution on the magnetic behaviour of BFO thin films. Single-phase, polycrystalline BFO thin films of ~200 nm thickness was prepared by the sol–gel spin coating method. The BFO films with grain size distributions varying from 25 nm to 280 nm were thermodynamically imparted using appropriate annealing temperature. Through this study, we show that with an optimal grain-size distribution, significantly higher magnetization can be achieved in the BFO films. In addition, the existence of spin glass behaviour in the BFO films is demonstrated by means of zero field cooled (ZFC) and field cooled (FC) magnetization curves.

2. Experimental

BFO thin films with uniform thickness of ~200 nm were deposited via the sol–gel assisted spin coating method. In a typical synthesis, bismuth nitrate pentahydrate, $Bi(NO_3)_3 \cdot 5H_2O$ and iron nitrate nonahydrate, $Fe(NO_3)_3 \cdot 9H_2O$ were weighed in stoichiometric proportion and dissolved in 2-methoxyethanol and acetic acid. A 10% excess of bismuth nitrate was added to compensate the bismuth loss. The pH of the sol was maintained between 1 and 2 by adding glacial acetic acid. The sols were spin coated on indium tin oxide (ITO) coated glass substrate at 4000 rpm for 40 s using spin NXG-p1 spin coater. The precursor films thus obtained were baked at 300 °C for 5 min. Both spin coating and baking processes were repeated at least four times in order to produce films of desired thickness. The films were finally annealed for 1 hour in ambient atmosphere using muffle furnace between 525 and 600 °C and were cooled in air.

The phase analysis of the thin films were carried out by X-ray diffraction (XRD) using Cu-K_α radiation ($\lambda = 1.54178$ Å) (Philips X-pert PRO). The glancing incidence angle was taken 0.5° to remove the ITO peaks from the XRD patterns. Surface morphology of the films was studied by atomic force microscopy (AFM) model ND-MDT Solver Next. The surface and cross sectional FE-SEM (Carl Zeiss Model No. Ultra Plus-55) were carried out to reveal microstructure and thickness, respectively. Magnetic measurements at 300 and 10 K were carried out by superconducting quantum interference device (SQUID) magnetometer.

3. Results and discussion

Fig. 1 shows the XRD patterns of BFO thin films grown on ITO coated glass substrates and after being subjected to different annealing temperatures: 525, 550, 575 and 600 °C. All the XRD patterns were refined by the multiprofile Rietveld technique using FULLPROF program [17]. The peak profile refinement function used in the refinement was pseudo-Voigt function. All the major reflection peaks in the XRD pattern are indexed to perovskite BFO with space group: *R3c*. A minor impurity peak of γ-Fe_2O_3 is also evident in the XRD patterns, which corresponds to the characteristic (3 1 1) peak of bulk maghemite with space group of $P4_332$. Table 1 summarizes the refined parameters obtained for the BFO films. The diffraction profile fits very well, as indicated by the refined parameter values. The low value of χ^2 (goodness of fit) suggest the goodness of refinement.

As the annealing temperature increases, the full-width-half-maximum (FWHM) of (0 1 2) peak decreases, indicating better crystallization of BFO-phase in the films. The volume fraction of γ-Fe_2O_3 phase as obtained from the refinement is nearly constant (~0.08) in all the annealed samples. The magnified view of (0 1 2) peak (inset of Fig. 1) depicts a shift towards lower angle with increase in annealing temperature. This shift is due to the difference in thermal expansion coefficients of ITO and BFO, which is more pronounced at higher annealing temperatures.

In Fig. 2 we show the AFM micrographs of BFO films annealed at 525, 550, 575 and 600 °C with their respective height profiles. The root mean square roughness (R_q) of the films was measured over an area of $50 \times 50\ \mu m^2$ and the estimated R_q values tend to increase with annealing temperature. A maximum R_q value of < 30 nm was obtained for the film annealed at 600 °C, suggesting that the smooth surface of the films is retained, even at higher annealing temperature.

Fig. 3(a) depicts a representative cross-sectional FESEM image of BFO films deposited on ITO coated glass substrate. As can be seen that the interfaces between the ITO and BFO film is well defined without any inter diffusion. The measured thickness of BFO film is ~200 nm. No variation in the film thickness was

Table 1
Refined parameters for the BFO films annealed at different temperatures.

Annealing temperature (°C)			Lattice parameters (Å)		Atom coordinates			R_B	R_F	χ^2
			a	*c*	*x*	*y*	*z*			
525	Bi	6a	5.578	13.872	0	0	0.28177	5.86	4.04	2.54
	Fe	6a			0	0	0			
	O	18b			0.67091	0.83479	0.54093			
550	Bi	6a	5.58	13.876	0	0	0.28399	8.06	5.34	2.95
	Fe	6a			0	0	0			
	O	18b			0.67111	0.83479	0.52888			
575	Bi	6a	5.591	13.898	0	0	0.28717	7.69	5.06	2.44
	Fe	6a			0	0	0			
	O	18b			0.63864	0.82491	0.53198			
600	Bi	6a	5.586	13.89	0	0	0.28617	7.99	5.96	2.84
	Fe	6a			0	0	0			
	O	18b			0.62839	0.83479	0.5258			

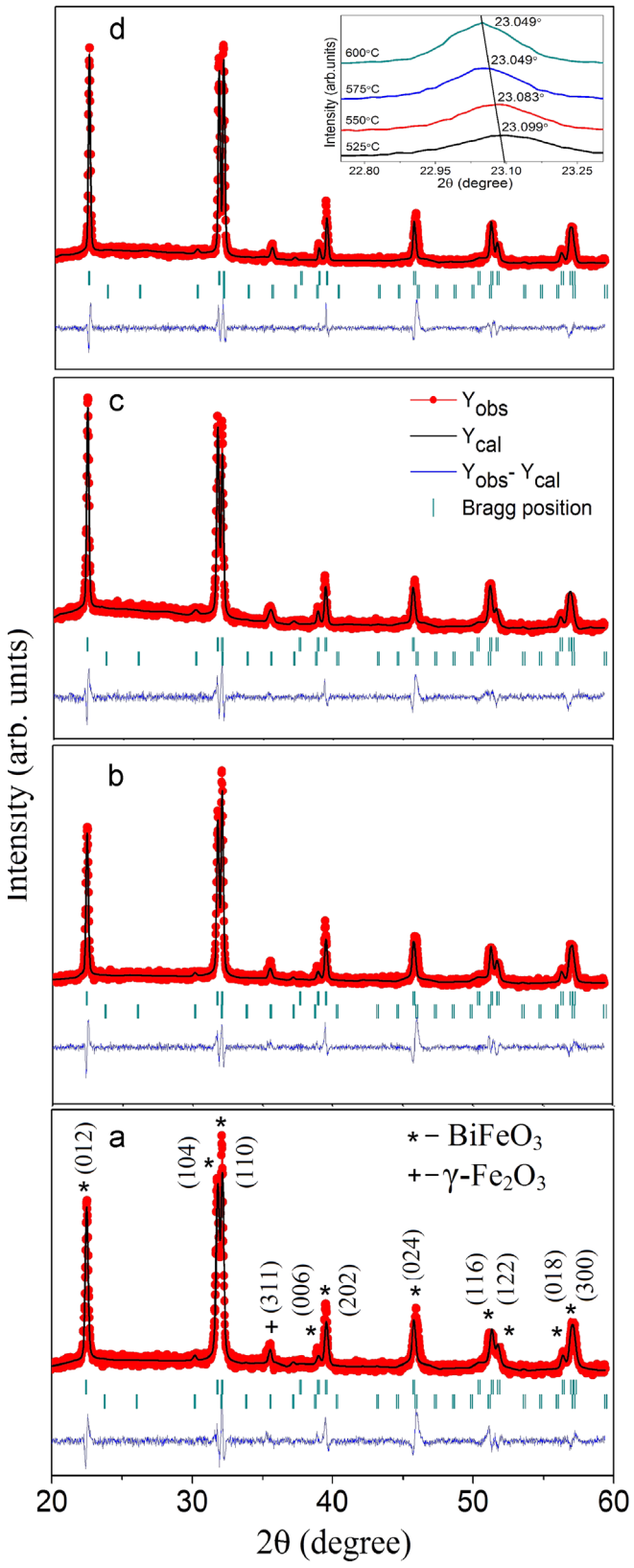

Fig. 1. Refined X-ray diffraction patterns of sol–gel driven BFO thin films after being subjected to different annealing temperatures: (a) 525, (b) 550, (c) 575 and (d) 600 °C. Solid red circle represents the observed pattern; continuous black line represents calculated pattern and the blue line represents difference between the observed and calculated patterns. Tick markers correspond to the position of the allowed Bragg reflections. The inset in (d) give the shift in (0 1 2) peak of BFO against annealing temperature.

observed with annealing temperature. Fig.3(b, c and d) show the FESEM surface morphology of the films annealed at 550, 575 and 600 °C, respectively. The microstructure of films reveals a well crystallized equiaxed BFO grains, separated by sharp grain boundaries. A little porosity is also observed in the films and the porosity fraction is below 0.01 in all the films, as calculated by areal analysis. It is evident from the micrographs that the grain-size is increasing with increase in annealing temperature and these observations are in agreement with the AFM analysis.

The estimated grain-size distribution values from the FESEM images are plotted as a function of annealing temperature and are shown in Fig. 4. The grain size values were measured using linear intercept method (ASTM E112) by considering a minimum number of 100 grains. The scale of x–y axis were kept constant for visual comparsion of grain size distribution. For the film annealed at 525 °C, majority of the grains lies in the size-distribution range of 25–105 nm and half of the grain fraction is below 65 nm. This size range remains the same on increasing annealing temperature to 550 °C; however, majority of the grain fraction is between 65–105 nm. With the further increase in annealing temperature (575 °C), the size range broadens and no grains with sizes below 45 nm are visible; whereas a significant fraction of grains below 45 nm is observed for the film annealed at 525 °C. Besides, coarser grains with sizes of >150 nm are also observed and their percentage increases from ~ 10 to 20% with increase in annealing temperature from 575 to 600 °C. The average grain size analysis shows a normal Gaussian fit with mean grain sizes of 56, 85, 93 and 105 nm for the films annealed at 525, 550, 575 and 600 °C, respectively (Fig. 4).

Fig. 5(a) and (b) show the in-plane *M–H* behaviour of BFO thin films obtained at 300 and 10 K, respectively. The *M–H* behaviour of the films at 300 K shows a well-saturated hysteresis loop suggesting the ferromagnetic nature of BFO thin films [18–22]. Inset 1 of Fig. 5 (a) represents the *M–H* behaviour of film without subtracting the diamagnetic contribution of glass substrate. The diamagnetic contribution was deducted by subtracting the slope of the linear portion of *M–H* loop at high magnetic field ($M/H = -\chi$). It is evident that the saturation magnetization (M_s) increases with annealing temperature up to 575 °C and then decreases for the film annealed at 600 °C (inset 2 of Fig. 5(a)). At 10 K, non-saturated *M–H* loops are observed (Fig. 5(b)), suggesting the spin glass behaviour of the films. The variation in magnetization at 4 T (inset of Fig. 5(b)) is similar to the films at 300 K. However, larger magnetization values are observed at 10 K. Fig. 5(c) shows the magnified view of *M–H* curves at 10 K. The variation of coercivity (H_c) and remanence (M_r) as a function of annealing temperature is shown in the inset. It is clear that both H_c and M_r values are increasing with temperature and found maximum for films annealed at 575 °C and then decreases. This shows that the grain size distribution of sample annealed at 575 °C provide maximum pinning to demagnetization of uncompensated moments.

The inherent magnetization in the film is mainly contributed by the uncompensated spins at grain boundaries and the presence of small fraction of magnetic γ-Fe_2O_3 phase. However, constant volume fraction of γ-Fe_2O_3 phase, as obtained from XRD refinement, excludes its contribution in magnetization variation of the films. Also the surface contribution of uncompensated moments is ignored as film with high surface roughness shows lower magnetization. Therefore, it is expected that the uncompensated moment present at the grain boundary is apparently different for different grain size distribution and this variation is responsible for the changes in magnetization values. Considering the fact that the integral multiple of the spin spiral length will constitute a compensated magnetic structure; grain sizes below or above the spiral length may provide uncompensated moments. Practically it is not feasible to obtain films with constant grain size; hence the presence of magnetization will be a cumulative effect of

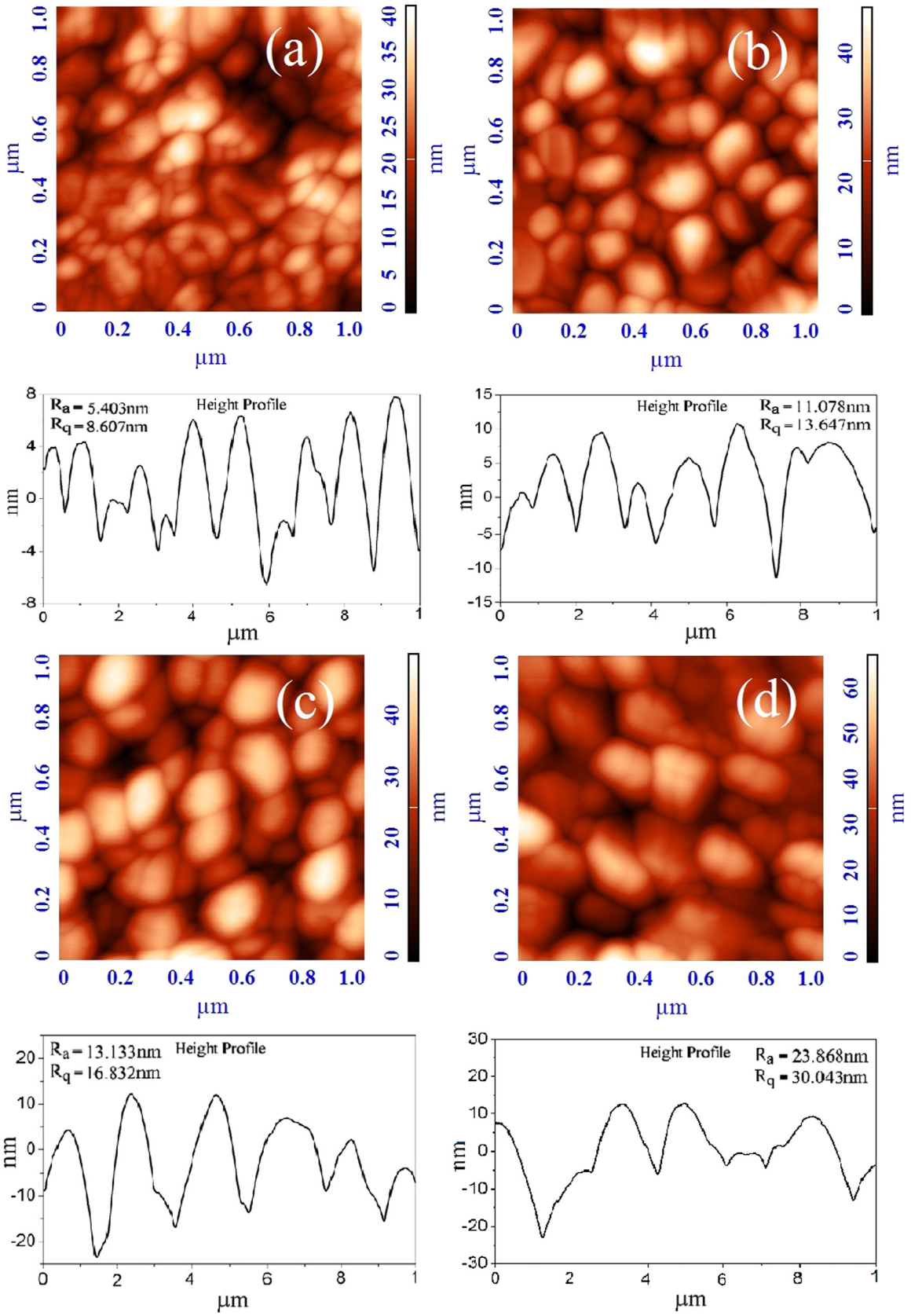

Fig. 2. AFM images of the BFO thin films annealed at (a) 525, (b) 550, (c) 575 and (d) 600 °C with their respective height profiles.

uncompensated moment present at the grain boundaries with different grain-size distribution. The above results are contradictory with the previously reported studies on nanopowders, wherein the magnetization increases with decrease in particle size [11–12,23]. In addition, the results of present study cannot be compared with the thickness dependent magnetic behaviour of BFO thin films, wherein the magnetization also found to decrease with thickness [14–16]. In this work, all the studied films are of uniform thickness (~200 nm) and the grain size effect is induced by varying annealing temperature, which lead to the changes in magnetization values. The obtained results thus suggest that the grain-size distribution plays an important role which lead to different surface spins to volume ratio [24]. In the present study, the highest magnetization (~12 emu/cm^3) at 300 K is observed for the films annealed at 575 °C. The average grain size of the BFO films annealed at 525 °C (~56 nm) is smaller than the film annealed at 575 °C (~93 nm), hence, the inverse relationship between size and magnetization may be ruled out in the present system [11]. Moreover, the BFO films annealed at 575 °C shows better crytallization, therefore an optimal grain size distribution and crystallization may be responsible for the enhanced magnetization in the sol–gel driven thin films.

Fig. 6 shows FC and ZFC magnetization curves of annealed BFO thin films, measured at an external field of 200 Oe in the temperature range of 10–300 K. The contribution of substrate was subtracted from the magnetization data. It can be noticed that the FC and ZFC curves are well bifurcated within the measured temperature range. The divergence between FC and ZFC increases progressively with decrease in temperature, which reveals the spin glass like behaviour [16]. As evident from the Fig. 6, the trends of FC–ZFC curves are almost similar for all the films, suggesting that the grain-size variation in the 200 nm thick BFO film has no effect on the temperature-dependent magnetization behaviour. A broad maxima and sharp minima around 25 K is visible in all the FC and ZFC curves of the BFO films. Magnetization (M) values for all the ZFC curves is increasing with decreasing temperature up to 60 K; whereas for all the FC curves, M increases up to 25 K. The initial gradual increase in M with decreasing temperature may be attributed to the local clustering of spins [22].

4. Conclusion

In summary, the effect of grain-size distribution induced by varying annealing temperature on the structural and magnetic properties of sol–gel driven BFO thin films was investigated. The grain-size distribution is found to broaden with increase in annealing temperature. The SQUID magnetic measurements demonstrated a weak ferromagnetic behaviour for the BFO films at 300 K as well as at 10 K, due to uncompensated spins generated by the breaking of spiral ordering. The observed magnetic properties in the BFO films depend entirely on the cumulative effect of uncompensated moments originating from the variation in grain-size distribution. An optimal grain-size distribution obtained at 575 °C

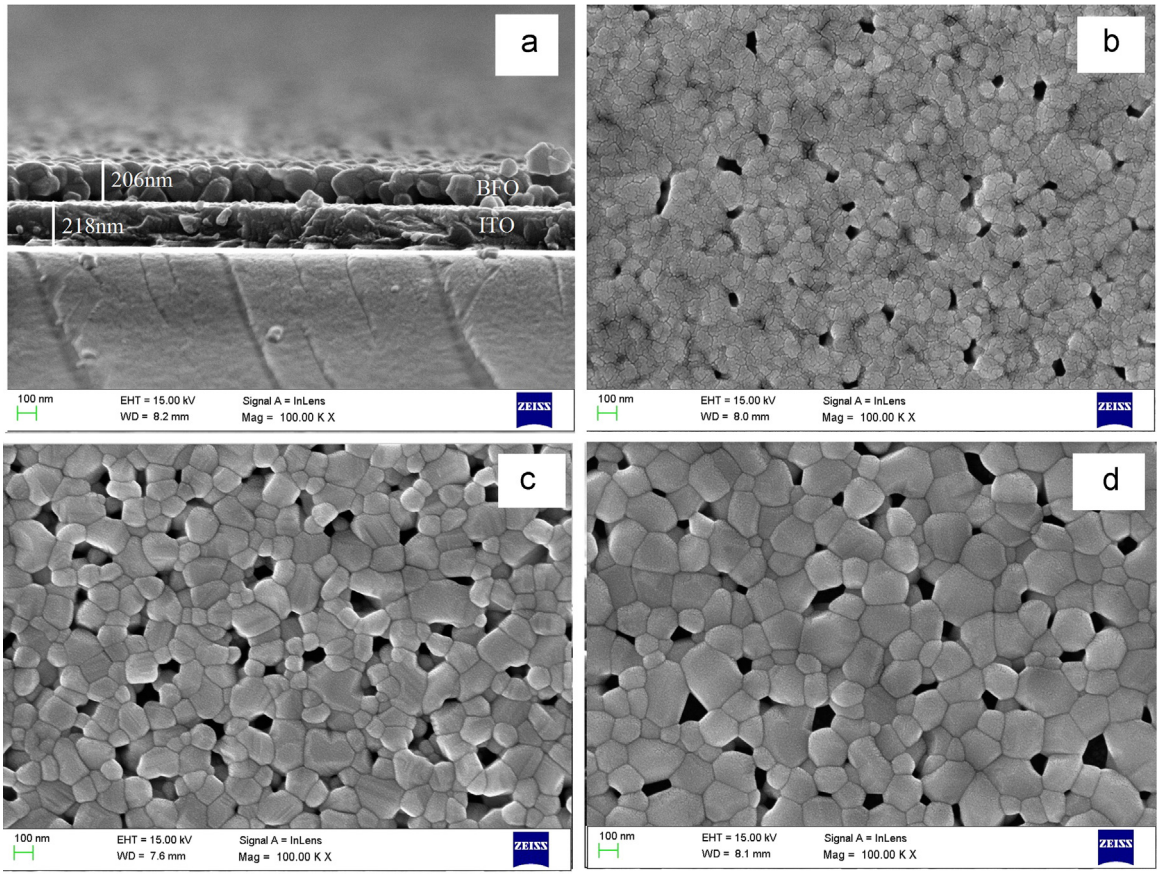

Fig. 3. FE-SEM micrographs of BFO thin films showing (a) cross-sectional image at 575 °C and (b), (c) and (d) surface morphology of films annealed at 550, 575 and 600 °C, respectively.

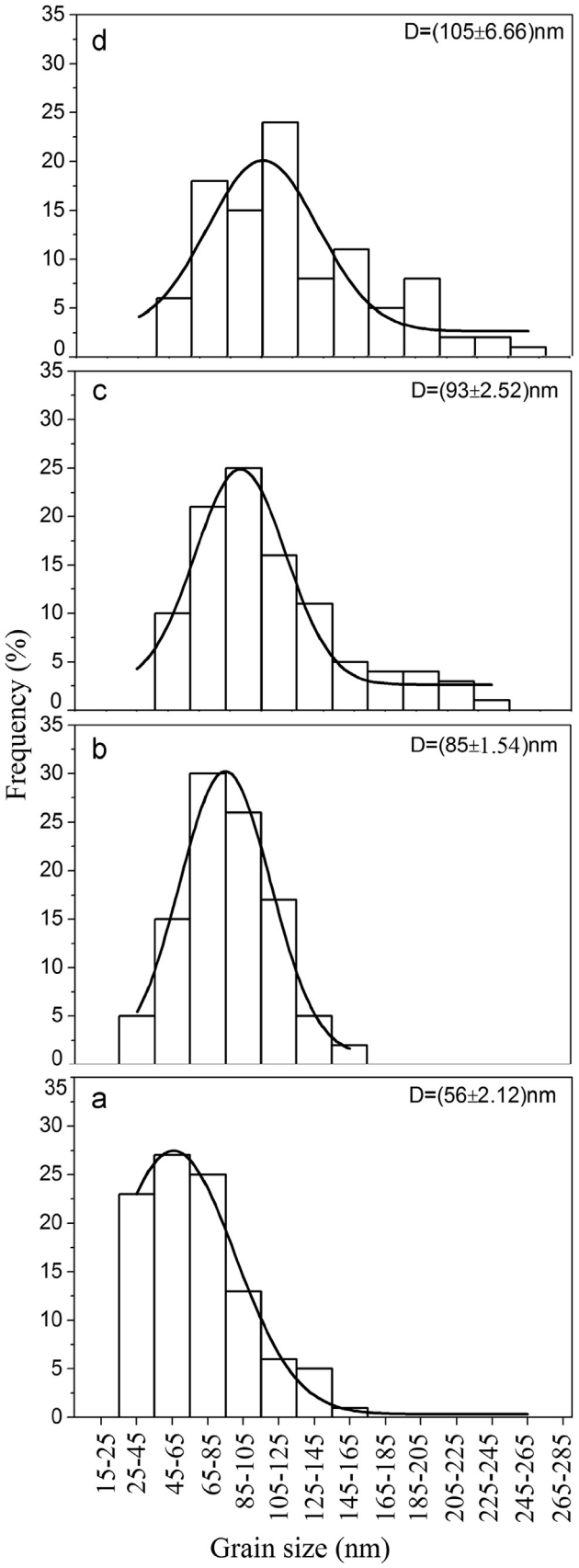

Fig. 4. Grain-size distributions in the BFO thin films annealed at (a) 525, (b) 550, (c) 575 and (d) 600 °C.

is responsible for the high magnetization in the BFO film. The FC–ZFC magnetization curves depict a rise in magnetization at lower temperature with an onset of spin glass state at ~300 K.

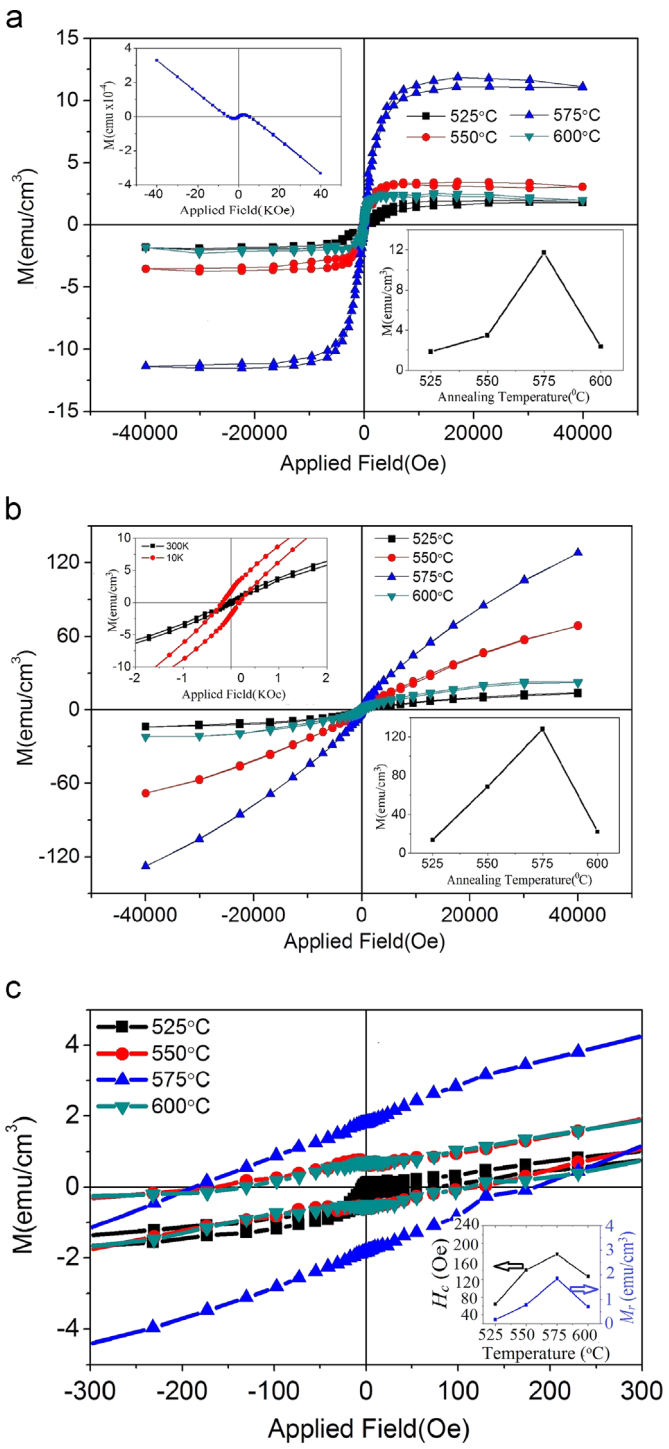

Fig. 5. *M–H* loops of BFO thin films obtained at (a) room temperature and (b) 10 K for the samples annealed at 525, 550, 575 and 600 °C. The inset in (a) shows the raw data of the film annealed at 575 °C and the variation in M_s with annealing temperature at 300 K. The inset in (b) shows the magnified view of the *M–H* loop at 300 and 10 K for the film annealed at 575 °C and the variation in M_s with annealing temperature at 10 K. (c) Magnified view of *M–H* loop at 10 K. The variation of H_c and M_r is shown in the inset.

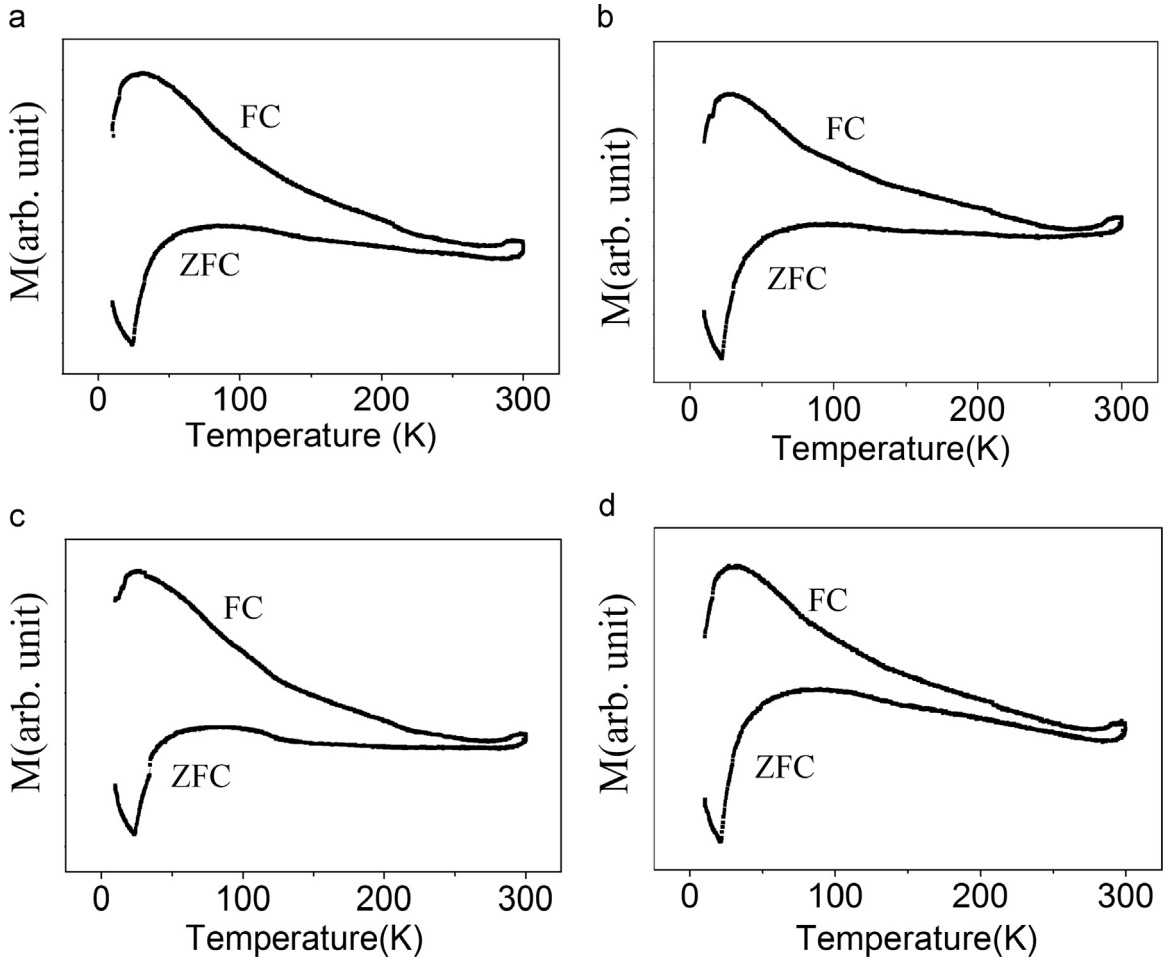

Fig. 6. FC and ZFC magnetization curves for the BFO thin films obtained at an applied magnetic field of 200 Oe for the samples annealed at (a) 525, (b) 550, (c) 575, and (d) 600 °C.

Acknowledgements

The author Shiwani Sharma gratefully acknowledge the University Grants Commission (UGC) for the fellowship (Letter no. SPMS/UGC/607). Author Puneet Sharma acknowledge funding granted by UGC 40-446/2011 (SR). The authors VTPV and MC acknowledge the funding granted by the project LO1201 under Ministry of Education, Youth and Sports in the framework of 'National Programme for Sustainability I', and the OPR&DI project, Centre for Nanomaterials, Advanced Technologies and Innovation, Technical University of Liberec CZ.1.05/2.1.00/01.0005.

References

[1] G. Catalan, J.F. Scott, Physics and application of bismuth ferrite, Adv. Mater. 21 (2009) 2463–2485.
[2] W. Eerenstein, N.D. Mathur, J.F. Scott, Multiferroic and magnetoelectric materials, Nature 442 (2006) 759–765.
[3] V.V. Lazenka, G. Zhang, J. Vanacken, I.I. Makoed, A.F. Ravinski, V. V. Moshchalkov, Structural trans-formation and magnetoelectric behavior in $Bi_{1-x}Gd_xFeO_3$ multiferroics, J. Phys. D: Appl. Phys. 45 (2012) 125002 7pp.
[4] S.V. Kiselev, R.P. Ozerov, G.S. Zhdanov, Detection of magnetic order in ferroelectric $BiFeO_3$ by neutron diffraction, Sov. Phys. Dokl. 7 (1963) 742–744.
[5] I. Sosnowska, T.P. Neumaier, E. Steichele, Spiral magnetic ordering in bismuth ferrite, J. Phys. C: Solid State Phys. 15 (1982) 4835–4846.
[6] J. Wang, J.B. Neaton, H. Zheng, V. Nagarajan, S.B. Ogale, B. Liu, D. Viehland, V. Vaithyanathan, D.G. Schlom, U.V. Waghmare, N.A. Spaldin, K.M. Rabe, M. Wutting, R. Ramesh, Epitaxial $BiFeO_3$ multiferroic thin film heterostructures, Sci 299 (2003) 1719–1722.
[7] V.R. Singh, A. Garg, D.C. Aggrawal, Structure and properties of lanthanum doped bismuth ferrite thin films, Solid State Commun. 149 (2009) 734–737.
[8] A. Lahmar, S. Habouti, C.-H. Solterbeck, M. Dietze, M. Es-Souni, Multiferroic properties of $Bi_{0.9}Gd_{0.1}Fe_{0.9}Mn_{0.1}O_3$ thin film, J. Appl. Phys. 107 (2010) 024104/1–024104/8.
[9] K.G. Yang, Y.L. Zhang, S.H. Yang, B. Wang, Structural, electrical, and magnetic properties of multiferroic $Bi_{1-x}LaxFe_{1-y}Co_yO_3$ thin films, J. Appl. Phys. 107 (2010) 124109/1–12409/6.
[10] V.A. Khomchenko, V.V. Shvartsman, P. Borisov, W. Kleemann, D.A. Kiselev, I. K. Bdikin, J.M. Vieira, A.L. Kholkin, Effect of Gd substitution on the crystal structure and multiferroic properties of $BiFeO_3$, Acta Mater. 57 (2009) 5137–5145.
[11] T. Park, G.C. Papaefthymiou, A.J. Viescas, A.R. Moodenbaugh, S.S. Wong, Size dependent magnetic properties of single crystalline multiferroic $BiFeO_3$ nanoparticles, Nano Lett. 7 (2007) 766–772.
[12] F. Huang, Z. Wang, X. Lu, J. Zhang, K. Min, W. Lin, R. Ti, T.T. Xu, J. He, C. Yue1, J. Zhu, Peculiar magnetism of $BiFeO_3$ nanoparticles with size approaching the period of the spiral spin structure, Sci. Rep. 3 (2013) 2907/1–2907/7.
[13] Y. Wang, Q.H. Jiang, H.C. He, C.W. Nan, Multiferroic $BiFeO_3$ thin films prepared via a simple sol–gel method, Appl. Phys. Lett. 88 (2006) 142503/1–142503/3.
[14] D.S. Rana, K. Takahashi, K.R. Mavani, I. Kawayama, H. Murakami, M. Tonouchi, Thickness dependence of the structure and magnetization of $BiFeO_3$ thin films on $(LaAlO_3)_{0.3}(Sr_2AlTaO_6)_{0.7}$ (001) substrate, Phys. Rev. B 75 (2007) (060405 (R)/1–060405/4).
[15] Y. Wang, Y. Lin, C.W. Nan, Thickness dependent size effect of $BiFeO_3$ films grown on $LaNiO_3$-buffered Si substrates, J. Appl. Phys. 104 (2008) 123912/1–123912/4.
[16] C.J. Cheng, C. Lu, Z. Chen, L. You, L. Chen, J. Wang, T. Wu, Thickness-dependent magnetism and spin-glass behaviors in compressively strained $BiFeO_3$ thin films, Appl. Phys. Lett. 98 (2011) 242502/1–242502/3.
[17] H.M. Rietveld, Line profiles of neutron powder-diffraction peaks for structure refinement, Acta Crystallogr. 22 (1967) 151–152.
[18] M.K. Singh, W. Prellier, M.P. Singh, R.S. Katiyar, J.F. Scott, Spin glass transition in single crystal $BiFeO_3$, Phys. Rev. B **77** (2008) 144403/1–144403/5.
[19] F. Bai, J. Wang, M. Wuttig, J.F. Li, N. Wang, A.P. Pyatakov, A.K. Zvezdin, L.

E. Cross, D. Viehland, Destruction of spin cycloid in (111) *c*-oriented $BiFeO_3$ thin films by epitiaxial constraint: Enhanced polarization and release of latent magnetization, Appl. Phys. Lett. 86 (2005) 032511/1–032511/3.
[20] G. Catalan, J.F. Scott, Physics and application of bismuth ferrite, Adv. Mater. 21 (2009) 2463–2485.
[21] D. Lebeugle, D. Colson, A. Forget, M. Viret, P. Bonville, J.F. Marucco, S. Fusil, Room-temperature coexistence of large electric polarization and magnetic order in $BiFeO_3$ single crystals, Phys. Rev. B 76 (2007) 024116/1–024116/8.
[22] M.K. Singh, R.S. Katiyar, W. Prellier, J.F. Scott, The Almeida–Thouless line in $BiFeO_3$: is bismuth ferrite a mean field spin glass? J. Phys.: Condens. Matter 21 (2009) 042202 (5 pp.).
[23] A. Jaiswal, R. Das, K. Vivekanand, P. Abraham, S. Adyanthaya, P. Poddar, Effect of reduced particle size on the magnetic properties of chemically synthesized $BiFeO_3$ nanocrystals, J. Phys. Chem. C 114 (2010) 2108–2115.
[24] J.T. Richardson, D.I. Yiagas, B. Turk, K. Forster, M.V. Twigg, Origin of superparamagnetism in nickel oxide, J. Appl. Phys. 70 (1991) 6977–6982.

J Mater Sci: Mater Electron (2016) 27:5909–5915
DOI 10.1007/s10854-016-4509-2

Grain size distribution dependent magnetic and ferroelectric properties in sol–gel driven $BiFeO_3$ thin films

Shiwani Sharma[1] · P. Saravanan[2] · O. P. Pandey[1] · Puneet Sharma[1]

Received: 11 November 2015 / Accepted: 9 February 2016 / Published online: 16 February 2016

Abstract The effect of thickness induced grain size distribution on the magnetic and ferroelectric behaviour of sol–gel driven $BiFeO_3$ (BFO) thin films was investigated in this study. FESEM micrographs showed well-crystallized equiaxed grains with minimal porosity. The magnetization (M) versus magnetic field (H) indicated the well saturated hysteresis loops at 300 K. The saturation magnetization (M_s) is found to decrease from 18.9 to 0.93 emu/cm^3 on increasing the film thickness from 156 to 388 nm. The high M_s value obtained in the BFO films due to the uncompensated spins originated at grain boundary tends to decrease with the film thickness. At low temperature (10 K), non-saturated M–H loops are observed due to spin freezing effect. The dielectric and ferroelectric properties improve with better growth and densification of grains in the BFO thin films with increasing thickness.

1 Introduction

Multiferroics has attracted attention of researchers worldwide due to its fundamental and technological applications [1]. Amongst various multiferroics, $BiFeO_3$ (BFO) is the only known material to possess ferroelectric Curie temperature $T_C = 1143$ K and antiferromagnetic Neel temperature $T_N = 643$ K well above the room temperature (RT). BFO crystallizes in a rhombohedrally distorted perovskite structure with *R3c* space group at RT. This is analogous to the hexagonal structure with six formula units of BFO having lattice constants $a_h = 5.587$ Å, $c_h = 13.867$ Å [2, 3]. The antiferromagnetic ordering of BFO is G-type having a spiral spin modulation with an incommensurate long-wavelength period of $\sim$620 Å [4]. Due to its antiferromagnetic nature; bulk BFO shows ineffectual magnetism that limits its application in magnetoelectric devices [2, 3]. Besides, the low resistivity and large leakage current—a characteristic of bulk BFO affects its ferroelectric properties [1, 5]. To overcome these limitations, attention has been diverted towards synthesis of BFO in the form of thin films. Till date, a variety techniques have been used to optimize the preparation conditions to develop quality BFO thin films [5–8]. The magnetic and ferroelectric properties in BFO are reportedly improved by adopting different methodology. Recently, a significant magnetization (M) of $\sim$150 emu/cm^3 and a greatly enhanced remanent polarization (P_r) of $\sim$55 μC/cm^2 with a strong magnetoelectric coupling was evidenced in the epitaxially grown BFO thin films [5]. The emergence of such high M was found to be contradictory with the other research groups stating that it could have aroused as a result of substantial Fe^{2+} fraction in the films [8].

Low level doping of rare earth metal ions at Bi^{3+} sites or by transition metal ions at Fe^{3+} sites is an appropriate means for enhancing the magneto-electric properties [9–12]. Besides, tuning the grain size by varying annealing temperature or the film thickness could be an alternative strategy for achieving enhanced magnetic and electrical properties, as the grain size variation can suppress the cycloidal spin structure. Along these lines, several investigations showing the thickness dependence of magnetic,

✉ Puneet Sharma
puneet.sharma@thapar.edu

[1] School of Physics and Materials Science, Thapar University, Patiala, Punjab 147004, India

[2] Defence Metallurgical Research Laboratory, Hyderabad 500058, India

dielectric and ferroelectric properties due to strain effect have been reported in literature [13–15]. For example Rana et al. [13] reported the strain effect on magnetization and structure with thickness. Significantly large M_s was also observed in epitaxially grown BFO thin films, which further decreases from 19.3 to 5.3 emu/cm^3 on increasing the film thickness from 40 to 115 nm [14]. Similarly, the effect of thickness on the magneto-electric properties was studied and the results were explained entirely on the basis of grain size and shape [16–18]. Huang et al. [16] reported a significant fall in M_s from 33 to around 4 emu/cm^3 as the film thickness increases from 35 to 230 nm. Tang et al. [17] reported improved crystallization, enhanced dielectric constant, reduced leakage current, and a decrease in M_s with increase in thickness from 210 to 830 nm. Hussain et al. [18] showed fully developed ferroelectric hysteresis loops for thicker films (t > 200 nm) and a rise in M_s from 2.32 to 26 emu/cm^3 with thickness decreasing from 480 to 40 nm due to suppression of spiral spin cycloid. The above studies indicate that the tailoring of film thickness modulates the spin cycloid of BFO and thereby, promotes the magnetic properties (with respect to its bulk counterpart) and brings a noticeable difference in the electrical properties due to better grain growth. Nevertheless, films with uniform thickness does not account for uniform grain sizes. A study on the thickness induced grain size distribution would therefore provide a better understanding on the structure-magnetic-ferroelectric property correlations in the BFO thin films. Accordingly, in the present work, a special emphasis is laid on the effect of thickness induced grain size distribution on the magnetic and electrical behaviour of polycrystalline BFO thin films. Thin films with variable thickness (156–388 nm) were prepared by sol–gel spin coating method. The effect of thickness induced grain size distribution on the structural, magnetic and electric properties were systematically investigated.

2 Experimental

BFO thin films with varying thickness were deposited on ITO coated glass substrate by sol–gel spin coating method. Bismuth nitrate pentahydrate $Bi(NO_3)_3{\cdot}5H_2O$ and iron nitrate nanohydrate $Fe(NO_3)_3{\cdot}9H_2O$ were weighed in stoichiometric proportion with the molar ratio of 1.10:1 (10 % excess of Bi was added to compensate the Bi loss). The starting precursor salts were dissolved initially at RT in 2-methoxyethanol and acetic acid on a magnetic stirrer for 2 h and then heated at constant temperature of 50 °C, until a clear reddish brown transparent sol of desired concentration was obtained. The sol was spin coated on the ITO substrate at 4000 rpm for 40 s using the spin NXG–p1 spin coater. The as-deposited films were pre-annealed at 300 °C for 5 min. The spin coating and pyrolysis cycle were repeated for 2, 4, 6 and 8 times in order to produce films of different thicknesses. The BFO films were finally annealed in ambient atmosphere using muffle furnace at 575 °C for 1 h and were allowed to cool in air.

The phase composition of the BFO thin films was carried out by X-ray diffraction (XRD) using Cu-Kα radiation (λ = 1.54178 Å) (Philips X-pert PRO); while the surface morphology and microstructure were analyzed by atomic force microscopy (AFM) Model ND-MDT Solver Next and

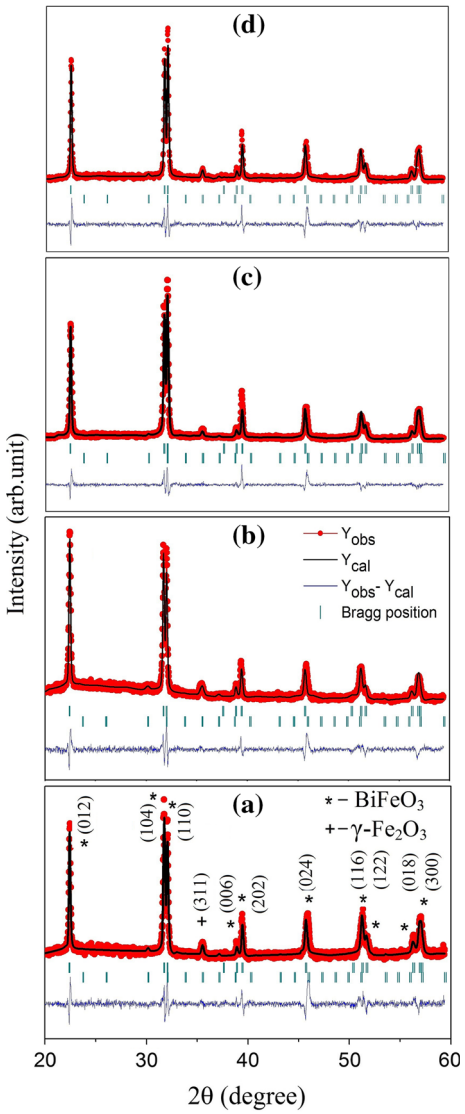

Fig. 1 Refined X-ray diffraction patterns of BFO thin films obtained at different thicknesses: **a** 156, **b** 206, **c** 270 and **d** 388 nm. *Solid red circle* represents the observed pattern; continuous *black line* represents the calculated pattern and the *blue line* represents difference between the observed and the calculated patterns. Ticks markers correspond to the position of the allowed Bragg reflections (Color figure online)

FE-SEM (Carl Zeiss Model No. Ultra Plus-55). Magnetization *(M)* versus magnetic field *(H)* curves were measured by a superconducting quantum interference device (SQUID) at 300 and 10 K. Electrical characterization was performed using RT66A ferroelectric tester (Radiant technologies).

3 Results and discussion

Figure 1 shows the of the XRD pattern of BFO thin films with different thicknesses. All the XRD patterns were refined by multiprofile Rietveld system using FULLPROF program [19]. Minor impurity peak corresponding to the characteristic (311) peak of γ-Fe_2O_3 (maghemite) with space group $P4_{-3}32$, is also evident. The refinement was done with *R3c*space group in the hexagonal lattice as phase I and $P4_332$ space group as phase II. The volume fraction of γ-Fe_2O_3 was found to be similar in all the films as obtained from Rietveld refinement.

Figure 2 represents both cross-sectional (a, c) and surface morphology (b, d) of the 156 and 388-nm thick BFO films. It is evident from the micrographs that the BFO/ITO/glass interfaces are well defined and distinguishable with BFO layer thicknesses of 156 and 388 nm. The microstructure of the 156 and 388 nm films (Fig. 2b, d) reveals the presence of crystallized equiaxed grains separated by sharp grain boundaries with minimal porosity. It is clear from the micrographs that the grain size is increased with increase of thickness. The grain size distribution as shown in Fig. 3, was obtained from the FESEM micrographs using linear intercept method (ASTM E112) considering a minimum number of 100 grains. The scale along the x–y axis is kept constant for visual comparison of grain size distribution. Average grain size analysis shows a normal Gaussian fit with mean grain sizes of 82, 93, 135 and 219 nm for 156, 206, 277 and 388 nm thick BFO films, respectively. It is evident from Fig. 3 that 20 % population of grains having size less than 65 nm for the 156-nm thick BFO film. As the thickness of the film increases, the grain-size distribution broadens; for the 388-nm thick BFO film, grain size distribution ranging from 65 to 365 nm is observed. Though, the grain size increases with thickness; the possibility of % of grains with sizes less than the integral multiple of spin cycloid period cannot be ruled out.

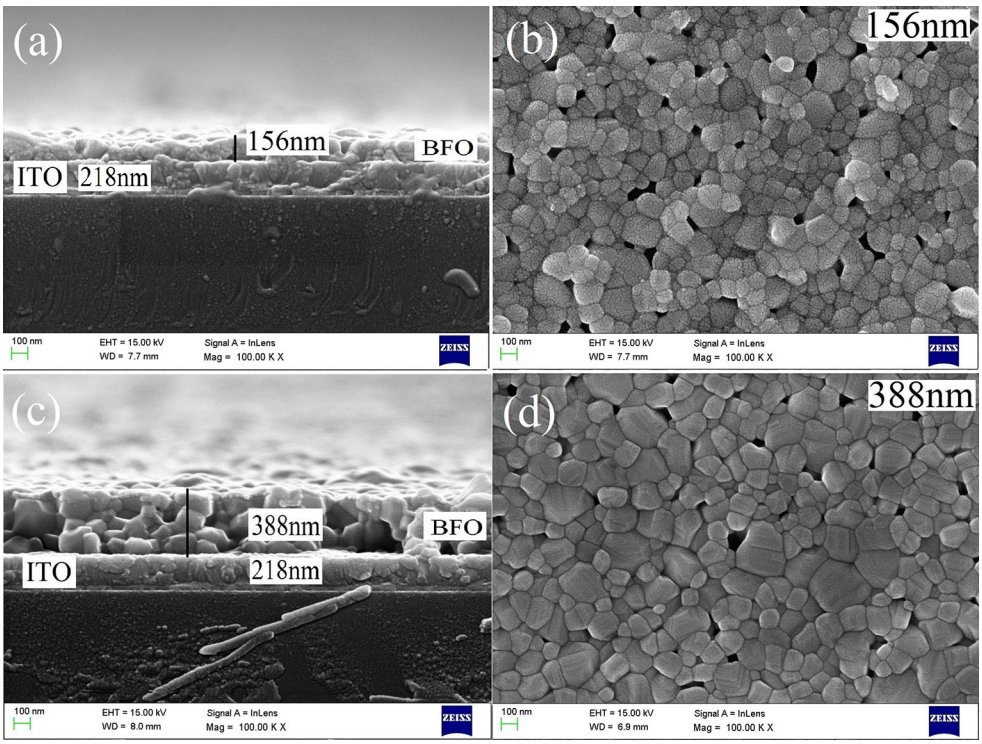

Fig. 2 FESEM micrographs of BFO films. **a**, **c** cross-sectional and **b**, **d** surface morphologies of the BFO films with thicknesses 156 and 388 nm, respectively

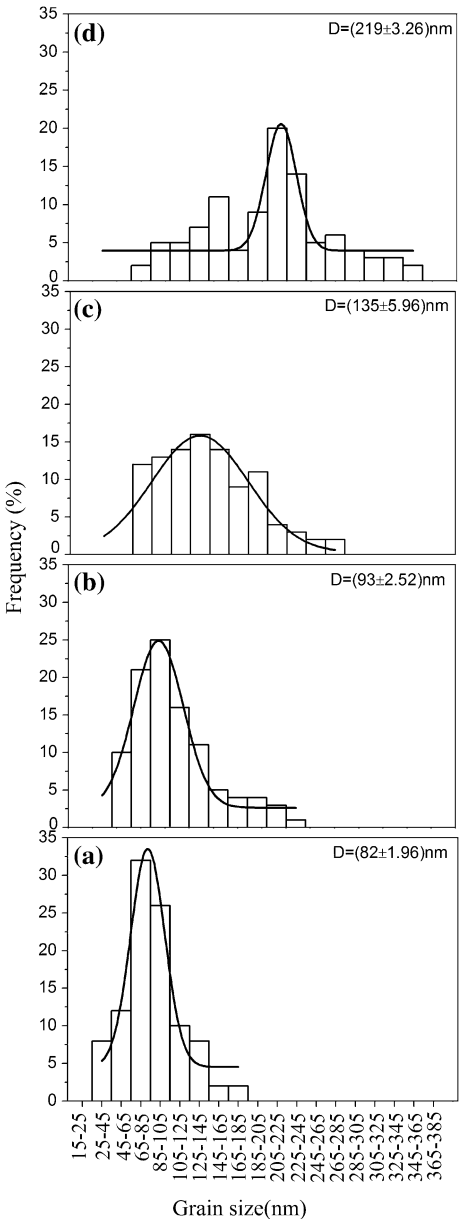

Fig. 3 The estimated grain size distributions in BFO thin films with different thickness: **a** 156, **b** 206, **c** 270 and **d** 388 nm

Figure 4 shows the two dimentional AFM micrographs of (1 × 1) μm^2 area of BFO films with varying thicknesses after being subjected to annealing at 575 °C. The AFM surface topography presents a smooth, uniform, continuous and densemorphology with minimal porosity, which is in agreement with the FESEM micrographs. The AFM micrographs apparently reveal an obvious increase in the grain size against the film thickness. Although the average grain size tends to increase with the thickness, a wide distribution in the grain size is clearly evident in the AFM images.

The thickness dependent *M–H* loops of BFO thin films measured at 300 and 10 K are shown in Fig. 5. At 300 K, a highly saturated *M–H* loop can be observed for all the BFO films and the estimated M_s values are found to decrease with the films thickness. A maximum M_s of $\sim$18.99 emu/cm^3 while a minimum of 0.93 emu/cm^3 were obtained for the 156 and 388-nm thick BFO films, respectively. As is visible from the FESEM micrographs (Fig. 2) and grain size distribution (Fig. 3), the grain size is not uniform for a particular film thickness; but it varies over a wide distribution range. The observed magnetization trend arises from the grain size distribution, where the relative proportion of the uncompensated spins at the grain boundaries becomes larger with decreasing film thickness. The grain size distribution for 156 and 206 nm thick films gives higher magnetization values. The fact that the integral multiple of the spin spiral constitute a compensated magnetic structure; the grain sizes below or above the spiral length may provide uncompensated moments at grain boundaries. Therefore, every individual grain is expected to exhibit two magnetic components i.e. antiferromagnetic (AFM) component within the grain as a core and a ferromagnetic (FM) component at the grain surface and the relative contribution of each component is dependent on the grain size. The uncompensated spin density at the grain surface will be higher for smaller grains as evident from the inset 2 of Fig. 5a that the magnetization increases with decrease in average grain size. Hence, the BFO grains can be modelled by a superposition of AFM-core and FM-surface and their magnetization is mainly contributed by the uncompensated spins at the grain surface [20–22]. The contribution to magnetization due to substantial amount of magnetic γ-Fe_2O_3 can be ruled out, as its fraction (0.08) is almost same in all the films as evident from the Rietveld refinement of the XRD patterns. At lower temperature (10 K), the *M–H* loops are non-saturated due to spin freezing at low temperature [23, 24]. The inset 1 in Fig. 5b shows an enlarged view of the *M–H* loops for the 206-nm thick BFO film at 300 and 10 K, indicating an increase in H_c at 10 K. Also shown in the inset 2 of Fig. 5b is an enlarged view of the hysteresis for all the films of varying thickness at 10 K.

Figure 6 shows the RT dielectric measurements in the frequency range of 100 Hz–1 MHz. At low frequencies, the dielectric constant (ε') increases and dielectric loss (tanδ) decreases with increasing thickness. The ε' at 100 Hz increases from 71 to 435 for 156 and 388 nm thick BFO films, respectively. The porosity decreases while the

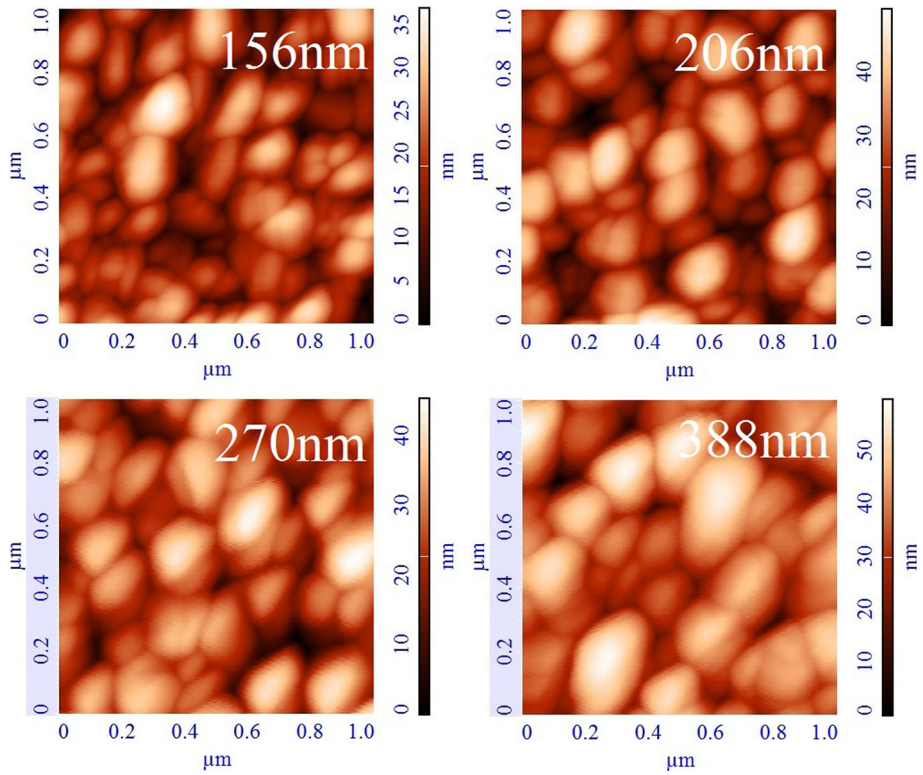

Fig. 4 AFM surface topography of the BFO thin films with varying thicknesses

density of the film increases with increase in film thickness (Figs. 2, 4). Therefore, increase in ε' and decrease in tanδ is observed with thickness because of reduction in the voids between the grains or the local defects, improved crystallization, densification and growth of grains [17]. There are different types of polarizations that contribute in enhancing the ε' at lower frequencies but lag to follow the field reversal at higher frequencies. Upon increasing the thickness, all the films presents a similar trend, i.e. increasing ε' and decreasing tanδ against frequency governing the cumulative effect of grains comprising the film. A sharp decrease in ε' with increasing frequency and decreasing film thickness is evident by the shifting of falling slope of ε' towards left in Fig. 6a. However, in the high frequency region, ε' gradually decreases and becomes almost constant for all the films of variable thickness. In Fig. 6b, we show the dielectric loss (tanδ) variation with frequency. A sudden decrease in tanδ up to 10 kHz is observed for all the films, which tends to become fairly constant in the high frequency region. The tanδ decreases with increasing film thickness from 11.2 for 156 nm BFO thick film to 5.8 for 388 nm thick BFO film at 100 Hz and 0.305 for 156 nm BFO thick film to 0.097 for 388 nm thick BFO film at 1 MHz. As evident from Fig. 3, the grain size distribution broadens with increasing thickness giving more fraction of bigger size grains due to which the pinning of domain walls gets restricted, causing a significant decrease in tanδ [17]. Though, the contribution from smaller size grains cannot be ignored, which may lead to somewhat higher value of tanδ in contradiction with the previously reported values [11, 17].

Figure 7 shows the RT ferroelectric hysteresis (PE) loops for the BFO films of varying thickness up to a frequency of 10 kHz. All the BFO films seem to be highly resistive, as they withstand an applied electric field of 600 kV/cm without undergoing any breakdown. The hysteresis loop for 156 nm thick BFO film is non-saturated. The thickness effect on polarization is clearly visible with increase in polarization and loops gaining saturation on increasing thickness from 156 to 388 nm [14, 17, 25]. An

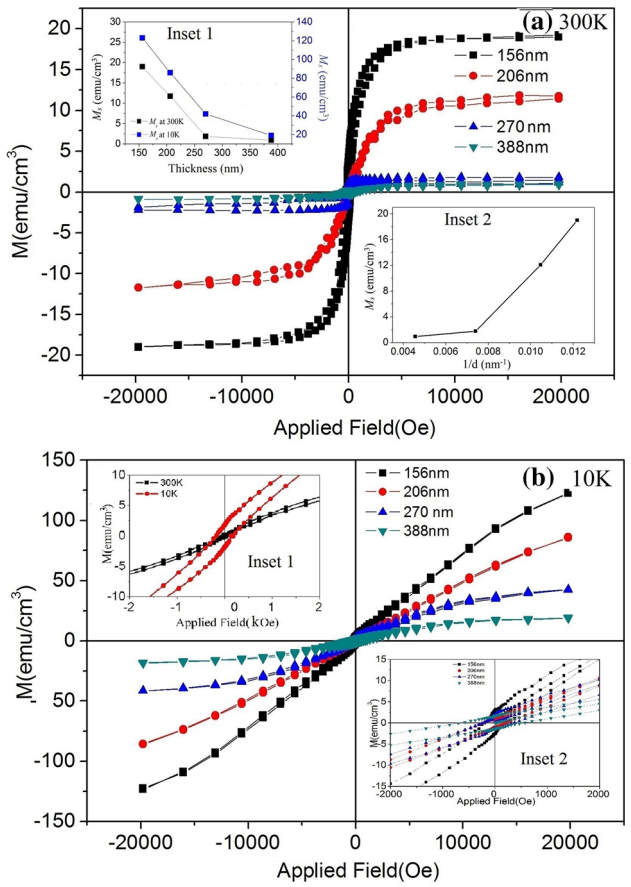

Fig. 5 Magnetic hysteresis loop of BFO thin films at RT (above) and at 10 K (below). The *insets 1* and *2* of figure **a** show the M_s variation with thickness at 300 and 10 K; and the variation in M_s (at 300 K) with 1/d (d-grain size), respectively. The *insets 1* and *2* of figure **b** show the enlarged view of the magnetic hysteresis loop of BFO thin films at 300 and 10 K for the 206 nm thick film and the hysteresis loop at 10 K, respectively

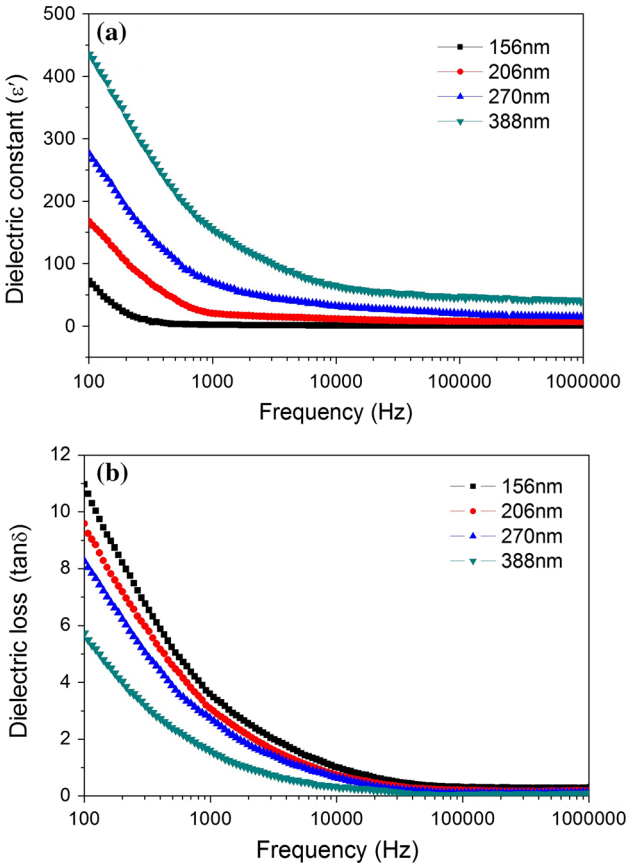

Fig. 6 Room temperature frequency dependent **a** dielectric constant and **b** dielectric loss curves for the BFO thin films at different thicknesses

increase in coercivity has been observed with increasing film thickness which is probably due to the presence of smaller size grains as is visible in the grain size distribution curves of Fig. 3 that makes polarization switching more difficult. The remnant polarization (P_r) increases from 0.0178 to 1.63 μC/cm^2 with thickness of BFO films. The observed increase in the ferroelectric properties is due to the better growth and densification of the films with increasing thickness.

4 Conclusion

The effect of thickness induced grain size distribution on the magnetic and ferroelectric behaviour of the BFO thin films was studied. The FESEM and AFM micrographs clearly indicated well crystallized grains with wide distribution. The observed trends in *M–H* curves indicated the strong dependence of magnetization on the grain size distribution. The occurrence of ferromagnetic behaviour at 300 K as well as at 10 K is due to the uncompensated spins at grain boundaries generated by the breaking of spiral ordering. At 10 K, the *M–H* loops are unsaturated due to spin freezing. The ferroelectric properties found to be

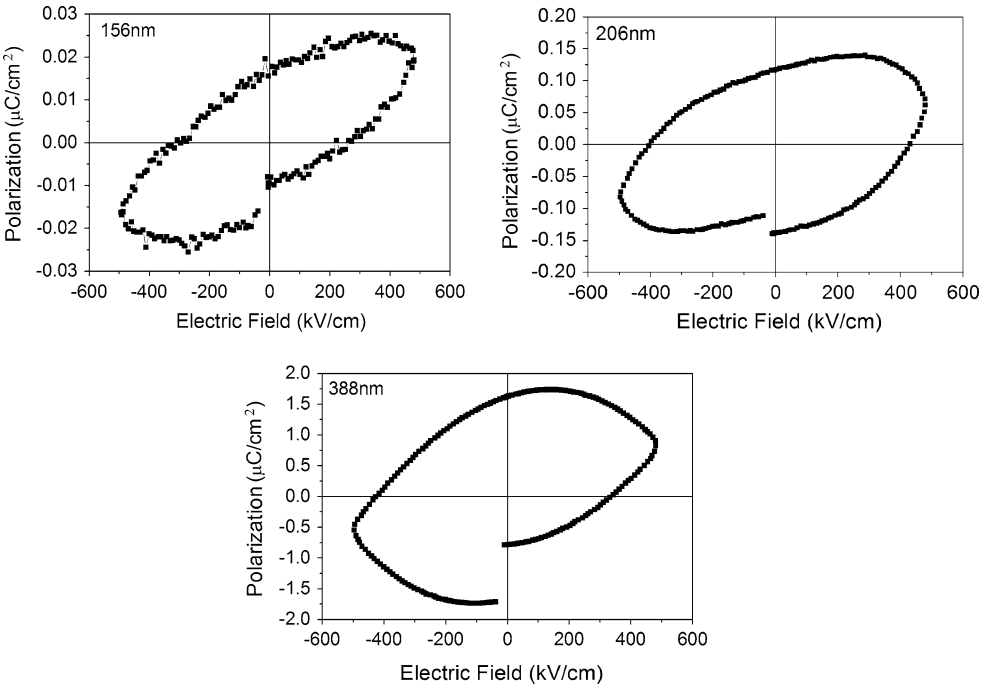

Fig. 7 Room temperature ferroelectric hysteresis loops of 156, 206 and 388 nm thick BFO films at a frequency of 10 kHz

improved due to better growth and densification with increasing film thickness. Appreciable increase in dielectric constant (ε') and corresponding decrease in dielectric loss (tanδ) against increase in BFO film thickness is observed.

Acknowledgments The author Shiwani Sharma gratefully acknowledge the University Grants Commission (UGC) for the fellowship (letter no. - SPMS/UGC/607). Author Puneet Sharma acknowledges funding granted by UGC 40-446/2011 (SR).

References

1. N.A. Hill, J. Phys. Chem. B **104**, 6694 (2000)
2. J.M. Moreau, C. Michel, R. Gerson, W.J. James, J. Phys. Chem. Solids **32**, 1315 (1971)
3. V.V. Lazenka, G. Zhang, J. Vanacken, I.I. Makoed, A.F. Ravinski, V.V. Moshchalkov, J. Phys. D Appl. Phys. **45**, 125002 (2012)
4. I. Sosnowska, T.P. Neumaier, E. Steichele, J. Phys. C Solid State Phys. **15**, 4835 (1982)
5. J. Wang, J.B. Neaton, H. Zheng, V. Nagarajan, S.B. Ogale, B. Liu, D. Viehland, V. Vaithyanathan, D.G. Schlom, U.V. Waghmare, N.A. Spaldin, K.M. Rabe, M. Wutting, R. Ramesh, Science **299**, 1719 (2003)
6. N.A. Spaldin, M. Fiebig, Science **309**, 391 (2005)
7. C. Ederer, N.A. Spaldin, Phys. Rev. B **71**, 224103 (2005)
8. W. Eerenstein, F.D. Morrison, J. Dho, M.G. Blamire, J.F. Scott, N.D. Mathur, Science **307**, 1203 (2005)
9. V.R. Singh, A. Garg, D.C. Aggrawal, Solid State Commun. **149**, 734 (2009)
10. A. Lahmar, S. Habouti, C.-H. Solterbeck, M. Dietze, M. Es-Souni, J. Appl. Phys. **107**, 024104 (2010)
11. K.G. Yang, Y.L. Zhang, S.H. Yang, B. Wang, J. Appl. Phys. **107**, 124109 (2010)
12. V.A. Khomchenko, V.V. Shvartsman, P. Borisov, W. Kleemann, D.A. Kiselev, I.K. Bdikin, J.M. Vieira, A.L. Kholkin, Acta Mater. **57**, 5137 (2009)
13. D.S. Rana, K. Takahashi, K.R. Mavani, I. Kawayama, H. Murakami, M. Tonouchi, Phys. Rev. B **75**, 060405 (2007)
14. Y. Wang, Y. Lin, C.W. Nan, J. Appl. Phys. **104**, 123912 (2008)
15. C.J. Cheng, C. Lu, Z. Chen, L. You, L. Chen, J. Wang, T. Wu, Appl. Phys. Lett. **98**, 242502 (2011)
16. F. Huang, X. Lu, W. Lin, Y. Kan, J. Zhang, Q. Chen, Z. Wang, L. Li, J. Zhu, Appl. Phys. Lett. **97**, 222901 (2010)
17. X. Tang, J. Dai, X. Zhu, J. Lin, Q. Chang, D. Wu, W. Song, Y. Sun, J. Am. Ceram. Soc. **95**(2), 538 (2012)
18. S. Hussain, S.K. Hasanain, G.H. Jaffari, S.I. Shah, Curr. Appl. Phys. **15**, 194 (2015)
19. H.M. Rietveld, Acta Crystallogr. **22**, 151 (1967)
20. F. Gao, Y. Yuan, K. Wang, Appl. Phys. Lett. **89**, 102506 (2006)
21. F. Huang, Z. Wang, X. Lu, J. Zhang, K. Min, W. Lin, R. Ti, T.T. Xu, J. He, C. Yue, J. Zhu, Sci. Rep. **3**, 2907 (2013)
22. T. Park, G.C. Papaefthymiou, A.J. Viescas, A.R. Moodenbaugh, S.S. Wong, Nano Lett. **7**, 766 (2007)
23. C. Ederer, N.A. Spaldin, Phys. Rev. B **71**, 060401 (2005)
24. G. Catalan, J.F. Scott, Adv. Mater. **21**, 2463 (2009)
25. Y. Wang, Q.H. Jiang, H.C. He, C.W. Nan, Appl. Phys. Lett. **88**, 142503 (2006)

Journal of Magnetism and Magnetic Materials 418 (2016) 188–193

Contents lists available at ScienceDirect

Journal of Magnetism and Magnetic Materials

journal homepage: www.elsevier.com/locate/jmmm

Effect of Gd-substitution on the ferroelectric and magnetic properties of $BiFeO_3$ processed by high-energy ball milling

Shiwani Sharma [a], Alok Mishra [a], P. Saravanan [b], O.P. Pandey [a], Puneet Sharma [a,*]

[a] School of Physics and Materials Science, Thapar University, Patiala 147004, Punjab, India
[b] Defence Metallurgical Research Laboratory, Hyderabad 500058, India

ARTICLE INFO

Article history:
Received 30 November 2015
Received in revised form
23 February 2016
Accepted 2 March 2016
Available online 3 March 2016

Keywords:
$BiFeO_3$
High-energy ball milling
Dielectric
Magnetization

ABSTRACT

Multiferroic $BiFeO_3$ was synthesized by means of high-energy ball milling (HEBM) followed by thermal annealing at various temperatures and the effect of Gd^{3+} substitution ($x=0.0$–0.20) at Bi^{3+} site was investigated in this study. It is found that the Gd-substitution tends to decrease the impurity phases and the crystallization of single phase $BiFeO_3$ is observed at $x=0.1$. Scanning electron micrograph of $Bi_{1-x}Gd_xFeO_3$ sintered sample indicated a decrease in particle size and change in shape with increasing x. For all the studied samples, the measured dielectric constant values tend to increase from 110 ($x=0.0$) to 250 ($x=0.10$). The dielectric loss is found to be more for the pure $BiFeO_3$ as compared to the $Bi_{1-x}Gd_xFeO_3$. Ferroelectric loops show a maximum polarization of 1.63 μC/cm^2 for the $Bi_{0.9}Gd_{0.1}FeO_3$. Magnetization (M) versus magnetic field (H) hysteresis loops at 300 K $BiFeO_3$ and $Bi_{0.9}Gd_{0.1}FeO_3$ demonstrated non-saturated loops, suggesting the antiferromagnetic nature of the samples. The M–H behavior of the $Bi_{1-x}Gd_xFeO_3$ at 300 K shows the antiferromagnetic nature of the samples. The estimated magnetization value at 10 kOe for the $Bi_{0.9}Gd_{0.1}FeO_3$ sample (0.23 emu/g) is found to be higher than that of the pure $BiFeO_3$ (0.037 emu/g).

1. Introduction

Multiferroic materials have recently gained a considerable attention due to it multifunctional device applications and underlying new physics. Among the multiferroics, $BiFeO_3$ is one of the widely investigated materials due to it ferroelectric and magnetic transition temperature well above room temperature (RT) [1,2]. $BiFeO_3$ is known to possess rhombohedrally distorted perovskite structure that belongs to a space group of $R3c$. The unit cell of $BiFeO_3$ can be represented as pseudo cubic ($a_c=3.963$ Å); and hexagonal ($a_h=5.587$ Å, $c_h=13.867$ Å) structure, where the pseudo cubic direction $[111]_c$ is considered equivalent to $[1\,0\,0]_h$ [3]. Over the past several years, considerable efforts have been made to achieve both strong ferroelectric (FE) and ferromagnetic (FM) polarizations. Researchers have made a considerable progress on the processing and microstructural aspects of $BiFeO_3$ [4–6]. Similarly, efforts also have been made to substitute A site and B site of $BiFeO_3$ by rare earth and transition metal ions, respectively. Effect of metal ion substitution has been thoroughly investigated on the structural, electric and magnetic properties [7–9]. Mathe et al. observed a structural phase transition to orthorhombic at $x=0.6$ and triclinic at $x=0.8$ with La^{3+} substitution at Bi^{3+} site. All the samples showed dispersion in dielectric data. The variation of dielectric constant (ε') with temperature shows a broad peak that broadens with change in composition and shifts corresponding to frequency change reflecting relaxor-type behavior [10]. Palkar et al. studied the coexistence of ferroelectricity and ferromagnetism in $Bi_{0.9-x}Tb_xLa_{0.1}FeO_3$ powder samples ($0<x<0.3$) and these samples were found to exhibit high dielectric constant and magneto-electric coupling at RT [11]. The magnetoelectric coupling was evidenced by the increase of the dielectric constant with the increase of applied magnetic field (H). For $Bi_{0.75}Ba_{0.25}FeO_3$ with $H=8$ kOe, the values of $[\boldsymbol{\varepsilon_r(H)-\varepsilon_r(0)/\varepsilon_r(0)}]$ were 1.7% and 1% at 80 and 300 K, respectively [12]. Fanggao et al. showed that substituting Gd^{3+} at Bi^{3+} site eliminates the impurity phases in $BiFeO_3$ ceramics; also the lattice constants a and c become smaller as the Gd^{3+} content is increased. A strong variation in the dielectric constant and loss has been observed by substitution of Gd [13]. Gd-substitution was found to induce structural phase transition from R3c to Pn2$_1a$ at $x=0.1$ and further increase in x suppresses the spontaneous polarization ($\boldsymbol{P_s}$) in $Bi_{1-x}Gd_xFeO_3$ resulting in a ferroelectric–paraelectric (Pn2$_1$a→ Pnma) phase transition around $0.2<x<0.3$ [14,15].

From the above, it is clear that the low level doping of rare earth at Bi^{3+} site can impart changes in the structure and brings a noticeable variation in the magnetic and electrical properties.

* Corresponding author.
E-mail address: puneet.sharma@thapar.edu (P. Sharma).

http://dx.doi.org/10.1016/j.jmmm.2016.03.006
0304-8853/

Apparently due to difference in the lattice parameters, the doping of Gd^{3+} at the Bi^{3+} has been chosen for their significant influence on the properties of multiferroic $BiFeO_3$. Due to smaller ionic radii (1.053 Å) of Gd^{3+} in comparison with Bi^{3+} (1.17 Å) [16]; its doping at the Bi^{3+} site lead to lattice contraction causing the average particle size to decrease. The difference in the ionic radii of Gd^{3+} in comparison with Bi^{3+} produces strain, which is responsible for imparting changes in the structural, dielectric and ferroelectric properties of $BiFeO_3$. Along these lines, in this paper we study the effect of doping of $Gd^{3+}$by solid state reaction method and its influence on the structural, dielectric, ferroelectric and magnetic properties.

2. Experimental

The polycrystalline $Bi_{1-x}Gd_xFeO_3$ ($x=0.0$, 0.05, 0.1, 0.15 and 0.2) were prepared by high energy ball milling followed by thermal annealing. The raw materials used for the experiments were Bi_2O_3 (Loba Chem), Gd_2O_3 (Loba Chem), and Fe_2O_3 (Sigma Aldrich) with 99% purity. The raw materials were weighed in their stoichiometric composition and then mixed manually using mortar and pestle for 30 min. Further, wet mixing was carried out for 3 h by a planetary ball mill using acetone as a solvent. The RPM and ball-to-charge ratio were 60 and 2:1, respectively. After mixing, the excess acetone was drained and the powder was dried in normal atmosphere. The dried powders were further subjected to high-energy ball milling in a tungsten carbide vial for 10 h. The RPM was fixed at 250 and the ball-to-charge ratio was 10:1. For determining the phase formation temperature, the as-milled powder samples were analyzed by differential thermal analysis (DTA) and thermo gravimetric analysis technique (TGA) using the Perkin Elmer (Pyris Diamond TG/DTA). Annealing of the milled $BiFeO_3$ sample was carried out in a tubular furnace at ambient atmosphere in the temperature range between 750 and 900 °C. The holding time was fixed to 1 h. The Gd-doped samples were thermally annealed at an optimal temperature of 830 °C for 1 h.

The phase identification of the annealed powders was carried out by X-ray diffraction (XRD) using Cu-Kα radiation ($\lambda=1.54178$ Å) (Philips X-pert PRO); Fourier transform infra-red (FTIR) measurements on the annealed powders were carried out by spectrum BX II instruments (Perkin Elmer) in the range of 400–2000 cm^{-1}. Further the powder were pressed into pellets of 10-mm diameter dye under 10 t/cm^2 pressure using a hydraulic press. The pressed pellets were sintered at temperature of 875 °C for 4 h. For dielectric and *P–E* loop measurements the sintered pellets were coated on both sides by Ag paste for better electrical contact with the electrodes. The ferroelectric loops were measured at RT using PE loop tracer (Radiant technologies). The dielectric properties were measured at RT using LCR meter Agilent 4284A. A scanning electron microscopy (SEM, JEOL model 6510) was employed for studying the microstructural features of milled powders. A thin coating of Au was sputtered onto the film surface to avoid any charging during the SEM analysis. The magnetic measurements were performed by vibrating sample magnetometer (VSM) at RT.

3. Results and discussion

Fig. 1 shows the TGA/DTA of the as-milled $BiFeO_3$ powder. The DTA of the synthesized sample shows minor endothermic peaks at 827, 859, and 948 °C. These peaks correspond to the occurrence of impurity phases at different temperatures, as evidenced in the XRD patterns (Fig. 2). $BiFeO_3$ is known to be very unstable at high

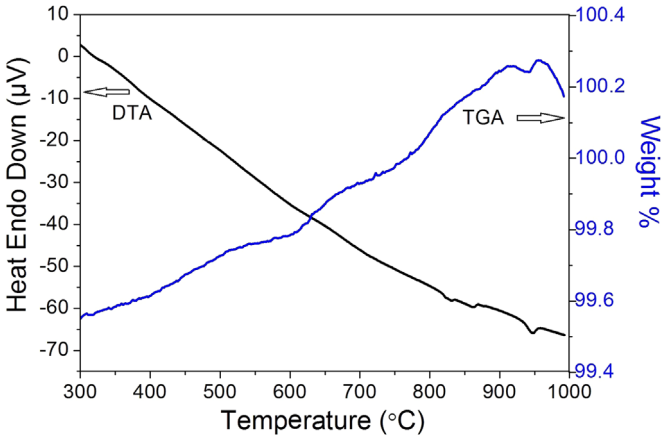

Fig. 1. DTA/TGA curves of the as-milled $BiFeO_3$ powder.

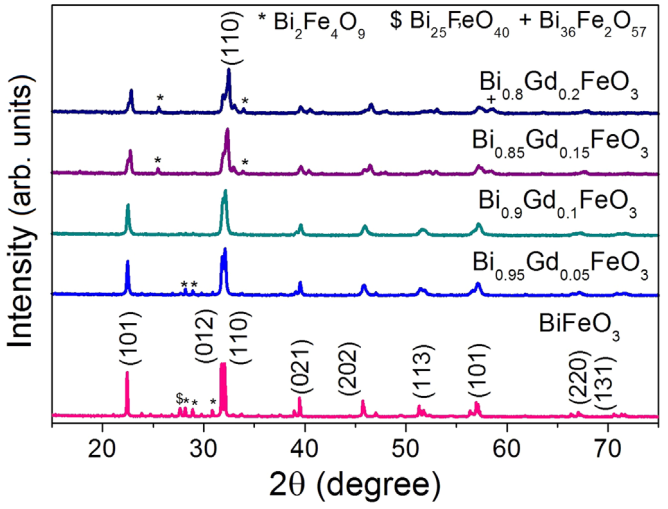

Fig. 2. X-ray diffraction patterns of $Bi_{1-x}Gd_xFeO_3$ ($x=0.05$, 0.1, 0.15 and 0.2).

temperature of β–γ transition and hence it rapidly get decomposed into parasitic phases like $Bi_2Fe_4O_9$ or Fe_2O_3 [1]. The corresponding TGA graph shows increase in weight within the measured temperature range. From the DTA curve, it is evident that the formation of pure $BiFeO_3$ phase is occurred at ~830 °C and accordingly, this temperature was chosen for annealing. The suitability of this annealing temperature on the formation of pure $BiFeO_3$ was further confirmed by subjecting the as-milled powders to annealing in the temperature range of 750–900 °C. Relatively, a larger amount of impurity phases was observed at all temperatures, expect for the sample annealed at 830 °C (XRD results are not shown). This is very much consistent with the results of DTA and for this reason, the Gd-doped samples were subjected to annealing at 830°C. Fig. 2 shows the X-ray diffraction pattern of $Bi_{1-x}Gd_xFeO_3$ ($x=0.0$, 0.05, 0.1, 0.15 and 0.2) annealed at 830 °C. The XRD patterns indicated the formation of pure phase $Bi_{1-x}Gd_xFeO_3$ (JCPDS # 14-0181) as the concentration of Gd is increased up to $x=0.1$. Any further increase in the concentration of Gd leads to the formation of secondary phases such as $Bi_2Fe_4O_9$ (JCPDS # 20-0836), $Bi_2Fe_4O_9$ (JCPDS # 20-0836) and $Bi_{36}Fe_2O_{57}$ (JCPDS # 42-0181).

Fig. 3 shows the SEM micrographs of sintered pellets of $BiFeO_3$ and $Bi_{0.8}Gd_{0.2}FeO_3$. The samples for the SEM analysis were prepared by carefully spreading a thin layer of powder on the double sided tape fixed to the specimen holder and subsequently coating it with a gold layer of approximately 10 nm thickness. It is evident from Fig. 3 that the particles of pure $BiFeO_3$ are larger and

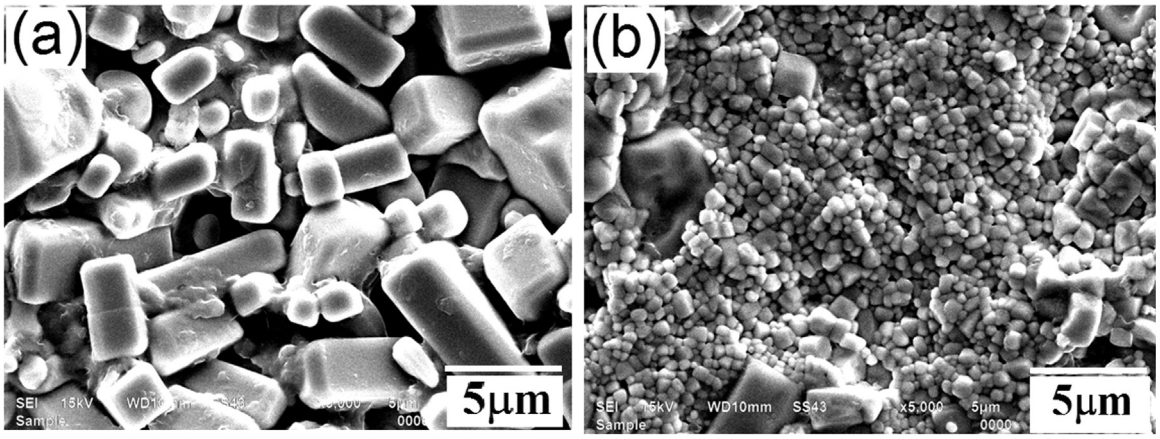

Fig. 3. SEM micrographs of the pure $BiFeO_3$ (a) and $Bi_{0.8}Gd_{0.2}FeO_3$ samples (b), after being processed by HEBM and sintering.

rectangular in shape with particle sizes in the range of 5-7 μm. As the concentration of Gd (x=0.1, and 0.2) is increased the particle becomes spheroidal and small as compared to the pure $BiFeO_3$. The particle size of $Bi_{0.8}Gd_{0.2}FeO_3$ is reduced to 0.50–0.80 μm. The smaller ionic radii (1.053 Å) of Gd^{3+} in comparison with Bi^{3+} (1.17 Å) [16] lead to lattice contraction causing the average particle size to decrease. The shift in XRD peaks to greater 2θ also confirms the substitution of smaller Gd^{3+} ions at Bi^{3+} site. Further partial merging of the (012) and (110) peaks in XRD (Fig. 2) indicates the structural distortion due to Gd doping [13–15]. The crystallite size is also confirmed by the Scherrer formula for the undoped and doped samples and found to decrease from 77.6 nm (x=0.0) to 32.5 nm (x=0.20).

Fig. 4 shows the FTIR spectra of undoped and doped samples $Bi_{1-x}Gd_xFeO_3$ (x=0.0, 0.05, 0.1, 0.15 and 0.20) in the range of 400–2000 cm^{-1}. A constant reflection is observed in the region 400 to 500 cm^{-1} in Fe–O bond of Fe_2O_3 up to 850 °C. At higher temperature (900 °C) this peak eventually disappears indicating the diffusion of Fe–O stretch (not shown here). Only one stretch is found in the region 400–525 cm^{-1} that corresponds to the presence of metal oxide bonds at lower doping concentration. However as the dopant concentration is increased, sharp reflections at 442 and 439 cm^{-1} are observed, which indicate the presence of Fe–O bond (stretching and bending) in this range. Besides, no additional peaks for the unreacted material are found in the FTIR spectra, indicating the complete substitution of Gd at the valence site.

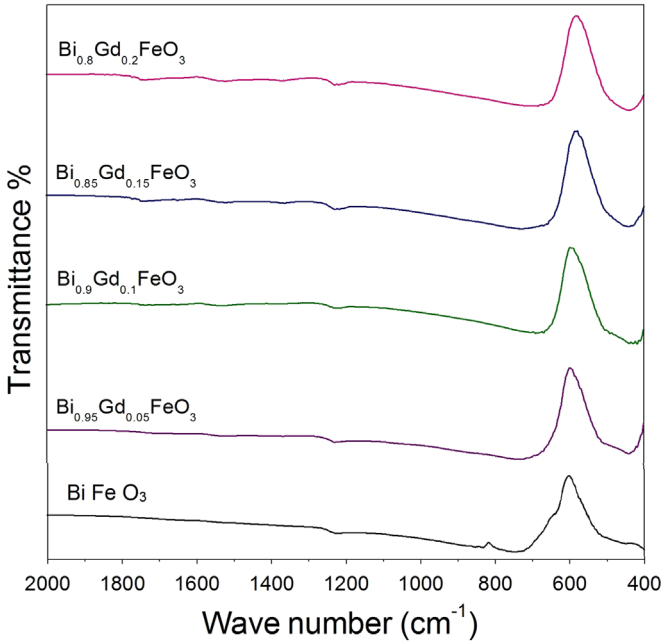

Fig. 4. FTIR spectra of $Bi_{1-x}Gd_xFeO_3$ (x=0, 0.05, 0.1, 0.15 and 0.2).

Fig. 5 shows the RT ferroelectric measurements of the doped samples $Bi_{1-x}Gd_xFeO_3$ (x=0.05, 0.1, 0.15 and 0.2) at a maximum applied field of 55 kV/cm. It can be noticed that there is no saturation in the P–E loops due to the leakage current [17,18]. The inset in Fig. 5 shows the polarization and coercivity behavior of $Bi_{1-x}Gd_xFeO_3$ with x. The remnant polarization P_r and maximum polarization is a function of Gd concentration x as shown in Table 1. As the concentration of Gd is increased, the polarization increases up to x=0.1 and then decreases with further increase of Gd. The polarization of the sample $Bi_{0.9}Gd_{0.1}FeO_3$ is high as compared to the other compositions. This shows that the high polarization is achieved at x=0.1. The coercivity and remnant polarization increases up to x=0.15 and decreases afterwards. The finer particle size of the Gd-doped sample could be the possible reason for the observed large coercivity in this sample.

Fig. 6 shows the RT dielectric constant (ε') measurements with respect to frequency in the range of 20 Hz to 1 MHz for the composition $Bi_{1-x}Gd_xFeO_3$ (x=0.0, 0.05, 0.1, 0.15 and 0.2) (as shown in Fig. 6(a)). The value of ε' is found to be higher (250) for x=0.1 attributed to the formation of pure phase. The measured ε' at RT for the pure phase composition is 110, which is comparable with

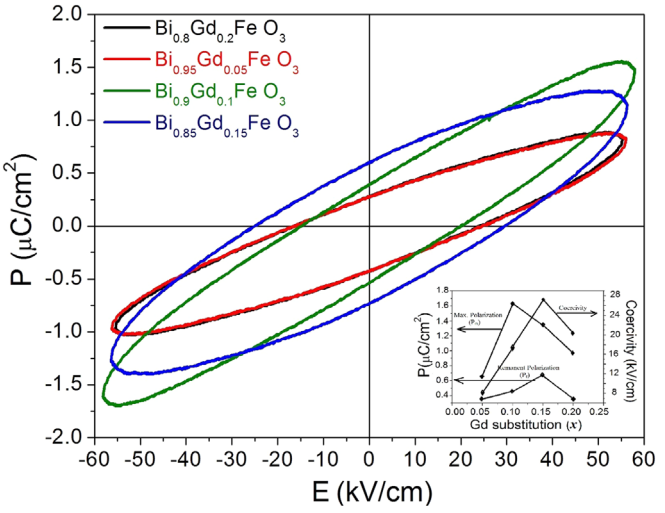

Fig. 5. RT ferroelectric hysteresis loops of $Bi_{1-x}Gd_xFeO_3$ (x=0–0.2). Inset shows the polarization and coercivity as a function of Gd-concentration.

Table 1
Polarization measurements of the $Bi_{1-x}Gd_xFeO_3$ (x=0.0, 0.05, 0.1, 0.15 and 0.20).

Sample composition	Coercivity (kV/cm)	Remnant polarization P_r (μC/cm^2)	Polarization P_m (μC/cm^2)
$Bi_{0.95}Gd_{0.05}FeO_3$	8.081	0.364	0.651
$Bi_{0.90}Gd_{0.1}FeO_3$	17.386	0.461	1.630
$Bi_{0.85}Gd_{0.15}FeO_3$	27.246	0.675	1.342
$Bi_{0.8}Gd_{0.2}FeO_3$	20.381	0.354	0.961

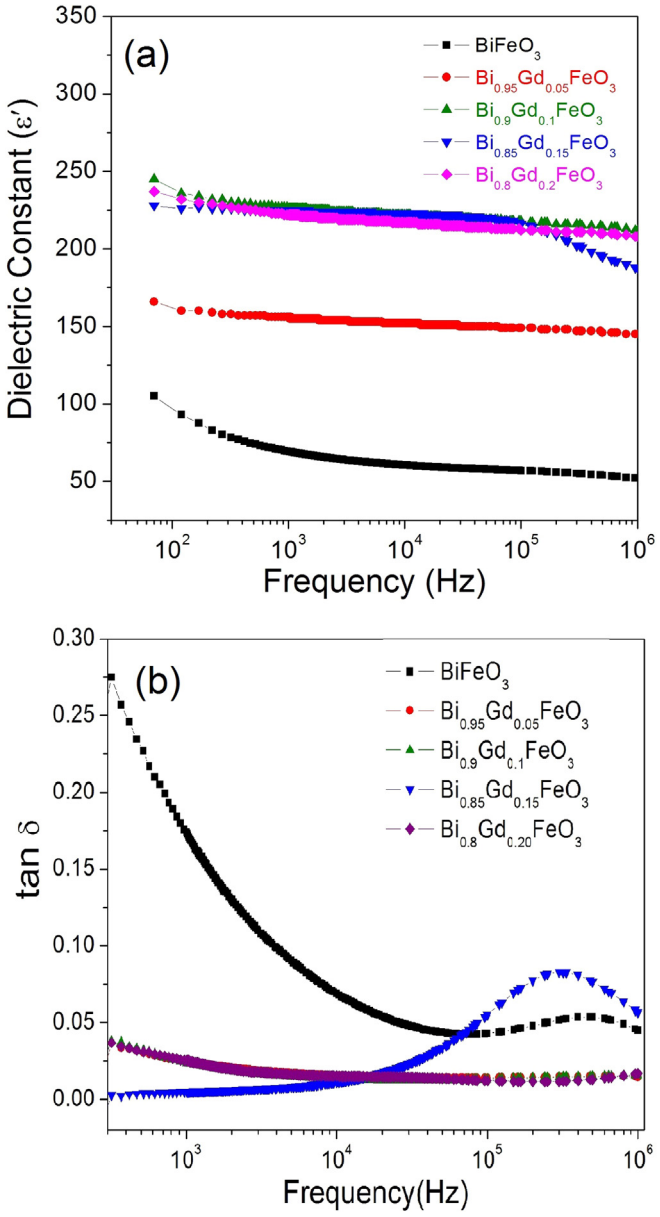

Fig. 6. RT frequency dependent (a) dielectric constant and (b) dielectric loss curves for the $Bi_{1-x}Gd_xFeO_3$ (x=0, 0.05, 0.1, 0.15 and 0.2).

the earlier reported values [17]. For all the samples, the estimated value of ε'is higher at lower frequency; it decreases as the frequency is increased and becomes nearly constant beyond 10 kHz. This property can be understood by the space charge relaxation phenomena, wherein at low frequency the space charge is able to follow the frequency reversal but at higher frequency the space charge may not have sufficient time to undergo relaxation [17,18]. There is drastic change in the ε' as the concentration of Gd (x=0.05, 0.1, 0.15 and 0.2) is increased as compared to pure $BiFeO_3$. It is clearly evident from the SEM images (Fig. 3) that the particle size decreases upon Gd-doping, which leads to increase in surface area of the particles. This surface area enhancement tends to increase the surface boundary resistance and thereby enhances the ε' and decreases tanδ. Decreased porosity due to densification of the system or the local defects on doping with Gd in comparison to the undoped $BiFeO_3$ leads to enhancement of dielectric constant [10,13]. Fig. 6(b) shows the dielectric loss (tanδ) measurements with frequency. The value of tanδ is found to be higher for $BiFeO_3$ which is comparable with the other reported values [10,13]. The value of tanδ is higher at lower frequency and decreases as the frequency is increased, as expected for $BiFeO_3$ and becomes nearly constant beyond 10 kHz for x=0.05, 0.10 and 0.20. At higher frequency (beyond 100 kHz), a relaxation peak is observed for x=0.00 and 0.15 due to the dielectric resonance giving maximum power dissipation. Fig. 7 shows the dielectric measurements with temperature (T) for undoped and Gd-doped $BiFeO_3$ samples. In the measured temperature range, the dielectric constant (ε') and dielectric losses (tan δ) decreases with the increase in frequency for all the samples. The ε' and tan δ increases gradually with temperature up to 200 °C and afterwards increases sharply due to the increased thermal conductivity [19,20]. An anomaly is observed near ~289, 334, 364 and 357 °C for x=0, 0.05, 0.10 and 0.15, respectively in both the ε' vs. T, as well as in tan δ vs. T plots. This may correspond to antiferroelectric to paraelectric phase transition which increases with Gd- doping up to x=0.10 and starts decreasing afterwards for x=0.15 composition in consistent with the earlier reported studies on bulk $BiFeO_3$ [21,22].

Fig. 8 shows the in-plane M-H behavior of undoped and Gd-doped $BiFeO_3$ obtained at RT. The M-H behavior shows the antiferromagnetic nature for the undoped and Gd-doped $BiFeO_3$ samples. $BiFeO_3$ is well known antiferromagnetic phase with Neel temperature (T_N) of ~643 K and is largely investigated by many others [1,23,24]. The spin cycloid structure and canting of the antiferromagnetically ordered spins are marginally modified on Gd-doping, resulting in only a small improvement in the magnetization. The magnetization value estimated at 10 kOe, increases from 0.037 to 0.42 emu/g as 'x' increases from 0 to 0.15. This could be probably due to the relatively smaller grain size in the Gd-doped samples, which tends to increase the magnetization values to some extent due to uncompensated moments at the grain boundaries.

4. Conclusion

Multiferroic $Bi_{1-x}Gd_xFeO_3$ was synthesized by high-energy ball milling technique. Single phase $Bi_{1-x}Gd_xFeO_3$ was obtained at x=0.1. This shows that for x=0.1, Gd has been incorporated with good dispersivity in $BiFeO_3$ crystal structure and any further increase in 'x' beyond 0.1 will lead to secondary phase formation. The SEM analysis revealed the decrease in grain size and change in grain-shape with increasing doping content of Gd. The P–E loops demonstrated a maximum polarization for the $Bi_{0.9}Gd_{0.1}FeO_3$ sample. The dielectric constant and dielectric losses are strongly dependent on the concentration of Gd^{3+}. The dielectric loss of pure $BiFeO_3$ is maximum as compared to all the Gd-doped

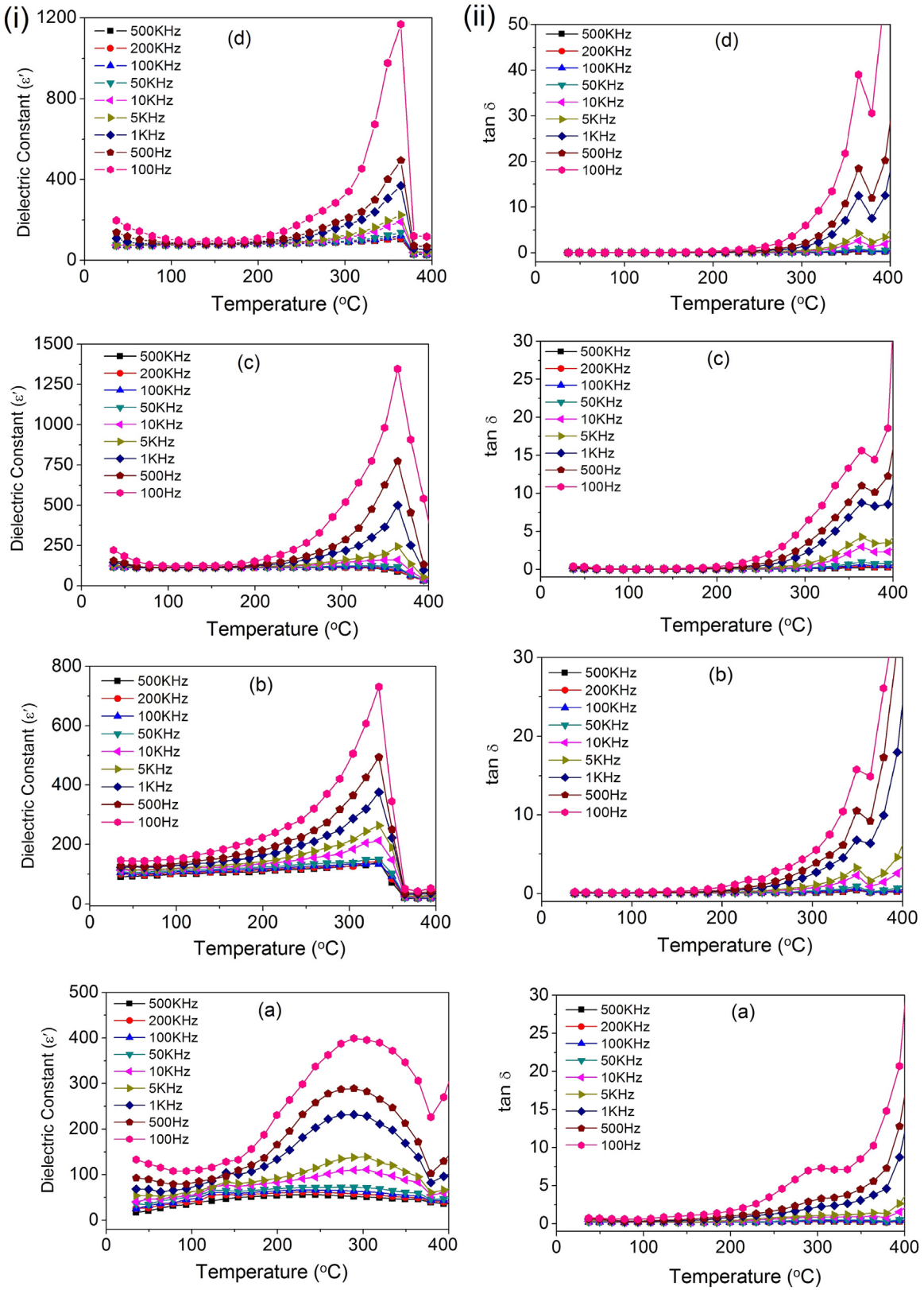

Fig. 7. (i) Dielectric constant versus temperature measurements for $Bi_{1-x}Gd_xFeO_3$ (a) $x=0$, (b) $x=0.05$, (c) $x=0.10$ and (d) $x=0.15$ compositions and (ii) dielectric loss versus temperature measurements for $Bi_{1-x}Gd_xFeO_3$ (a) $x=0$, (b) $x=0.05$, (c) $x=0.10$ and (d) $x=0.15$ compositions.

samples. Decreased porosity or the local defects, increase in the surface boundary resistance due to decrease in particle size on Gd-doping, enhances the ε' and decreases tan δ. The antiferroelectric to paraelectric phase transition temperature increases with Gd-doping upto $x=0.10$ and starts decreasing afterwards for $x=0.15$ composition. The M–H behavior of the $Bi_{1-x}Gd_xFeO_3$ at 300 K shows the antiferromagnetic nature of the samples. The spin cycloid structure and canting of the antiferromagnetically ordered

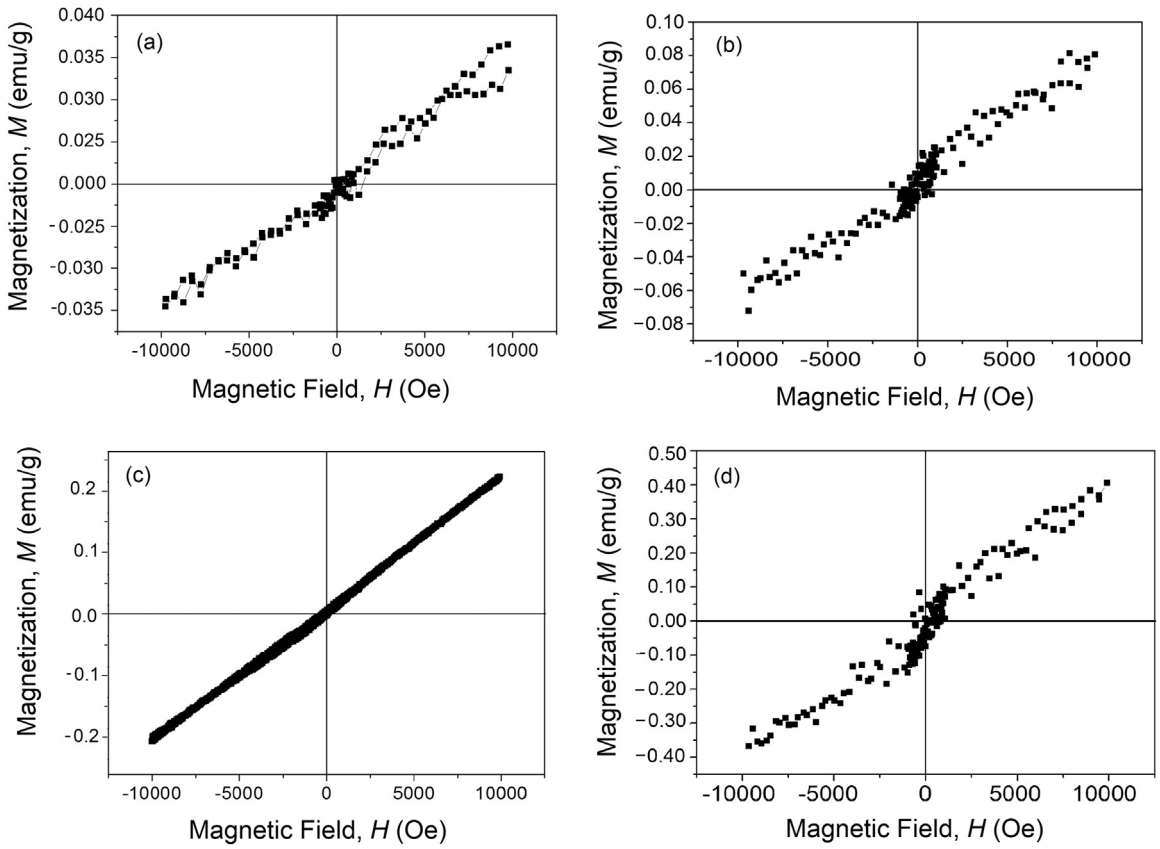

Fig. 8. *M–H* loops of (a) $BiFeO_3$, (b) $Bi_{0.95}Gd_{0.05}FeO_3$, (c) $Bi_{0.9}Gd_{0.1}FeO_3$ and (d) $Bi_{0.85}Gd_{0.15}FeO_3$ samples obtained at RT.

spins are not strongly modified, resulting in only a small improvement in the magnetization on Gd doping.

Acknowledgments

The author Shiwani Sharma gratefully acknowledge the University Grants Commission, India (UGC) for the fellowship (letter no.-SPMS/UGC/607). Author Puneet Sharma acknowledge funding Granted by UGC 40-446/2011 (SR).

References

[1] G. Catalan, J.F. Scott, Physics and application of bismuth ferrite, Adv. Mater. 21 (2009) 2463–2485.
[2] W. Eerenstein, N.D. Mathur, J.F. Scott, Multiferroic and magnetoelectric materials, Nature 442 (2006) 759–765.
[3] V.V. Lazenka, G. Zhang, J. Vanacken, I.I. Makoed, A.F. Ravinski, V.V. Moshchalkov, Structural trans-formation and magnetoelectric behavior in $Bi_{1-x}Gd_xFeO_3$ multiferroics, J. Phys. D: Appl. Phys. 45 (2012) 125002 7pp.
[4] A.K. Pradhan, Kai Zhang, D. Hunter, J.B. Dadson, G.B. Loutts, Magnetic and electrical properties of single phase multiferroic, J. Appl. Phys. 97 (2005) 093903.
[5] Jong Kuk Kim, Sang Su Kim, Won-Jeong Kim, Sol–gel synthesis and properties of multiferroic $BiFeO_3$, Mater. Lett. 59 (2005) 4006–4009.
[6] W.N. Su, D.H. Wang, Q.Q. Cao, Z.D. Han, J. Yin, J.R. Zhang, Y.W. Du, Large polarization and enhanced magnetic properties in $BiFeO_3$ ceramic prepared by high-pressure synthesis, Appl. Phys. Lett. 91 (2007) 092905.
[7] Shan-Tao Zhang, Yi Zhang, Ming-Hui Lu, Chao-Ling Du, Yan-Feng Chen, Zhi-Guo Liu, Yong-Yuan Zhu, Nai-Ben Ming, Substitution-induced phase transition and enhanced multiferroic properties of $Bi_{1-x}La_xFeO_3$ ceramics, Appl. Phys. Lett. 88 (2006) 162901.
[8] G.L. Yuan, Siu Wing Ora, Structural transformation and ferroelectro magnetic behavior in single-phase $Bi_{1-x}Nd_xFeO_3$ multiferroic ceramics, Appl. Phys. Lett. 89 (2006) 052905.
[9] Deepti Kothari, V. Raghavendra Reddy, Ajay Gupta, Vasant Sathe, A. Banerjee, Multiferroic properties of polycrystalline Bi_{1-x} Ca_xFeO_3, Appl. Phys. Lett. 91 (2007) 202505.
[10] V.L. Mathe, K.K. Patankar, M.B. Kothalei, S.B. Kulkarni, P.B. Joshi, S.A. Patil, Preparation, structural analysis and dielectric properties of $Bi_xLa_{1-x}FeO_3$ perovskite Pramana, J. Phys. 58 (2002) 1105.
[11] V.R. Palkar, Darshan C. Kundaliya, S.K. Malik, S. Bhattacharya1, Magnetoelectricity at room temperature in the $Bi_{0.9-x}Tb_xLa_{0.1}FeO_3$ system, Phys. Rev. B 69 (2004) 212102.
[12] D.H. Wang, W.C. Goh, M. Ning, C.K. Ong, Effect of Ba doping on magnetic, ferroelectric, and magnetoelectric properties in multiferroic $BiFeO_3$ at room temperature, Appl. Phys. Lett. 88 (2006) 212907.
[13] Chang Fanggao, Song Guili, Fang Kun, Qin Ping, Zeng Qijun, Effect of gadolinium substitution on dielectric properties of bismuth ferrite, J. Rare Earth, Spec. (24) (2006) 273–276.
[14] V.A. Khomchenko, D.A. Kiselev, I.K. Bdikin, V.V. Shvartsman, P. Borisov, W. Kleemann, J.M. Vieira, A.L. Kholkin, Crystal structure and multiferroic properties of Gd-substituted $BiFeO_3$, Appl. Phys. Lett. 93 (2008) 262905.
[15] V.A. Khomchenko, V.V. Shvartsman, P. Borisov, W. Kleemann, D.A. Kiselev, I. K. Bdikin, J.M. Vieira, A.L. Kholkin, Effect of Gd substitution on the crystal structure and multiferroic properties of $BiFeO_3$, Acta Mater. 57 (2009) 5137–5145.
[16] R.D. Shannon Revised, Effective ionic radii and systematic studies of interatomie distances in halides and chaleogenides, Acta Crystallogr. A32 (1976) 751.
[17] Z.K. Cheng, A.H. Li, X.L. Wang, S.K. Dou, K. Ozawa, H. Kimura, S.J. Zhang, T. R. Shrout, Structure, ferroelectric properties, and magnetic properties of the La-doped bismuth ferrite, J. Appl. Phys. 103 (2008) 07E507.
[18] S. Kazhugasalamoorthy, P. Jegatheesan, R. Mohandoss, N.V. Giridharan, B. Karthikeyan, R. Justin Joseyphus, S. Dhanuskodi, Investigations on the properties of pure and rare earth modified bismuth ferrite ceramics, J. Alloy. Compd. 493 (1–2) (2010) 569.
[19] A.K. Jonscher, F. Meca, H.M. Millany, Charge-carrier contributions to dielectric loss, J. Phys. C: Solid State Phys. 12 (1979) L29329.
[20] A.K. Jonscher, Dielectric relaxation in solids, J. Phys. D 32 (1999) R57–R70.
[21] V. Goian, S. Kamba, S. Greicius, D. Nuzhnyy, S. Karimi, I.M. Reaney, Terahertz and infrared studies of antiferroelectric phase transition in multiferroic $Bi_{0.85}Nd_{0.15}FeO_3$, J. Appl. Phys. 110 (2011) 074112.
[22] E. Palaimiene, J. Macutkevic, D.V. Karpinsky, A.L. Kholkin, J. Banys, Dielectric investigations of polycrystalline samarium bismuth ferrite ceramic, Appl. Phys. Lett. 106 (2015) 012906.
[23] T. Park, G.C. Papaefthymiou, A.J. Viescas, A.R. Moodenbaugh, S.S. Wong, Size dependent magnetic properties of single crystalline multiferroic $BiFeO_3$ nanoparticles, Nano Lett. 7 (2007) 766–772.
[24] F. Huang, Z. Wang, X. Lu, J. Zhang, K. Min, W. Lin, R. Ti, T.T. Xu, J. He, C. Yue1, J. Zhu, Peculiar magnetism of $BiFeO_3$ nanoparticles with size approaching the period of the spiral spin structure, Sci. Rep. 3 (2013) 2907/1–2907/7.